Doctorate School in Sciences and Technologies of Chemistry and Materials
Curriculum: Nanochemistry

Dipartimento di Chimica e Chimica Industriale, Università di Genova

Dipartimento di Nanochimica, Istituto Italiano di Tecnologia

Structural Evolution of PdCu and PtCu Nanocrystal Catalysts over Redox Treatments

Lea Pasquale

Supervisors: Prof. Liberato Manna
Dr. Massimo Colombo
Prof. Riccardo Ferrando

XXXI Cycle Ph.D. (2015–2018)

Abstract

This thesis presents the main results obtained in my research activity as a PhD student on the synthesis of PdCu and PtCu bimetallic nanocrystals (NCs) and their application as catalysts for CO oxidation as a probe reaction. Focusing on Cu and keeping constant the NC size and the support material, the role of the noble metal in the alloy/dealloy/migration process of noble metal-Cu alloyed NCs was studied. The role of the support material in the same transformations was also objected of study. NCs with defined size and composition were successfully synthesized by means of colloidal synthesis methods. The NCs were further deposited on a SiO_2 support and studies of catalytic activity were performed on NCs exposed to oxidizing and reducing pre-treatments before each catalytic test. The catalytic activity data were also collected on γ-Al_2O_3 support to investigate the correlation between the activity and the structural properties of such NCs. For this purpose, different analysis techniques were used as routine ex situ methods to characterize these materials. In situ methods such as diffuse reflectance infrared Fourier transform spectroscopy and X-ray absorption fine structure spectroscopy were used to monitor the structure evolution of the metals under controlled conditions. The use of in situ and operando methods has significantly highlighted that the structure of the metallic particles can be dramatically modified under reaction conditions in terms of geometry and chemical composition. The analysis and synthesis techniques and the main results obtained on structural changes in the NC catalysts under different conditions are widely described. The publications and scientific communications on these topics presented at international conferences are the following:

Publications:

1. Destro, P.; Kokumai, T.; Scarpellini, A.; Pasquale, L.; Manna, L.; Colombo, M.; Zanchet, D., The crucial role of the support in the transformations of bimetallic nanoparticles and catalytic performance. ACS Catal 2018, 8, 1031-1037.
2. Pasquale, L.; Najafishirtari, S.; Brescia, R.; Scarpellini, A.; Manna, L.; Colombo, M., Gas atmosphere induced structural changes of bimetallic noble metal-copper nanocrystals: the role of the noble metal" (in preparation).
3. Pasquale, L.; Najafishirtari, S.; Brescia, R.; Scarpellini, A.; Manna, L.; Colombo, M., Revealing the synergy between oxide and alloy phases on the performance of bimetallic PdCu and PtCu catalysts for CO oxidation reaction" (in preparation).

Communications to conferences:

1. Pasquale, L.; Brescia, R.; Scarpellini, A.; Manna, L.; Colombo M., Effect of redox treatments on the structure evolution of γ-Al_2O_3 supported bimetallic noble metal copper nanocrystal catalysts. International Meeting on Nanoalloys IMN 2018, 22nd-25th May 2018, Orlèans, France.
2. Pasquale, L.; Manna, L.; Colombo, M., The role of the noble metal in the transformations of supported copper-based bimetallic nanocrystals upon oxidative or reductive pre-treatments. North American Catalysis Society Meeting 2017 (NAM25), 4th-9th June 2017, Denver, Colorado.
3. Pasquale, L.; Brescia, R.; Scarpellini, A.; Manna, L.; Colombo, M., Gas atmosphere induced structural changes of bimetallic noble metal-copper nanocrystals: the role of the noble metal. Catalysis Fundamentals and Practice Summer School 17th-21st July 2017, Liverpool, UK.
4. Pasquale, L.; Manna, L.; Colombo, M., The effect of red-ox treatments on the catalytic activity of PtCu and PdCu NCs: an *in-situ* DRIFTS study." 13th European Congress on Catalysis EUROPACAT 2017. 27th-31th August, Florence, Italy.
5. Pasquale, L.; Brescia, R.; Scarpellini, A.; Manna, L.; Colombo, M.,. Dynamic structural changes of γ-Al_2O_3 supported bimetallic noble metal-copper nanocrystal catalysts over redox treatments. Designing Nanoparticle Systems for Catalysis Faraday Discussion, 16th – 18th May 2018, London, United Kingdom.
6. Pasquale, L.; Najafishirtari, S.; Brescia, R.; Scarpellini, A.; Manna, L.; Colombo, M., Probing the evolution of PdCu and PtCu bimetallic nanocrystal catalysts under operando conditions by in-situ X-ray absorption spectroscopy. International Meeting on Nanoalloys IMN 2019, 4th-7th June 2019, Genoa, Italy.

Contents

Chapter 1

Introduction

Bimetallic nanoparticle's based catalysts are among the most interesting materials for heterogeneous catalytic processes, thanks to the possibility of tuning both the electronic and geometric properties of a metal through alloying it with a second one. Such integration creates a vast number of possibilities for varying the surface structure and composition of metal catalysts, enabling the development of novel nanocatalysts with high performance in terms of activity, selectivity and stability.[1] In particular, due to the success in the synthesis of colloidal metallic nanoparticles in the recent decade, size, shape and composition of bimetallic nanocrystals (NCs) have become controllable to a significant extent.[2, 3]

On the other hand, these NCs can undergo extensive structural evolution upon exposure to the reactants in the reaction conditions, such as change in surface composition, chemical state, structure and reactivity.[4-10] Ultimately, in analogy with monometallic NCs, also the bimetallic NCs can suffer from sintering and/or be re-dispersed in certain conditions and gas atmosphere. Ostwald ripening and particle disintegration induced by reactants are function of three main interactions: adsorbate-metal, metal-support and metal-metal interactions,[11] and have been the subject of study mainly for monometallic systems.[12, 13]

Understanding how electronic and/or geometric modifications of monometallic system by alloying influence these phenomena is still challenging and only a few studies concerning this topic are reported in literature.[14-16] Indeed, in the case of bimetallic systems, the two NC components were characterized by different interactions with the support, and the presence of the second metal altered these interactions as well.[17]

Within this context, this thesis addresses how the metal-metal interactions affect the Ostwald ripening and particle disintegration phenomena in bimetallic NCs exposed to either oxidizing and reducing atmospheres. Focusing on Cu, and keeping constant the NC size and the support material, the role of Pd and Pt metals in the alloy/dealloy/migration process of noble metal-Cu bimetallic alloyed NCs was studied, in analogy to what observed for the AuCu systems,[19,20] along with the role of the support that has a significant effect on the structural evolution of the alloyed NCs.

Additionally, the work highlighted how the catalytic activity in the CO oxidation, used as model reaction, strictly depended on the operating atmosphere, which induced structural changes such as phase segregation and species migration on the support surface.

Specifically, colloidal synthesis was adopted as the main route to prepare PdCu and PtCu NCs in order to control size, shape, and composition. The as-synthesized bimetallic NCs were anchored on different supports such as Al_2O_3 and SiO_2, and then, subjected to a dedicated study where their transformations upon different pre-treatments under oxidizing or reducing atmospheres were deeply investigated. The transformations that the NCs underwent upon different activation treatments were correlated with the catalytic activity in the CO oxidation reaction. The catalysts were characterized by means of common techniques such as TEM, XRD, SAED and STEM-HAADF-EDS to investigate the composition, structure and morphology of the prepared materials and to study the transformations and attempt to identify the nature of the active sites. Besides ex-situ characterization of the tested catalytic materials, operando and in situ studies were also performed such as *in situ* Diffuse Reflectance Infrared Fourier Transform Spectroscopy by the probe molecule of CO and *in situ* X-ray Absorption Spectroscopy with synchrotron radiation source.

Within this context, the basics of the colloidal chemistry will be discussed in this chapter, followed by a description of some of the applications of bimetallic NCs in catalysis, referring specifically to their transformations driven by temperature and gas atmospheres, as well as the role of the support in such transformations.

1.1 Basic Principles of Design of Nanocrystal-Colloidal Synthesis

Metal nanoparticles, typically 1 to 100 nm, have been intensely studied in recent years. They exhibit properties (optical, electronic, magnetic, catalytic and so on) that are quite different from those of individual atoms or their bulk counterparts due to the quantum-size and surface effects.[18, 19] More importantly, the properties are usually size- and structure-dependent, and have attracted research attention from both basic science or application viewpoints during the last two decades.

Since the material properties can be finely tuned by varying the size and shape, high control over the synthesis of such systems is of key importance to fully exploit the potential of those systems. Two different strategies can be selected to fabricate nanocrystals: the top-down physical processes and the bottom-up chemical methods. The physical processes can produce large quantities of nanocrystals by a process of "dismantling" bulk crystals. Following this approach, however, the synthesis of uniformly sized nanocrystals and their size-control is very difficult to achieve. On the other hand, colloidal chemical synthetic methods can be used to synthesize uniform nanocrystals with a controlled particle size starting from atomic or molecular components.[20] The colloidal chemistry approach is one of the most powerful methods to prepare metallic NCs with well-defined shapes.[21]

Colloidal nanocrystals are synthesized through wet chemical procedures and are typically made of a crystalline core with the desired chemical composition and a monolayer surface shell of coordinating organic ligands that provide the solubility and the colloidal stability. The synthesis is generally done in an organic medium containing the chemical precursors or reactants, solvents,

and surfactants (also called capping agents). The latter substances can control both the reduction rate of the metal precursors and the aggregation process of metal atoms.[22]

The formation of nanocrystals involves the following steps: precursor solution formation from metal salts with ligands, precursor reaction leading to the nucleation step, formation of NCs and their separation from the reaction solution. Upon heating at high temperatures (150-400°C) the precursors, containing the atomic species needed to build the NCs, decompose thermally or chemically by the addition of a secondary chemical agent, to form the monomers necessary for the nucleation and growth of the nanocrystals. The organic ligands used at this stage (i.e. amines, phosphines, thiols, carboxylic acids) are molecules stable at high temperatures and capable of binding to the surface of the growing crystals regulating their growth and shape, while preventing their aggregation. In the subsequent step, the monomers rapidly react forming the nuclei of nanocrystals. Finally, these nuclei, if stable, can grow forming small NCs by the addition of the remaining monomers (Fig. 1.1).

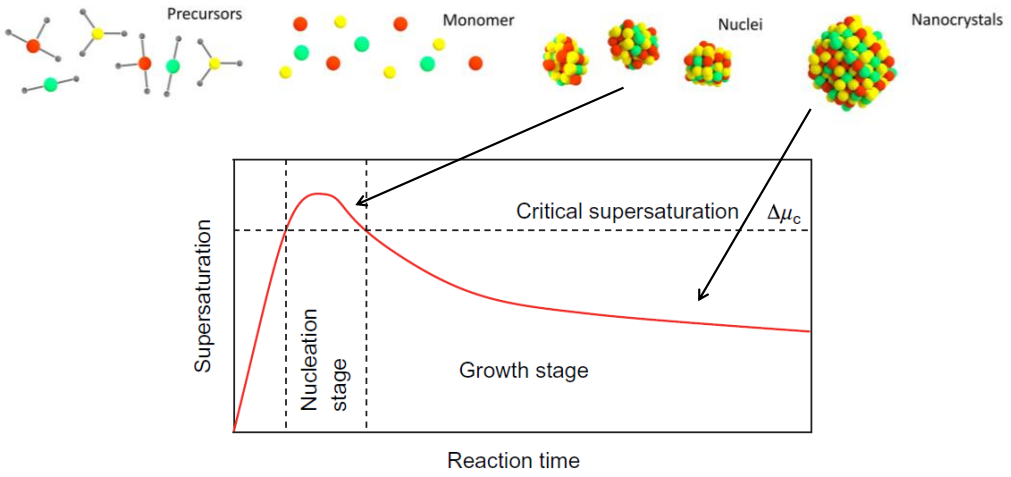

Fig. 1.1 – Scheme of the mechanism of colloidal synthesis. The formation of nanocrystals involves three stages which are characterized by the level of the supersaturation. In the first stage, a critical supersaturation $\Delta\mu_c$ is approached by the increase of monomer concentration. Reached this point, the nucleation is induced as the second stage during which the nuclei start growing by consuming more monomers. Once the concentration of monomers has dropped below the critical supersaturation, the nucleation stops and the particles grow.[21]

Several key factors, such as redox potentials of distinct metal precursors, surface tension and interface energy, surfactant and facet-specific capping agent, reducing agent, and experimental conditions (concentration of reactants, mole ratio between precursors, temperature, time, atmosphere, pressure), can be controlled to obtain monodisperse NCs. By adjusting kinetic and thermodynamic factors,[23] reduction rate or decomposition rate of metallic precursors, the desired NC composition, elemental distribution, size, geometric structure, and phase structure can be achieved at the synthesis level.

A challenge in the synthesis of colloidal NCs is the control over the size distribution. This aspect can be tuned by the manipulation of the synthesis conditions in the kinetically-controlled NC growth of the synthesis method.[24] For instance, the reaction temperature plays a fundamental role

during the synthesis. The atoms in the forming crystals, in fact, need to have enough thermal energy to rearrange in ordered structures. A high reaction temperature leads to less stable complexes, higher reactivity of monomers with increased diffusion rate and weaker binding of capping agents on the surface. This leads to the formation of big particles with poor control over the size. Another important parameter that should be taken into account is the concentration of monomers. If their concentration is high, the critical size is small: small nanocrystals are stable and can grow faster than larger ones. This case is also known as "focusing" process and monodisperse systems can be obtained as a result of it. When the concentration of monomer is below a certain threshold, small NCs are not stable anymore so that they are consumed during the growth of bigger NCs. The size distribution in this case gets broader and the process is called "defocusing". These two modes are illustrated in Fig. 1.2.

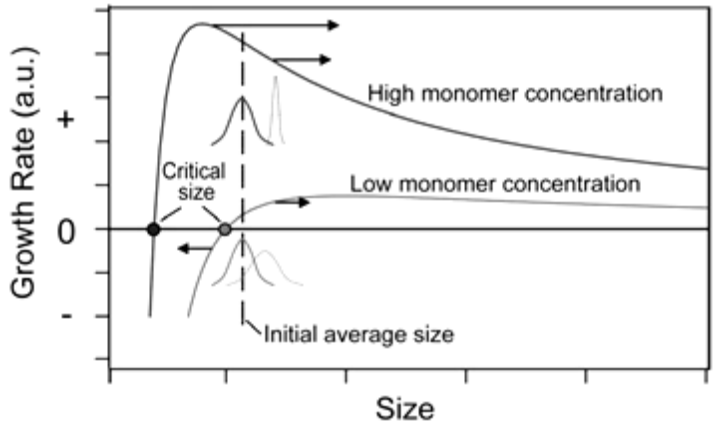

Fig. 1.2 – Growth rate of colloidal nanocrystals as a function of their size.[25] Reprinted with the permission from [25]. Copyright (2004) Springer Nature.

The shape control of colloidal NCs can be regulated by means of the use of the so called capping agents during the NC growth step. Indeed, the choice of specific surfactants can lead to NCs with specific shape (i.e. roads, spheres, platelets, disk-shaped NCs) by binding preferentially to different facets of a growing crystal.[23]

In Fig. 1.3 are shown some examples of strategies to manipulate the shape of the NCs.[26] In general, the growth rate of a crystal surface depends on its surface energy, so that high-energy facets grow faster than low energy facets in a kinetic regime (Fig. 1.3a). One possibility is that ligands can bind preferentially to a specific lattice plane lowering thus its energy. This effect can be used to selectively manipulate the growth rate of the targeted facet, resulting in the formation of rod or platelet-shaped NCs (Fig. 1.3b). Sequential elimination of high energy facets could result in more complex structures by the persistent growing of an intermediate-energy facet (Fig. 1.3c). Finally, when a material can grow in more than one crystal structure (a phenomenon known as polymorphism), the surface energies of the facets of different NCs can be manipulated to favor the attachment of targeted facets and obtain more complex nanostructures such as tetrapods (Fig. 1.3d).

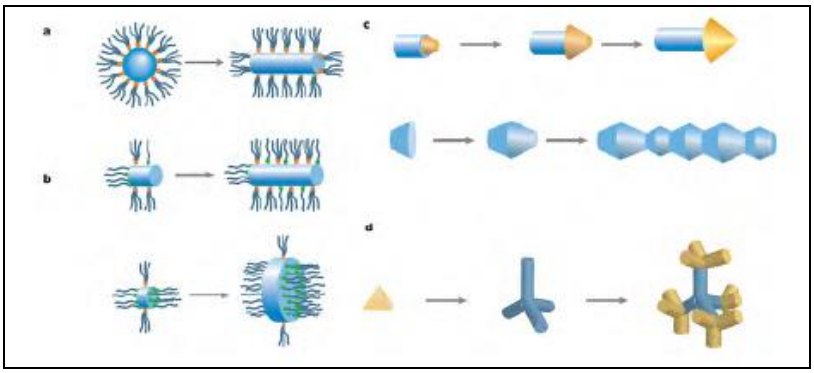

Fig. 1.3 – Schematic illustration of different shape evolutions. The yellow and green dots represent metal coordinating groups with different affinity to nanocrystal facets.[25] Reprinted with the permission from [25]. Copyright (2004) Springer Nature.

1.2 Bimetallic Nanocrystals

The addition of a second metallic element makes the structures of bimetallic NCs much more complex than their monometallic counterparts. Indeed, their architecture can differ in terms of atomic ordering (alloyed or intermetallic), crystal structure, internal structure (with different numbers of twin defects and/or stacking faults), shape or type of facet, and configuration (dimeric, dendritic, or core-shell, including concentric/nonconcentric),[3, 27, 28] as illustrated in Fig. 1.4a.

The alloy structure includes intermetallic compounds and solid solutions according to the distributions of two components elements and atomic ordering (Fig. 1.4b). A solid solution consists of disordered atomic arrangement of the two metals, forming substitutional or interstitial alloys depending on the size of the guest metal. In contrast, an intermetallic compound refers to a system that has both long-range atomic order of the constituent atoms and well-defined stoichiometry. Co-reduction or thermal decomposition of two metallic precursors are commonly used in the synthesis method known as continuous growth.[29] The first mentioned method involves the simultaneous reduction of two metal containing precursors to zerovalent atoms, M^0 and N^0, which then nucleate and grow together to generate M−N NCs. Post-synthesis annealing in an inert atmosphere is needed to promote the transformation from an alloy to an intermetallic compound.[30]

Concave or hollow alloy NCs can also be created by galvanic replacement reaction route in which the metal salt of the second metal is reduced by sacrificial metal seeds.[31] The dissolution of seeded metal and the deposition of growing metal take place simultaneously on one NC.

Core-shell NCs are comprised of an inner core (metal M) and a shell made of another metal (N), typically denoted by M@N. The seed-mediated approach (Fig. 1.5c) is usually used to prepare this type of structures and it consists in the first reduction of one kind of precursor to form the inner core; then, a second metal precursor is decomposed and grows on the surface of the core.[32]

In addition to the above mentioned bimetallic NCs, there are several other structural types, including those in the dendritic (i.e. highly branched nanocrystals, multipods, stars, pentacles, sea-urchin-like, and flowers, among others) and heterostructured forms (i.e. dimers, dumbbell structures, and Janus particles).[33]

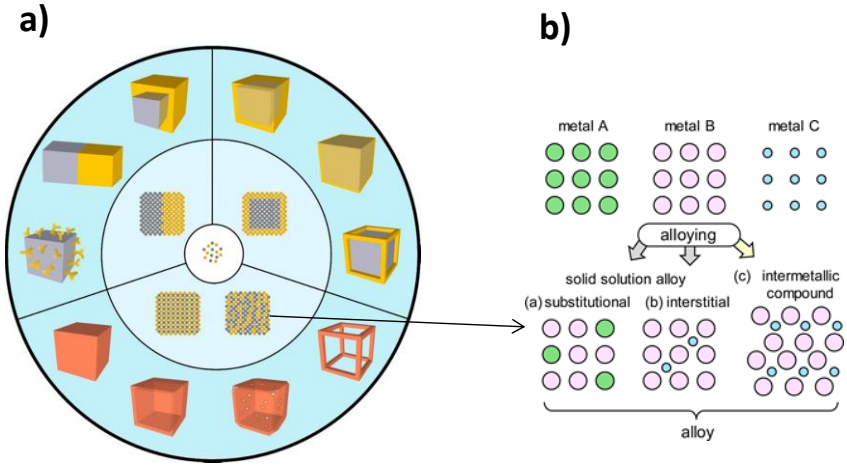

Fig. 1.4 – (a) Schematic illustration showing the evolution from two types of metal atoms (center) to four types of atomic distributions (middle ring) and then a large number of bimetallic nanocrystals with distinct architectures (outer ring).[3] (b) Classification of alloy structure in solid solution alloy and intermetallic compound. Reprinted with the permission from [3]. Copyright (2016) American Chemical Society.

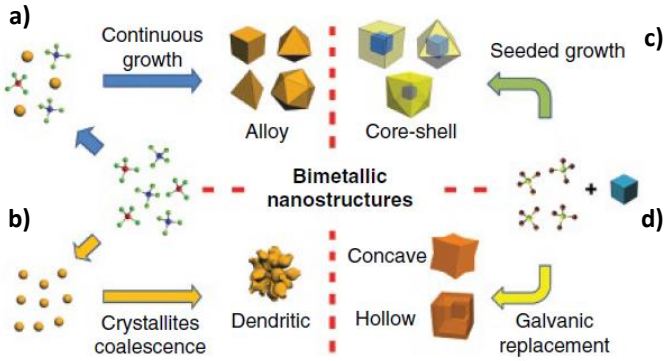

Fig. 1.5 – Four routes towards shape-controlled bimetallic NCs: (a) continuous growth, (b) crystallites coalescence, (c) seeded growth and (d) galvanic replacement reaction.[29] Reprinted with permission from [29]. Copyright (2012) Royal Society of Chemistry.

1.3 Colloidal NCs in Catalysis

1.3.1 Bimetallic Nanostructure-Dependent Catalytic Performance

Among the many applications of the colloidal NCs that have been explored, catalysis is of great importance. Heterogeneous catalysis is among the earliest known applications of nanomaterials, although this has been recognized only few decades ago. Indeed, in the design and application of this class of materials, one deals with the manipulation of materials at nanoscale.

There are several physical and chemical properties of bimetallic nanostructures that are highly shape-dependent, surface- and structure-sensitive (including their composition, elemental distribution, size, geometric structure, and phase structure) and which influence the performances of heterogeneous catalysts.[34, 35]

For example, bimetallic NCs with optimized composition can lead to enhanced catalytic properties compared to the corresponding monometallic NCs arising from synergistic effects of the different metal elements, where the metal-to-metal interaction can modify their electronic property, lead to lattice strain, and alternate reaction pathways.[36, 37] Indeed, by the combination of theoretical and experimental data, it was found by Zhang et al.[38] that, among the different PdCu NC compositions investigated, the optimal one (leading to the highest catalytic activity for CO oxidation reaction) was identified for a Pd/Cu ratio of 50:50. This composition featured the weakest adsorption strength of O_2 in terms of the most pronounced charge transfer between Pd and Cu atoms (Fig. 1.6).

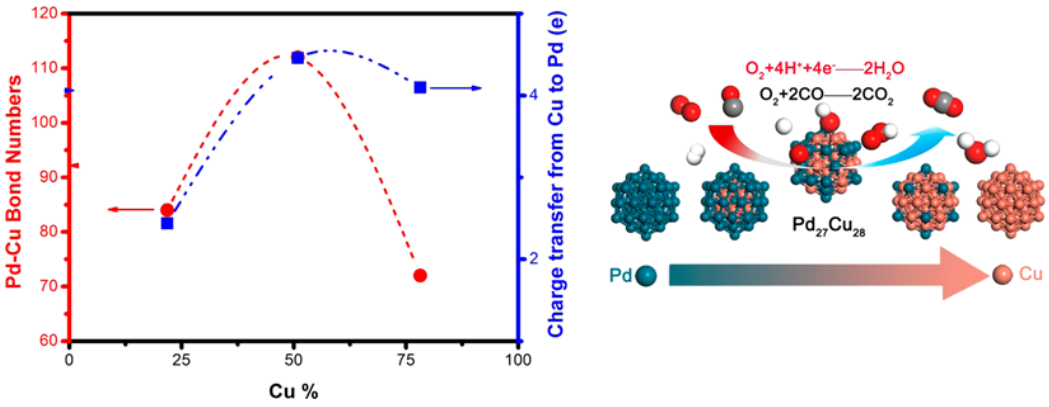

Fig. 1.6 - Plots of the total number of Pd−Cu bonds (red) and charge transfer from Cu to Pd (blue) as a function of Cu % in PdCu nanoalloys.[38] Reprinted with permission from [38]. Copyright (2017) American Chemical Society.

Studying the effect of the phase structure-property correlation, Zhan et al.[8] have prepared AuCu alloy NCs with face centered cubic (fcc) and face centered tetragonal (fct) structures, and have evaluated their activities in the CO oxidation reaction when supported on TiO_2 (Fig.1.7a). They demonstrated a remarkable difference in phase segregation and catalytic performance depending on the crystal structure. The fcc- and fct-AuCu alloy NCs tended to form Au/CuO and AuCu/CuO core/shell structures, respectively, during the thermal pre-treatment of alloy NCs at 250 °C in air for 1 h due to the different thermodynamic barriers for Cu diffusion onto the alloy surface. As a result, a remarkable difference in the catalytic activity was achieved (Fig. 1.7b) mainly depending on the lower ability for CO adsorption on the AuCu/CuO NC catalyst.

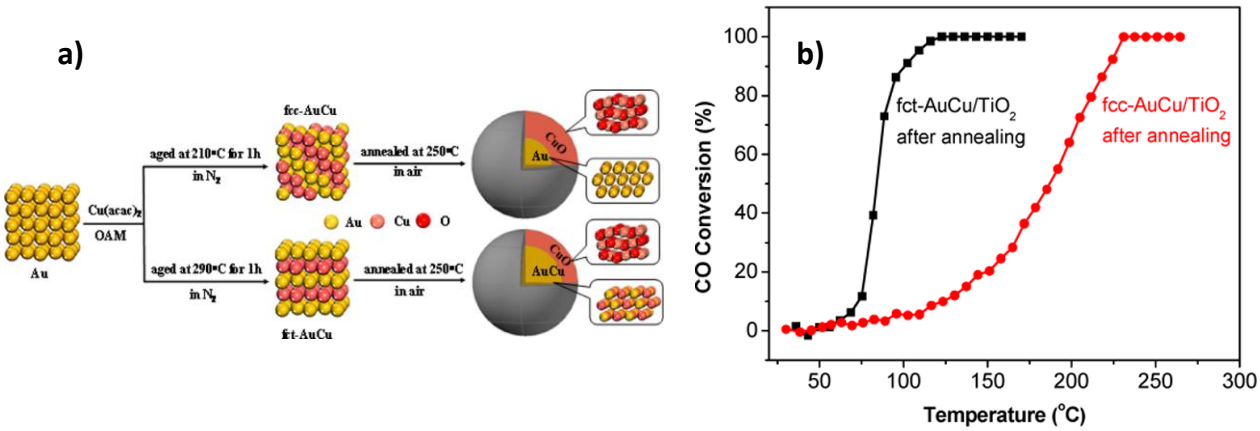

Fig. 1.7 – (a) Schematic illustration of the synthesis AuCu NCs with fcc and fct structures. (b) CO oxidation light-off curves.[8] Reprinted with permission from [8]. Copyright (2017) American Chemical Society.

1.3.2 Effect of Gas Environment on the NC Structure Modifications

The composition and structure of bimetallic surfaces of NCs can be readily modified from their original structures when such NCs are exposed to different gas environments, leading to the so-called NC surface segregation process.[1, 10, 39] The driving forces of the NC restructuring are thermodynamics due to the different surface energies of the two constituent metals and/or the different adsorption energies of molecules on the atoms of the two metals.[33]

The continuous supply of reactant molecules in an environment of reactant gases at relatively high pressure and the large mobility of atoms at a relatively high temperature typically causes extensive restructuring of the NCs. The high temperature of catalysts provides sufficient energy to atoms of the subsurface to migrate to the topmost surface layer through thermal diffusion. If the reactant molecules preferentially bind to atoms of one of the two metals, the one with the higher binding energy in the topmost surface layer segregates to the surface.

In addition to the binding energy factor, for A_mB_n bimetallic nanoparticles, the degree of segregation or mixing for two different metals also depends on the surface energy of the A and B elements, their relative atomic size, charge transfer, strength of binding to surface ligands and specific electronic/magnetic effects.[28] In particular, the element with lowest surface energy tends to segregate to the surface unless the presence of facet-specific capping agents, while the electron transfer from less to more electronegative elements favors A-B mixing. Phase separation is also depending on the size of NCs. In smaller NCs the interfacial energy dominates and it is lower than the enthalpy of demixing so that the NCs preserve their alloyed structure.

Several works have demonstrated how oxidative and reductive conditions can induce the surface reconstruction that alters the catalytic mechanism, especially at the nanoscale.[6, 40] Additionally, among different adsorbate molecules inducing surface segregation, carbon monoxide is one of the most studied molecules that bind to metal atoms with varying strength. Indeed, there are a number of experimental and theoretical studies which report its use for this purpose with a variety of bimetallic systems, including PdAu[41], AuNi[42], PdCu[43], PtCu[5, 44], PdRh[45], and AuCu[46].

As an example, segregation of $Pd_{0.5}Cu_{0.5}$(110) single crystal was studied by the adsorption of hydrocarbons or hydrogen that induces Pd segregation in Pd catalysts significantly when alloyed with Cu.[47] A similar behavior of restructuring was observed on Pd_xCu_{1-x} NCs supported on zeolite under reaction conditions of CO hydrogenation.[48] The CO adsorption and H_2 induce segregation of Pd atoms to the surface under high-pressure reaction conditions.

Surface restructuring of PtCu bimetallic NCs in H_2 and CO was also studied by Oxford et al..[44] In an environment of CO, the Pt of PtCu nanoparticles segregated to the surface and Cu migrated to the core, as a result of the larger adsorption energy of CO on Pt atoms in contrast to Cu atoms. However, there is a reverse restructuring behavior under H_2, in which Cu segregates and forms a Cu-rich surface region. In this restructuring, the lower surface energy of Cu plays a major role. Moreover, the restructuring behavior of PtCu NCs is different from that of PtCu surface alloy formed on a Pt single crystal. For the PtCu surface alloy formed on Pt single crystals in a CO environment, Cu in the sub-monolayer segregates to the surface and forms a PtCu surface layer, driven by the stronger binding energy of CO on Pt coordinating with Cu compared to that on a pure Pt surface. The fully occupied Cu 3d shell is expected to partially transfer electrons to the Pt 4f shell, which enhances the back donation of electrons from Pt to the anti-p bond of a CO molecule.

Another study conducted by Shan et al.[5] addressed how surface structures affect the dispersion of metal sites on the surface of shape-controlled PtCu NCs (Fig. 1.8). This study utilized different pre-treatment conditions to vary the surface composition and structure of bimetallic PtCu NCs, which correspondingly changed their catalytic performance in CO oxidation. Two types of bimetallic PtCu NCs with different morphologies were synthesized in regular cubes (RNCs) and concave cubes (CNCs) and exhibited dramatically different catalytic activities in CO oxidation reaction after various pre-treatment procedures. PtCu CNCs showed improved catalytic activities after either H_2 reduction or H_2/CO treatment in comparison to the untreated CNCs. PtCu RNCs showed higher activity and lower activation energy only after H_2 reduction, compared to the untreated RNCs. On the contrary, the H_2/CO treatment decreased the activity of RNCs. The structure-activity correlation evidenced that a reaction of PtCu RNC-as synthesized with H_2 at 200 °C generated a near-surface alloy consisting of a Pt skin layer, a Cu-rich subsurface, and a Pt-rich deep layer. This near-surface alloy of PtCu RNC-as synthesized-H_2 exhibited a much higher catalytic activity in CO oxidation compared to the PtCu RNC-as synthesized. A further reaction of PtCu RNC-as synthesized-H_2 with CO forms a PtCu alloy surface, which exhibited enhanced catalytic performance in CO oxidation.

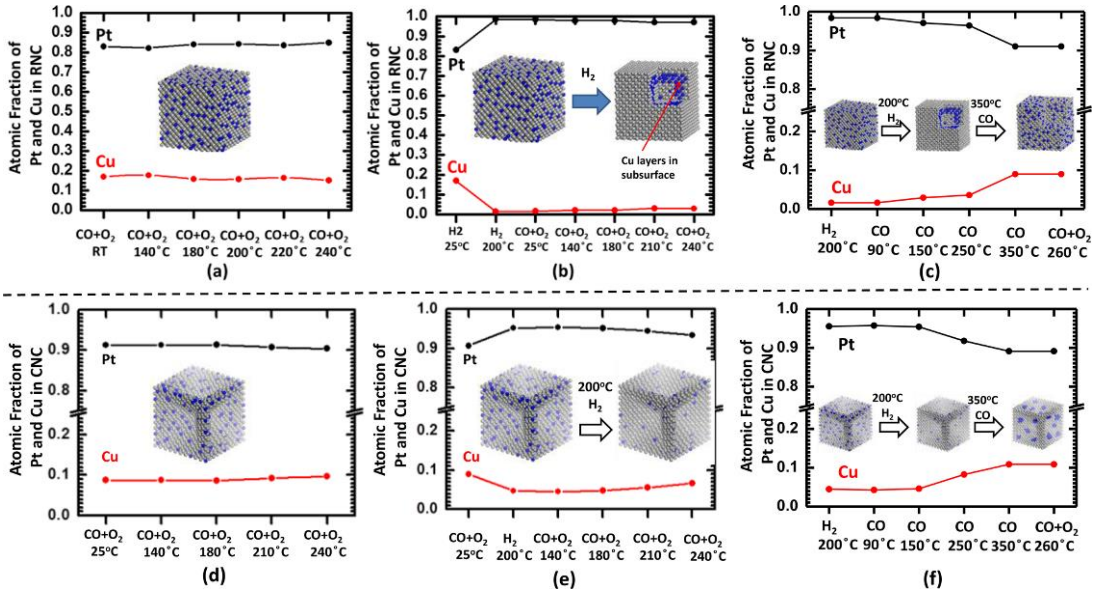

Fig. 1.8 - Surface evolution of PtCu RNCs and PtCu CNCs regarding the composition and dispersion of Pt and Cu fractions after post-synthesis and then in the CO oxidation reaction: (a–c) PtCu RNCs of (a) untreated, (b) treated in H_2, (c) treated in H_2 and then in CO; (d–f) PtCu CNCs of (d) untreated, (e) treated in H_2, and (f) treated in H_2 and then in CO. The inserted structure models depict the surface evolution under these gas atmospheres.[5] Reprinted with permission from [5]. Copyright (2017) American Chemical Society.

1.3.3 Role of the Support

Supported transition metal particles are among the most relevant catalysts currently applied in the field of heterogeneous catalysis[49]. The properties of heterogeneous catalysts are often determined by the synergy between inorganic support, typically metal oxides, and supported phases. Indeed, usually, the catalyst metal NCs, typically transition metal NCs, are dispersed on a high surface area support to be more accessible to reactants. In this way, the exposure of a large number of low coordination sites acting as active sites can enhance the catalytic activity.[50] As already mentioned, the NC morphology and surface composition are the most important factors that influence the catalytic performance. However, most industrial catalysts are supported on oxides to improve their efficiency and catalytic performance. Upon supporting nanoparticles onto oxide supports, their morphology, composition, and catalytic performance may change owing to their interaction with the support.[51, 52]

Conventional methods for catalyst preparation involve impregnation of (co)precipitation usually resulting in a material with a relevant level of inhomogeneity in terms of properties at the nanoscale.[53] Another strategy for the manufacturing of heterogeneous catalysts is the so-called "precursor concept" in which preformed colloidal metallic NCs with desired morphology, size and composition are deposited on a support. In this way, it is possible to control and stabilize the metal prior to the deposition on the support, diminishing the contribution of the support on NC formation and *vice versa*. This expedient permits to address independently the influence of catalyst parameters of the transition metal NCs and metal oxide support.[54]

However, the main drawback of the colloidal NC synthesis is the organic stabilizing ligands that cover the NC surface. So that additional step is required to activate the catalyst to fully expose the surface of the metal active sites avoiding modification of metal NCs. Generally, thermal methods, under mild temperatures (>400 °C) and in oxidizing conditions,[55] or chemical procedures[56] are involved depending on the type of capping agents covering the NCs.

For a long time, it has been assumed that the oxide supports acts manly as "inert" component to disperse and stabilize the NCs preventing their sintering. According to this view, the metal is the only active species in the catalytic process. However, this approach has changed over the years. Indeed, many studies have progressively shown that when the NCs are supported, their morphology, composition and catalytic performance may also change due to their interaction with the support in response to the treatment conditions.[57] Specifically, the morphology of the particles is determined by the surface free energy, meaning that their surface structure may vary depending on the metal-support interaction. The ability of the latter component is thus that to stabilize different surface facets and/or surface states.[50]

Complex dynamic processes between nanoscale catalysts and their support have been extensively studied, such as Ostwald ripening and particle disintegration induced by reactants as function of adsorbate-metal, metal-support and metal-metal interactions,[11] NC stabilization against sintering by functionalization of the support surface or support porosity,[12, 13] encapsulation of active NCs in porous oxide shell due to the interaction metal-oxide interface (strong metal-support interaction - SMSI) or high dispersion.[14] Additionally, NC structure and shape transformations in response to reaction gases,[15, 16] oxygen release property in the reduction of metal oxide support by the diffusion of O atoms from oxide surface to metal NCs in the so-called "oxygen spillover"[58] and perturbation in the electronic structure of metal NCs due to the electronic exchange at the interface metal-support can be mentioned.[17, 51] Additional factors such as the reduction of the dimension of the oxide support (i.e. generating oxide nanostructures, nanowires or thin films), point defects on the surface support (i.e. isolated cation, anion vacancies, hydroxyl groups)[59], or selective doping[57] may completely change the nature of the support modifying the interaction with the metal.

However, the above mentioned studies have been made to elucidate the exact mechanisms involved in the interaction between the monometallic particles, single crystal or films and the support. Understanding how electronic and/or geometric modification of monometallic system by alloying influence these phenomena is still challenging and only few studies concerning this topic are reported in the literature.[14-16]

In analogy with monometallic catalysts, also these NCs can suffer sintering and/or be re-dispersed in certain conditions and gas atmosphere. Indeed, in the case of bimetallic systems, the two NC components will be characterized by different interactions with the support, and the presence of the second metal will alter these interactions as well.[16] For example, it has been shown by Huang et al.[51] that PtCu alloyed NCs supported on TiO_2 undergo extensive transformations when exposed either to an oxidizing or a reducing environments, resulting in a surface reconstruction that is totally different from that the bulk one, highlighting the important

role of the support in the dispersion and morphology of the alloyed NCs. Xi et al.[60] demonstrated a strategy to stabilize Cu in PdCu NCs supported on $WO_{2.72}$ nanorods in an acid environment by the strong interaction between the NCs and the support. Divins et al.[14] proved that the surface rearrangement of RhPd NCs under working conditions for ethanol steam reforming was strongly influenced by the oxygen storage-release capability of reducible ceria support altering the oxidation state and the surface reorganization of the metal atoms.

From a chemical perspective, the above mentioned oxides are classified as reducible oxides, that can easily accept electronic charge from a donor species and, consequently, the metal cations change their formal oxidation state from M^{n+} to $M^{(n-1)+}$. On the other hand, non-reducible oxides such as Al_2O_3, SiO_2, ZrO_2, MgO are commonly used in catalysis thanks to the low reactivity and the chemical inertness. Indeed, they have a valence band deep in energy (several eV below the vacuum level) and a conduction band that is high in energy, close to the vacuum level. This explains the high cost to extract electrons from the 2p levels of the O^{2-} ions from the valance band and the moderate tendency to accept electronic charge in the high position of the conductive band.[57]

Despite the weak interaction of the on-reducible oxides with the metals, it was found that these supports play a key role in the structure evolution of NCs in selected atmospheres. For example, a study conducted by Destro et al.[52] revealed how the type of support direct impacts on the nature and the location of CuO_x species forming during the dealloying/alloying processes for γ-Al_2O_3 and SiO_2 supported $Au_{1-x}Cu_x$ NCs during the oxidative and reductive treatments (Fig. 1.9a). Specifically, under oxidizing conditions, Cu was dealloyed from Au and the formed CuO_x species had a different fate as a function of the support: while they were finely dispersed on alumina, and partially migrate away from the Au NCs, CuO_x species on silica formed small clusters located in the proximity of the Au NCs with limited Cu migration on the support. The reducing atmosphere restored the AuCu alloyed NCs when supported on alumina. A partial realloy also occurred on the silica supported AuCu NCs, resulting in the formation of depleted Cu-alloy NCs and isolated metallic Cu phase. Another recent study conducted by Nie et al.[61] shows as the Al_2O_3 support affected the shape, chemical composition and structure of Pd-Pt catalyst in comparison to unsupported Pd-Pt clusters with changing temperature, feed composition and atmospheres (Fig. 1.9b).

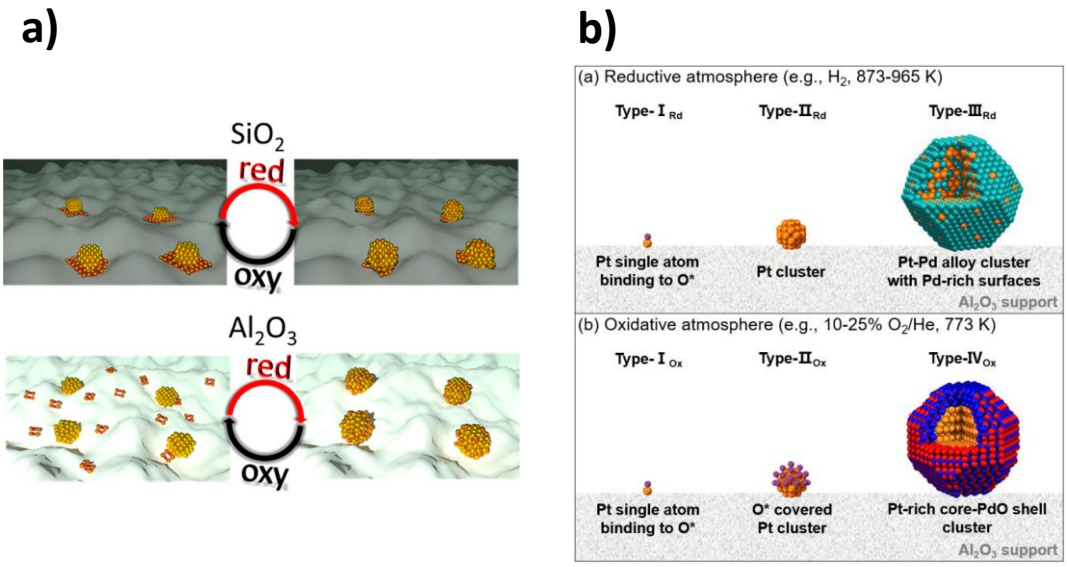

Fig. 1.9 - (a) Impact the support on the transformation of $Au_{1-x}Cu_x$ NCs exposed to different pre-treatments.[52] Reprinted with permission from [52]. Copyright (2018) American Chemical Society. (b) Schematic illustration of the morphologies of nanostructures in the Pt-Pd/Al_2O_3 catalyst under reductive and oxidative atmospheres.[61] Reprinted with permission from [61]. Copyright (2017) American Chemical Society.

1.4 In Situ/Operando Characterization Techniques

The characterization of bimetallic catalysts compared to the monometallic ones was found to be more challenging since the addition of a guest metal changed the electronic properties and geometry of the active sites of the host metal. These modifications are driven by an interplay of thermodynamic factors, such as different surface energies and adsorption energies for the constituent metals towards the adsorbed atoms, and kinetic factors related to the diffusion barriers of metal atoms.

Moreover, as above mentioned, the structure of the supported NCs and active sites can change in terms of size (i.e. the fraction of atoms with low-coordination at the step edges or corners is higher for smaller NCs), shape, oxidation state and composition during activation or exposure to the dynamic reaction conditions. Typically, the latter are referred to reactant gases or mixtures with certain composition of a catalytic reaction under high temperature and pressure.

In operando and *in situ* studies have shown that the surface structure and chemistry of a catalyst under or during the reaction conditions can be different when compared with those observed before and after the reaction. As an example, in Fig. 1.10 are reported four possibilities of evolution of a catalyst before, during and after the catalysis. For the possibilities 3 and 4, in which the chemical state of the as-prepared NCs is different from that after the reaction, it is thus necessary to track the structure evolution during the process.

The difficulty of predicting these changes necessitates the use of *in situ* or *operando* characterization techniques to measure the structure of the NCs as well as to track changes occurring under relevant reaction conditions. [49] Specifically, *in situ* characterization refers to

measurements performed under specific conditions of temperature, pressure, concentration, or other experimental parameters. Instead, *operando* characterization has been established to describe the system under reaction conditions with simultaneous activity measurements.[62]

Among the different *in situ/operando* techniques, it is possible to mention X-ray based techniques such as X-ray diffraction (XRD), X-ray absorption fine structure (XAFS) spectroscopy, and the more advanced photon-in/out-techniques (X-ray emission spectroscopy (XES), high energy resolution fluorescence detected HERFD-XAS, and resonant inelastic X-ray scattering (RIXS)), providing information about crystalline and amorphous bulk phases, small clusters and even single site species.[49] Other spectroscopic techniques include infrared (IR) spectroscopy by means of carbon monoxide adsorption on metals, Raman spectroscopy, UV-Vis spectroscopy and X-ray photon–electron spectroscopy (XPS). In recent years, advancements have been made in methods that have primarily been used under ultra-high vacuum conditions to make measurements also under higher pressure. This is the case of the ambient-pressure XPS instruments used to study chemical reactions on solid surface thanks to the high surface sensitivity and elemental specificity[1]. In this thesis, *in situ/operando* DRIFTS and XAFS techniques will be presented and used to identify the nature of surface species and phases, respectively, present in the NC systems upon exposure to the redox and catalytic conditions.

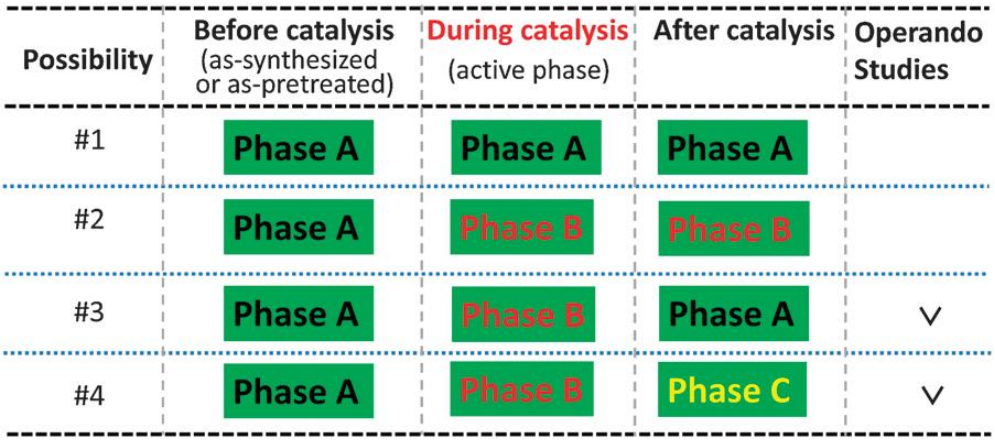

Fig. 1.10 - Schematic view of different possibilities of the evolution of catalyst phases before, during and after catalysis.[33] Reprinted with permission from [33]. Copyright (2017) American Chemical Society.

References

1. Tao, F. F.; Zhang, S.; Nguyen, L.; Zhang, X., Action of bimetallic nanocatalysts under reaction conditions and during catalysis: evolution of chemistry from high vacuum conditions to reaction conditions. *Chem Soc Rev* 2012, 41, 7980-7993.

2. Xu, Y.; Chen, L.; Wang, X.; Yao, W.; Zhang, Q., Recent advances in noble metal based composite nanocatalysts: colloidal synthesis, properties, and catalytic applications. *Nanoscale* 2015, 7, 10559-10583.

3. Gilroy, K. D.; Ruditskiy, A.; Peng, H.-C.; Qin, D.; Xia, Y., Bimetallic nanocrystals: syntheses, properties, and applications. *Chem Rev* 2016, 116, 10414-10472.

4. Shan, S.; Petkov, V.; Prasai, B.; Wu, J.; Joseph, P.; Skeete, Z.; Kim, E.; Mott, D.; Malis, O.; Luo, J., Catalytic activity of bimetallic catalysts highly sensitive to the atomic composition and phase structure at the nanoscale. *Nanoscale* 2015, 7, 18936-18948.

5. Shan, J.; Zhang, S.; Choksi, T.; Nguyen, L.; Bonifacio, C. S.; Li, Y.; Zhu, W.; Tang, Y.; Zhang, Y.; Yang, J. C., Tuning catalytic performance through a single or sequential post-synthesis reaction(s) in a gas phase. *ACS Catal* 2016, 7, 191-204.

6. Mu, R.; Guo, X.; Fu, Q.; Bao, X., Oscillation of surface structure and reactivity of PtNi bimetallic catalysts with redox treatments at variable temperatures. *J Phys Chem C* 2011, 115, 20590-20595.

7. Nikolaev, S.; Golubina, E.; Shilina, M., The effect of H_2 treatment at 423–573K on the structure and synergistic activity of Pd–Cu alloy catalysts for low-temperature CO oxidation. *Appl Catal B* 2017, 208, 116-127.

8. Zhan, W.; Wang, J.; Wang, H.; Zhang, J.; Liu, X.; Zhang, P.; Chi, M.; Guo, Y.; Guo, Y.; Lu, G., Crystal structural effect of AuCu alloy nanoparticles on catalytic CO oxidation. *J Am Chem Soc* 2017, 139, 26, 8846-8854.

9. Tao, F.; Grass, M. E.; Zhang, Y.; Butcher, D. R.; Aksoy, F.; Aloni, S.; Altoe, V.; Alayoglu, S.; Renzas, J. R.; Tsung, C.-K., Evolution of structure and chemistry of bimetallic nanoparticle catalysts under reaction conditions. *J Am Chem Soc* 2010, 132, 8697-8703.

10. Peng, L.; Ringe, E.; Van Duyne, R. P.; Marks, L. D., Segregation in bimetallic nanoparticles. *Phys Chem Chem Phys* 2015, 17, 27940-27951.

11. Ouyang, R.; Liu, J.-X.; Li, W.-X., Atomistic theory of Ostwald ripening and disintegration of supported metal particles under reaction conditions. *J Am Chem Soc* 2013, 135, 1760-1771.

12. Hansen, T. W.; DeLaRiva, A. T.; Challa, S. R.; Datye, A. K., Sintering of catalytic nanoparticles: particle migration or Ostwald ripening? *Acc Chem Res* 2013, 46, 1720-1730.

13. Challa, S. R.; Delariva, A. T.; Hansen, T. W.; Helveg, S.; Sehested, J.; Hansen, P. L.; Garzon, F.; Datye, A. K., Relating rates of catalyst sintering to the disappearance of individual nanoparticles during Ostwald ripening. *J Am Chem Soc* 2011, 133, 20672-20675.

14. Divins, N. J.; Angurell, I.; Escudero, C.; Pérez-Dieste, V.; Llorca, J., Influence of the support on surface rearrangements of bimetallic nanoparticles in real catalysts. *Science* 2014, 346, 620-623.

15. Xu, S.; Walter, E. D.; Zhao, Z.; Hu, M. Y.; Han, X.; Hu, J. Z.; Bao, X., Dynamic structural changes of SiO_2 supported Pt–Ni bimetallic catalysts over redox treatments revealed by NMR and EPR. *J Phys Chem C* 2015, 119, 21219-21226.

16. Carter, J. H.; Althahban, S.; Nowicka, E.; Freakley, S. J.; Morgan, D. J.; Shah, P. M.; Golunski, S.; Kiely, C. J.; Hutchings, G. J., Synergy and anti-synergy between palladium and gold in nanoparticles dispersed on a reducible support. *ACS Catal* 2016, 6, 6623-6633.

17. Vedyagin, A. A.; Volodin, A. M.; Kenzhin, R. M.; Stoyanovskii, V. O.; Shubin, Y. V.; Plyusnin, P. E.; Mishakov, I. V., Effect of metal-metal and metal-support interaction on activity and stability of Pd-Rh/alumina in CO oxidation. *Catal Today* 2017, 293, 73-81.

18. Jia, C.-J.; Schüth, F., Colloidal metal nanoparticles as a component of designed catalyst. *Phys Chem Chem Phys* 2011, 13, 2457-2487.

19. Pietryga, J. M.; Park, Y.-S.; Lim, J.; Fidler, A. F.; Bae, W. K.; Brovelli, S.; Spectroscopic and device aspects of nanocrystal quantum dots. *Chem Rev* 2016, 116, 10513-10622.

20. Kudera, S.; Manna, L., Bottom-Up Synthesis of Nanosized Objects. In *Colloidal Foundations of Nanoscience*, Elsevier: 2014; pp 47-80.

21. Van Embden, J.; Chesman, A. S. R.; Jasieniak, J. J., The heat-up synthesis of colloidal nanocrystals. *Chem Mater* 2015, 27, 2246-2285.

22. Xia, Y.; Gilroy, K. D.; Peng, H. C.; Xia, X., Seed-mediated growth of colloidal metal nanocrystals. *Angew Chem Int Ed* 2017, 56, 60-95.

23. Xia, Y.; Xia, X.; Peng, H.-C., Shape-controlled synthesis of colloidal metal nanocrystals: thermodynamic versus kinetic products. *J Am Chem Soc* 2015, 137, 7947-7966.

24. Kwon, S. G.; Hyeon, T., Colloidal chemical synthesis and formation kinetics of uniformly sized nanocrystals of metals, oxides, and chalcogenides. *Acc Chem Res* 2008, 41, 1696-1709.

25. Yin, Z.; Zhou, W.; Gao, Y.; Ma, D.; Kiely, C. J.; Bao, X., Supported Pd–Cu bimetallic nanoparticles that have high activity for the electrochemical oxidation of methanol. *Chem–A Eur J* 2012, 18, 4887-4893.

26. Yin, Y.; Alivisatos, A. P., Colloidal nanocrystal synthesis and the organic–inorganic interface. *Nature* 2004, 437, 664.

27. Zhang, Y.-W., *Bimetallic Nanostructures: Shape-controlled Synthesis for Catalysis, Plasmonics, and Sensing Applications*. John Wiley & Sons: 2018.

28. Ferrando, R.; Jellinek, J.; Johnston, R. L., Nanoalloys: from theory to applications of alloy clusters and nanoparticles. *Chem Rev* 2008, 108, 845-910.

29. Gu, J.; Zhang, Y.-W.; Tao, F. F., Shape control of bimetallic nanocatalysts through well-designed colloidal chemistry approaches. *Chem Soc Rev* 2012, 41, 8050-8065.

30. Yan, Y.; Du, J. S.; Gilroy, K. D.; Yang, D.; Xia, Y.; Zhang, H., Intermetallic nanocrystals: syntheses and catalytic applications. *Adv Mater* 2017, 29, 1605997.

31. Zhang, H.; Jin, M.; Xia, Y., Noble-metal nanocrystals with concave surfaces: synthesis and applications. *Angew Chem Int Ed* 2012, 51, 7656-7673.

32. Ghosh Chaudhuri, R.; Paria, S., Core/shell nanoparticles: classes, properties, synthesis mechanisms, characterization, and applications. *Chem Rev* 2011, 112, 2373-2433.

33. Tao, F. F., Synthesis, catalysis, surface chemistry and structure of bimetallic nanocatalysts. *Chem Soc Rev* 2012, 41, 7977-7979.

34. Cao, S.; Tao, F. F.; Tang, Y.; Li, Y.; Yu, J., Size-and shape-dependent catalytic performances of oxidation and reduction reactions on nanocatalysts. *Chem Soc Rev* 2016, 45, 4747-4765.

35. An, K.; Somorjai, G. A., Size and shape control of metal nanoparticles for reaction selectivity in catalysis. *ChemCatChem* 2012, 4, 1512-1524.

36. Singh, A. K.; Xu, Q., Synergistic catalysis over bimetallic alloy nanoparticles. *ChemCatChem* 2013, 5, 652-676.

37. Notar Francesco, I.; Fontaine-Vive, F.; Antoniotti, S., Synergy in the catalytic activity of bimetallic nanoparticles and new synthetic methods for the preparation of fine chemicals. *ChemCatChem* 2014, 6, 2784-2791.

38. Zhang, W.; Shan, S.; Luo, J.; Fisher, A.; Chen, J.-F.; Zhong, C.-J.; Zhu, J.; Cheng, D., Origin of Enhanced Activities for CO Oxidation and O_2 Reaction over Composition-Optimized $Pd_{50}Cu_{50}$ Nanoalloy Catalysts. *J Phys Chem C* 2016, 121, 11010-11020.

39. Calvo, F., Thermodynamics of nanoalloys. *Phys Chem Chem Phys* 2015, 17, 27922-27939.

40. Ma, T.; Fu, Q.; Su, H. Y.; Liu, H. Y.; Cui, Y.; Wang, Z.; Mu, R. T.; Li, W. X.; Bao, X. H., Reversible structural modulation of Fe–Pt bimetallic surfaces and its effect on reactivity. *ChemPhysChem* 2009, 10, 1013-1016.

41. Alayoglu, S.; Tao, F.; Altoe, V.; Specht, C.; Zhu, Z.; Aksoy, F.; Butcher, D. R.; Renzas, R. J.; Liu, Z.; Somorjai, G. A., Surface composition and catalytic evolution of Au_xPd_{1-x} (x= 0.25, 0.50 and 0.75) nanoparticles under CO/O_2 reaction in torr pressure regime and at 200 C. *Catal Lett* 2011, 141, 633-640.

42. Vestergaard, E. K.; Vang, R. T.; Knudsen, J.; Pedersen, T. M.; An, T.; Lægsgaard, E.; Stensgaard, I.; Hammer, B.; Besenbacher, F., Adsorbate-induced alloy phase separation: A direct view by high-pressure scanning tunneling microscopy. *Phys Rev Lett* 2005, 95, 126101.

43. McCue, A. J.; Anderson, J. A., CO induced surface segregation as a means of improving surface composition and enhancing performance of CuPd bimetallic catalysts. *J Catal* 2015, 329, 538-546.

44. Oxford, S. M.; Lee, P. L.; Chupas, P. J.; Chapman, K. W.; Kung, M. C.; Kung, H. H., Study of supported PtCu and PdAu bimetallic nanoparticles using in-situ X-ray tools†. *J Phys Chem C* 2010, 114, 17085-17091.

45. Tao, F.; Grass, M. E.; Zhang, Y.; Butcher, D. R.; Renzas, J. R.; Liu, Z.; Chung, J. Y.; Mun, B. S.; Salmeron, M.; Somorjai, G. A., Reaction-driven restructuring of Rh-Pd and Pt-Pd core-shell nanoparticles. *Science* 2008, 322, 932-934.

46. Liu, X.; Wang, A.; Li, L.; Zhang, T.; Mou, C.-Y.; Lee, J.-F., Structural changes of Au–Cu bimetallic catalysts in CO oxidation: in situ XRD, EPR, XANES, and FT-IR characterizations. *J Catal* 2011, 278, 288-296.

47. Noakes, T.; Bailey, P.; Laroze, S.; Bloxham, L.; Raval, R.; Baddeley, C., Pd/Cu alloys as hydrodechlorination catalysts: a medium-energy ion scattering study of surface composition under exposure to chlorinated hydrocarbons. *Surf Interface Anal* 2000, 30, 81-84.

48. Anderson, J. A.; López-Granados, M.; Fernández-García, M., Role of the support in syngas conversion over Pd/Cu–KL zeolite catalysts. *J Catal* 1998, 176, 235-245.

49. Sharapa, D. I.; Doronkin, D. E.; Studt, F.; Grunwaldt, J. D.; Behrens, S., Moving frontiers in transition metal catalysis: synthesis, characterization and modeling. *Adv Mater* 2019, 31, 1807381.

50. Macquarrie, D., I. Chorkendorff and JW Niemantsverdriet. Concepts of modern catalysis and kinetics. *Appl Organomet Chem* 2005, 19, 696-696.

51. Huang, J.; Song, Y.; Ma, D.; Zheng, Y.; Chen, M.; Wan, H., The effect of the support on the surface composition of PtCu alloy nanocatalysts: in situ XPS and HS-LEIS studies. *Chinese J Catal* 2017, 38, 1229-1236.

52. Destro, P.; Kokumai, T. M.; Scarpellini, A.; Pasquale, L.; Manna, L.; Colombo, M.; Zanchet, D., The crucial role of the support in the transformations of bimetallic nanoparticles and catalytic performance. *ACS Catal* 2018, 8, 2, 1031-1037.

53. Henry, C. R., Surface studies of supported model catalysts. *Surf Sci Rep* 1998, 31, 231-325.

54. Bönnemann, H.; Richards, R. M., Nanoscopic metal particles− synthetic methods and potential applications. *Eur J Inorg Chem* 2001, 2001, 2455-2480.

55. Cargnello, M.; Chen, C.; Diroll, B. T.; Doan-Nguyen, V. V.; Gorte, R. J.; Murray, C. B., Efficient removal of organic ligands from supported nanocrystals by fast thermal annealing enables catalytic studies on well-defined active phases. *J Am Chem Soc* 2015, 137, 6906-6911.

56. Niu, Z.; Li, Y., Removal and utilization of capping agents in nanocatalysis. *Chem Mater* 2013, 26, 72-83.

57. Pacchioni, G.; Freund, H.-J., Controlling the charge state of supported nanoparticles in catalysis: lessons from model systems. *Chem Soc Rev* 2018, 47, 8474-8502.

58. Kong, D.; Wang, G.; Pan, Y.; Hu, S.; Hou, J.; Pan, H.; Campbell, C. T.; Zhu, J., Growth, structure, and stability of Ag on CeO_2 (111): synchrotron radiation photoemission studies. *J Phys Chem C* 2011, 115, 6715-6725.

59. Tuller, H. L.; Bishop, S. R., Point defects in oxides: tailoring materials through defect engineering. *Annu Rev Mater Res* 2011, 41, 369-398.

60. Xi, Z.; Li, J.; Su, D.; Muzzio, M.; Yu, C.; Li, Q.; Sun, S., Stabilizing CuPd nanoparticles via CuPd coupling to $WO_{2.72}$ nanorods in electrochemical oxidation of formic acid. *J Am Chem Soc* 2017, 139, 15191-15196.

61. Nie, H.; Howe, J.; Lachkov, P.; Chin, Y.-H., Chemical and structural dynamics of nanostructures in bimetallic Pt-Pd catalysts, their inhomogeneity, and their roles in methane oxidation. *ACS Catal* 2019, 9, 6, 5445-5461.

62. Chakrabarti, A.; Ford, M. E.; Gregory, D.; Hu, R.; Keturakis, C. J.; Lwin, S.; Tang, Y.; Yang, Z.; Zhu, M.; Banares, M. A., A decade+ of operando spectroscopy studies. *Catal Today* 2017, 283, 27-53.

Chapter 2

Analysis and Synthesis Techniques

This chapter presents the fundamental principles of the characterization techniques along with their detailed experimental procedures, giving insights into the different kind of information they can provide. The protocols used for the synthesis of the starting colloidal NCs as well as the preparation of the catalysts are also reported.

2.1 Experimental Procedures and Data Processing Methods

2.1.1 Electron Microscopy

Transmission electron microscopy (TEM) can be used to acquire not only morphological information about the sample, but also structural and chemical characterizations. Specifically, it can provide direct observations on morphology, shape and size of nanostructures.[1] When combined with a scanning transmission electron microscopy (STEM), energy dispersive X-ray (EDX) spectroscopy, or selected area electron diffraction (SAED), it can provide information on how elements are localized/distributed along the nanostructures or about their crystal structure.

TEM is commonly known as a characterization technique of materials down to the atomic scale.[2] A high energy beam of electrons with an accelerating voltage around 100 kV interacts with a thin sample and the transmitted electrons that were able to pass through the specimen are detected by a fluorescent screen or a digital camera which converts the electron signal to an image. Compared to the optical microscope, the accelerated electrons, with a much shorter wavelength than the visible light, are used to achieve higher resolution according to the De Broglie equation ($\lambda = h/p$, where h is the Plank constant and p is the electron momentum, i.e. for $E = h/(c/\lambda)$ = 200 keV, λ = 0.062 Å).

In imaging mode, an image can be generated by detecting those electrons which can pass through an objective aperture located on the back focal plane which allows only the direct beam to pass (Fig. 2.1). In this way, a bright-field (BF) image is formed in which the specimen appears darker on a bright background. In the dark-field (DF) mode, by moving the objective aperture, the direct beam is blocked and only the diffracted beams are allowed to pass the objective

aperture. In the DF mode, in contrast to the BF imaging one, the specimen appears bright on a dark background.[3]

High-resolution transmission electron microscopy (HRTEM) is achieved when working with an accelerating voltage higher than 200 kV generating an e-beam that allows for direct imaging of the atoms/atomic columns/crystal structure of materials or atomic scale with imaging details down to 0.5 Å. To create a phase contrast image, the transmitted and the diffraction beams are used to create an interference image. In particular, the interactions of the incident beam with the sample result in a phase shift of a part of the electron beam giving rise to a diffracted beam while the rest of the beam is transmitted. The interaction between the transmitted and phase shifted electron beams exiting the sample results in the change of electron beam amplitude.[4]

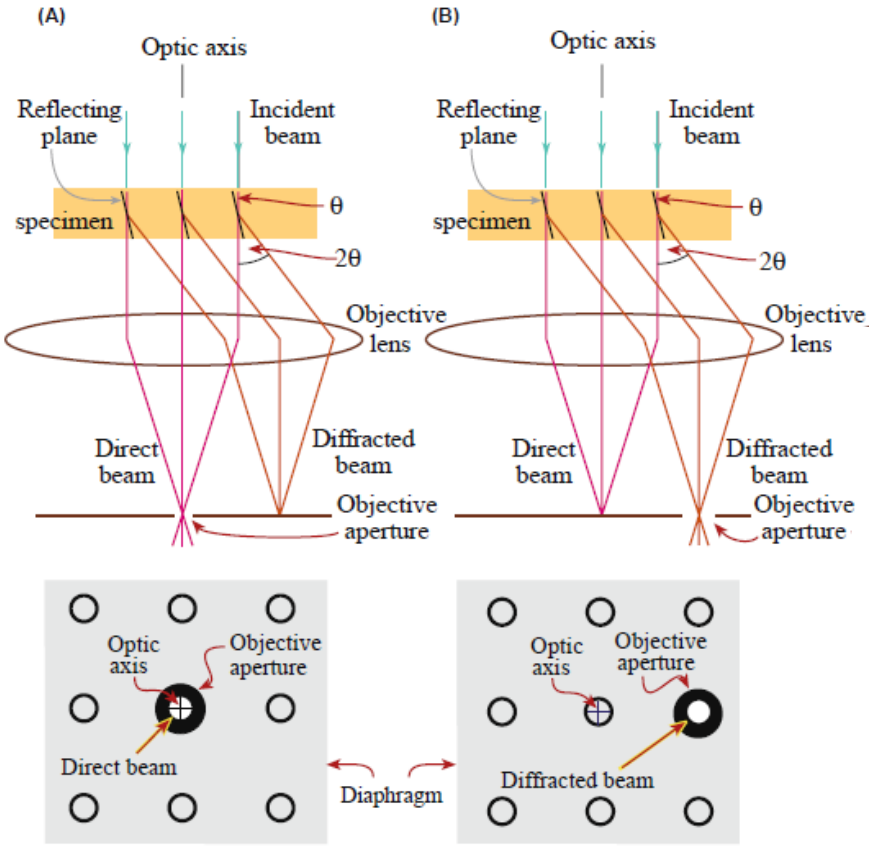

Fig. 2.1 – Diagrams showing how the objective lens and objective aperture are used in combination to produce (a) bright-field imaging, and (b) dark-field imaging.[2] Reprinted with the permission from [2]. Copyright (2009) Springer Nature.

Selected area electron diffraction (SAED) is a TEM experimental technique that allows for the determination of the crystal structure of the sample under analysis/e-beam irradiation. For a few particular orientations of a crystallite relative to the incident beam, the Bragg's law is satisfied and a crystallite strongly diffracts the incident electrons. The resulting diffraction patterns, which typically consist of either spots (in case of single crystals) or rings (in case of polycrystalline or powder samples), can be used to identify the spacing of the scattering lattice planes, and, consequently, the corresponding crystal structure.[5]

In scanning transmission electron microscopy (STEM), a focused beam is scanned over the sample and the scattered electrons at high angle can be used to produce images with high contrast with intensities proportional to the square of the atomic number. STEM images are usually recorded in dark-field mode, using a high-angle annular dark-field (HAADF) detector located just below the specimen. It collects electrons that are transmitted through the specimen and scattered within a certain angular range.[2]

Energy dispersive X-ray (EDX) spectroscopy is an analytical technique that provides a spatial mapping of the atomic composition within a sample, thanks to the characteristic X-ray radiations emitted by the constituent elements in response to the interaction of the e-beam with the sample. The BF-TEM images were recorded using a JEOL JEM-1011 instrument with a thermionic tungsten source operated at 100 kV. The samples were prepared by drop-casting the diluted NC solution or the catalyst powder suspended in toluene or chloroform onto a carbon coated 200 mesh copper grids. HRTEM analysis was carried out by a JEOL JEM-2200FS microscope equipped with a field emission gun working at 200 kV, a CEOS spherical aberration corrector in the objective lens allowing for a spatial resolution of 0.9 Å, and an in-column Omega energy filter. The chemical composition of the NCs was determined by EDX performed in a HAADF-STEM mode with a Bruker XFlash 5060 EDX detector.

For TEM analyses, 100 μL of diluted colloidal NC solution was deposited onto carbon-coated grids, and dried automatically. For the catalyst powder, 2 mg of the sample was suspended in toluene or chloroform and mildly sonicated. About 100 μL of the supernatant was then deposited onto ultrathin carbon-coated Cu grids. The STEM-EDX qualitative maps were acquired using Cu Kα and Pd/Pt Lα narrow lines to avoid artifact signals due to neighboring X-ray peaks. For HRTEM and STEM-EDX analyses, the sample is prepared by drop-casting a NC solution onto ultra-thin carbon-coated Ni grids, after O_2 and Ar plasma treatment at 20 W for 2 min. The SAED patterns were acquired using a FEI Tecnai F20T TEM (Schottky emitter, 200 kV) at constant camera length with the sample placed at the eucentric height and after carefully focusing the NC images. The camera length was calibrated using a nanocrystalline Au sputtered film on a standard carbon covered Cu grid. The NC average size and its distribution were obtained using ImageJ program. For the catalysts, more than 100 particles were processed by manual counting using Gatan Digital Micrograph software from analysis of the HAADF electron micrographs to determine the particles size distribution.

2.1.2 X-Ray Diffraction

X-ray diffraction (XRD) is a non-destructive technique used to identify the crystalline phases present in the samples. X-rays are electromagnetic radiations characterized by a wavelength comparable to the interatomic distance and, penetrating deeply into the material due to their low absorption coefficient, generate diffraction phenomena that convey information on the position of atoms in the lattice planes of the crystalline cell and on the interplanar distances. When an X-ray hits an atom, the innermost electrons enter into oscillation: each atom thus becomes a source

of a spherical wave. The diffuse waves can give constructive or destructive interferences in space and are at the origin of the diffraction phenomenon.[6]

The X-ray diffraction is based on the constructive interference of a monochromatic X-ray beam with a crystalline sample: the rays affect the different families of parallel lattice planes, characterized by the hkl indices, forming an angle of incidence θ. The rays are then reflected at the same angle θ. Since the angle measured experimentally is the one between the incident beam and the diffracted one, the data are plotted in 2θ scale. The interaction of incident X-rays with the sample produces constructive interference only in specific directions determined by Bragg's law:

(2.1) $$n\lambda = 2d_{hkl}\sin\theta_{hkl}$$

where λ is the wavelength of the incident radiation, θ the angle of reflection (that is equal to the angle of incidence), n a positive integer and d_{hkl} is the distance between two consecutive crystalline planes with assigned Miller hkl indices (Fig. 2.2). Through equation (2.1) the real space, related to the interplanar distance d_{hkl}, is converted into the reciprocal space, observable through the angles 2θ at which the peaks appear. The angular position of the peaks is determined by the interplanar distances, while the intensities of the peaks reveal the position of the atoms in the planes. The distance d_{hkl} is therefore obtained from the angle θ of each reflection. Every crystalline phase is associated with a certain series of diffraction peaks which allows his identification.

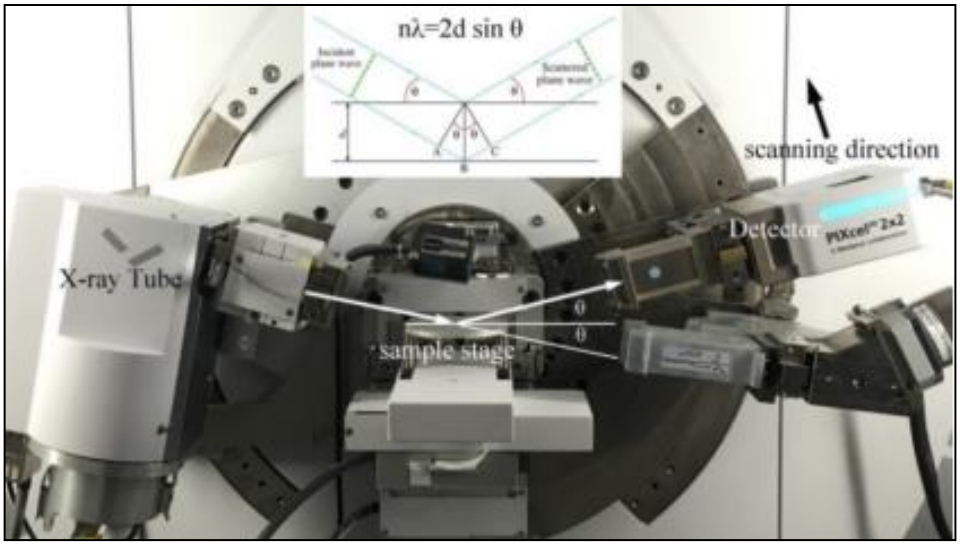

Fig. 2.2 – PANalytical Empyrean X-ray diffractometer within the inset the X-ray scattered by atoms in an ordered lattice.

In this regard, this technique was used in this thesis work to characterize the crystalline structure of the colloidal NCs at the synthesis level, to determine the NC average size and to monitor the transformation of the supported NCs upon exposure of the catalysts to different environments. The XRD pattern of the sample was obtained on a PANalytical Empyrean X-ray diffractometer

equipped with a 1.8 kW Cu Kα ceramic X-ray tube, PIXcel^{3D} 2×2 area detector, operating at 45 kV and 40 mA. XRD spectra were collected on a dropped concentrated NC solution or a catalyst powdered sample onto a zero-diffraction silicon substrate. The diffraction pattern was performed at ambient conditions in a parallel-beam geometry and symmetric reflection mode over an angular range 30°-90°, with a step size of 0.05°. High score 4.1 software from PANalytical was used for phase identification.

The Sherrer formula can be used to estimate the average size d_p of the NC crystalline domains according to the following equation:

$$d_p = \frac{K\lambda}{\beta \cos\vartheta} \tag{2.2}$$

where K is a dimensionless shape factor and generally assumed to be 0.89 for spherical NCs, λ is the X-ray wavelength (Cu Kα = 1.54 Å), β *i*s the full width at half maximum of the peak and θ is the Bragg angle.

2.1.3 Diffuse Reflectance Infrared Fourier Transform Spectroscopy

In situ diffuse reflectance infrared fourier transform spectroscopy (DRIFTS) is a useful technique in catalysis. It is used for the identification of surface-bound molecular species, such as reactants and intermediate species or gas phase products during the exposure of the sample to a reactive environment. It also reveals the presence of surface acidic hydroxyl groups, surface basic sites, or defects such as oxygen vacancies.[7, 8]

Monitoring the adsorption of probe molecules, such as CO, NO, NO_2 by infrared spectroscopy has been reported to give information about the chemical nature of surface or adsorbed species, as well as their structures and the strengths of chemical bonds. By the correlation of the adsorption bands to the specific electronic state of the active sites, it is possible to identify and to study the properties of the latter ones.[9] Indeed, the species adsorbed on the catalyst surface are identified by detecting molecular vibrations, due to the dipole moment changes, that are located in the mid-region infrared energy (200–4000 cm^{-1}).

In principle, the focused infrared beam is directed into the sample using an ellipsoidal mirror and then absorbed, transmitted and reflected by the sample. The diffusely scattered radiation from the sample surface is then collected with second parabolic mirrors and focused on the detector, resulting in a vibrational spectrum as a function of the wavelength of the incident radiation.[10] A schematic diagram of DRIFT spectroscopy is reported in Fig. 2.3.

The infrared absorption spectrum is described by the Kubelka-Munk function:

$$\frac{\mu(\bar{\nu})}{s} = \frac{(1-R_\infty)^2}{2R_\infty} = F(R_\infty) \tag{2.3}$$

where μ is the absorption coefficient of the sample dependent on the wavenumbers $\bar{\nu} = 1/\lambda$, s the scattering coefficient and R_∞ the reflectance of an infinitely thick sample. As an approximation, if the scattering coefficient s is assumed constant, the equation (2.3) transforms the measured spectrum R_∞ in the absorption spectrum $\mu(\bar{\nu})$.

In situ DRIFT measurements were collected using a Bruker Optics Vertex 70 FTIR spectrometer, equipped with a Praying Mantis cell. Liquid nitrogen cooled Mercury Cadmium Telluride (MCT) detector was used for data acquisition and OPUS software for data processing. The outlet gaseous species were analyzed with a mass spectrometer (Pfeiffer Omnistar). Four-port selector valve was used to switch between two different gas streams, one used for the treatments and the other containing the probe species. In a typical experiment, the cell was loaded with 30 mg of catalyst packed on the top of about 80 mg of γ-Al_2O_3 (crushed and sieved to obtain particle size <63 μm).

The measurements consisted of two steps: a pre-treatment and a measurement step. Pre-treatment options included 1) oxidizing; 2) reducing and 3) reducing + O_2 exposure at room temperature. Spectra were also collected at 130 °C on $PdCu/Al_2O_3$, at 100 °C on $PtCu/Al_2O_3$ and $PdCu/SiO_2$, and at 80 °C on $PtCu/SiO_2$ catalysts. The conditions used for the oxidizing and reducing treatments were the same used in the catalytic tests described later in the section 2.1.8, except for the heating rate, which was set to 10 °C min^{-1}, and the flow rate (80 mL min^{-1}).

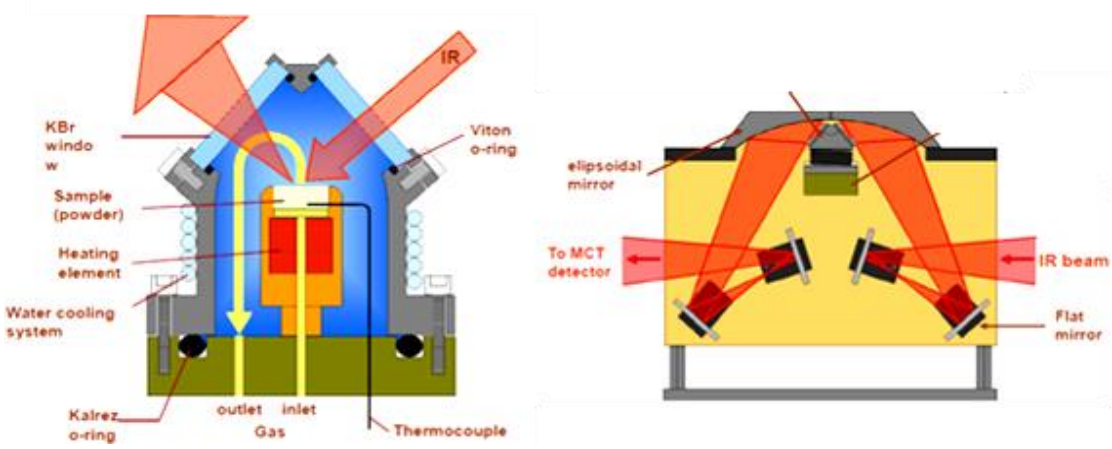

Fig. 2.3 – Schematic of diffuse reflectance infrared spectroscopy measurement setup.

The measurement sequence was the following: the sample was cooled to room temperature under a He flow, and a background spectrum was recorded at 25 °C directly after the catalyst pre-treatment. After collection of the background, the He gas stream was replaced by a stream containing 0.2% v/v CO balanced with He. Nine absorption spectra were collected every 10 s from the gas switch. After 6 min from the beginning of the absorption process, additional 5 spectra were collected every 60 s. Then, the catalyst was purged with He and desorption spectra were acquired with the same frequency as in the adsorption phase.

An overview of the IR bands reported in the literature for surface species relevant for the assignment of the bands in this thesis is presented in Table 2.1.

Table 2.1 – Summary of the assignments of carbonyl bands after CO adsorption on various species and their corresponding IR wavenumbers.

Structure of the CO adsorbed on various sites	IR wavenumbers (cm^{-1})
Linear Pd^0-CO species[7, 11]	2100
Bridged Pd^0-CO species[7, 11]	1960
Multi-bonded Pd^0-CO species[7]	1860
Linear Pd^+-CO species[7]	2135-2110
Linear Pd^{2+}-CO species[7]	2215-2145
Linear Cu^0-CO species[11]	2110-2080
Linear Cu^+-CO species[12]	2140-2110
Linear Cu^{2+}-CO species[12]	2145 and above
Linear Pt^0-CO species[7]	2100-2060
Bridged Pt^0-CO species[7]	1850
Linear Pt^{2+}-CO species[13]	2205-2180
Linear Pt^+-CO species[13]	2130-2120

2.1.4 X-Ray Absorption Fine Structure Spectroscopy

X-ray absorption fine structure (XAFS) spectroscopy is used for determining the chemical state and the local structure of a selected element, without the requirement for long-range order in the sample.[14, 15] The experiment is performed exposing the sample to a high flux of monochromatic X-ray beam of specific energy. Part of this energy can be absorbed by atoms in the sample resulting in the excitation or ejection of a core electron to excited electronic states or the continuum, creating photo-electrons. Data acquisition can be done in transmission or in fluorescence mode. In transmission mode, the absorption of the incident beam is recorded by two ionization chambers placed before the sample to measure the intensity of incident X-ray (I_o) and after the sample to measure the intensity transmitted X-ray (I_t). The X-ray absorption coefficient (μ) is thus determined by the following equation:

$$\mu(E) \propto \ln \frac{I_o}{I_t} \tag{2.4}$$

In the fluorescence mode, the number of fluorescence X-rays emitted after an electron fills up the hole in the pre-exited core is measured. X-ray absorption spectra are measured at an absorption edge where the incident X-ray energy equals the energy required to excite an electron to an unoccupied electron orbital leading to a sharp increase in absorption. The X-ray absorption spectrum can be separated into two distinct regions (Fig. 2.4a): X-ray absorption near-edge structure (XANES) is the region close to the absorption edge which occurs typically within 60

eV of the main absorption edge and extended X-ray absorption fine structure (EXAFS) related to the area at higher energies and addressed to the oscillations of the excited photoelectrons around the absorbing atoms. The XANES region can provide information regarding the oxidation state and the binding geometry of the absorbing atom. Generally, the XANES spectra are analyzed by fingerprinting the measured spectrum with a spectrum of the known compound. On the other hand, the EXAFS region can be used to determine the interatomic distances, coordination number, type of neighboring and degree of local species bonding disorder around the absorbing atom (Fig. 2.4b).[16]

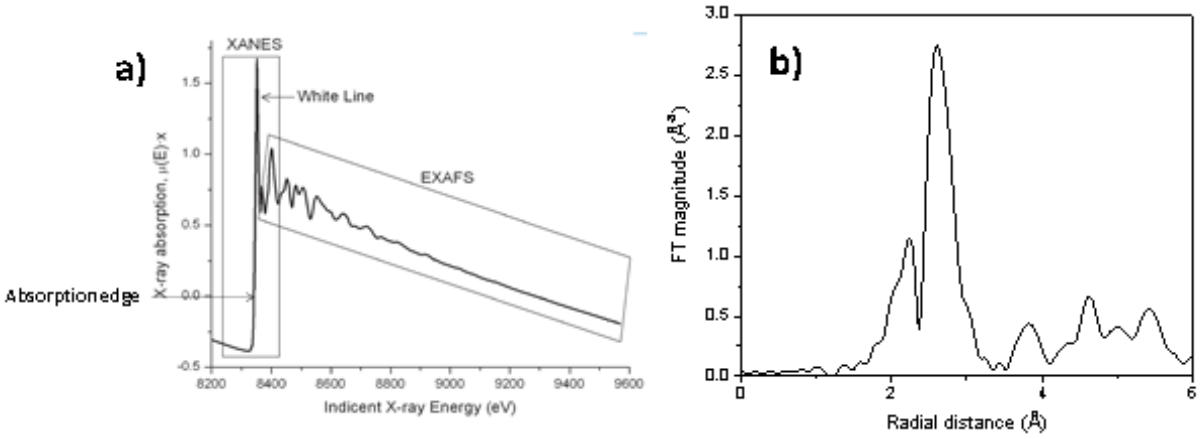

Fig. 2.4 – (a) XAFS spectrum of platinum foil recorded in transmission mode and (b) the Fourier transform of the EXAFS function from a platinum foil.

The EXAFS spectrum can be understood in term of the EXAFS function written as a sum of the contribution from all scattering paths of the photoelectron:[16]

$$\chi(k) = \sum_i \frac{S_0^2 N_i F_i(k)}{k R_i^2} \exp\left(-\frac{2 R_i}{\lambda(k)}\right) \exp\left(-2k^2\sigma_i^2\right) \sin\left(2k R_i + \delta_i(k)\right) \tag{2.5}$$

where k is the wave vector related to the photoelectron kinetic energy, i the label of the coordination shells around the absorbing atom, R_i the distance between the absorbing atom to the scattering atom (interpreted as the half of the path length for multiple scattering events), N_i the degeneracy (equal to the number of atoms of the same species in the same coordination shell), $F(k)$ the effective scattering amplitude for a spherical wave, S_0^2 the amplitude reduction factor (that takes into account the relaxation effects in the absorbing atom in the presence of a core hole vacated by the photoelectron), $\exp(-2R_i/\lambda(k))$ the exponential attenuation of electrons propagating through the material, $\exp(-2k^2\sigma_i^2)$ the effect of lattice vibrations that contains the Debye-Waller factor (σ^2) (which is related to thermal or the static disorder) and $\sin(2kR+\delta(k))$ (which is the total phase shift). Therefore, the EXAFS spectra are analyzed by extracting the $\chi(k)$ from the experimental data and then performing a curve fit to a theoretical scattering path. This is constructed considering a model structure close to the measured material and, by means

of a computer code, it is thus possible to estimate the unknown function in the EXAFS equation based on this model structure.

The *R*-factor is one of the parameters that gives information about the goodness of the fit and it is the sum of the square of the differences between the data and the fit at each data point, divided by the sum of the squares of the data at each corresponding point:

$$R-\text{factor} = \frac{\sum_i (\text{data}_i - \text{fit}_i)^2}{\sum_i \text{data}_i^2} \quad (2.6)$$

R-factor less than 0.05 are considered to reflect a reasonable fit.

By Fourier transforming the EXAFS function, it is possible to separate the different sine waves that contribute to the equation and thus to visualize the different coordination shells (Fig. 2.4b). It should be taken into account that the *R* positions do not correspond exactly to the interatomic distances since the phase shift is not observed.

To get a more complete picture of the dynamic changes in the catalyst structure, which occur in response to a variation of the gas environment and of the temperature, XAFS was implemented to study the transformations of NCs supported on Al_2O_3 at different absorption energy edges. Such analysis could provide electronic and structural information about the coordination of Cu, Pt and Pd in the as-synthesized materials as well as their evolution upon oxidative/reductive annealing conditions or during the CO oxidation reaction.

To study the dynamic transformations of the PdCu and PtCu alloys upon oxidative and reductive pre-treatments, Quick X-ray absorption spectroscopy data were recorded in transmission mode at the Cu K edge (8979 eV), Pt LIII edge (11564 eV) and Pd K edge (24350 eV) on the ROCK (Rocking Optics for Chemical Kinetics) beamline of synchrotron SOLEIL (France). Indeed, from the analysis of in-situ data, it was possible to monitor both the change of oxidation state of the elements as well as verify the interaction noble metal-Cu-support, more specifically the neighbors' number and the bond distance, providing information about the modification that the system undergone during the pre-treatments.

For in situ measurements during the oxidation/reduction pre-treatments, the calcined catalyst was exposed to 60 mL min^{-1} of a mixture of 6% v/v O_2/He and 5% v/v H_2/He following the scheme reported in Fig. 2.5. Spectra acquisition was also recorded on the samples in He at room temperature before each treatment for data comparison. Thanks to the edge jumping capability of the Quick-EXAFS monochromator,[17] both the edges of elements composing the bimetallic catalyst were characterized simultaneously. Indeed, Si(111) and Si(311) crystals were alternatively used as a monochromator for the Cu and Pd/Pt edges. Data acquisition was recorded for 1 min at one edge before changing the monochromator by the other one (with about 30 s of dead time for the exchange) and then spend the subsequent minute at the other edge of interest. The cell allows to perform in situ treatments of the catalyst under controlled conditions such as temperature, pressure and chemical environments, during the experiment according to the assembled system described by La Fontaine et al.[18] The calibration of the energy scale was

ensured by the simultaneous measurement of the absorption spectrum of the correspondent metallic foil of the elements composing the bimetallic catalysts set between the second and third ionization chambers.

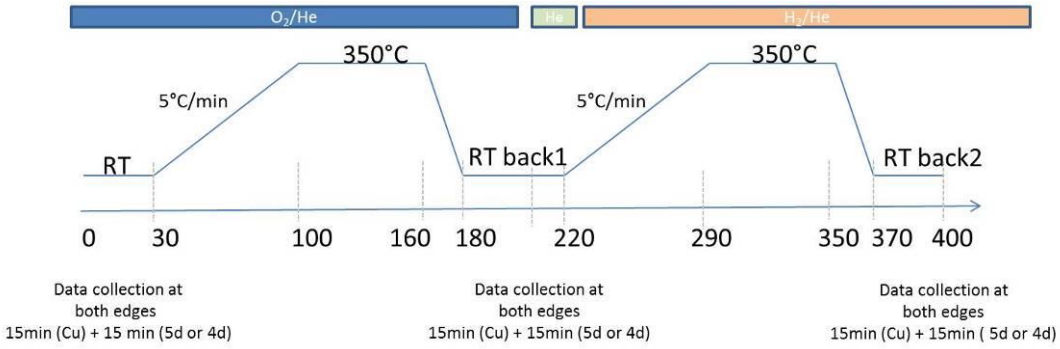

Fig. 2.5 – Scheme of the protocol used in the ROCK beamline.

To monitor the nanoscale modifications that the PdCu and PtCu alloys undergone during the exposure to CO oxidation reaction and thus to correlate their catalytic and the structural properties, the catalysts were loaded into an in situ plug-flow reactor cell[19, 20] and XAFS spectra were collected in transmission mode at the Cu K edge (8979 eV), Pt LIII edge (11564 eV) and Pd K edge (24350 eV) at the SuperXAS beamline of the Swiss Light Source (SLS) at Paul Scherrer Institute (PSI Synchrotron), Switzerland. For in situ measurements during the CO oxidation reaction, the catalysts, after each oxidation/reduction pre-treatment, were exposed to 40 mL min^{-1} of a mixture of 1% v/v CO and 6% v/v O_2/He following the scheme reported in Fig. 2.6.

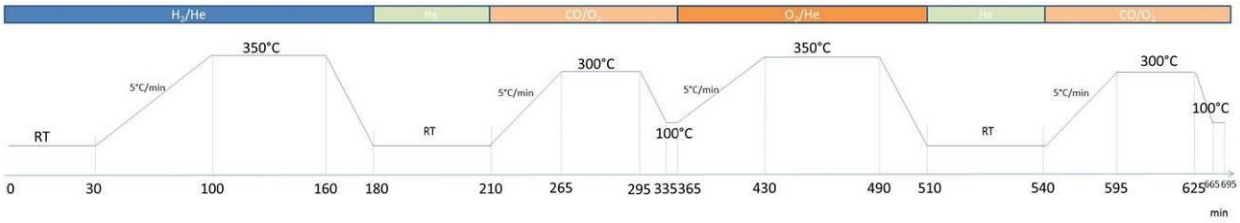

Fig. 2.6 – Scheme of the protocol used in the SuperXAS beamline.

The programs ATHENA (version 0.9.26) and ARTEMIS (version 0.9.26) within Demeter package were used to reduce and fit the data to obtain structural parameter (N, $\sigma^{2,}$ and R). Data reduction consisted of the pre-edge subtraction, background determination, normalization and conversion to k space. Then, the k^2-weighted EXAFS functions $\chi(k)$ were Fourier transformed and fit in R space using the equation (2.5) simulating the experimental signal. The fitting was performed for the first and second shell scattering at both edges to determine the identity, number and positions of the nearest neighbors and thus to generate the cluster around the selected absorbers. Initially, the ATOMS and FEFF packages implemented inside the program were employed to generate ab initio the scattering paths for the defined clusters starting from model compounds of known structure. The theoretical models for the Cu-substitute Pd and Pt alloys were built on structures containing 50% noble metal and 50% Cu atoms randomly distributed in a fcc lattice. In the case of palladium and copper oxides phases, four model clusters

were constructed around the Pd and Cu absorber atoms with respect to the structural data for PdO (ICSD 24692), Pd_2O (ICSD 77651) and CuO (ICSD 61323), Cu_2O (ICSD 26963), respectively. Finally, regarding the modeling of the clusters of $Cu_xPd_{1-x}O$ phase, the PdO and CuO lattices in which the Pd and Cu absorber atoms were randomly replaced with the Cu and Pd atoms, respectively, were used as initial structural data for the model. Then, a certain number of scattering paths were included in the modeling fitting the k^2-weighted EXAFS functions in the selected k range. The structural parameters of the above equation (2.5) were assumed to be adjustable. In particular, the values of amplitude reduction factor (S_o^2) were obtained from fitting the standards (Cu, Pd and Pt foils) and their values were fixed in the analysis of the sample. The others parameters or variables i.e. reference energy (E_o), degeneracy of selected path (N) for each shell, interatomic distance (R), Debye-Waller factor (σ^2) were obtained from the fittings; the reported Fourier transform of the EXAFS spectra and the best fits are not phase corrected. The calculations of the coordination number at each shell as the product of NS_o^2 along with the R and σ^2 corresponding to each shell are reported in Appendix A for the data reduction from ROCK beamline and in Appendix B from the SuperXAS beamline experiments.

2.1.4.1 Chemometric Tools

As this time-resolved technique produced a huge amount of data, the determination of the number of the intermediate species cannot be easily done by visualizing the XAFS spectra alone even if the observation of the isosbestic points is a good tool to estimate them. Indeed, these points indicate the formation of intermediate species without obtaining their structure quantitatively.[16] Furthermore, the identification of the chemical species involved during the treatments becomes less straightforward by XAFS due to the lack of known spectral fingerprints for the NCs compared to the bulk phases for which the spectra are reported in the literature. For these reasons, chemometric tools combining Principal Component Analysis (PCA) and Multivariate Curve Resolution with Alternating Least Squares (MCR-ALS)[21, 22] were used to estimate the number of components and extract the pure spectra of the intermediate species during the *in situ* characterizations of catalysts. By using this statistical analysis implemented on the toolbox MATLAB package, it is possible to estimate the numbers of components in a mixture of unknowns involved during the transformations extracting their pure spectra profile and concentration profile for each component.

Experimental data were arranged to yield a matrix $\boldsymbol{D}$ ($m \times n$) containing the m spectra recorded along the reaction with n the number of energy points (Fig. 2.7). This matrix was processed using the MCR-ALS method to unravel the mechanisms leading to the formation of active species. The number of variability sources, related to the number of chemical species, was analyzed using PCA by Singular Value Decomposition (SVD), and Evolving Factor Analysis (EFA).

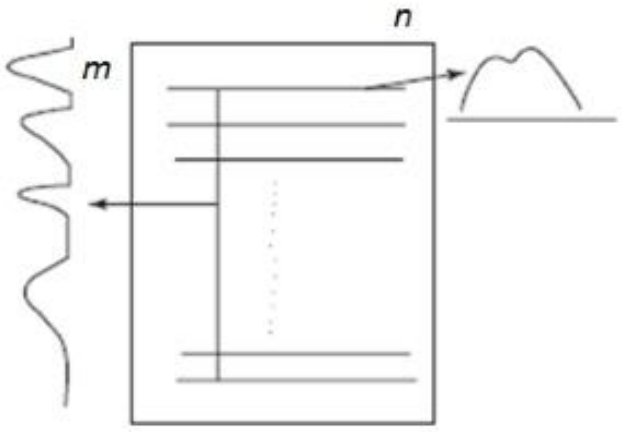

Fig. 2.7 - Schematic representation of the data matrix **D** ($m \times n$). Reprinted with the permission from [Chau F.T., Liang Y.T., Gao J.B. and Shao X.G., Chemometrics: from basics to wavelet transform. John Wiley & Sons, Inc. 2004]. Copyright (2004) John Wiley and Sons.

2.1.4.1.1 Multivariate Curve Resolution with Alternating Least Square

MCR-ALS method decomposes the data matrix **D**, assuming that the experimental data follow a linear model, as follows:

(2.7) $$\mathbf{D} = \mathbf{C}\mathbf{S}^{T} + \mathbf{E}$$

where the terms CS^T is the product of the matrix containing concentration profiles **C** and the matrix containing XAFS spectra $\mathbf{S}^T$ of the κ species of the unknown mixtures. **E** is the matrix of residuals, which contains the variability not explained by the model, ideally close to the experimental error. The superscript T means the transpose of matrix **S**, where XAFS spectra are column profiles. Matrices **C** and $\mathbf{S}^T$ are responsible for the observed data variance. The dimensions of these matrices are **D** ($m \times n$), **C** ($m \times \kappa$), $\mathbf{S}^T$ ($\kappa \times n$) and **E** ($m \times n$) (Fig. 2.8).

MCR-ALS analyses the matrix **D** as an iterative resolution method, in which at each iterative cycle of the optimization process, matrices **C** and $\mathbf{S}^T$ are calculated under constraints so that they minimize the error in the reproduction of the original data set **D**, in order to obtain a solution with chemical meaning (Fig. 2.9). Generally, MCR-ALS is performed according to the following three fundamental steps:

1. Evaluation of the number of components κ that make a significant contribution to the signal response and that are related to the number of chemical species presented in the studied system. This first step can be carried out with PCA by SVD, that express the relevant information contained in a data matrix **D** ($m \times n$) in a reduced number of hierarchized variables known as principal components.

2. Search for matrices of the initial estimations of **C** (concentration profiles) or **S** (spectral profiles). For this purpose, EFA is used.

3. Finally, ALS algorithm is applied to obtain the spectral and the concentration profiles of the species involved in the process. In this last step, some constrain can be applied to drive the final solution towards a chemical meaning.

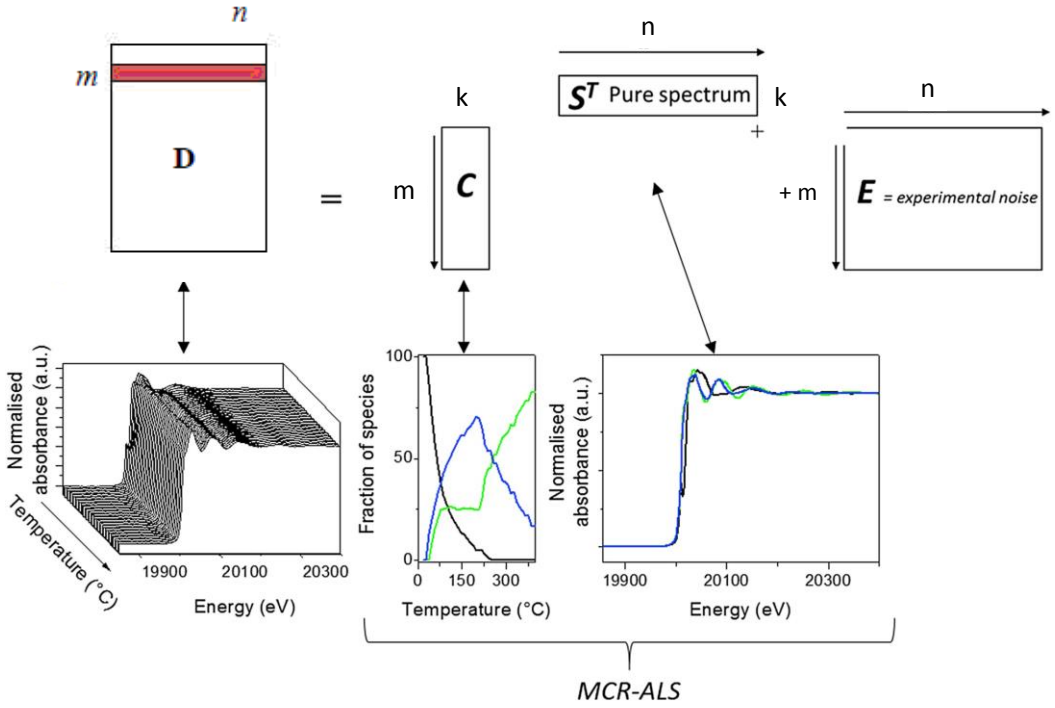

Fig. 2.8 - Schematic representation of the MCR-ALS analysis of the time-resolved experimental XAFS data **D**. **C** and $\mathbf{S}^T$ are the concentration matrix of the species and the XAFS spectra matrix, respectively.[21] Reprinted with the permission from [21]. Copyright (2016) Springer Nature.

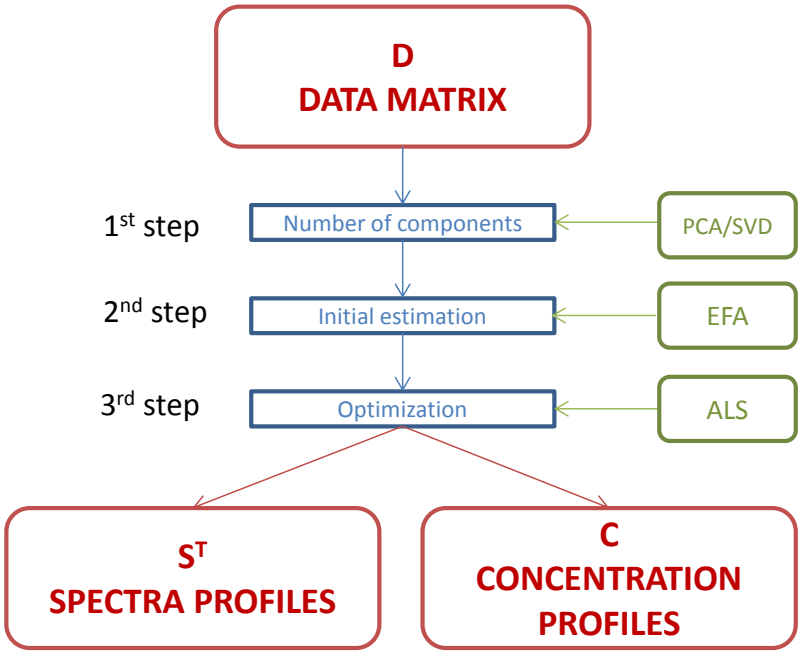

Fig. 2.9 - Scheme of the resolution process of the MCR-ALS method.

2.1.4.1.2 Principal Components and Evolving Factor Analysis

The PCA is a technique able to reduce the dimensionality of a data set, consisting of a large number of interrelated variables, to eliminate spurious information (instrumental noise, etc.) and to evaluate the relative relevance of the variables. This is achieved by introducing a new set of variables, the principal components (PCs), which are linear combinations of the original variables. The most important feature of PCs is that they are orthogonal to each other, not related and ordered with respect to the percentage of variability present in the original data set.[23]

The PCA is a rotation process of the original data of the matrix **D** carried out in such a way that the first new axis is oriented in the direction of maximum variance of the data, the second perpendicular to the first and in the direction of the next maximum variance of the data, and so on for all new *m* axes. This representation in the row space facilitates the analysis of the relationships between the data by identifying the common directions of variability (PCs) (Fig. 2.10). This happens through a linear transformation of the variables that projects the original ones into a new system in which the new variable with the greatest variance is projected on the first axis (PC_1), the new variable, second by variance size, on the second axis (PC_2) and so on. The reduction of complexity is limited to analyzing the principal (by variance) among the new variables. PCs with a low percentage of variability are linked to the contribution of measurement errors or irrelevant information.

Correlation-based PCA requires that each variable has zero mean and unit variance, while covariance only asks for zero-mean normalization. Therefore, before proceeding with the calculation of the new coordinates with respect to the PCs space, the average of the respective column (mean centering) is subtracted from each variable and the result is divided by the standard deviation of the same (autoscaling). This transformation makes it possible to translate the data at the origin of the reference system since each column will have an average of zero and also makes it possible to make the variability of each variable equally important.[24]

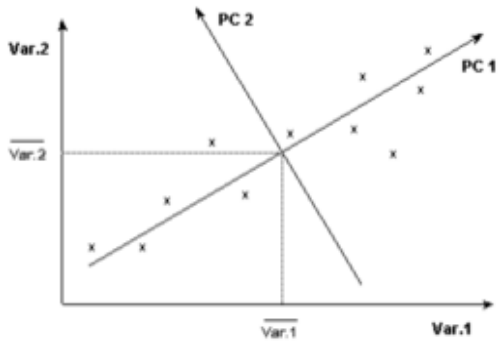

Fig. 2.10 - PCs in a bidimensional data set.

The idea on which the PCA is based is that if two or more original variables are correlated then it is possible to identify a common direction of variability that can be described by a single PC.[25] Fig. 2.11 shows the geometric interpretation of the axes of maximum variability of a two-

variable data set (var. 1 and var. 2). The loadings represent the direction cosines p_1 and p_2, which is the cosines of the angles between the direction of the PCs and the axes of the space of the variables. The scores represent the coordinates of the data in the reference system represented by the PCs. The dispersion of data along these axes can be calculated through variance. The two PCs are orthogonal and PC_2 represents very limited data variability. The perpendicular distances of the data from the PCs are the residues.

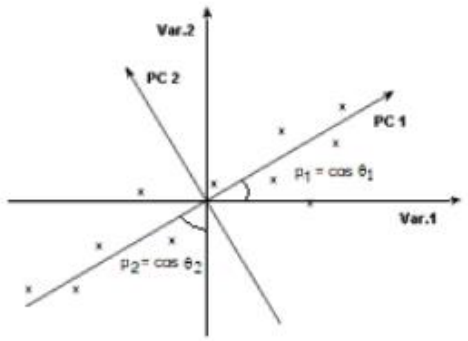

Fig. 2.11 - PC_1 scores and loadings in a bidimensional data set.

The intrinsic dimensionality of the data set is much smaller than the number of variables measured and the number of PCs needed to explain the non-noise variability is very small. One of the objectives of PCA is therefore to choose the number of significant PCs. This can be done according to the following criteria:

- the eigenvalue criterion provides that the PCs whose corresponding eigenvalues are less than one or, the components that have greater variance than the average are not considered This criterion is based on the fact that the data sets are scaled down and therefore it can be assumed that the eigenvalue associated with each PC represents the number of variables whose variability is captured by that principal component;

- a second criterion only takes components that represent 80-90% of the overall variability;

- the choice of the number of PCs sufficient to reproduce with a good approximation the original data set can be made through the scree plot of the eigenvalues, constructed by placing the order numbers of the PCs on the abscissa axis and in the ordinate the eigenvalues to corresponding ones. The point where the slope of the curve is clearly leveling off (the elbow) indicates the number of PCs that should be considered (Fig. 2.12).

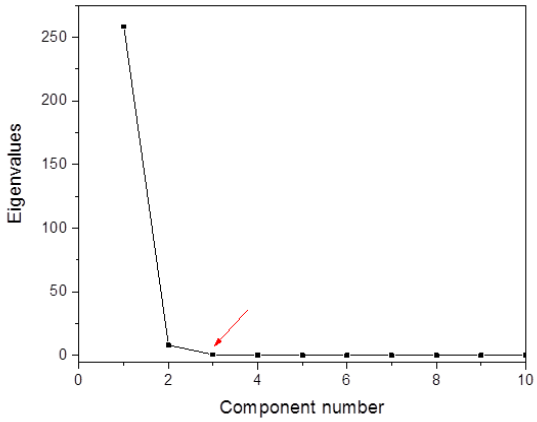

Fig. 2.12 - Scree plot of eigenvalues of ten PCs of an experimental data set.

The principal components (PCs) are calculated decomposing the eigenvectors of the variance-covariance matrix of **D** with the algorithm called singular value decomposition (SVD).[23, 24]

(2.8) $$\mathbf{D}^T\mathbf{D}\mathbf{p_1} = \lambda_1\mathbf{p_1}$$

where $\mathbf{p}_1$ is the vector ($m \times 1$) of the coefficients (called loadings) for the first main component. The vector of the p_1 loadings represents the cosine directors of the first PC, and is the eigenvector of the covariance matrix of **D** (i.e. $\mathbf{D}^T\mathbf{D}$) corresponding to the largest eigenvalue λ_1 of $\mathbf{D}^T\mathbf{D}$, which is a measure of the variance explained by the first PC.[26] What has just been described for the first eigenvector can be iterated to determine all the S = PC rank of the PCA model; that is, all the loadings p_s (s = 1, 2, ..., S) of the PCA model, which are orthonormal. The vector of the scores t_s, i.e. the projection of the original data along the PC direction, is given by

(2.9) $$\mathbf{t}_s = \mathbf{D}\mathbf{p}_s$$

Note that the score vectors are orthonormal. The data matrix **D** can be represented as the scalar product of the S-vector loadings and scores

(2.10) $$\mathbf{D} = \sum_{s=1}^{S} \mathbf{t}_s\mathbf{p}_s^T$$

If the number of PCs that are considered is the maximum possible, the original representation of the data and that obtainable from the PCA are perfectly equivalent. Instead of assuming that only the first A PCs are maintained, and defining the matrix of the scores $\mathbf{T} = (t_1, t_2, ..., t_A)$ and the matrix of the loadings $\mathbf{P} = (p_1, p_2, ..., p_A)$, the (4) becomes

(2.11) $$\mathbf{D} = \sum_{s=1}^{A} \mathbf{t}_s\mathbf{p}_s^T + \sum_{s=1}^{A} \mathbf{t}_s\mathbf{p}_s^T = \mathbf{T}\mathbf{P}^T + \mathbf{E} = \hat{\mathbf{X}} + \mathbf{E}$$

where **E** is the ($m \times n$) matrix of the residuals generated by the (S - A) PCs discarded of the PCA model, when **D** is reconstructed using only the first A PCs. The residual matrix **E** reflects the variability of data that is not captured when not all PCs are considered.

While PCA aims to reduce the size of the data matrix, the Evolving Factors Analysis (EFA) tries to explain the correlations between a set of variables observed through a set of unobservable variables. The fundamental idea of EFA technique is to follow the singular values of the data matrix **D** (in this case not mean-centered) as rows are added.

The process, shown in Fig. 2.13, starts from the first row of the data matrix, e.g. the first spectrum measured, for which singular values are calculated. Afterward a second row is added and SVD is performed on two rows, and so on for the whole matrix **D**. As this process evolves forward on the ordered variable, it is known as forwarding EFA. When EFA is performed in the opposite direction, analyzing an increasing number of rows, beginning from the end, the so-called backward EFA is obtained. Since the number of rows considered, and thus the number of factors, evolves as the method proceeds, the technique is known as evolving factor analysis.[24]

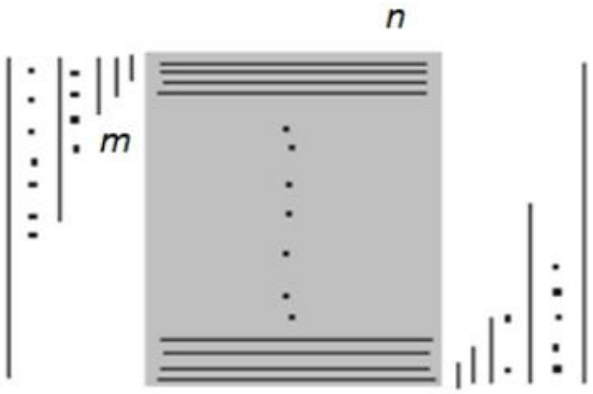

Fig. 2.13 - Schematic diagram of the process of forward EFA algorithm. The process can be conducted in both the forward and backward directions. It embraces the spectra to be factor-analyzed in a stepwise increasing way and then collects the eigenvalues to be plotted against the retention time points. Reprinted with the permission from [Chau F.T., Liang Y.T., Gao J.B. and Shao X.G., Chemometrics: from basics to wavelet transform. John Wiley & Sons, Inc. 2004]. Copyright (2004) John Wiley and Sons.

As an example, in Fig. 2.14a the EFA plot for $PdCu/Al_2O_3$ sample at the Pd K-edge during the reductive pre-treatment along with the principal component eigenvalues (in log units) obtained from the forward and backward analysis versus the delay time are reported. A threshold separating major contributions from noise is set at *log* eig. = 0, which leads to two significant contributions observed (Fig. 2.14b). The analysis on the forward direction gives a similar result of the backward one in terms of contributions: in the forward EFA the appearance of each component is observed (represented by black lines), since the number of singular values above the noise level equals the number of the underlying species; in the same way, the backward EFA shows the disappearance of each component (red lines) from the system. Therefore an EFA plot gives information about the number of the components, which have a significant signal compared to the noise, and their region of existence called concentration region.

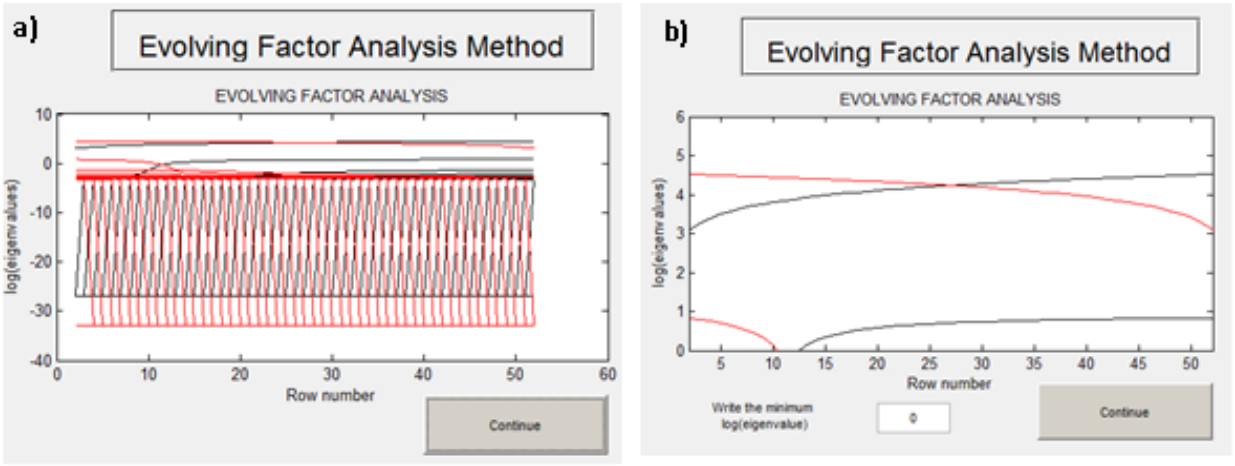

Fig. 2.14 - EFA plot for transient absorption data of $PdCu/Al_2O_3$ sample at the Pd K-edge during the reductive pre-treatment. Black lines denote forward EFA while the red lines denote backward EFA. Eigenvalues (in log units) are plotted as a function of the row number of the data matrix (a) along with the noise and (b) with the minimum log eig set to 0 for the removal of the noise. The only assumption of the method is that the component that first appears will first disappear in an evolving pattern.

2.1.4.1.3 Alternative Least Square Algorithm

Once the number of species is estimated, Alternative Least Square (ALS) optimization can start using initial estimates of either the **C** or the $\mathbf{S}^T$ matrix. Furthermore, the MCR-ALS method imposes **C** and $\mathbf{S}^T$ to follow physically and chemically meaningful constraints like non-negativity of XAFS absorbance and concentration, unimodality (profiles without double peaks) and closure (the concentrations of all the components is equal to a constant value) for instance.

The iterative ALS optimization of matrices **C** and $\mathbf{S}^T$ occurs applying constraints according to the relation

(2.12) $$\left\|\mathbf{D}-\mathbf{C}\mathbf{S}^{\mathbf{T}}\right\|^2 = \min$$

Iterations are carried out alternatively on **C** or on $\mathbf{S}^T$, temporarily fixing the remaining parameters and according to the following steps:

1. Given **D** and the initial estimate of $\mathbf{S}^T$, a minimization of **C** is carried out by the least square calculation considering relation (2.12) and the constraints for **C**.

2. Given **D** and the so-calculated **C** matrix, a minimization of $\mathbf{S}^T$ is carried out by the least square calculation considering relation (2.12) and the constraints for $\mathbf{S}^T$.

3. Then the reproduction of **D** using matrices **C** and $\mathbf{S}^T$ determined in steps 1 and 2 is done. If the convergence criterion is fulfilled, the process is finished. If not, the program goes back to step 1.

Therefore the iteration procedure is stopped when convergence is achieved or when a preselected number of cycles is reached. The attainment of convergence occurs when, in two consecutive iterative cycles, relative differences between the residual of one iteration and the next is less than a previously selected value (usually chosen at 0.1%).[27]

Although MCR-ALS does not require previous knowledge about the chemical system under study, additional knowledge, when existing, can be used to improve the results. The introduction of new information is carried out through the implementation of constraints. The constraints can be based on either chemical or mathematical feature of the data set. There are several ways to classify constraints: the main ones related either to the nature of the constraints or to the way they are implemented. The former sets the elements in a profile to be equal to a certain value, whereas inequality constraint forces the element in a profile to be unequal (higher or lower) than a certain value.[22, 28]

Fig. 2.15 shows the effect of some of these constraints on the correction of a profile. The first is the most general constraint, nonnegativity, is applied when it can be assumed that the measured values in an experiment will always be positive. This restriction is applied easily to spectrophotometric systems, in which it is supposed that the spectral profiles always have positive values of absorbance. This constraint forces the value in a profile to be equal or greater than zero. It is an example of an inequality constraint.

Unimodality allows the presence of only one maximum per profile. It was useful in many concentration profiles related to processes, like reaction profiles or peaks in a chromatographic elution process. It is important to note that this constraint does not only apply to peaks, but also to profiles that have a constant maximum (plateau) or a decreasing tendency.

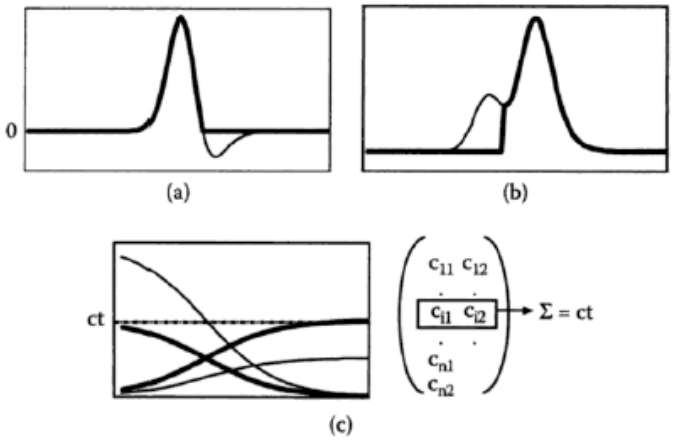

Fig. 2.15 – Effects of some constraints on the shape of resolved profiles. The thin and thick lines represent the profile before and after being constrained, respectively. Constrains shown are (a) nonnegativity, (b) unimodality and (c) closure.

The closure constraint is applied to closed reaction systems, where the principle of mass balance is fulfilled. With this constraint, the sum of concentrations of all of the species involved in the

reaction (the suitable elements in each row of the **C** matrix) is forced to be equal to a constant value (the total concentration) at each stage in the reaction.

The parameters normally used to evaluate the goodness of the MCR-ALS are the explained data variance and the lack of fit parameters.[27]

The amount of variability of the original data set explained is evaluated by the coefficient of determination r^2 given by

(2.13) $$r^2 = \sqrt{\frac{\sum_{i,j} d_{ij}^2 - \sum_{i,j} e_{ij}^2}{\sum_{i,j} d_{ij}^2}}$$

where d_{ij} is an element of the experimental data matrix **D** and e_{ij} is the related residual obtained from the difference between this element and that reproduced from the matrix $\mathbf{CS}^T$ by MCR-ALS.

The lack of fit (*lof*) can be used as a global estimator of the fitting error of the transient spectra data. The equation defining this parameter is

(2.14) $$lof\,(\%) = \sqrt{\frac{\sum_{i,j} e_{ij}^2}{\sum_{i,j} d_{ij}^2}}$$

where d_{ij} and e_{ij} are the same as above.

Two different lacks of fit values are calculated, differing on the definition of the input data matrix **D** (either the raw experimental data matrix or the PCA reproduced data matrix using the same number of components as in the MCR-ALS model). These two lacks of fit values are evaluated and shown at the end of each iterative cycle, when all constraints have been already applied and finally given in the results at the end of the optimization. These values are useful to understand whether experimental data were well fitted and also to evaluate whether the ALS optimization fit approached PCA fit.

2.1.5 Inductively Coupled Plasma Optical Emission Spectroscopy

Inductively coupled plasma optical emission spectroscopy (ICP-OES) is an analytical technique that gives information about the elemental composition of a sample. The basic principle of this measurement is based on the measurement of the characteristic radiation emitted from the element as a result of a decay process to the ground state of the excited atoms or ions.

The sample to be examined is introduced into the plasma source via a peristaltic pump with multiple channels and nebulizers. The channels used for taking the sample are carried to the

pneumatic nebulizer with concentric glass tubes, positioned inside a nebulization chamber where the sample is mixed with the argon. The high-speed gas splits the liquid into droplets of various sizes (<10 mm) that are injected into the plasma torch. In the plasma, the aerosol is rapidly dissolved giving rise to solid micro-particles which at increasing temperatures are vaporized, atomized and ionized. Since in the plasma all atoms are excited simultaneously, the light emitted is a combination of all the wavelengths associated with the descending electronic transitions of the single atoms and ions present in the sample and in the plasma gas. In the instrument, this multi-line emission is collected and separated into the individual wavelengths by means of a selection system based on the coupling of a diffraction grating with a prism. The result is a spatial dispersion and the intensities of the individual atomic lines are simultaneously determined by a planar charge-transfer detector. For this purpose, a two-dimensional "Echelle" lattice is used which separates the polychromatic radiation in the various wavelengths. By measuring the intensity of each wavelength, it is possible to determine the concentration of the corresponding element in the sample by interpolation along the calibration curves obtained by measuring the intensities of each line previously measured from standard element solutions of known concentrations.

The measurements were carried on an iCAP 6000 Series ICP-OES spectrometer (Thermo Scientific) for quantification of the elemental composition of NCs and the metal loading of mono- and bimetallic catalysts. The sample (specific volume of NC colloidal solution or weight of powder catalyst) was digested in aqua regia HCl:HNO_3 3:1 v/v (Sigma Aldrich for trace analysis) at room temperature overnight for the colloidal solution and at 100 °C for 2 hours in the case of the powders. Ultrapure Milli-Q water (18.2 MΩ cm) was added to the sample, and any remaining solids were filtered using a polytetrafluorethylene membrane filter with 0.45 mm pore size before the ICP-OES measurements. Calibration was done for each element with standards at 0.1, 1.0 and 10.0 ppm for the related element to guarantee a linear function of concentration as a function of the intensity. The concentration of the sample solutions
was calculated based on the concentration vs. intensity function obtained. All chemical analyses performed by ICP-OES were affected by an error of about 5-10%.

2.1.6 Thermal Gravimetric Analysis

Thermogravimetric analysis (TGA) is an analytical technique by which the mass is measured as a function of temperature or time while the sample is subjected to a controlled temperature program in a controlled atmosphere. This analysis is commonly used to study several processes such as mass change, thermal decomposition, degradation, oxidation and reduction, absorption and desorption of gases, sublimation and vaporization. The measurement system mainly consists of a thermobalance, a pan for sample loading with a thermocouple, a programmable furnace and a gas purging system through the balance to create inert, oxidizing or reducing atmospheres.

This type of analysis was used to define the optimal conditions for the removal of organic ligands from the surface of the NCs and, thus, to select a defined temperature during the calcination process of the catalyst. The TGA was performed with a Q500 instrument from TA

Instruments. After solvent evaporation, the sample (~3 mg of NCs) was equilibrated at 30 ºC for 30 min, then heated to 600 ºC with a 10 ºC min^{-1} heating rate under 50 mL min^{-1} of nitrogen, while the change of the sample weight loss was recorded continuously.

2.1.7 Catalytic Setup Plan

Fig. 2.16 shows a schematic diagram of the experimental setup used for the pre-treatments and the catalytic activity measurements for CO oxidation reaction of the sample. The experiments were performed in a flow reactor consisting of a vertical quartz tube (internal diameter: 6 mm) where the catalyst is placed between two beds of quartz wool. In the case of the alumina-based catalyst, the powder was diluted with silica (2:1 weight ratio). All gases were introduced into the reactor via calibrated mass flow controllers (MFC) and a tubular furnace was used to heat the reactor. One thermocouple was placed inside the catalyst to monitor the temperature. For the pre-treatments, the catalyst was exposed to a reducing (5% v/v H_2 diluted with He) or to an oxidative (6% v/v O_2 diluted with He) atmospheres at a temperature of 350 °C for 1 h. The heating rate used in both treatments was 5 °C min^{-1}. For the activity measurements, the reactor was heated from room temperature to 300 °C with a heating rate of 5 °C min^{-1}, keep at 300 °C for 30 min, and then cooled to 100 °C at the same rate and keep at 100 °C for 30 min. Figure 2.17 reports the temperature values during the tests. The feed gas was a mixture of 1% v/v of CO and 6% v/v O_2 balanced with He, with a flow rate of 60 Ncc min^{-1} corresponding to a weight hourly space velocity (WHSV) of 4783800 Ncc h^{-1} ($g_{active\ phase}$). The concentration of the outlet gases was measured using a microreactor system coupled with a gas analyzer (Advance Optima AO2020 Series Continuous Gas Analyzer) to detect the CO and CO_2 concentrations at the reactor outlet. The CO conversion was defined as:

$$CO_{conversion} = \frac{c_{CO(in)} - c_{CO(out)}}{c_{CO(in)}} = \frac{\left(c_{CO(out)} + c_{CO_2(out)}\right) - c_{CO(out)}}{\left(c_{CO(out)} + c_{CO_2(out)}\right)} \quad (2.15)$$

where $c_{CO(in)}$ and $c_{CO(out)}$ are the CO concentration at the entrance and at the outlet of the reactor, and $c_{CO2(out)}$ the CO_2 concentration at the outlet of the reactor.

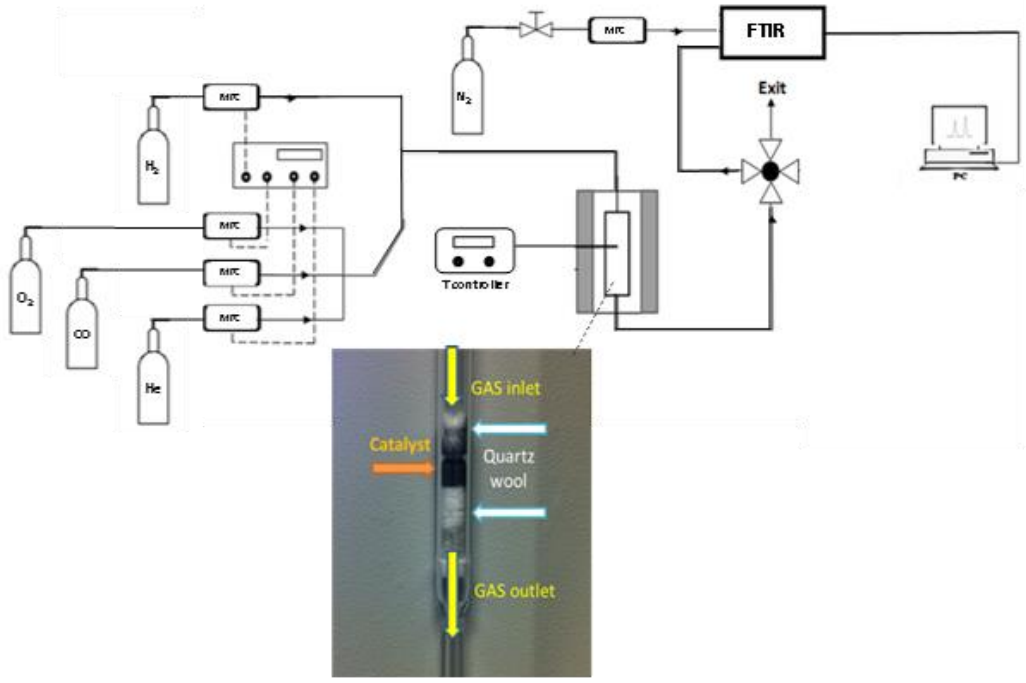

Fig. 2.16 – Experimental setup used in the activity measurements for the CO oxidation reaction.

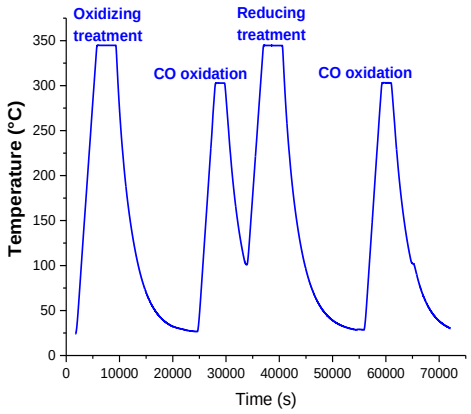

Fig. 2.17 – Temperature values during the pre-treatments and catalytic tests for supported NCs.

2.2 Bi- and Monometallic NC Colloidal Synthesis

PdCu and PtCu bimetallic NCs were synthesized by means of wet chemistry methods, which allowed the control of their size shape and composition. Monometallic Cu, Pd and Pt NCs were also prepared with the same approach as a basis of comparison with the two bimetallic catalysts. Palladium(II) acetylacetonate (97%), copper(II) acetylacetonate (97%), benzyl ether (99.8%), 1,2-hexadecanediol (90%), oleic acid (OlAc, 90%), oleylamine (OlAm, 70%), platinum(II) acetylacetonate (98%), 1-Octadecene (ODE, 90%), borane morpholine complex (MB, 95%), tertbutylamine-borane complex (TBAB, 97%), copper (I) acetate (97%), trioctylamine (98%) and solvents (anhydrous chloroform, anhydrous isopropanol, toluene and hexane) were purchased from Sigma-Aldrich and used as received without further purification. γ-Al_2O_3

powder (extrudate from Sigma-Aldrich, crushed and sieved to 90 μm mean particles size, BET specific surface area 190 m^2 g^{-1}) was purchased from Strem Chemicals. SiO_2 powder (Aerosil 380, average particle size of 7.0 nm, BET specific surface area 380 m^2 g^{-1}) was purchased from Evonik.

2.2.1 PdCu NCs

PdCu NCs were prepared by modifying the one-pot procedures reported by Shan et al.[29] and Yin et al.[30], in which spherical Pd_nCu_{100-n} NCs in a range of composition n = 21–75 and size 5.7 ± 0.5 - 5.5 ± 0.8 nm were synthesized.

In a typical synthesis of NCs with atomic Pd/Cu ratio 50/50, 0.25 mmol palladium(II) acetylacetonate and 0.25 mmol copper(II) acetylacetonate were dissolved in 20 mL of benzyl ether. 1 mmol of 1,2-hexadecanediol dissolved in 5 mL of benzyl ether was added as the reducing agent. The mixture was heated slowly to 105 °C under the N_2 atmosphere, followed by the addition of 0.714 mL of OlAc and 0.741 mL of OlAm as capping agents to the as-formed dark solution. After the injection, N_2 purging was stopped, and the temperature was increased to 220 °C keeping the reaction mixture at reflux for 30 min. The final product was cooled down to room temperature and transferred to the glovebox. The particles were precipitated out by adding 25 mL of anhydrous isopropanol and centrifuging at 1000 rcf for 30 min. In the second washing step, 200 μL of anhydrous chloroform was used to wash the wall of the vials, then 100 μL of OlAm and 25 mL of isopropanol were added. The particles were precipitated by centrifugation at 1000 rcf for 10 min and then dispersed in anhydrous chloroform.

Typical BF-TEM image of spherical PdCu NCs with the corresponding size distribution histogram and XRD pattern are reported in Fig. 2.18. The NCs had an average size of about 5 nm based on 755 particles and XRD analysis confirmed the formation of PdCu solid solution as the only crystalline phase. Indeed, the obtained diffraction peaks in the XRD patterns shifted to higher angles compared to the pure phase of Pd due to the incorporation of Cu in the lattice. The lattice parameter, *a*, calculated using the interplanar distance d_{111} from the (111) diffraction peaks, resulted to be 3.75 Å.

The atomic fraction of Cu in the bimetallic NCs measured by ICP-OES and STEM-EDX matched the required target of Pd:Cu = 50:50 within the experimental error. Further evaluation of the Cu content in the alloy was made from the peak shift in the XRD pattern assuming a linear relationship between the lattice constant of alloy and concentration of the constituent alloy (Vegard's law).[31, 32]

The NC structure and the element distribution examined using HAADF-STEM image and EDX (Fig. 2.19) show the homogeneous distribution of Pd and Cu within the NCs. The HRTEM image of the alloy highlights multiply-twin structures as planar defects of a single nanocrystal. The fast Fourier transform (FFT) pattern was consistent with [110] zone axis projection of fcc-PdCu structure with a d-spacing of 3.77 Å, in agreement with that observed by XRD analysis.

This value was found to be between the lattice spacing of Pd (3.89 Å) and Cu (3.62 Å) indicating the alloy formation.

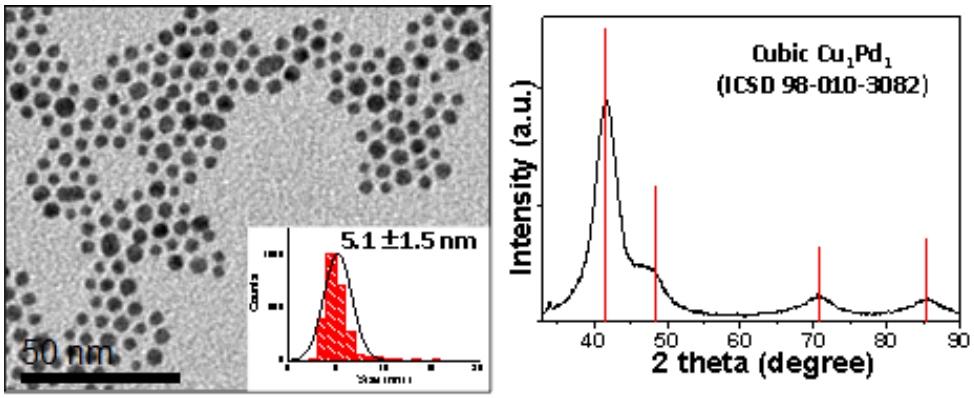

Fig. 2.18 – Typical BF-TEM image of the as-prepared $Pd_{50}Cu_{50}$ with the corresponding size distribution histogram and X-ray diffraction (XRD) pattern of the sample $Pd_{50}Cu_{50}$. The reference pattern (vertical lines) for cubic Pd_1Cu_1 (ICSD 98-010-3082) is reported.

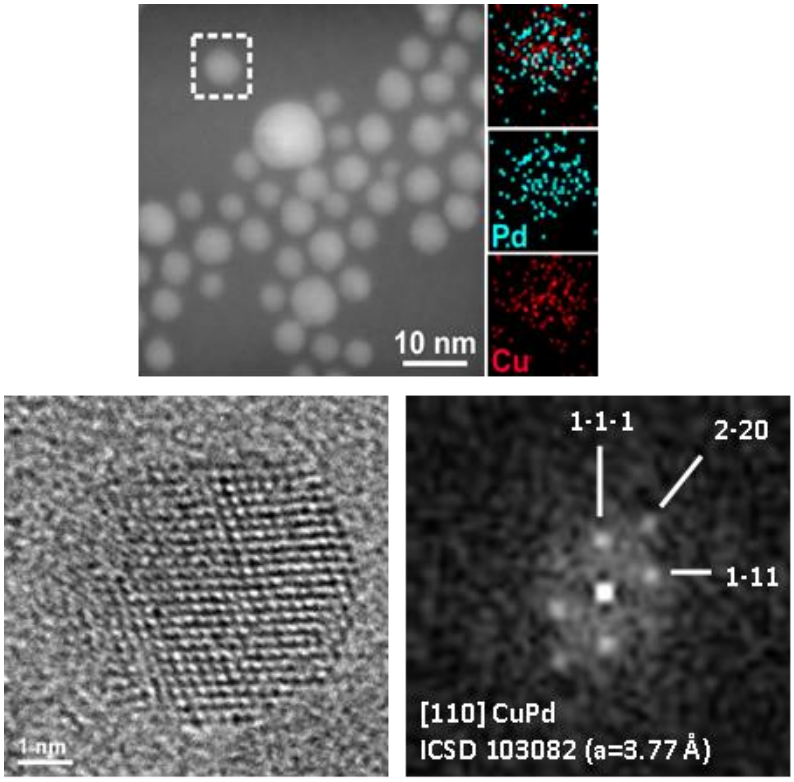

Fig. 2.19 - PdCu NCs: (a) HAADF-STEM image and corresponding quantitative EDX maps for Pd and Cu. Scale bars are in 10 nm. (b) High resolution TEM image of a single NC matching with the [110] zone axis projection of the fcc structure with 3.77 Å d-spacing with the corresponding (b) FFT pattern.

2.2.2 PtCu NCs

PtCu NCs, with an atomic Pt/Cu ratio of 50/50, were synthesized using the procedure reported by Yu et al.[33] with minor modifications.

PtCu NCs were synthesized by mixing at room temperature 0.5 mmol of copper(II) acetylacetonate, 0.5 mmol of platinum(II) acetylacetonate and 5 mL of OlAm. The solution was heated to 280 °C at a rate of 5 °C min^{-1}, and then it was cooled down to room temperature. The solution was diluted with 5 mL of ODE at 80 °C to avoid the agglomeration and the coalescence of NCs that occur during the cooling. A black product was precipitated by adding 40 mL of ethanol and separated by centrifugation at 8421 rcf for 5 min. In the second washing step, 200 µL of toluene was used to wash the wall of the vials, then 40 mL of ethanol was added, and the particles were precipitated by centrifugation at 8421 rcf for 5 min. Finally, the NCs were dispersed in toluene.

The typical TEM image of PtCu NCs with the corresponding size distribution histogram is reported in Fig. 2.20. The average particle size is 4.9 ± 1.8 nm based on 1445 particles, slightly smaller compared to that obtained by Yu et al.[33] (6.0 ± 0.5 nm).

The XRD pattern collected from the PtCu NCs was in agreement with a cubic structure, corresponding to a PtCu alloy (Fig. 2.21). According to Vegard's law[34], a 29% (atomic percentage) Cu can be estimated in the PtCu alloy NCs. This result was in disagreement with that obtained from ICP-OES and SEM-EDX analyses, in which an atomic Pt/Cu ratio of 49/51 was achieved. This number indicates a possible alloy inhomogeneity or a principle of segregation between Cu and Pt in the NCs. The sharp peaks observed at about 2θ° and 24° were attributed to the crystallization of organics, as confirmed by their substantial decrease following an O_2 plasma cleaning.

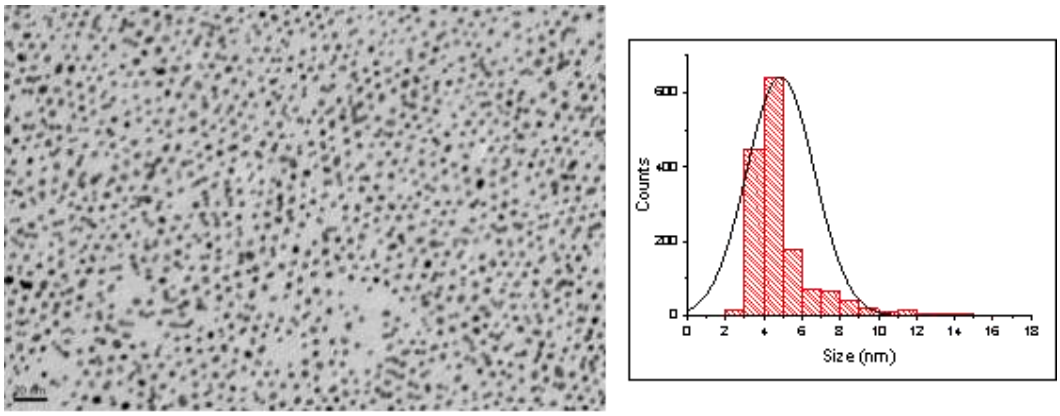

Fig. 2.20 – BF-TEM image of the as-prepared PtCu NCs with the corresponding size distribution histogram.

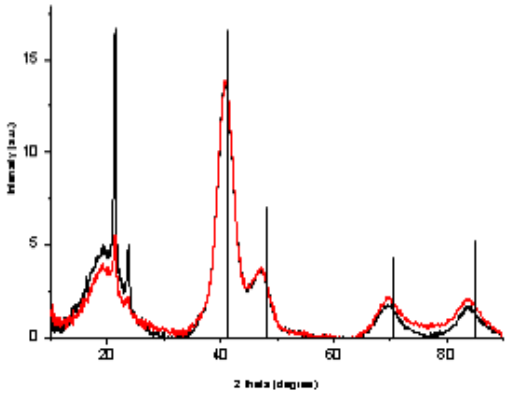

Fig. 2.21 - Overlapping X-ray diffraction (XRD) pattern of as-prepared PtCu NCs before (black) and after plasma cleaning (red). The reference pattern (vertical lines) for cubic Cu_1Pt_1 (ICSD 98-010-8402) is reported.

The homogeneous distribution of Pt and Cu within the NCs was clearly seen by the examination of HAADF-STEM images and EDX (Fig. 2.22). The HRTEM image of the alloy shows multiply-twin structures as planar defects of a single nanocrystal. The fast Fourier transform (FFT) pattern was consistent with [100] zone axis projection of fcc-PtCu structure with 3.78 Å d-spacing, in agreement with that observed by XRD analysis in which the lattice parameter, *a*, calculated using the interplanar distance d_{111} from the (111) diffraction peaks, resulted to be 3.80 Å. These values were found to be between the lattice spacing of Pt (3.94 Å) and Cu (3.62 Å) indicating the alloy formation.

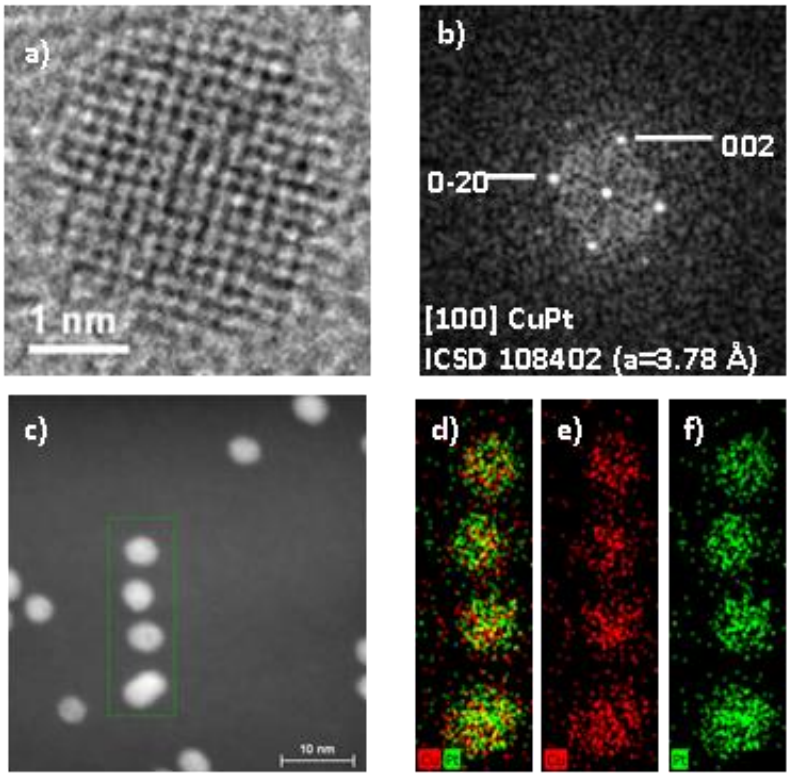

Fig. 2.22 – PtCu NCs: (a) HRTEM image of a single NC matching with the [100] zone axis projection of the fcc structure with 3.78 Å d-spacing with the corresponding (b) FFT pattern; (c) HAADF-STEM image and corresponding quantitative (d-f) EDX maps for Pt and Cu.

2.2.3 Pd NCs

Pd NCs were prepared according to the procedure reported by Jin et al..[35] Typically, a solution containing 0.33 mmol of palladium(II) acetylacetonate, 8 mL of ODE and 10 mL of OlAm was heated to 100 °C under N_2 flux. 0.33 mmol of MB dissolved in 2 mL of OlAm was added into the above solution. The resulting solution was heated to 130 °C and was further aged at this temperature for 20 min. After 30 min at this temperature, the solution was cooled to room temperature. Here, the NCs were washed one time adding 30 mL of anhydrous ethanol and precipitated by centrifugation at 1000 rcf for 5 min. The final product was collected and dispersed in hexane.

Typical TEM image of Pd NCs with the corresponding size distribution histogram is reported in Fig. 2.23a. The average size of Pd NCs was 5.2 ± 1.0 nm based on 1375 particles. The XRD pattern collected from the NCs (Fig. 2.23b) was in agreement with cubic Pd structure.

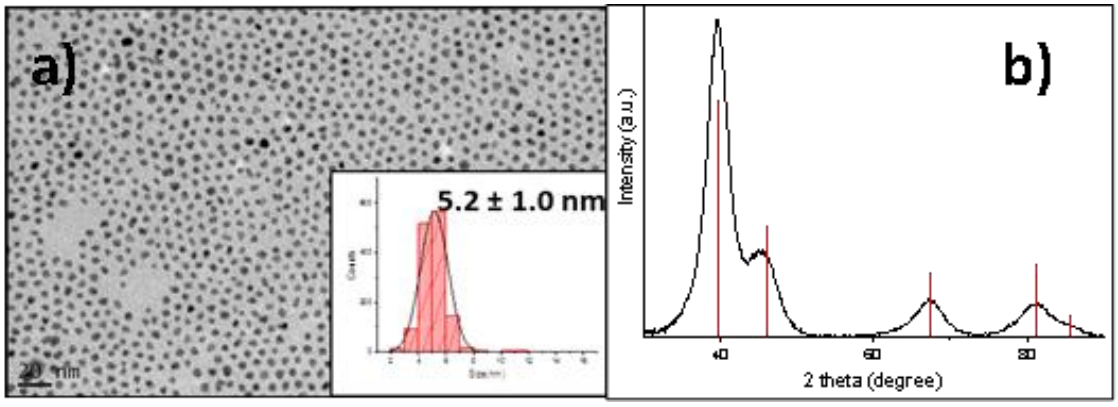

Fig. 2.23 – (a) BF-TEM image of the as-synthesized Pd colloidal NCs, their size distribution and (b) XRD pattern with the expected peak position reference for fcc Pd (ICSD 180881).

2.2.4 Pt NCs

Pt NCs were synthesized using the procedure reported in ref [36]. In a typical synthesis, 0.13 mmol of platinum(II) acetylacetonate was mixed with 10 mL of OlAm. The mixture was heated to 100 °C under argon atmosphere. After 20 min, 3 mmol of TBAB dissolved in 5 mL of OlAm was injected into the above solution. The temperature was raised to 120 °C and kept at that value for 1 h before it was allowed to return to room temperature. For the washing procedure, repeated two times, 30 mL of ethanol were added, and the particles were precipitated by centrifugation at 6654 rcf for 5 min. The final product was collected and dispersed in hexane.

Typical TEM image of Pt NCs with the corresponding size distribution histograms is reported in Fig. 2.24a. The average size of the Pd NCs was 2.8 ± 1.1 nm based on 174 particles. The XRD pattern collected from the NCs (Fig. 2.24b) was in agreement with a fcc Pt structure.

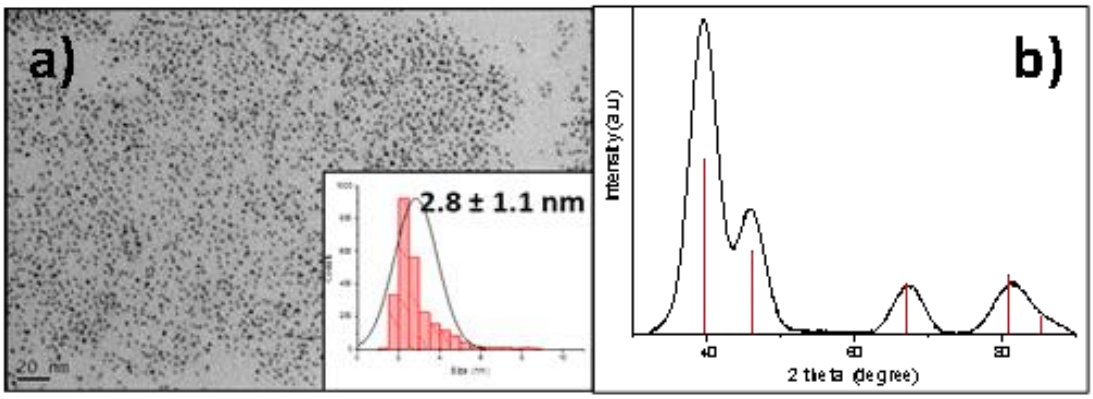

Fig. 2.24 – (a) BF-TEM image of the as-synthesized Pt colloidal NCs, their size distribution and (b) XRD pattern with the expected peak position reference for fcc Pt (ICSD 180981).

2.2.5 Cu NCs

Cu NCs were synthesized using the method reported in ref [37]: 4 mmol of copper(I) acetate was mixed with 6.6 mmol of oleic acid and 15 mL of trioctylamine and degassed at 180 °C under an inert atmosphere of N_2 for 1 h. Then, the solution was quickly heated to 270 °C and kept at this temperature for 15 min. The color turned progressively from green to brown after the production of a burgundy solution. The particles were precipitated by adding 25 mL of ethanol and separated by centrifugation at 6654 rcf for 5 min, and were then dispersed in hexane generating a final green oxidized Cu_2O nanoparticle solution.

Typical TEM image of Cu NCs with the corresponding size distribution histograms is reported in Fig. 2.25a. The average size of Pd NCs was 6.8 ± 1.7 nm based on 405 particles. The XRD pattern collected from the NCs (Fig. 2.25b) was in agreement with a fcc-Cu_2O structure. As reported by Yin et al.[37], the presence of sharper peaks indexed to the fcc of metal Cu in the pattern of Cu NCs can be ascribed to precipitated material from the reaction mixture with a size larger than 5 nm.

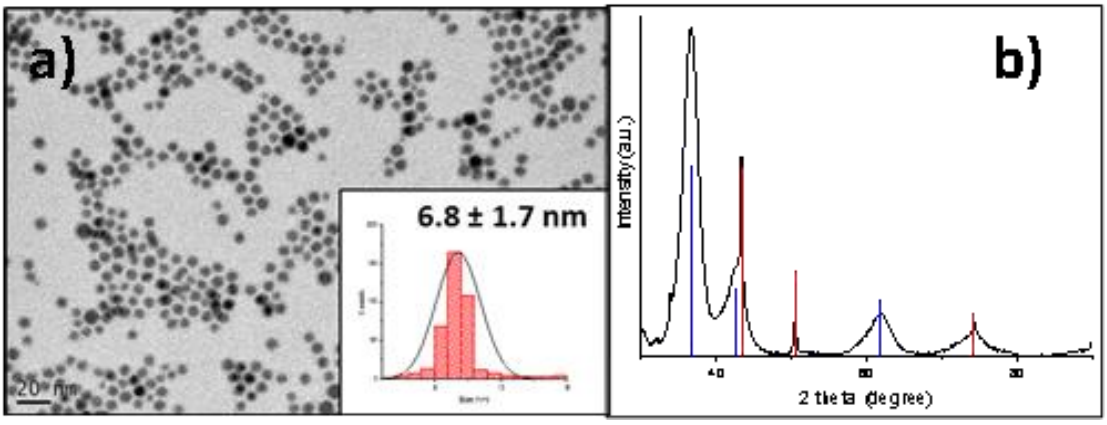

Fig. 2.25 – (a) BF-TEM image of the as-synthesized Cu colloidal NCs, their size distribution and (b) XRD pattern with the expected peak position reference for fcc Cu (red, ICSD 53757) and fcc Cu_2O_1 (blue, ICSD 53322).

2.3 Catalyst Preparation

2.3.1 Alumina Supported NC Catalysts

Alumina-supported catalysts were prepared by a colloidal deposition method. Typically, a dispersion of γ-Al_2O_3 powder, in hexane for Cu, Pd and Pt NCs, in chloroform for PdCu NCs and toluene for PtCu NCs, was sonicated for 5 min. A solution containing an appropriate volume of NCs was prepared, and then added to the support dispersion and left under fast stirring for 2 h. The powder was recovered by centrifugation at 1000 rcf for 5 min. The sample was finally dried in a vacuum oven at 40 °C for 1 h. The resulting powder was calcined at 450 °C for 3 h in a muffle furnace to completely remove any capping ligand from the surface of the NCs. The calcination conditions were chosen based on the results of the TGA, performed under air flow on colloidal NC solution (Figs. 2.26 and 2.27). Indeed, based on the TGA measurements of the bi and monometallic NCs, the organic ligands could be completely removed in air when the temperature reached 400 – 450 °C.

The target mass loading for all catalyst samples was fixed to 2 wt.%. The actual loading of the metals in each catalyst sample according to ICP-OES is reported in Table 2.2. In the case of the preparation of Cu/Al_2O_3 catalyst, the loading was fixed to 1 wt.% to avoid the sintering of the NCs after calcination, which was observed in the case of the 2 wt.% sample. The final metal target was achieved for all the systems assuring the effectiveness of the colloidal deposition method.

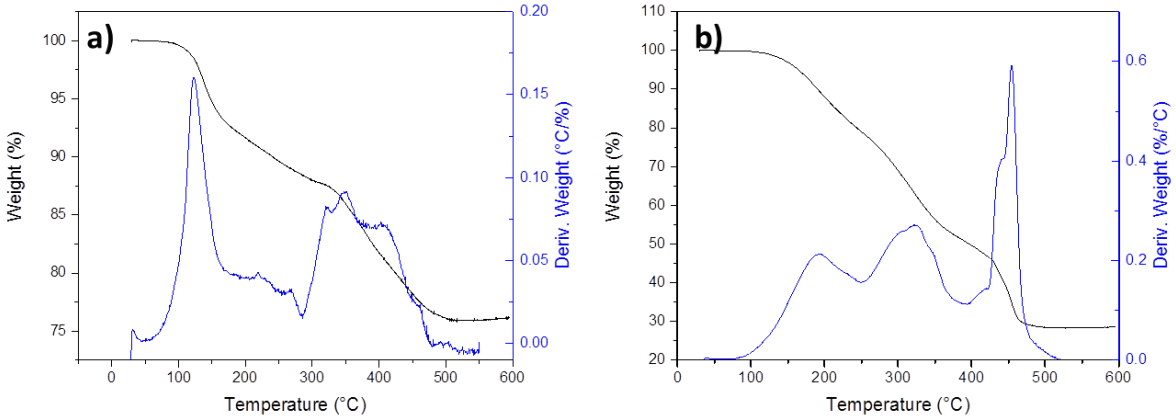

Fig. 2.26 – TGA measurement of (a) PdCu and (b) PtCu NCs under air flow.

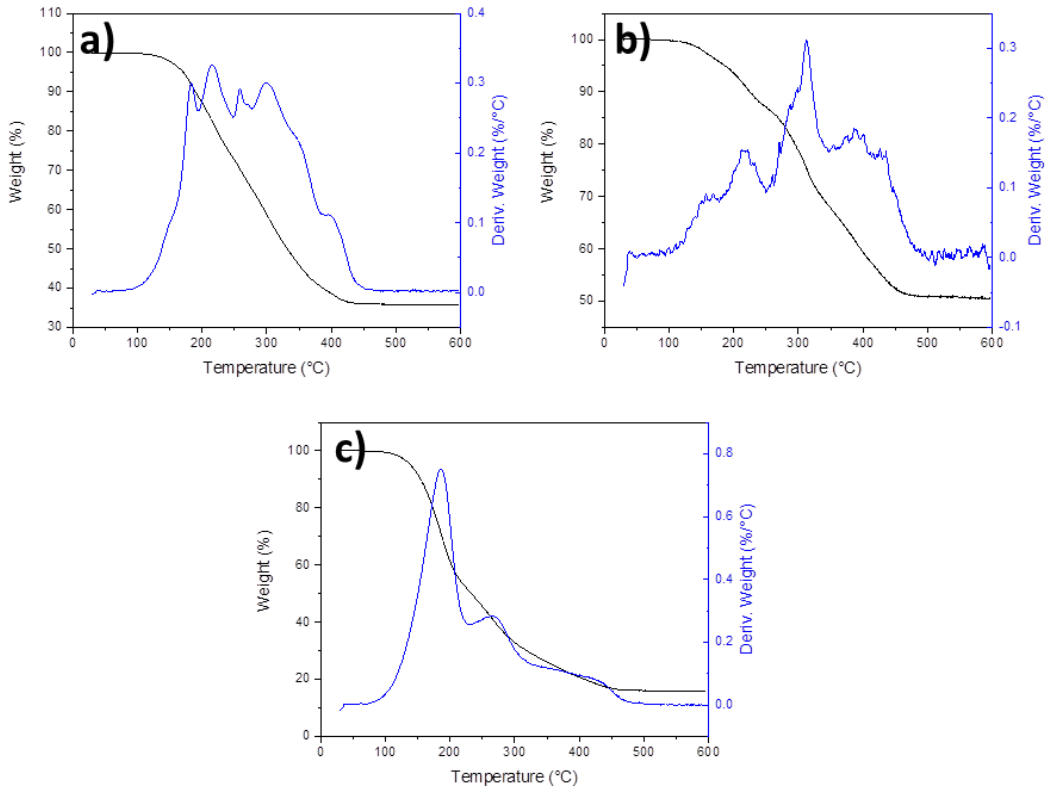

Fig. 2.27 – TGA measurement of (a) Pd, (b) Cu and (c) Pt NCs under air flow.

Table 2.2. Final total metal load obtained from ICP-OES for the mono- and bimetallic alumina supported NC catalysts (NM = noble metal).

Sample	**wt% metal load** **(NM + Cu)**
$Pd_{50}Cu_{50}/Al_2O_3$	1.9 ± 0.2[(1)]
$Pt_{50}Cu_{50}/Al_2O_3$	2.0 ± 0.1
Pd/Al_2O_3	1.9 ± 0.1
Pt/Al_2O_3	2.5 ± 0.2
Cu/Al_2O_3	0.8 ± 0.0

(1) Standard deviation of four repeated tests.

To verify the dispersion of NCs on the support and the preservation of the NCs upon the calcination treatment, the samples were analyzed by TEM. Figs. 2.28 - 2.32 show typical TEM images of PdCu and PtCu NCs supported on γ-Al_2O_3 before and after calcination along with the TEM images of the monometallic catalysts. The NCs were found to be uniformly dispersed on the support and no sintering was observed after calcination. XRD analysis could not be applied to the Al_2O_3 supported samples. Due to the low metal loading, the small particle size and the presence of Al_2O_3, the XRD profiles are indeed mostly dominated by the support signal.

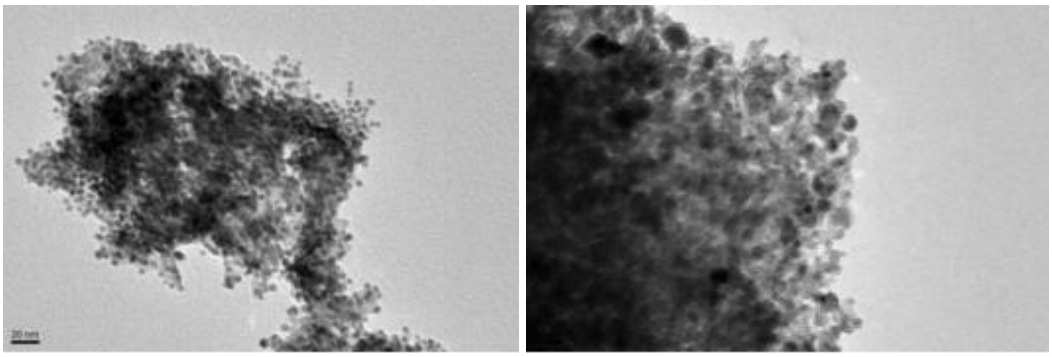

Fig. 2.28 – BF-TEM images of $PdCu/Al_2O_3$ catalyst before (left) and after (right) calcination.

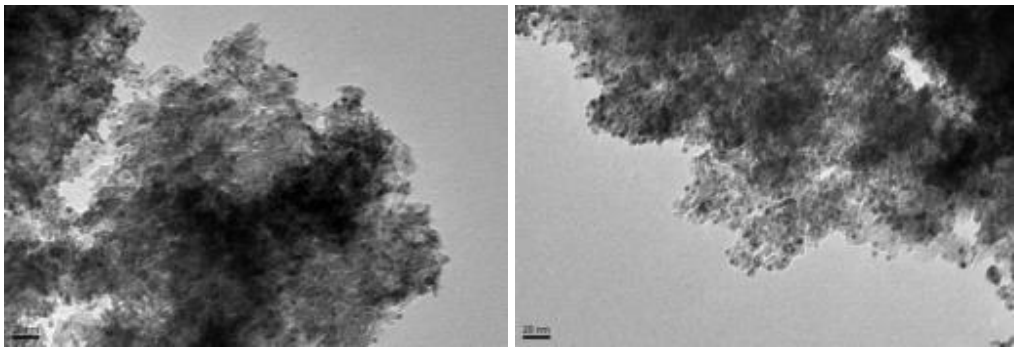

Fig. 2.29 – BF-TEM images of $PtCu/Al_2O_3$ catalyst before (left) and after (right) calcination.

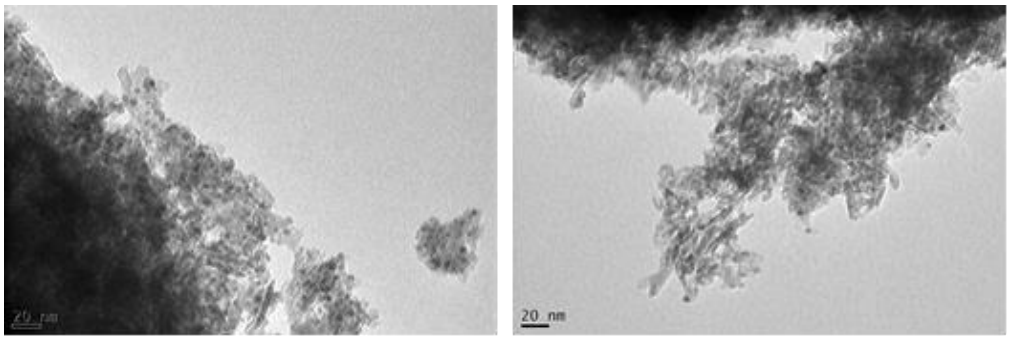

Fig. 2.30 – BF-TEM images of Pd/Al_2O_3 catalyst before (left) and after (right) calcination.

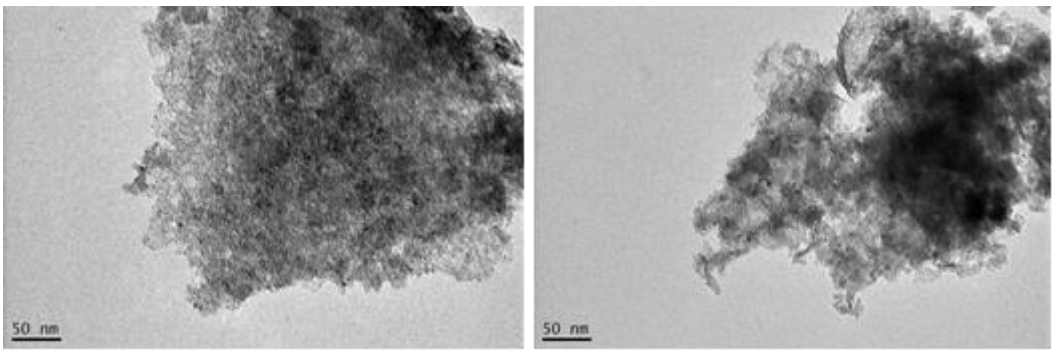

Fig. 2.31 – BF-TEM images of Pt/Al_2O_3 catalyst before (left) and after (right) calcination.

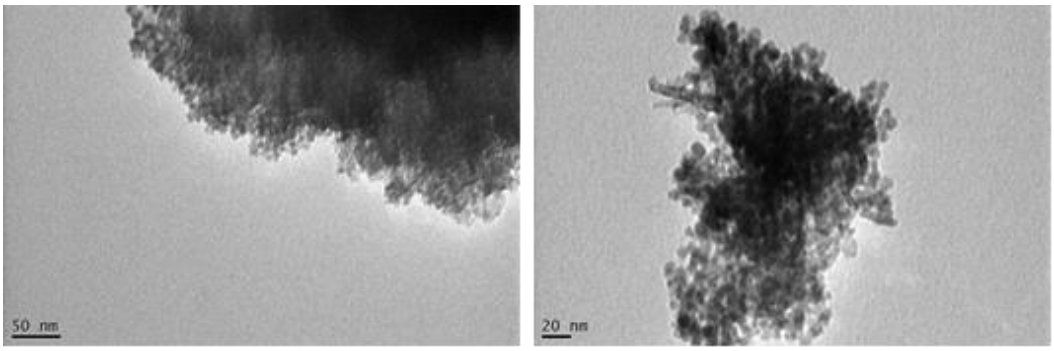

Fig. 2.32 – BF-TEM images of Cu/Al_2O_3 catalyst before (left) and after (right) calcination.

2.3.2 Silica Supported NC Catalysts

In the case of SiO_2 powder, the same colloidal deposition procedure of the alumina one was applied, but instead of leaving the support dispersion under fast stirring for 2 h, the suspension was sonicated for 2h. The final metal loading obtained from the ICP-OES measurement for silica supported mono- and bimetallic NC catalysts is reported in Table 2.3, considering a target mass loading for all catalyst samples fixed to 2 wt.%. Also in the case of the silica supported NC catalysts, the final metal target was achieved for all the systems assuring the effectiveness of the colloidal deposition method.

Table 2.3. Final total metal load obtained from ICP-OES for the mono- and bimetallic silica supported NC catalysts (NM = noble metal).

Sample	**wt% metal load** **(NM + Cu)**
$Pd_{50}Cu_{50}/SiO_2$	2.0 ± 0.2[(1)]
$Pt_{50}Cu_{50}/SiO_2$	1.8 ± 0.2
Pd/SiO_2	2.1 ± 0.1
Pt/SiO_2	2.0 ± 0.2
Cu/SiO_2	2.1 ± 0.1

[(1)] Standard deviation of four repeated tests.

The TEM results in the Figs. 2.33–2.37 indicate a good dispersion of the NCs on SiO_2, without evidence of sintering after the calcination, thanks to the high surface area of the SiO_2 support and the homogeneous dispersion of the NCs obtained by sonication. XRD analyses of the SiO_2 supported PdCu and PtCu catalysts were carried out in order to investigate if structural transformations involving the NCs occurred during the calcination step. For $PdCu/SiO_2$ catalyst the pattern was in agreement with a tetragonal structure, corresponding to Pd_1O_1. For the $PtCu/SiO_2$ catalyst, the diffraction peak positions matched those of metallic Pt (Fig. 2.38).

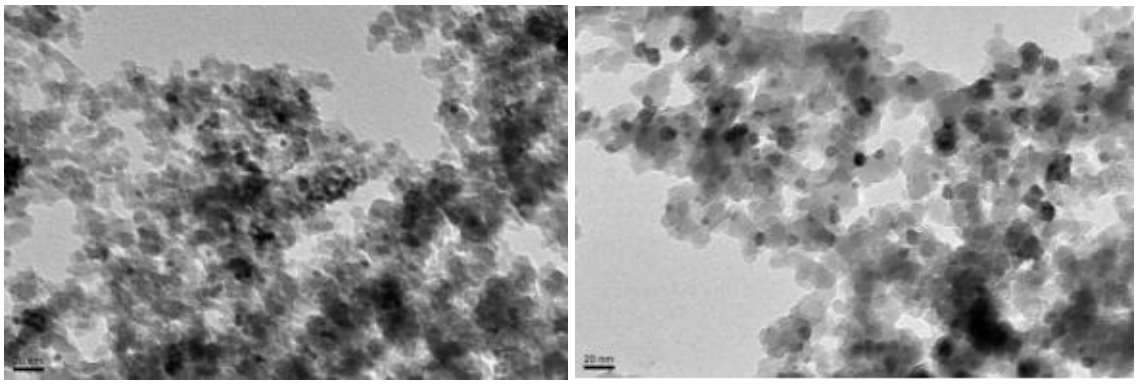

Fig.2. 33 - BF-TEM images of $PdCu/SiO_2$ catalyst before (left) and after (right) calcination.

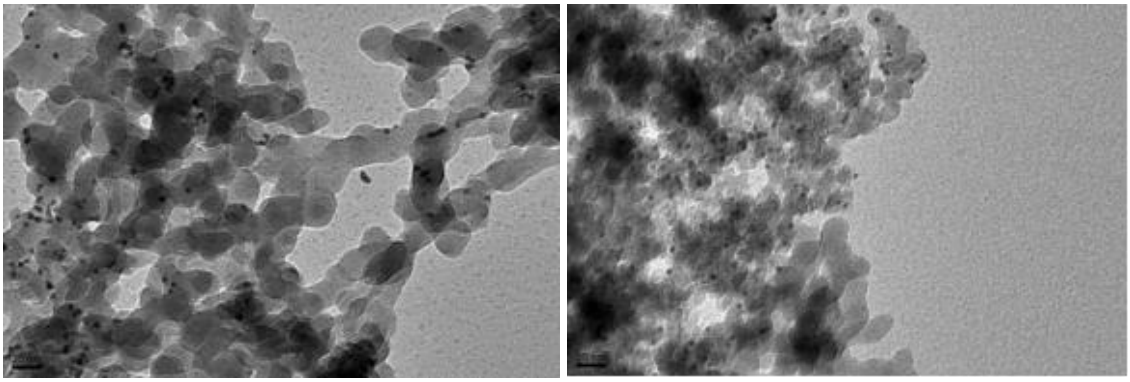

Fig. 2.34 - BF-TEM images of $PtCu/SiO_2$ catalyst before (left) and after (right) calcination.

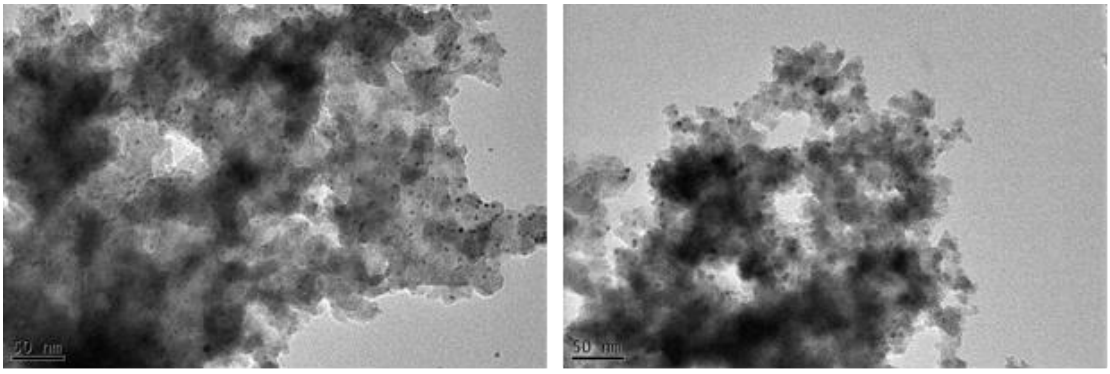

Fig. 2.35 - BF-TEM images of Pd/SiO_2 catalyst before (left) and after (right) calcination.

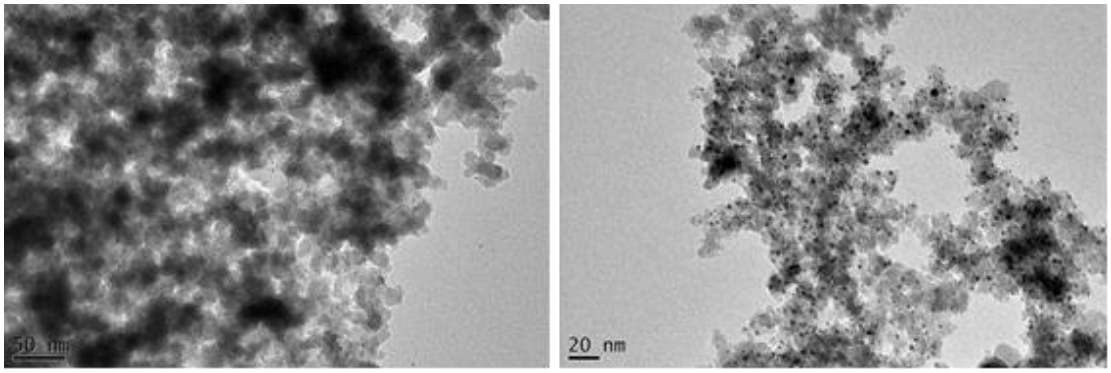

Fig. 2.36 - BF-TEM images of Pt/SiO_2 catalyst before (left) and after (right) calcination.

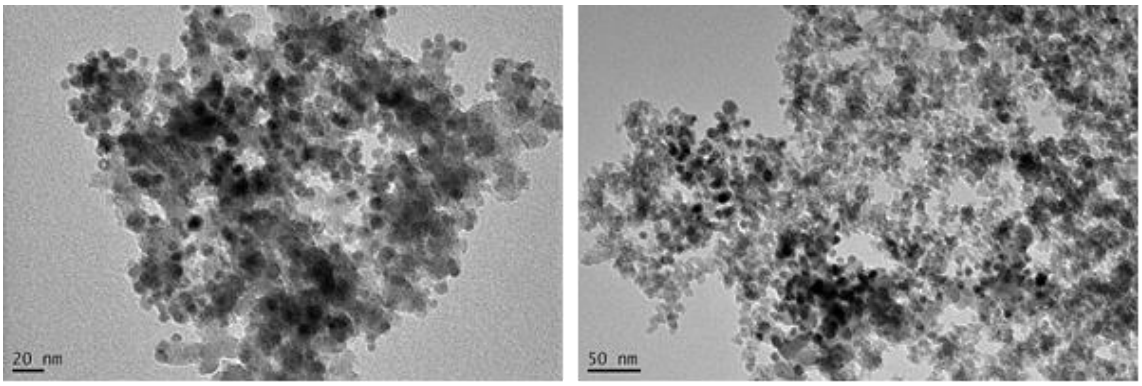

Fig. 2.37 - BF-TEM images of Cu/SiO_2 catalyst before (left) and after (right) calcination.

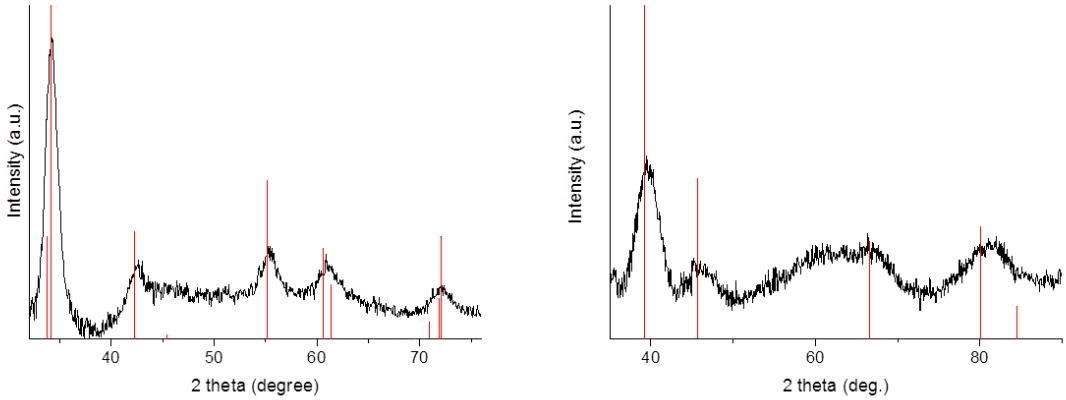

Fig. 2.38 - X-ray diffraction (XRD) patterns of the $PdCu/SiO_2$ (above right) and $PtCu/SiO_2$ (below) catalysts after calcination. The reference patterns (red vertical lines) for tetragonal Pd_1O_1 (ICSD 98-002-6598) and cubic Pt (ICSD 98-004-1525) are reported.

In conclusion, a colloidal synthesis method was developed to synthesize two different systems PdCu and PtCu NCs with controllable size, shape and composition. In addition, the corresponding monometallic NCs were also synthesized as a basis of comparison for the subsequent bimetallic NC characterizations. The NCs were then successfully deposited on the Al_2O_3 and SiO_2 supports achieving the targeted metal-loading for each catalyst.

In the next Chapters 3 and 4, the here discussed model catalysts were used to identify the impact of the noble metal on the alloy/dealloy processes occurring during the exposure to redox treatments and the role of the supports were systematically discussed. Besides, the CO oxidation was used as a probe reaction to investigate how the structural changes of the NCs as a consequence of the pre-treatments affected their catalytic properties. The electronic and structural modifications will be studied in details by ex situ and in situ characterization techniques.

References

1. Zhang, Y.-W., *Bimetallic Nanostructures: Shape-controlled Synthesis for Catalysis, Plasmonics, and Sensing Applications*. Wiley: 2018.

2. Williams, D. B.; Carter, C. B., The Transmission Electron Microscope. In *Transmission Electron Microscopy*, Springer: 1996; pp 3-17.

3. Carter, C. B., *Transmission Electron Microscopy: a Textbook for Materials Science. Spectrometry*. Springer: 2009.

4. Wang, Z., Transmission electron microscopy of shape-controlled nanocrystals and their assemblies. J Phys Chem B 2000, 104, 1153-1173.

5. Egerton, R. F., *Physical Principles of Electron Microscopy*. Springer: 2005.

6. Bragg, W. H.; Bragg, W. L., The reflection of X-rays by crystals. *Proc R Soc London A* 1913, 88, 428-438.

7. Hadjiivanov, K. I.; Vayssilov, G. N., Characterization of oxide surfaces and zeolites by carbon monoxide as an IR probe molecule. *Adv Catal* 2002, 47, 307-511.

8. Niemantsverdriet, J. W., *Spectroscopy in Catalysis: an Introduction*. John Wiley & Sons: 2007.

9. Howe, R. F., In Situ Infrared Methods. *In-Situ Spectroscopy in Heterogeneous Catalysis*, Haw J. F. (Ed), Wiley 2002 pp.139-177.

10. Armaroli, T.; Bécue, T.; Gautier, S., Diffuse reflection infrared spectroscopy (DRIFTS): application to the in situ analysis of catalysts. *Oil Gas Sci Technol* 2004, 59, 215-237.

11. Skoda, F.; Astier, M. P.; Pajonk, G. M.; Primet, M., Surface characterization of palladium-copper bimetallic catalysts by FTIR spectroscopy and test reactions. *Catal Lett* 1994, 29, 159-168.

12. Akonwie, L. N.; Kazachkin, D.; Luebke, D.; d'Itri, J. L., Effect of catalyst pre-reduction temperature on the reaction of 1, 2-dichloroethane and H_2 catalyzed by SiO_2-supported PtCu bimetallics. *Appl Catal A* 2012, 415, 59-69.

13. Davydov, A., *Molecular Spectroscopy of Oxide Catalyst Surfaces*. Wiley: 2003.

14. Newville, M., Fundamentals of XAFS. *Rev Mineral Geochem* 2014, 78, 33-74.

15. Kelly, S.; Hesterberg, D.; Ravel, B., Analysis of soils and minerals using X-ray absorption spectroscopy. *Methods of soil analysis. SSSA Book Series 5.5* 2008, 5, 387-464.

16. Calvin, S., *XAFS for Everyone*. CRC Press: 2013.

17. Briois, V.; La Fontaine, C.; Belin, S.; Barthe, L.; Moreno, T.; Pinty, V.; Carcy, A.; Girardot, R.; Fonda, E. In *ROCK: the new Quick-EXAFS beamline at SOLEIL*, Journal of Physics: Conference Series, IOP Publishing: 2016; pp 12149-12154.

18. La Fontaine, C.; Barthe, L.; Rochet, A.; Briois, V., X-ray absorption spectroscopy and heterogeneous catalysis: Performances at the SOLEIL's SAMBA beamline. *Catal Today* 2013, 205, 148-158.

19. Kopelent, R.; van Bokhoven, J. A.; Szlachetko, J.; Edebeli, J.; Paun, C.; Nachtegaal, M.; Safonova, O. V., Catalytically active and spectator Ce^{3+} in ceria-supported metal catalysts. Angew Chem Int Ed 2015, 54, 8728-8731.

20. Chiarello, G. L.; Nachtegaal, M.; Marchionni, V.; Quaroni, L.; Ferri, D., Adding diffuse reflectance infrared Fourier transform spectroscopy capability to extended x-ray-absorption fine structure in a new cell to study solid catalysts in combination with a modulation approach. *Rev Sci Instrum* 2014, 85, 074102.

21. Voronov, A.; Urakawa, A.; van Beek, W.; Tsakoumis, N. E.; Emerich, H.; Rønning, M., Multivariate curve resolution applied to in situ X-ray absorption spectroscopy data: an efficient tool for data processing and analysis. *Anal Chim Acta* 2014, 840, 20-27.

22. de Juan, A.; Tauler, R., Chemometrics applied to unravel multicomponent processes and mixtures: Revisiting latest trends in multivariate resolution. *Anal Chim Acta* 2003, 500, 195-210.

23. Burnham, A. J.; Viveros, R.; MacGregor, J. F., Frameworks for latent variable multivariate regression. *J Chemom* 1996, 10, 31-45.

24. Wise, B. M.; Gallagher, N. B., The process chemometrics approach to process monitoring and fault detection. *J Process Contr* 1996, 6, 329-348.

25. Valle, S.; Li, W.; Qin, S. J., Selection of the number of principal components: the variance of the reconstruction error criterion with a comparison to other methods. *Ind Eng Chem Res* 1999, 38, 4389-4401.

26. Eriksson, L.; Byrne, T.; Johansson, E.; Trygg, J.; Vikström, C., *Multi-and Megavariate Data Analysis Basic Principles and Applications*. Vol. 1, Umetrics Academy: 2013.

27. Jaumot, J.; Gargallo, R.; de Juan, A.; Tauler, R., A graphical user-friendly interface for MCR-ALS: a new tool for multivariate curve resolution in MATLAB. *Chemometr Intell Lab* 2005, 76, 101-110.

28. Tauler, R.; Smilde, A.; Kowalski, B., Selectivity, local rank, three-way data analysis and ambiguity in multivariate curve resolution. *J Chemom* 1995, 9, 31-58.

29. Shan, S.; Petkov, V.; Prasai, B.; Wu, J.; Joseph, P.; Skeete, Z.; Kim, E.; Mott, D.; Malis, O.; Luo, J., Catalytic activity of bimetallic catalysts highly sensitive to the atomic composition and phase structure at the nanoscale. *Nanoscale* 2015, 7, 18936-18948.

30. Yin, Z.; Zhou, W.; Gao, Y.; Ma, D.; Kiely, C. J.; Bao, X., Supported Pd–Cu bimetallic nanoparticles that have high activity for the electrochemical oxidation of methanol. *Chem–A Eur J* 2012, 18, 4887-4893.

31. Subramanian, P.; Laughlin, D., Cu-Pd (copper-palladium). *J Phase Equilibria* 1991, 12, 231-243.

32. Subramanian, P., *Phase diagrams of binary copper alloys*. Vol. 10, ASM Int: 1994.

33. Yu, Y.; Yang, W.; Sun, X.; Zhu, W.; Li, X.-Z.; Sellmyer, D. J.; Sun, S., Monodisperse MPt (M= Fe, Co, Ni, Cu, Zn) nanoparticles prepared from a facile oleylamine reduction of metal salts. *Nano Lett* 2014, 14, 2778-2782.

34. Predel, B. Cu-Pt (Copper-Platinum). In: Madelung, O. (Ed), "Cr-Cs–Cu-Zr" Vol. 5d, Springer 1994, pp 1-6.

35. Jin, T.; Guo, S.; Zuo, J.-l.; Sun, S., Synthesis and assembly of Pd nanoparticles on graphene for enhanced electrooxidation of formic acid. *Nanoscale* 2013, 5, 160-163.

36. Li, D.; Wang, C.; Tripkovic, D.; Sun, S.; Markovic, N. M.; Stamenkovic, V. R., Surfactant removal for colloidal nanoparticles from solution synthesis: the effect on catalytic performance. *ACS Catal* 2012, 2, 1358-1362.

37. Yin, M.; Wu, C.-K.; Lou, Y.; Burda, C.; Koberstein, J. T.; Zhu, Y.; O'Brien, S., Copper oxide nanocrystals. *J Am Chem Soc* 2005, 127, 9506-9511.

Chapter 3

Structural Changes in the PdCu Nanocrystal Catalysts Under Different Conditions

The catalytic properties of heterogeneous catalysts can be dramatically influenced by exposure of the catalytic material to different gases and/or temperature conditions. In the case of NPs based heterogeneous catalysts, such changes might arise from the fact that the catalytically active NPs may change their surface morphology, structure and surface chemical composition in response to different temperatures and gas environments. In particular, oxidizing and reducing atmospheres are common reaction environments in many industrial reaction processes, such as partial oxidation reactions or hydrogenation reactions.[1-4]

As an example of these transformations, Najafishirtari et al.[5] reported the effect of different redox treatments on AuCu NCs supported on Al_2O_3, correlating the observed structural changes with the catalytic activity in the CO oxidation reaction. By means of different characterization techniques it was claimed that, under oxidizing, high temperature (350 °C) conditions, phase segregation between gold and copper occurred. Copper was found to be finely dispersed on the support, likely in the form of oxide clusters, while gold remained localized in the NCs, resulting in poor CO oxidation activity. On the other hand, the exposure to a reducing environment at the same temperature restored the AuCu alloy and significantly enhanced the catalytic activity of the catalyst. The catalytic activity of the NCs in CO oxidation was strictly dependent on the operating atmosphere, correlating with the observed structural changes, such as phase segregation, that occur in the catalyst.

In addition, another study conducted by Destro et al.,[6] reported the impact of the support (i.e. γ-Al_2O_3 vs. SiO_2) on the structural evolution of $Au_{1-x}Cu_x$ colloidal NCs with well-controlled size and composition upon heating in selected atmospheres. In that work, it was proved that the support plays a key role in the phase segregation between gold and copper and in the atmosphere induced migration of Cu species. Indeed, it was shown by means of different characterization techniques that, under oxidizing conditions, Cu was dealloyed from Au and the formed CuO_x species had different fate as a function of the support: while they were finely dispersed on alumina, and partially migrated away from the Au NCs, CuO_x species on silica formed small clusters located in the proximity of the Au NCs with limited Cu migration on the support. It is noteworthy that changing the gas to a reducing atmosphere restored the AuCu alloyed NCs when supported on alumina. This means that changing the gas atmosphere reversed the migration process of copper, which returned to the Au NPs and was eventually realloyed. A partial realloy also occurred on the silica supported AuCu NCs, resulting in the formation of depleted Cu-alloy

NCs and isolated metallic Cu phase. For such a bimetallic system, and under the investigated conditions, Cu was the only element that underwent Ostwald ripening and particle disintegration as a function of the reacting atmosphere. It is noteworthy that the presence of Au NCs made these phenomena fully reversible.

In the works of Najafishirtari and Destro et al., the role of the noble metal in these transformations had not been investigated. In this Chapter, we tackle this challenge by studying the structural transformations of another noble metal-Cu alloy model system, namely $Pd_{50}Cu_{50}$ NCs. In analogy to the work of Destro et al., alumina and silica were selected as support material. First, the impact of a protocol based on reducing and oxidizing conditions were assessed, leading to the identification of the different species present on the catalyst surface upon each pre-treatment. In a second stage, the effects of such pre-treatments on the CO oxidation activity of PdCu based catalysts were studied, and a structure-activity correlation has been proposed.

3.1 Characterization of Alumina Supported NC Catalysts

3.1.1 NCs Under Oxidative and Reductive Treatments

To track the structural changes of $PdCu/Al_2O_3$ catalyst under different conditions, the samples were characterized by TEM after oxidizing and reducing treatments. The HAADF-STEM images of two catalysts are shown in Fig. 3.1. An increase of the average size of PdCu NCs was observed, with the formation of a flocky shell on the NC surface (Fig. 3.2). In particular, final average size distribution of 7.8 ± 2.0 nm (based on 86 particles) after oxidation and of 5.9 ± 1.6 nm (on 133 particles) after reduction was found. These values are higher compared to those measured for the as-synthetized NCs (4.9 ± 1.8 nm) (Fig. 2.18).

Furthermore, the elemental mapping of the alumina supported NCs was performed using STEM-EDX (Fig. 3.3) to understand the spatial distribution of elements after the two treatments. After oxidation, EDX maps evidenced that Cu atoms were predominately associated with the Pd atoms within NPs entities and only a small amount of Cu was delocalized and dispersed on the alumina support. In particular, larger NPs exhibited Cu-rich shell surrounding a Pd-rich core (Fig. 3.4). After reduction, Pd and Cu atoms were localized in the same region of the support, still in NP entities (Fig. 3.3b).

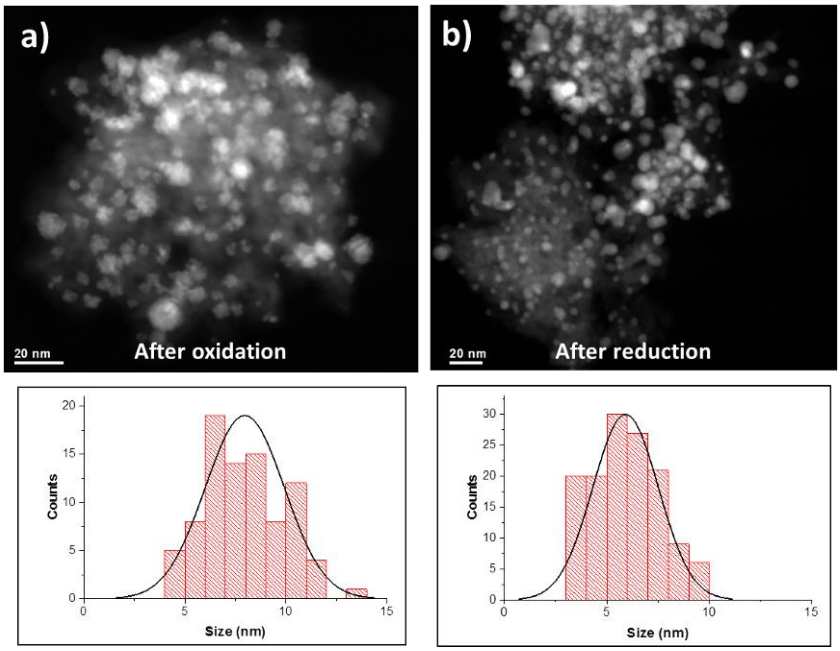

Fig. 3.1 – HAADF-STEM images of $PdCu/Al_2O_3$ catalyst after (a) oxidizing and (b) reducing treatments with the corresponding size distribution histogram.

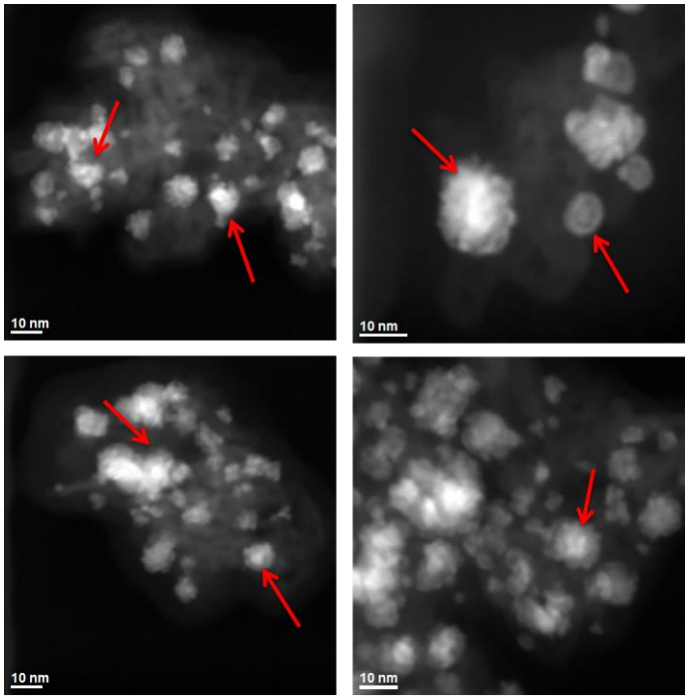

Fig. 3.2 – HAADF-STEM images of $PdCu/Al_2O_3$ catalyst after oxidizing treatment.

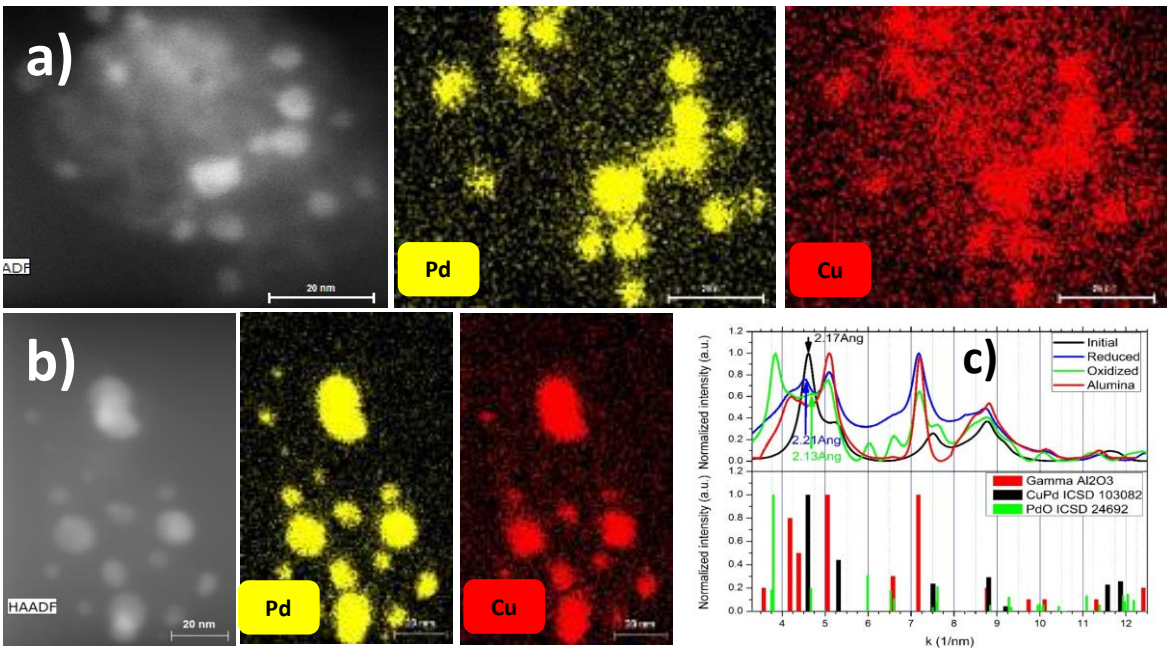

Fig. 3.3 – HAAD-STEM images of 2 wt.% $PdCu/Al_2O_3$ catalyst and corresponding quantitative EDX maps for Pd and Cu after (a) oxidizing and (b) reducing treatments; (c) azimuthally integrated, background-subtracted SAED patterns after oxidation and reduction in comparison to PdCu NCs (reference patterns: Pd_1Cu_1 ICSD 103082 (black line), Pd_1O_1 ICSD 24692 (green line), γ-Al_2O_3 ICSD 100425 (red line)). (The reference pattern for $Cu_{0.3}Pd_{0.7}O$ was calculated by modifying the tetragonal cell of PdO (ICSD 24692). The new cell has Cu and Pd ions with fractional occupancies (0.3 and 0.7, respectively) in the sites of Pd ions and parameters, a = b = 3.005 Å and c = 5.29 Å, calculated according to the plots in ref. [7] for $Cu_xPd_{1-x}O$, with x = 0.3).

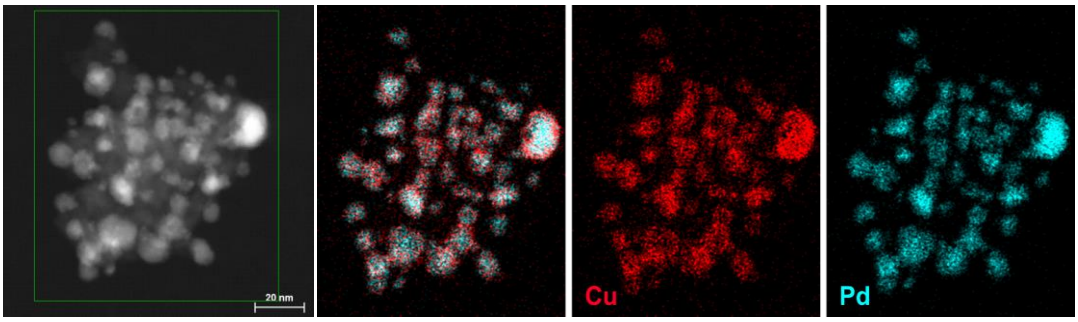

Fig. 3.4 – HAADF-STEM images of 2 wt.% $PdCu/Al_2O_3$ catalysts after oxidizing treatment with the corresponding quantitative EDX maps for Pd and Cu.

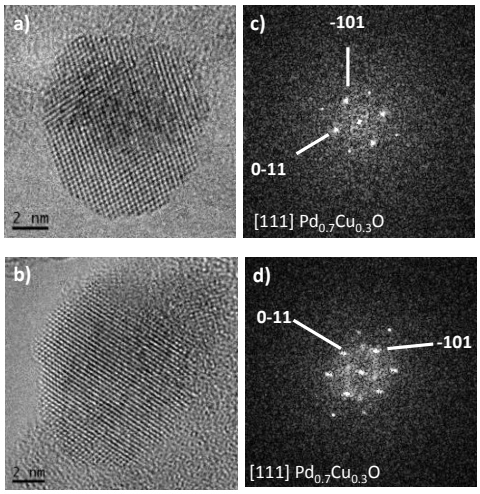

Fig. 3.5 – (a, b) HRTEM images of single PdCu NC of 2 wt% $PdCu/Al_2O_3$ catalyst after oxidation matching with the [111] zone axis projection of the $Pd_{0.7}Cu_{0.3}O$ with the corresponding (c, d) FFT patterns.

The identification of crystalline phases by XRD analysis could not be applied to the Al_2O_3 supported samples due to the low metal loading, the small particle size and the predominance of Al_2O_3 support signal in the XRD profiles. To demonstrate this, as an example, in Fig. 3.6 the XRD pattern of $PdCu/Al_2O_3$ catalyst acquired after reduction is reported. For these reasons, SAED patterns of $PdCu/Al_2O_3$ catalysts were collected after the two treatments and compared with the pattern of the as-synthesized NCs (Fig. 3.3c). Since the peaks of γ-Al_2O_3 partially overlapped with the peaks of the NCs, SAED pattern of pure γ-Al_2O_3 was collected and subtracted from those of catalyst samples.

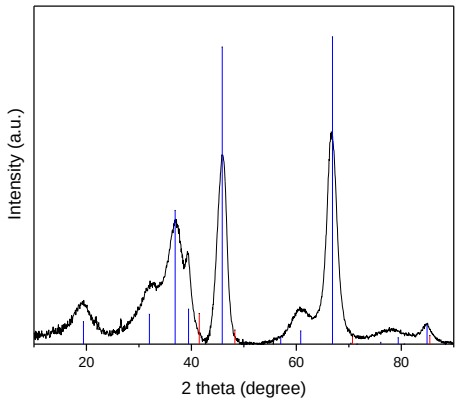

Fig. 3.6 – XRD pattern of the $PdCu/Al_2O_3$ catalyst after reduction. The theoretical peaks for cubic γ-Al_2O_3 ICSD 100425 (blue line) and cubic Pd_1Cu_1 ICSD 103082 (red line) are reported.

After oxidation, the $PdCu/Al_2O_3$ pattern was consistent with the formation of a $Cu_xPd_{1-x}O$ solid solution.[7] This assertion was justified by the fact that the PdO diffraction peaks were slightly shifted to higher 2θ values compared to the reference ones (see caption of Fig. 3.3). This shift could be due to the random replacement of Pd^{2+} with Cu^{2+} in the palladium oxide lattice. This assignment was confirmed by STEM-EDX, in which an average atomic composition of Pd:Cu:O = 2.4:1:2.3 corresponding to the formula $Pd_{0.7}Cu_{0.3}O_{0.7}$ was found, and by FFT analysis in agreement with the [111] $Pd_{0.7}Cu_{0.3}O$ projection (Fig. 3.5). After reduction, the pattern showed characteristic peaks related to the fcc phase of PdCu. Indeed, the comparison with the pattern of

the as-synthesized NCs suggested that the recovery of the PdCu alloy, with 36 atomic % of Cu (estimated by Vegard's law)[8] occurred.

On the basis of these results, it was possible to estimate whether the measured increase of NPs size could be fully ascribed to the formation of $Pd_{0.7}Cu_{0.3}O_{0.7}$ NCs. First, considering the number of Pd atoms in the unit cell equal to 4, as well as the known unit cell volume of PdCu (53.41 $Å^3$ in the Pd_1Cu_1 card ICSD 103082), the number of Pd atoms in the NC was calculated from the following expression:

(3.1) $$N_{Pd\ atoms\ in\ PdCu\ NC} = \frac{N_{Pd\ atoms\ per\ unit\ cell}}{V_{PdCu\ unit\ cell}} V_{PdCu\ NC}$$

where $V_{PdCu\ NC}$ is the volume calculated by the average of the NC size. The number of Cu atoms in the NC is equal to that of Pd being the atomic Pd:Cu ratio = 50:50. The expected volume $V_{Pd0.3Cu0.7O\ NC}$ of oxidized NC was calculated considering the unit cell volume equal to 47.77 $Å^3$ and the number of Cu atoms per unit cell of $Pd_{0.3}Cu_{0.7}O$ equal to 0.6 as follows, assuming that the NC has a spherical shape:

(3.2) $$V_{Pd\,0.3Cu0.7O\,NC,\,Cu} = \frac{N_{Cu\ atoms\ in\ Pd\,0.3Cu0.7O\,NC}}{N_{Cu\ atoms\ per\ Pd\,0.3Cu0.7O\ unit\ cell}} V_{Pd\,0.3Cu0.7O\ unit\ cell}$$

The unit cell volume of $Cu_{0.3}Pd_{0.7}O$ was calculated by modifying the tetragonal cell of PdO (ICSD 24692). The new cell has Cu and Pd ions with fractional occupancies (0.3 and 0.7, respectively) in the sites of Pd ions and parameters, a = b = 3.005 Å and c = 5.29 Å, calculated according to the plots in ref. [7] for $Cu_xPd_{1-x}O$, with x = 0.3.
The size of NC is then given by:

(3.3) $$d_{Pd\,0.3Cu0.7O\,NC,Cu} = 2\,r_{Pd\,0.5Cu0.7O\,NC,Cu} = 2\sqrt[3]{\frac{3V_{Pd\,0.3Cu0.7O,Cu}}{4\pi}}$$

where *d* and *r* are the diameter and radius of NC, respectively.

From the experimental data, the average size of the starting $Pd_{0.5}Cu_{0.5}$ NC is 4.9 ± 1.8 nm while that calculated for oxidized NC with the equation (3.3) is 7.0 nm, value in agreement with that observed in the HAADF-STEM images (7.8 ± 2.0 nm). This means that the growth of NC size is 42.8 % referred to the starting diameter.

To probe the surface composition and get information about the electronic features of the metals in upper layers of the bimetallic particles, DRIFT tests on the catalysts after the oxidizing and reducing treatments were performed using CO as a probe molecule. In Fig. 3.7 are reported the DRIFT spectra recorded in the carbonyl region during the adsorption and desorption of CO at room temperature for the alumina supported PdCu bimetallic catalyst after the two mentioned treatments.

The CO adsorption on the oxidized $PdCu/Al_2O_3$ catalyst (Fig. 3.9a and b) resulted in the appearance of two overlapping bands at 2154 and 2138 cm^{-1}. The latter was found to be in the intermediate position between that observed for oxidized Pd/Al_2O_3 catalyst (2109 cm^{-1}) assigned

to Pd^{+}-CO species (Fig. 3.8) and for oxidized Cu/Al_2O_3 catalyst (2124 cm^{-1}) attributed to Cu^{+}-CO species (Fig. 3.7). This suggested that a mixed Pd-Cu oxide species were formed to which CO was adsorbed linearly. The high-frequency band at 2154 cm^{-1} was typical for CO linearly adsorbed on Pd^{2+} atoms, as recorded for the monometallic catalyst.[9] After reduction (Fig. 3.9c and d), three main bands centered at about 2122, 2070 and 1991 cm^{-1} with a shoulder at 1942 cm^{-1} appeared. The assignments of the three latter vibrational bands are well established and attributed to CO bonded to surface Pd atoms in the linear, bridged and three-fold hollow bonded forms, respectively.[10] As the surface coverage increased by exposure time, the CO stretching frequency of Pd bounded CO shifted to a higher frequency (about 10 cm^{-1}) due to the dipole-dipole coupling between adsorbed CO on Pd surface. Although the frequency of the band at 2122 cm^{-1} was in the range of CO adsorbed on Cu^{+} (2110-2140 cm^{-1}), the lack of stability of the band under evacuation conditions precluded this assignment.[9] The attribution of this band to CO adsorbed on Cu^{0} can be possible assuming an electronic modification by neighboring Pd atoms that increase the CO-Cu^{0} strength. Indeed, the frequency of the bands assignable to linearly bonded Pd^{0}-CO and Cu^{0}-CO carbonyls in the spectra of reduced Pd/Al_2O_3 and Cu/Al_2O_3 catalysts were about 16 cm^{-1} higher and 4 cm^{-1} lower, respectively, than those recorded for the bimetallic catalyst. This confirmed the presence of an electron transfer from Cu to Pd such that the electronic properties of palladium atoms were strongly modified by copper addition. After 10 min of evacuation, the incomplete disappearance of the band at 2122 cm^{-1} implied that the $PdCu/Al_2O_3$ sample might not be fully reduced due to the presence of residual Cu^{+} species on which CO was strongly adsorbed in addition to reduce Cu^{0}. This was supported by SAED characterization, which suggested that the copper was not completely reintroduced in the alloy.

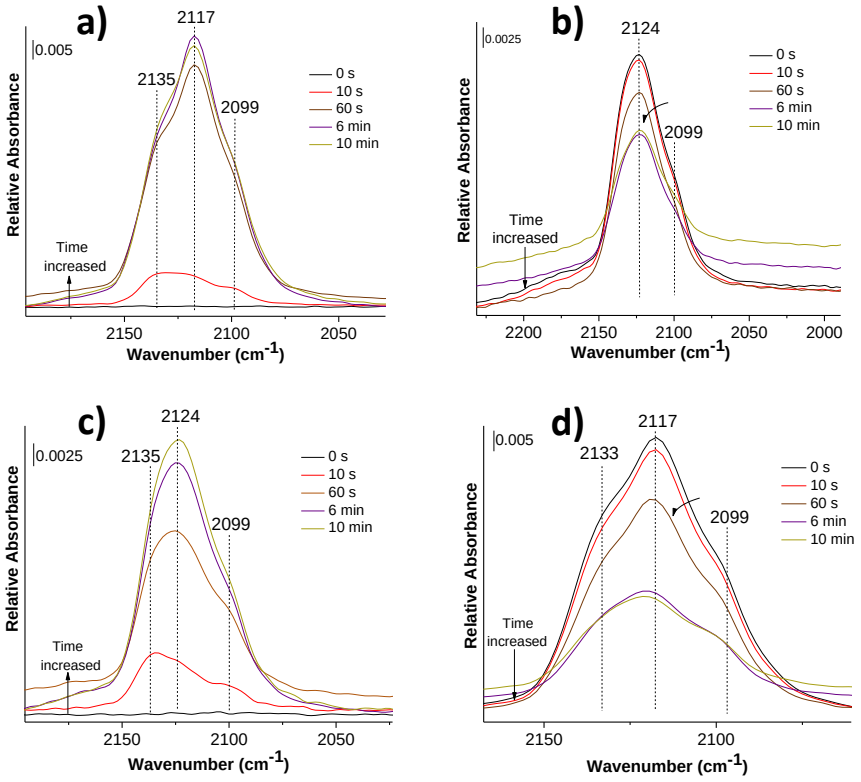

Fig. 3.7 – DRIFT spectra in the carbonyl region recorded during the adsorption (a, c) and desorption (b, d) of CO at room temperature on Cu/Al_2O_3 catalyst after the (a, b) oxidizing and (c, d) reduction treatments.

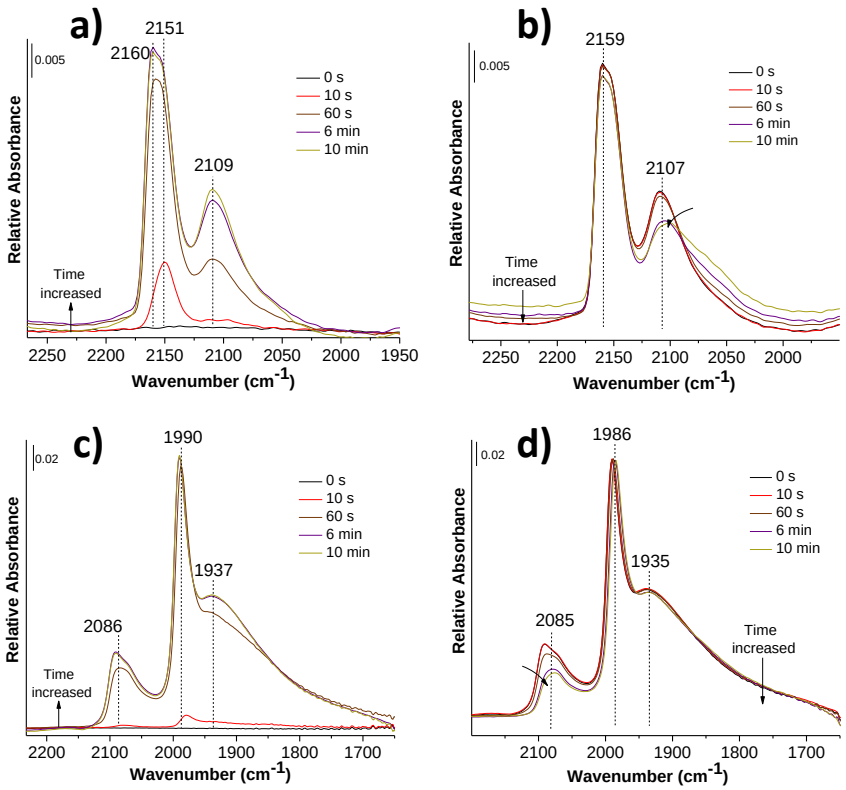

Fig. 3.8 – DRIFT spectra in the carbonyl region recorded during the adsorption (a, c) and desorption (b, d) of CO at room temperature on Pd/Al_2O_3 catalyst after the (a, b) oxidizing and (c, d) reduction treatments.

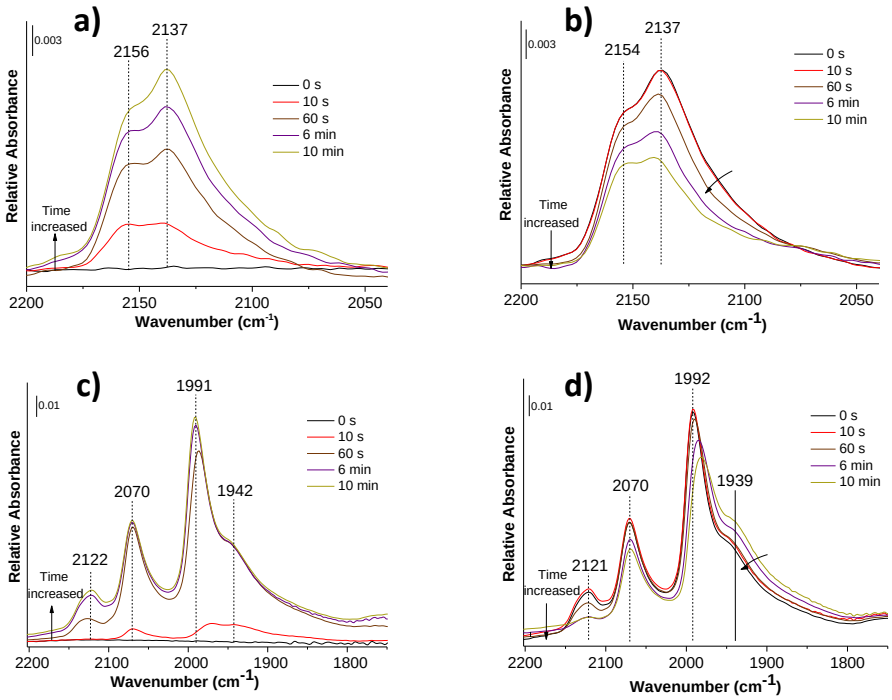

Fig. 3.9 – DRIFT spectra in the carbonyl region recorded during the adsorption (a, c) and desorption (b, d) of CO at room temperature on $PdCu/Al_2O_3$ catalyst after the (a, b) oxidizing and (c, d) reduction treatments.

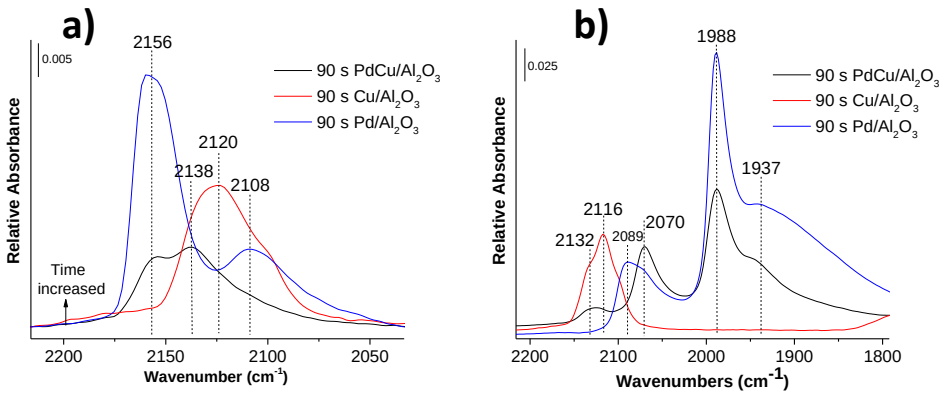

Fig. 3.10 – Comparison between the DRIFTS spectra taken after 90 s of exposure to the probe gas in the carbonyl region recorded during the adsorption of CO at room temperature on $PdCu/Al_2O_3$, Pd/Al_2O_3 and Cu/Al_2O_3 catalysts after the (a) oxidizing and (b) reducing pre-treatments.

To get a more complete picture of the dynamic changes in the catalysts structure in response to variation of the gas environments and temperature, XAFS measurements were carried out. The spectra were collected in transmission mode at the Pd and Cu absorption edges at the ROCK beamline of the synchrotron SOLEIL.

An initial XAFS spectrum was collected in He as starting point of the measurement. The Pd and Cu K-edge XANES spectra were similar to those of PdO and CuO standards (Fig. 3.11a and b).

The EXAFS analysis, reported in Fig. 3.11c and d, confirmed the presence of the CuO phase and the formation of PdCuO mixed oxides species with Cu-O and Pd-O as first neighbors. This was consistent with the oxidation occurring during the calcinations step, necessary for the removal of the organic ligands from the NC surface.

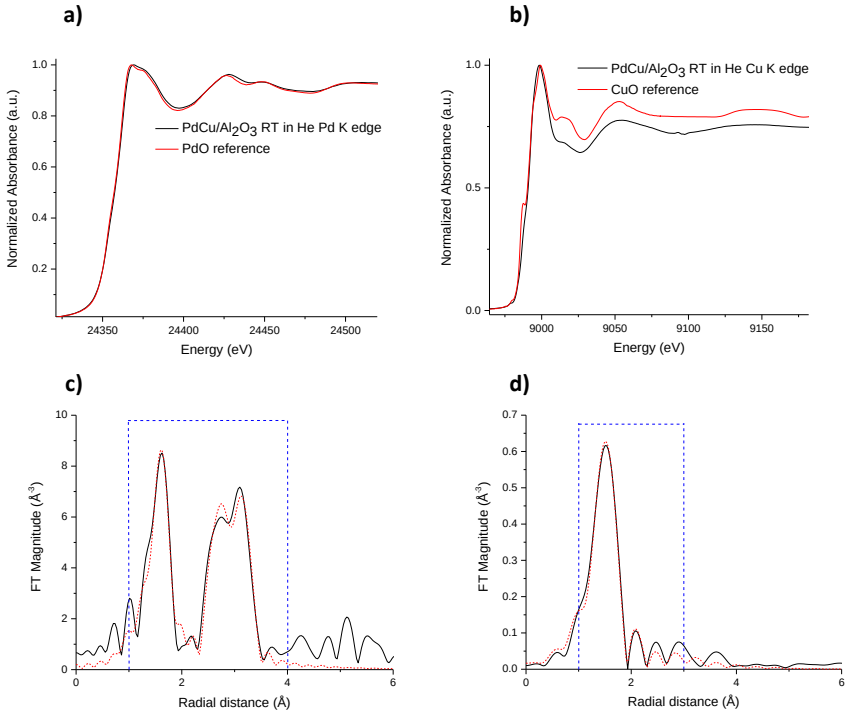

Fig. 3.11 – XANES spectra of $PdCu/Al_2O_3$ sample collected at RT in He at the (a) Pd K-edge and (b) Cu K-edge along with the PdO and CuO reference foils. The magnitude with the best fit (dashed lines) of the Fourier transform of fitted EXAFS spectra for the $PdCu/Al_2O_3$ catalyst at room temperature in He at (c) the Pd K-edge and (d) at the Cu K-edge (k range for the Fourier transform 2.5-12.4 $Å^{-1}$, the R-range for the fitting was 1-3/4 Å – dashed blue line window in the figure. In Tables A.1 and A.2 (Appendix A) are reported the structural parameters obtained from the fitted EXAFS spectra).

3.1.1.1 XAFS Characterization During Reduction

Fig. 3.12 shows the Quick-XAFS spectra recorded during the reduction at the Pd edge of the 2 wt% $PdCu/Al_2O_3$ catalyst after calcination. During the reduction, at temperatures between 40 °C and 120 °C, fast changes in both the intensity and the position of the rising edge were measured at the Pd K-edge. These changes were coupled with a progressive increase of the transmitted radiation around 2391 eV. These modifications of the XANES shape are related to the reduction of Pd(II) species to Pd^0 species, since the starting and the final spectra, respectively, are similar to the ones published in[11] for the crystalline references PdO and Pd metallic foil. It needs to be highlighted that the shape of the Pd XANES spectra showed small deviations and differed from the bulk metal and crystalline oxide references due to the nanoparticulate nature of the sample. Indeed, the size and morphology of the cluster, the interatomic distance and the presence of heterometallic bonds in the case of bimetallic clusters led to changes in position, shape and intensity of the near edge part of the absorption spectrum.[12]

The structure of the pivotal species involved during the treatment was then analyzed in-depth thanks to the MCR-ALS method applied to the respective dataset. The two Principal Components (PCs) obtained for the catalyst during reduction are presented in Fig. 3.13. The minimum number of components was selected by analyzing the plot of the eigenvalues as a function of the number of components, i.e. the so-called scree plot. The increase in the number of components leads to a decrease in the eigenvalues. The x-value where a break in the slope of the scree plot is identified, gives the minimum number of components that need to be considered in the system. According to the matrix rank determined by PCA, the MCR-ALS minimization was thus done in this case with two components. The profile of the two obtained components named D_r (descending component) and A_r (ascending component) formed during the reduction treatment as a function of temperature with the corresponding spectra are reported in Fig. 3.14.

The composition profile determined by MCR-ALS evidenced a significant reduction of the component D_r and a corresponding increase of the component A_r at T>50 °C. By the comparison of the D_r and A_r component spectra obtained from the MCR-ALS method (Fig. 3.14b) with different standards, it is possible to claim that the D_r spectrum displayed XANES and EXAFS features similar to the one reported for a PdO reference[11] and the A_r spectrum shows features similar to metallic palladium reference.

From the fitting procedure of the Fourier transform of the EXAFS signals recorded for the two components D_r and A_r (Fig. 3.15), the D_r one is described by a mixed O and Cu coordination shell at the distance of 2.03 Å and 3.06 Å, together with a Pd-Cu contribution at 3.45 Å (Table A.1 in Appendix A). These structural parameters allowed to assign the PdCuO mixed oxide-like

species to the D_r component. Indeed, the obtained *R-factor* of 0.015, that represented the mean square misfit between the data and the fit of the Fourier transform, was considered to reflect a reasonable fit since it is less than 0.05.[13] The best EXAFS fitting for the A_r component (*R-factor* 0.013) was instead obtained with a Pd-Pd contribution at 2.70 Å and Pd-Cu one at 2.64 Å, characteristic of the PdCu phase. The large contribution of Pd-Pd distances found in the first coordination shell suggested the formation of a Pd-rich PdCu disordered alloy. This observation is in line with the results obtained from the XRD data, in which the composition of the reduced NCs does not fully match with the starting NC alloy but a Pd-rich alloy was found.

To sum up, the time evolution of the components at the Pd K edge during reduction was consistent with the progressive reduction of PdCuO mixed oxides (component D_r) to Pd-rich PdCu disordered alloy (component A_r).

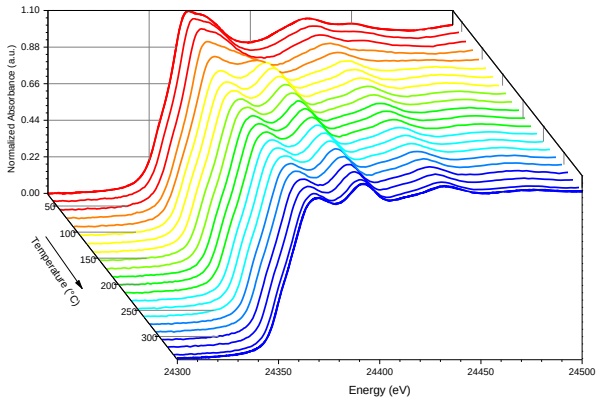

Fig. 3.12 – In situ XANES evolution of the $PdCu/Al_2O_3$ catalyst at the Pd K-edge during the reduction treatment.

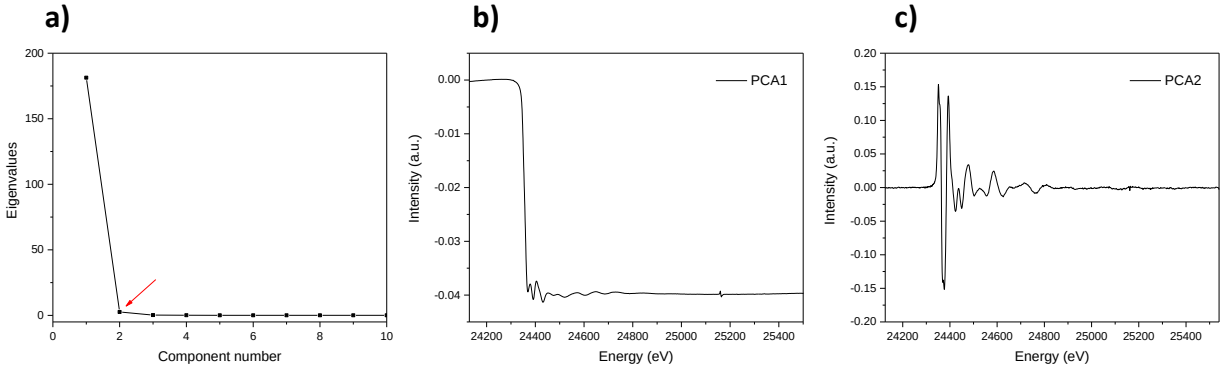

Fig. 3.13 – (a) Screen plot of the eigenvalues obtained by PCA of the Pd K edge for $PdCu/Al_2O_3$ catalyst during reduction and plot of the (b) first and (c) second PCs.

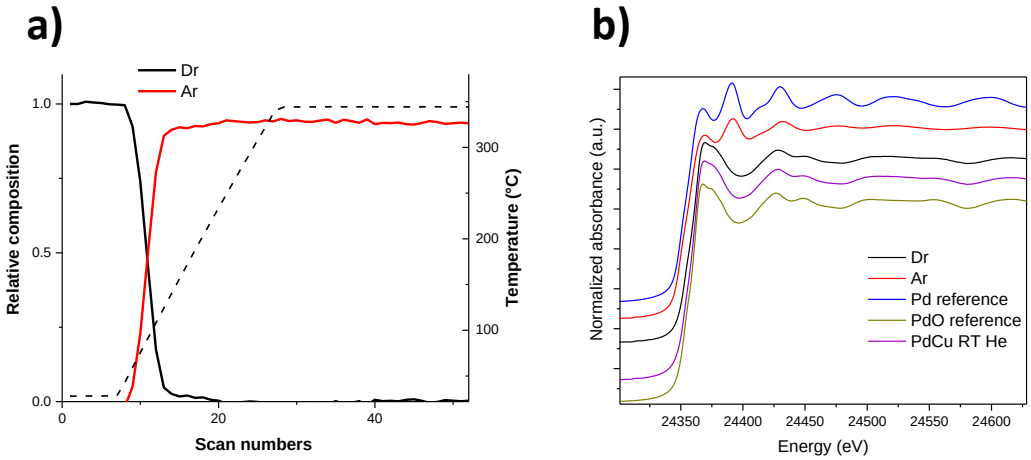

Fig. 3.14 – (a) Concentration profile of components determined by MCR-ALS as a function of the temperature during reduction at the Pd-K edge and (b) XANES spectra of the species formed during the reduction determined by MCR-ALS for the $PdCu/Al_2O_3$ catalyst along with the XANES spectra of crystalline references Pd metallic and PdO foils and $PdCu/Al_2O_3$ sample spectrum collected at room temperature in He.

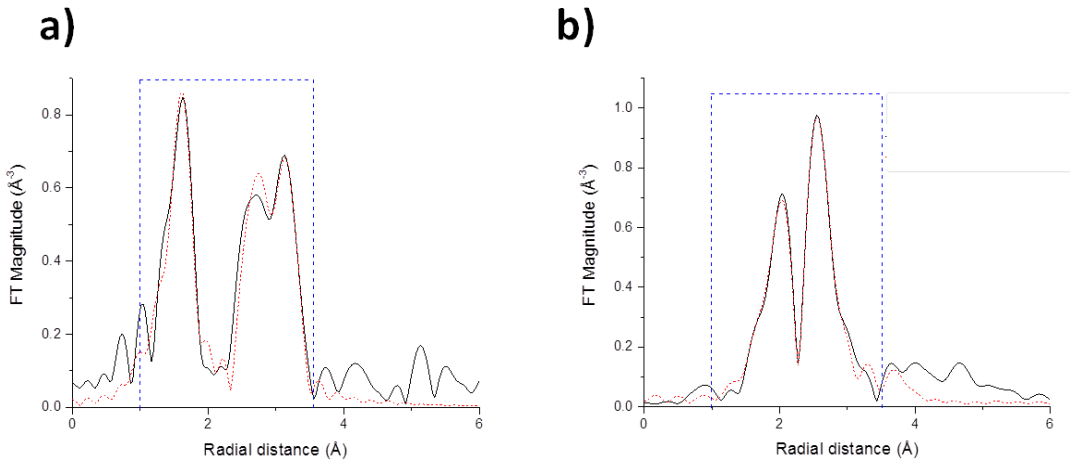

Fig. 3.15 – (a) Fourier transform (FT) magnitude with the best fit (dashed lines) of EXAFS spectra for (a) D_r and (b) A_r of the $PdCu/Al_2O_3$ catalyst during the reduction at the Pd K-edge (k range for the Fourier transform 2.5-12.4 Å^{-1}, the R-range for the fitting was 1-3/4 Å – dashed blue line window in the figure. In Tables A.1 and A.2 (Appendix A) are reported the structural parameters obtained from the fitted EXAFS spectra).

The realloy process during the reduction was also corroborated by the analysis of the evolution of the Cu K-edge spectra (Fig. 3.16). Indeed, the XANES spectra presented a decrease of the white line intensity at 8995 eV with increasing temperature until it disappeared at the end of the reduction. Furthermore, a shift of the rising edge at lower energy was clearly evidenced together whit the appearance of a marked shoulder in the rising edge at 8981 eV. These modifications of the XANES shape are related to the reduction of Cu(II) species to Cu(0) species.[14] Referring to the location of shoulders in the rising edge of CuO, Cu_2O and metallic Cu foil, the changes observed for the catalyst under reduction strongly suggests the formation of an intermediate Cu(I) species.

According to the matrix rank determined by PCA and to the break in the slope of the scree plot (Fig. 3.17a), three PCs were determined as representative to the set of quick-XANES data and displayed in Fig. 3.17b - d.

The concentration profile as a function of temperature determined by MCR-ALS evidenced a two-step reduction process in which the component D_r started to be significantly reduced into the intermediate component I_r at T~50 °C and then the formation of the component A_r started to be significant at T>150 °C. The comparison between the pure component spectra with the reference ones (Fig. 3.18b) suggested that the D_r seemed to be a fingerprint of the CuO phase, the I_r of Cu_2O one and A_r to the metallic copper structure.

The best fit of the Fourier transforms of the EXAFS spectra for the component D_r (Fig. 3.19) (*R-factor* 0.004) presented a single intense contribution of Cu-O and Cu-Pd coordination shells at 1.94 Å and at 3.17 Å, characteristic of PdCuO mixed oxide species. The best fit of I_r component (*R- factor* 0.008) was based on the contribution of two phases. Specifically, a contribution of Cu-O and Cu-Cu at 1.94 Å and 3.00 Å related to Cu_2O phase was found. Adding a refined contribution of Cu-Cu located at 2.65 Å referred to the PdCu phase improved the fit result. Finally, the A_r component was mainly characterized by a single Cu-Cu coordination shell at 2.48 Å related to metallic copper with a minor contribution of Cu-Cu shell at 2.58 Å of PdCu species and Cu-O shell at 1.86 Å for Cu_2O phase. To be highlighted that the total coordination number (CN) founded for the PdCu NC alloy at the Pd and Cu absorption edges of 7.30 ± 0.47 at 2.71 Å and 1.58 ± 1.56 at 2.58 Å, respectively, was lower than that of the bulk one ($CN_{Pd\text{-}Pd/Pd\text{-}Cu}$ <12, $CN_{Cu\text{-}Cu/Cu\text{-}Pd}$< 12) and it was attributed to nanosize of PdCu particles.[15]

To summarize, the fitting carried out at the Cu K edge lead to the conclusive formation of a PdCuO mixed oxide (component D_r) at the initial stage of the reduction. As the temperature increased, Cu_2O and CuPd alloy were formed as intermediate species (component I_r). The presence of the Cu(I) as intermediate species is commonly evidenced by XANES and depends strongly on the system. It was found for the systems in which the copper is supported on Al_2O_3, SiO_2, ZrO_2 supports compared to the bulk powders in which the direct reduction of CuO to metallic Cu is reported.[14, 16, 17] Finally, disordered CuPd alloy phases and metallic copper with a minor contribution of Cu_2O formed in the last step of the reduction, indicating that the initial alloy structure was not fully recovered.

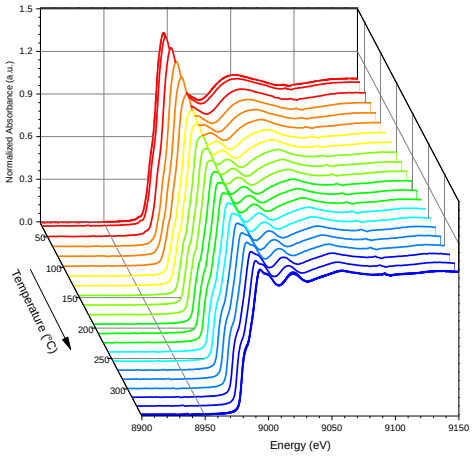

Fig. 3.16 – In situ XANES evolution of the $PdCu/Al_2O_3$ catalyst at the Cu K-edge during the reduction treatment.

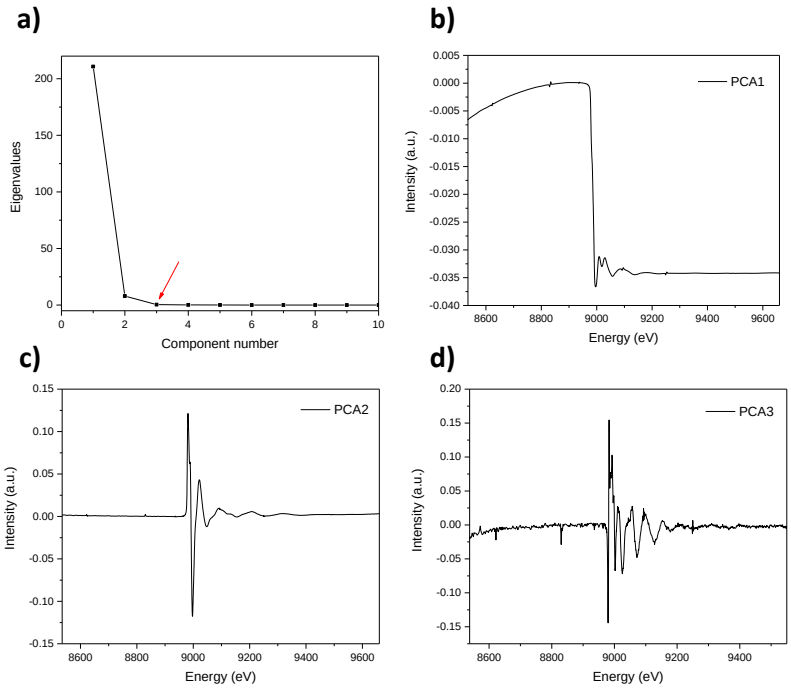

Fig. 3.17 – (a) Screen plot of the eigenvalues obtained by PCA of the Cu K edge for $PdCu/Al_2O_3$ catalyst during reduction and plot of the (b) first, (c) second and (d) third PCs.

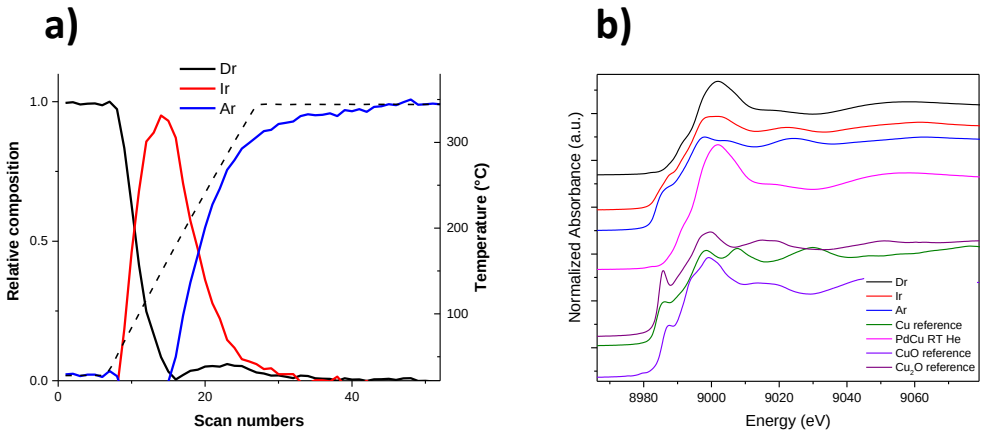

Fig. 3.18 – (a) Concentration profile of components determined by MCR-ALS as a function of the temperature during reduction at the Cu-K edge and (b) XANES spectra of the species formed during the reduction determined by MCR-ALS for the $PdCu/Al_2O_3$ catalyst along with the XANES spectra of crystalline references Cu metallic, CuO and Cu_2O foils and $PdCu/Al_2O_3$ catalyst spectrum collected at room temperature in He.

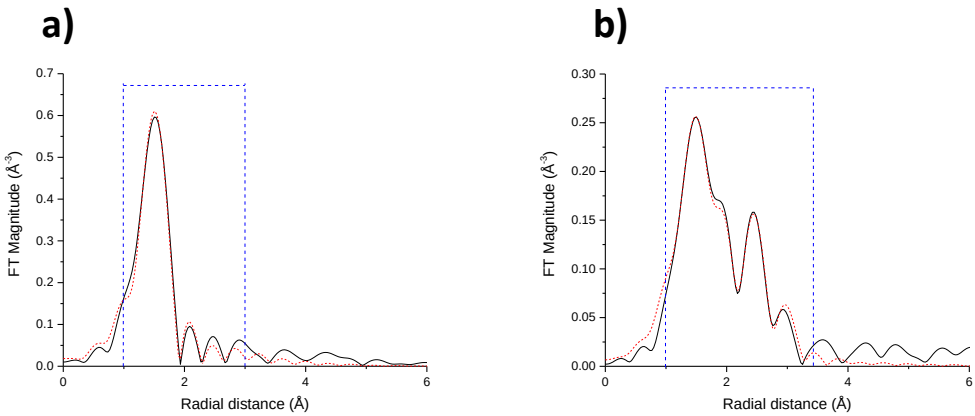

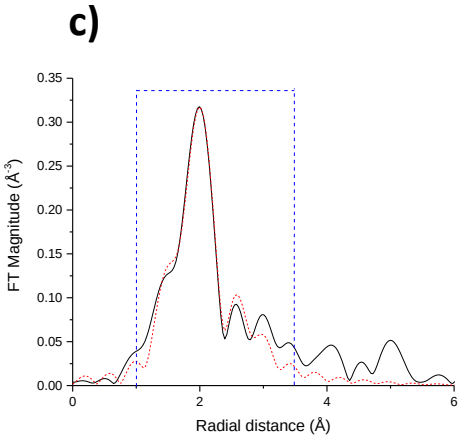

Fig. 3.19 – (a) FT magnitude with the best fit (dashed lines) of EXAFS spectra for (a) D_r, (b) I_r and (c) A_r of the $PdCu/Al_2O_3$ catalyst during the reduction at the Cu K-edge (k range for the Fourier transform 2.5-12.4 $Å^{-1}$, the R-range for the fitting was 1-3/4 Å – dashed blue line window in the figure. In Tables A.1 and A.2 (Appendix A) are reported the structural parameters obtained from the fitted EXAFS spectra).

3.1.1.2 XAFS Characterization During Oxidation

To describe the evolution of the system during the oxidation pre-treatment at the Pd K-edge (Fig. 3.20), two PCs have been revealed by chemometric method as the optimal number of species that allowed to describe the system, as evident from the scree plot in Fig. 3.21.

The evolution of the concentration profiles of the two PCs as a function of temperature, along with their pure spectra, are presented in Fig. 3.22. Specifically, the concentration of the component D_o started to decrease gradually at about 150 °C under the exposure to oxygen and becoming increasingly evident during the heating ramp in the oxidation atmosphere with a simultaneous increase of the component A_o. An initial visual inspection of the pure XANES spectra of the components respect to the references ones (Fig. 3.22b) showed that the shape of the features of the XANES and EXAFS parts of D_o were consistent with what has been seen in bulk PdCu[11] while A_o component features were similar to those of PdO reference.

The qualitative description of these two PCs was then corroborated by means of the analysis of the Fourier transform (FT) of Pd K edge EXAFS oscillation of the representative components during oxidation (Fig. 3.23). The best agreement between the observed and calculated EXAFS for D_o (*R-factor* 0.017) was achieved by using a structural model derived from the PdCu alloy. In particular, a Pd-rich PdCu disordered alloy was obtained from the fit. The component A_o was instead fitted using a structural model of PdCuO mixed oxide structure (Fig. 3.23b and Table A.1 in Appendix A).

To sum up, the transformation of the component D_o related to the Pd-rich PdCu alloy to the I_o referred to PdCuO mixed oxide was observed during the oxidation at the Pd K edge.

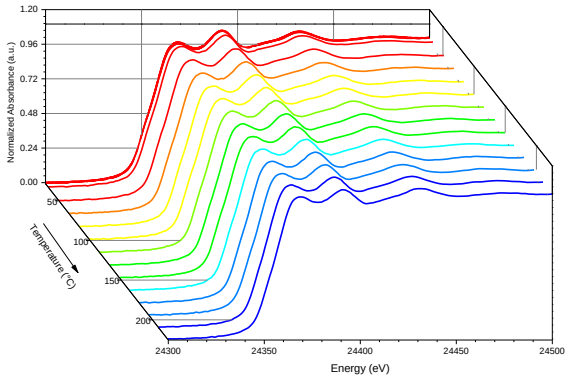

Fig. 3.20 – In situ XANES evolution of the $PdCu/Al_2O_3$ catalyst at the Pd K-edge during the oxidation treatment.

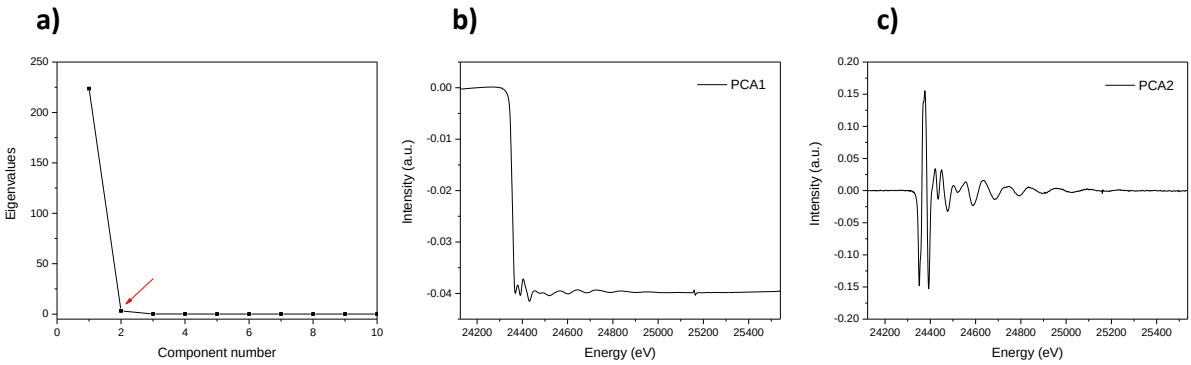

Fig. 3.21 – (a) Screen plot of the eigenvalues obtained by PCA of the Pd K edge for $PdCu/Al_2O_3$ catalyst during oxidation and plot of the (b) first and (c) second PCs.

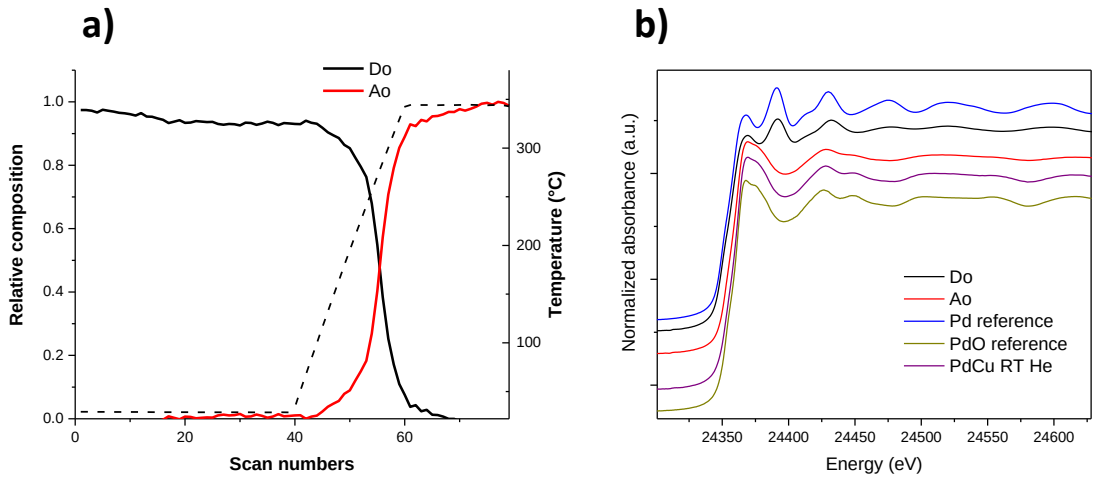

Fig. 3.22 – (a) Concentration profile of components determined by MCR-ALS as a function of the temperature during oxidation at the Pd-K edge and (b) XANES spectra of the species formed during the oxidation determined by MCR-ALS for the $PdCu/Al_2O_3$ catalyst along with the XANES spectra of crystalline references Pd metallic and PdO foils and $PdCu/Al_2O_3$ sample spectrum collected at RT in He.

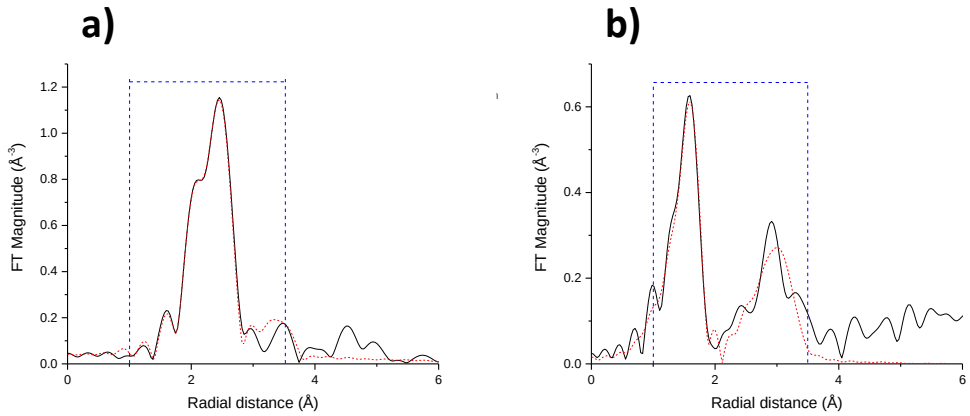

Fig. 3.23 – (a) FT magnitude with the best fit (dashed lines) of EXAFS spectra for (a) Do and (b) Ao of the $PdCu/Al_2O_3$ catalyst during the oxidation at the Pd K-edge (k range for the Fourier transform 2.5-12.4 $Å^{-1}$, the R-range for the fitting was 1-3/4 Å – dashed blue line window in the figure. In Tables A.1 and A.2 (Appendix A) are reported the structural parameters obtained from the fitted EXAFS spectra.).

Fig. 3.24 shows the XAFS data measured at Cu K-edge during the oxidation treatment. The matrix rank for the MCR-ALS was set to three as evidenced by the break in the scree plot of the eigenvalues obtained by PCA reported in Fig. 3.25a, along with the representation of the first three components representative of the system during oxidation (Fig. 3.25 b - d).

The identified components named D_o (descending), I_o (intermediate) and A_o (ascending) were presented as a function of temperature in Fig. 3.26 along with the corresponding spectra. Initially, already a room temperature under the exposure to the oxygen, the decrease of the constituent D_o proceed parallel with the appearance of constituent I_o; as soon as the temperature started to increase in the heating ramp, the component A_o, increased progressively until reaching the complete oxidation at 350 °C. The comparison between the derivate spectra with the reference ones (Fig. 3.26b) revealed the formation of the intermediate Cu_2O phase as component I_o confirmed comparing his absorption edge lied in between those of the constituents D_o and A_o, related to the Cu^{+2} and Cu^0 species, respectively.

The EXAFS signal and Fourier transform of the components D_o and I_o required two contributions for a better fit with an *R-factor* values of 0.018 and 0.010, respectively (Fig. 3.27 and Table A.2 in Appendix A), one from Cu and Pd atom in an ordered CuPd alloy and one from O atoms in the Cu_2O phase. In particular, the contribution of the first one decreased from D_o to I_o with the increasing of the second one (CN_{Cu-O} equal to 0.49±0.48 for D_o to 2.02±2.0 for I_o). Finally, the best fit for A_o suggested the formation of a PdCuO mixed oxide phase with the first shell of 2.59±0.2 O neighbors and the second one of 5.12±0.04 Pd next-neighbors.

To summarize, during the oxidation at the Cu K edge, the initial order alloy segregated already at room temperature with the formation of Cu_2O as intermediate species. A heat treatment at 350 °C is required to fully oxidize the copper oxide species in the +2 oxidation state, restoring the system to the initial situation recorded after the calcination.

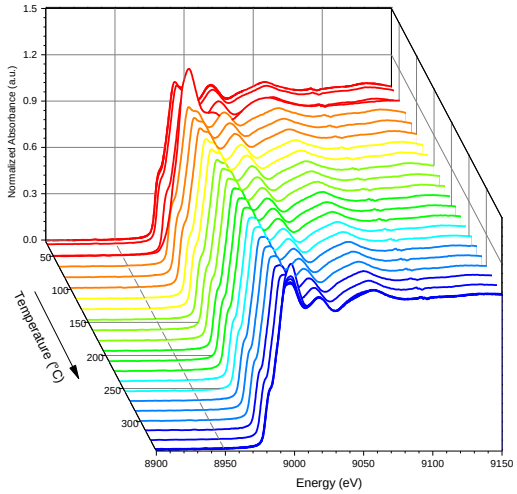

Fig. 3.24 – In situ XANES evolution of the $PdCu/Al_2O_3$ catalyst at the Cu K-edge after the oxidation treatment.

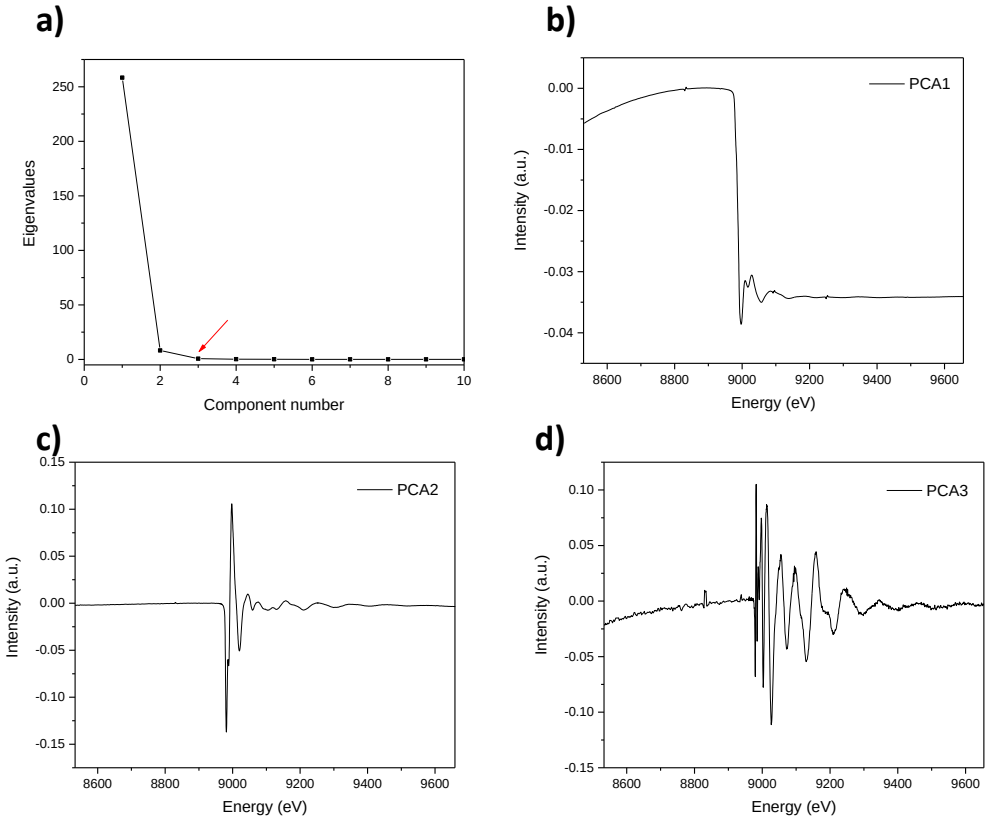

Fig. 3.25 – (a) Screen plot of the eigenvalues obtained by PCA of the Cu K edge for $PdCu/Al_2O_3$ catalyst during oxidation and plot of the (b) first, (c) second and (d) third PCs.

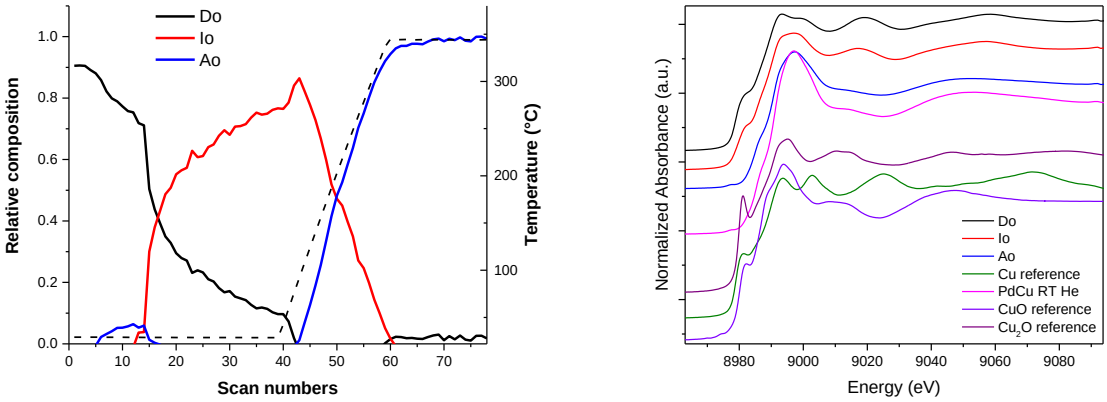

Fig. 3.26 – (a) Concentration profile of components determined by MCR-ALS as a function of the temperature during oxidation at the Cu-K edge and (b) XANES spectra of the species formed during the oxidation determined by MCR-ALS for the $PdCu/Al_2O_3$ catalyst along with the XANES spectra of crystalline references Cu metallic, CuO and Cu_2O foils and $PdCu/Al_2O_3$ catalyst spectrum collected at room temperature in He.

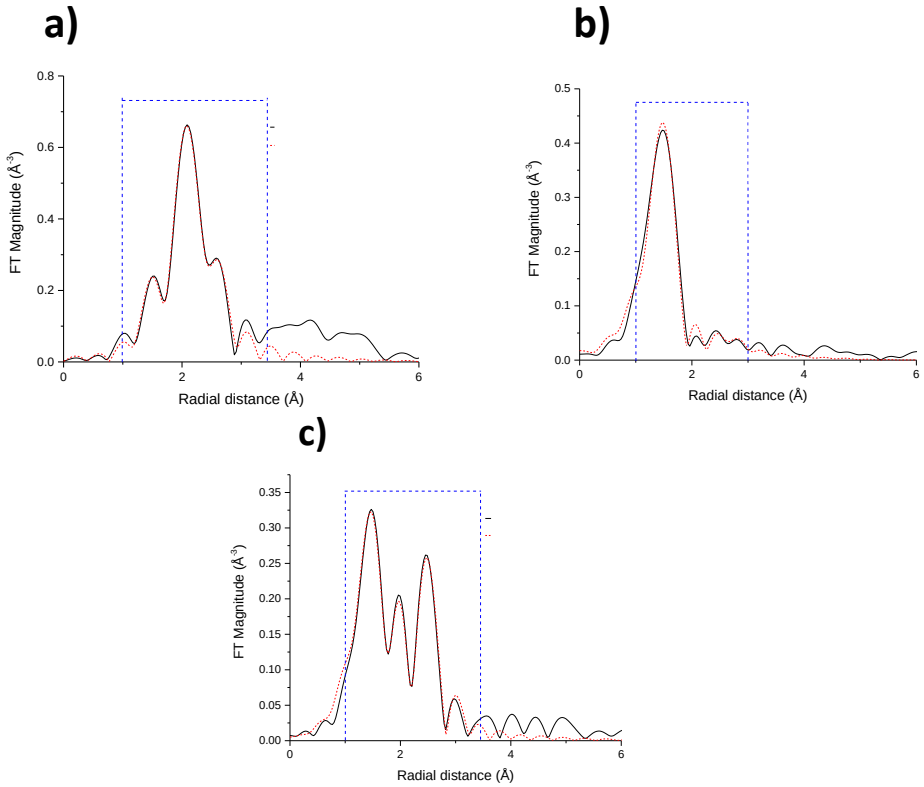

Fig. 3.27 – (a) FT magnitude with the best fit (dashed lines) of EXAFS spectra for (a) D_o, (b) I_o and (c) A_o of the $PdCu/Al_2O_3$ catalyst during the oxidation at the Cu K-edge (k range for the Fourier transform 2.5-12.4 $Å^{-1}$, the R-range for the fitting was 1-3/4 Å – dashed blue line window in the figure. In Tables A.1 and A.2 (Appendix A) are reported the structural parameters obtained from the fitted EXAFS spectra).

3.1.2 Catalytic Activity in the CO Oxidation Reaction

As already mentioned in Chapter I, the catalytic properties of bimetallic NCs are dependent on the elemental compositions of the whole NCs and the surface elemental distributions. The different phase structures exhibited different properties due to different coordination environments, electronic energy level of the metals and spatial distribution of the constituent atoms.[18]

Indeed, the observed reversible transformations that occurred under oxidative and reductive gas atmospheres led to a different scenario when these NCs were exposed to the CO oxidation reaction. The catalytic activity of the $PdCu/Al_2O_3$ catalyst is shown in Fig. 3.28. After oxidation, the CO conversion measured during the heating and cooling phases of the experiment almost overlapped. In both experiment phases, complete conversion was achieved at about 200 °C. A remarkable difference was observed above this temperature, where the appearance of significant oscillations in CO conversion was observed only during the heating phase of the experiment. This behavior could be explained by changes in the structure and in the chemical state of supported Pd NCs, as reported by Slavinskaya et al.[19] for Al_2O_3 supported Pd catalyst.

After reductive treatment, the $PdCu/Al_2O_3$ catalyst showed a continuous increase in CO conversion with the increase of the temperature, achieving complete consumption of CO at about 180 °C; during the following cooling phase, a lower activity compared to the heating phase was observed. Overall, the NCs were found to be more active for the CO oxidation after being exposed to reductive pre-treatment conditions as opposed to oxidative pre-treatment ones.

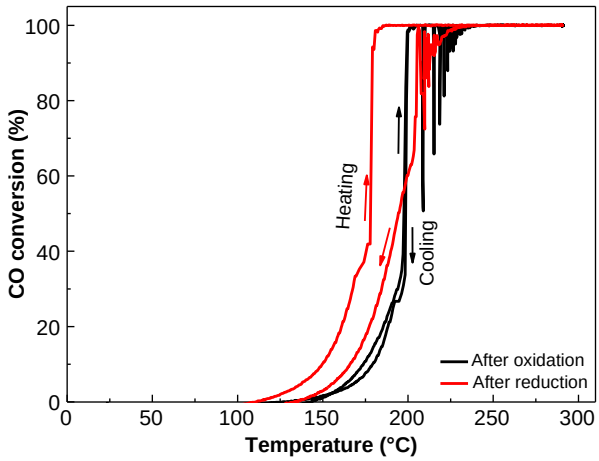

Fig. 3.28 – Catalytic activity of $PdCu/Al_2O_3$ catalyst in CO oxidation after the oxidizing and reducing pre-treatments during the third repeated test.

As a preliminary interpretation of these data, in analogy to what observed for the AuCu system[5], the difference in the activity can be explained by difference in the electronic states of Pd and Cu atoms under different atmospheres. Specifically, as reported previously, oxidizing the catalysts led to a segregation between the noble metal and Cu. Such a segregation resulted in the formation of PdCu mixed oxide, which in turn resulted in a decreased catalytic activity. Reducing the catalyst restored partially the PdCu alloyed NCs in presence of metallic Cu and a low fraction of Cu_2O phase, and enhanced the catalytic activity, highlighting the importance of

the interface between the noble metal and the Cu oxide species for the catalytic activity in the CO oxidation reaction. As reported by Zhou et al.,[20] several disputes are present in literature about the oxidation state of active Pd species for CO oxidation. A common assertion is that the PdO is a poor CO oxidation catalyst compared to the Pd metallic state. In addition, lower dispersion of Pd improves the catalytic activity, by the decrease of the Pd oxidation to PdO or ionic Pd^{2+} species, less active than metallic Pd.

Additional experiments were performed in order to understand how the NC surface composition evolved during exposure to oxygen at low temperatures. For this purpose, the reduced $PdCu/Al_2O_3$ catalyst was exposed to O_2 at both ambient temperature and at 130 °C (i.e. a temperature above the light-off) and the changes in the surface composition were monitored by DRIFTS (Fig. 3.29). The reduced catalyst after O_2 exposure at room temperature and at 130 °C showed a significant decrease in the band intensity associated with CO bonded to Pd^0 in the linear (2070 cm^{-1}), bridge (1990 cm^{-1}) and multi- (1942 cm^{-1}) forms. The intensity of the Cu/Cu^+ band (2126 cm^{-1}) remained almost constant after the treatment at room temperature, while after the exposure to O_2 at 130 °C a clear Cu^+ surface enrichment occurred.

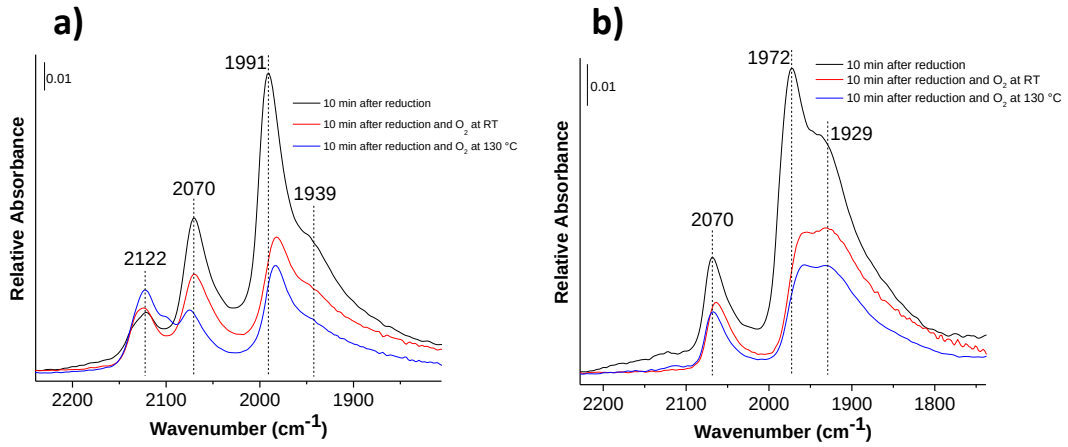

Fig. 3.29 – DRIFT spectra in the carbonyl region recorded during adsorption (a) and desorption (b) of CO at room temperature recorded after 10 min on $PdCu/Al_2O_3$ catalyst after reduction treatment and the exposure to O_2 flow at room temperature for 30 min and 130 °C.

In addition to these transformations induced by O_2 and H_2, metal NC surface reconstruction can also be induced by CO. Several examples of CO-induced surface segregation are indeed reported in the literature.[21-24] For example, McCue at al.[25] reported for a series of copper-rich $CuPd/Al_2O_3$ systems with different composition, a different extent of Pd surface enrichment induced by CO depending on the Cu:Pd ratio until the formation of Pd-Pd dimers on the surface of the catalyst. These changes in surface composition were then correlated with the activity of the catalyst in the selective acetylene hydrogenation reaction.

In situ time-resolved XAFS spectroscopy was applied during the reaction cycles to gain a deeper understanding of the NC transformations under reacting atmospheres. XAFS spectra were collected in transmission mode at the Cu and Pd absorption edges at the SuperXAS beamline of the Swiss Light Source (SLS) at PSI. The XANES spectra collected during the overall CO reaction cycle are presented in Figs. 3.30 and 3.31, where each reaction cycle after oxidation and

reduction pre-treatments has been divided in four segments. Along with these results, the EXAFS simulations of the spectra collected at the beginning of the test after the exposure for 15 min to the reaction environment, the spectra measured at the end of the heating ramp up to 300 °C, and the one obtained at the end of the cooling ramp down to 100 °C are reported in Appendix B. In this way, we isolated the species formed during the reaction by considering them as borderline phases of the above mentioned steps, among which structural transformations can occur. To be noted that the XANES spectra acquired at the end of the reductive and oxidized treatments before starting the CO cycle reaction were in agreement with those obtained from the SOLEIL synchrotron (see Fig. B.1 in Appendix B).

As mentioned in ref.[26], isosbestic point suggested that series of spectra were generated from different mixtures of only two components mixed in different amounts. Indeed, it is improbable the appearance of these points when three or more constitutes are present in the mixture since they should have the same normalized absorption at the same energy. Because of this explanation, from the analysis of the XAFS spectra during the CO oxidation reaction for the Pd and Cu K-edge after the reductive and oxidative treatments, it is possible to claim that, where the isosbestic points (black arrows in the Figures) were present along during the steps of the reaction, two constituent components were involved in each segment with no intermediate species being formed.

Figures 3.30 and 3.31 display the in situ Pd and Cu K-edge XANES spectra obtained from the heating and cooling reaction phases over the $PdCu/Al_2O_3$ catalyst sample. XANES spectra of bulk PdO, CuO and Cu_2O and Pd, Cu foil standard samples were used as references. As mentioned above, during the discussion of the SOLEIL synchrotron data, the identification of the chemical species involved during the reaction process by the direct comparison of the spectra with those for the bulk standards was less straightforward due to the nanometer size of the particles involved. For this reason, only a qualitative evaluation could be done, due to the lack of known spectral fingerprints for these species.

Visual inspection of the XANES region at the Pd and Cu K-edges for the reduced sample (Fig. 3.30) showed that the first experiment phase, recorded as the temperature increased from room temperature to 300 °C, showed the progressive evolution of the XANES profile towards that of the PdO reference material. The dealloying process was also confirmed at the Cu K-edge (Fig. 3.30b) in which a progressive increase of the white line peak at 8998 eV, corresponding to a fraction of oxidized copper sites,[27, 28] appeared under the exposure of reaction environment during the heating ramp. The second and third regions related to the static segment at 300 °C for 30 min and the cooling ramp down to 100 °C, respectively, at both edges (Fig. 3.30 c, d, e and f) did not display significant changes in the near-edge structure compared to the last spectrum acquired at the end of the heating ramp. Only a progressive increase in the white line intensity and shift of the absorption edge to higher energy by 8 eV and 1 eV for Pd and Cu K-edge, respectively, suggested the progressive oxidation of Pd and Cu metal at both edges to PdO and CuO. In comparison, a 1.5 eV shift was observed based on the PdO reference compound suggesting that incomplete oxidation to Pd^0 had taken place at the end of the reaction. No

relevant modification was also observed in the last phase of the experiment, i.e. the permanence at 100 °C for 30 min (Fig. 3.30g and h).

EXAFS analysis reported in Tables B.1 and B.2 (Appendix B) for the spectrum acquired at the beginning of the test after the exposure for 15 min to the reaction environment confirmed the initial presence of a disordered Pd-rich alloy in which part of the copper is in the form of Cu_2O. On the other hand, at the end of the heating ramp, a final state in which PdO and Cu_2O are the predominant phases was revealed with a small contribution of Pd_2O and CuO. The presence of copper oxide in the oxidation state +1 as species was commonly evidenced for various copper supported catalyst[14, 29] and probably formed due to the partially reducing CO environment. In this case, the EXAFS data were modeled also including the first and second shells of PdCu alloy (Pd-Pd1 coordination at 2.42 Å and Cu-Cu1 at 2.67Å) revealing the presence of a remaining ordered alloy. In the cooling phase down to 100 °C, the first nearest neighbor Pd-O coordination at 2.00 Å related to the PdO phase and Cu-O1 of CuO phase at 2.25 Å gradually increased along with the reduction of Pd-Pd1 and Cu-Cu1 coordination shells belonging to the ordered alloy.

In particular, by using the estimated Cu-O1 and Pd-O1 coordination number CN in first shell nearest neighbor of the copper oxide and palladium oxide in the +2 oxidation state, it was possible to determine the relative amount of each phase present and hence an estimation to the overall extent of oxidation. As reported by Prestat et al.[11], the fraction of the oxidized species can be calculated according the following relationship $CN_{(Cu\text{-}O) \text{ or } (Pd\text{-}O) \text{ observed}}$ = 4 x % of Cu-O or Pd-O and considering that these two phases, in general, have 4 Cu-O/Pd-O single bonds. Pd and Cu remained 60% and 10% oxidized, respectively, at the end of the heating ramp and 66% and 30%, respectively, at the end of the cooling ramp.

After the oxidation treatment (Fig. 3.31), during the exposure to the reaction environment in the heating ramp up to 300 °C, the XANES spectra at the Pd and Cu K-edges gradually changed with time-on-stream, as illustrated by the blue arrow in Fig. 3.31a and b. In particular, at the Pd K-edge the spectral features at around 24390 and 24430 eV decreased in intensity, and the edge shifted towards lower energies. On the other hand, the Cu K-edge shifted to higher energy, the white line intensity decreased, and a feature in the edge became less noticeable. By comparison with the references, the positions of the absorption edge approached the value measured on the PdO and CuO standards. The same scenario was revealed during the acquisition of the XANES spectra during the cooling phase down to 100 °C (Figs. 3.31e and f). Indeed, the collected spectra presented the same shape of those recorded at the end of the heating and the cooling ramp.

The fitting of EXAFS spectra (Tables B.3 and B.4 in Appendix B) in the heating phase revealed that the Pd-O1 contribution from the PdO phase diminished (feature at 2436 eV become smaller) whereas the Pd-O1 one related to the Pd_2O phase increased (shoulder and feature at 24385 eV). On the other hand, the co-presence of Cu_2O phase (Cu-O1 neighbors at 1.90 Å) with a small fraction of CuO one (Cu-O1 neighbors at 2.20 Å) was obtained from the EXAFS fit. In this case, the attempt to evidence and to construct a theoretical model based on the PdCuO mixed oxide compound as known structure present after oxidation treatment was unsuccessful. Probably,

already at room temperature the exposure to CO/O_2 mixture led to a reconstruction of this mixed oxide phase forming PdO and CuO as distinct phases. At the end of the cooling phase, almost the same phases compared to those obtained at the beginning of the heating ramp were detected within the error. To be noticed that in general the calculated amount of the PdCu order alloy found during the cycle performed after oxidation compared to that one after reduction was lower.

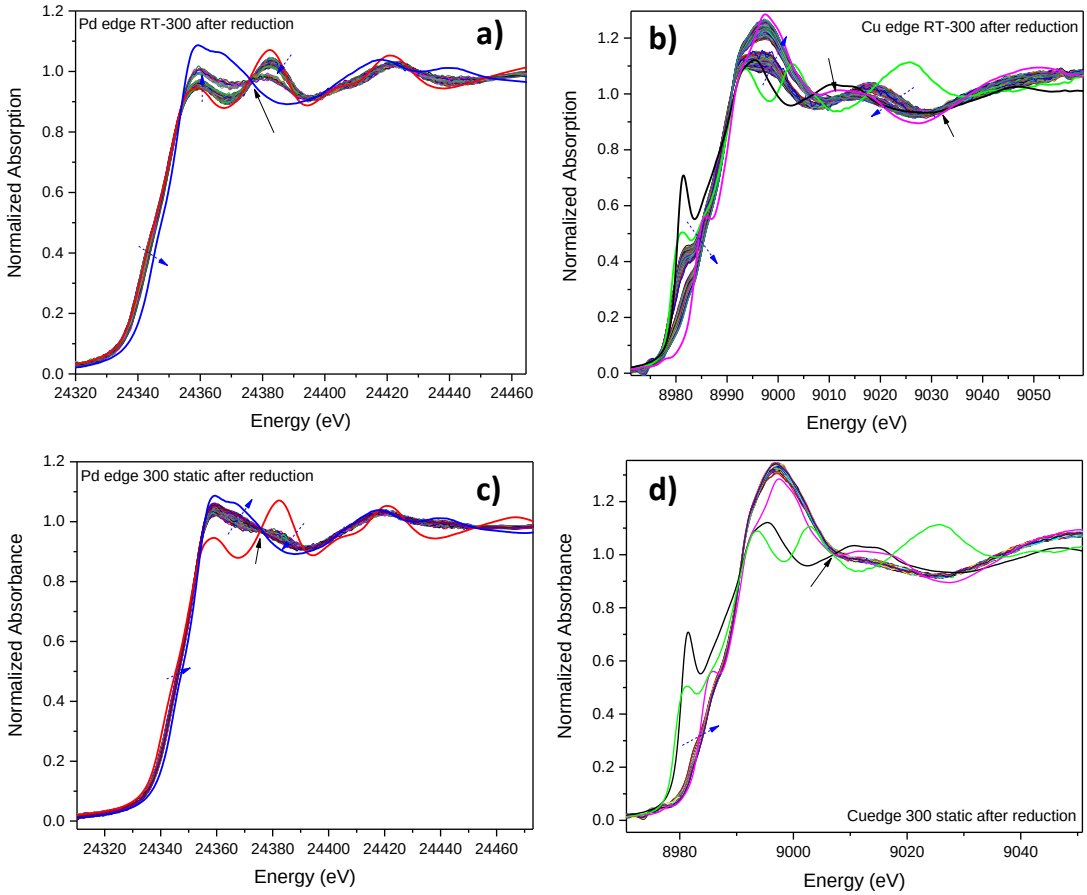

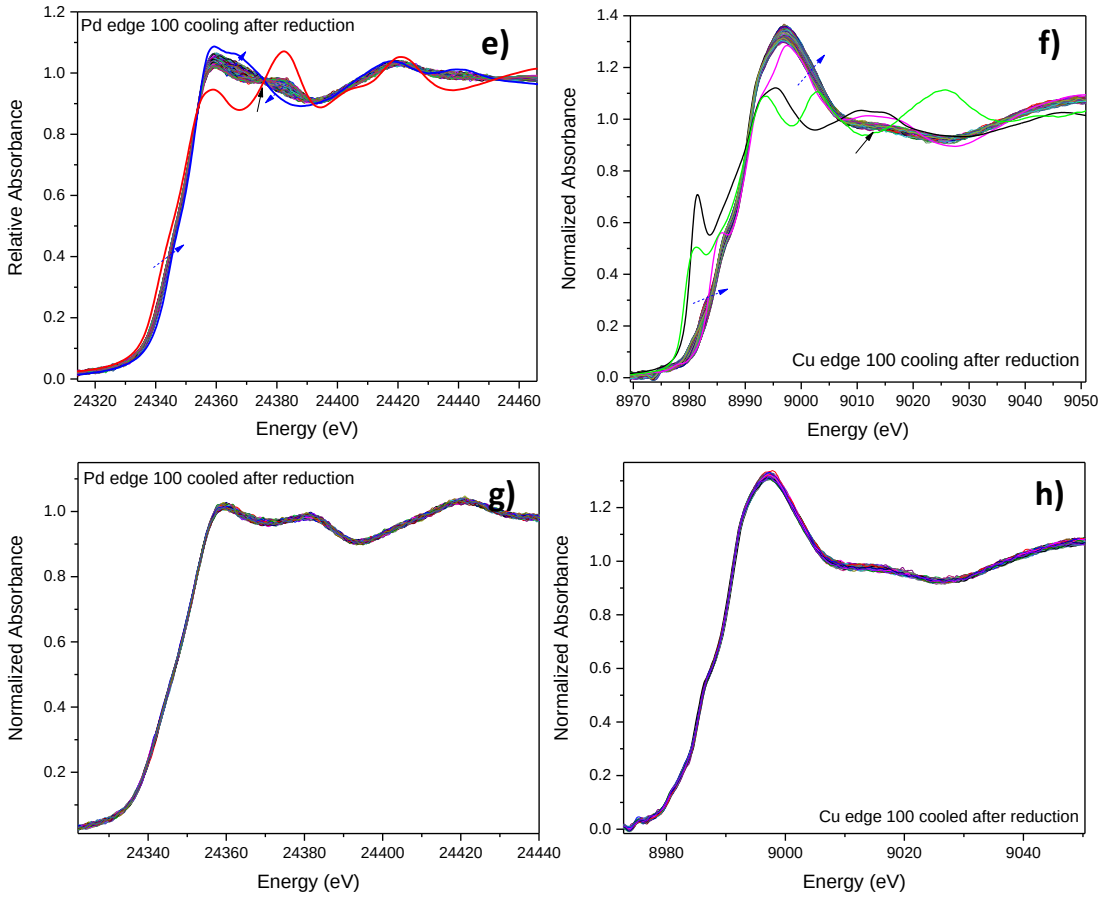

Fig. 3.30 – XANES evolution of the $PdCu/Al_2O_3$ catalyst at the (a, c, e, g) Pd K-edge and (b, d, f, h) Cu K-edge after reduction treatment during the CO oxidation reaction: (a, b) in the heating ramp up to 300 °C, (c, d) static at 300 °C for 30 min, (e, f) in the cooling ramp down to 100 °C and (g, h) static at 100 °C for 30 min. The XANES spectra of the Pd (in red), PdO (in blue), Cu (in green), Cu_2O (in black) and CuO (in magenta) standards are reported. The blue dashed arrows indicate the direction of the evolution of the spectra during the acquisition while the black ones the isosbestic points.

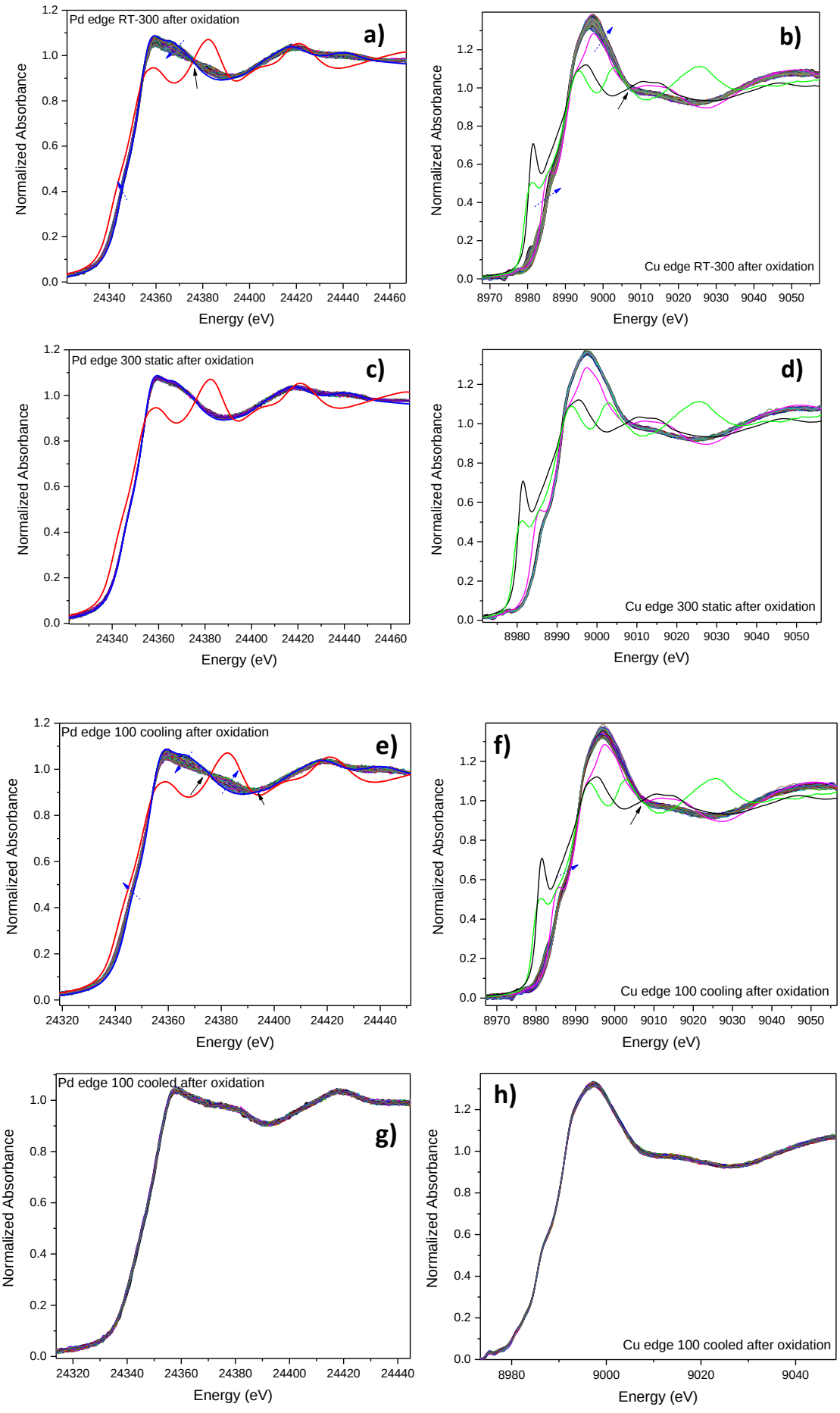
Pd edge RT-300 after oxidation
a)
Normalized Absorbance
Energy (eV)
b)
Cu edge RT-300 after oxidation
Pd edge 300 static after oxidation
c)
d)
Cu edge 300 static after oxidation
Pd edge 100 cooling after oxidation
e)
f)
Cu edge 100 cooling after oxidation
Pd edge 100 cooled after oxidation
g)
h)
Cu edge 100 cooled after oxidation

Fig. 3.31 – XANES evolution of the $PdCu/Al_2O_3$ catalyst at the (a, c, e, g) Pd K-edge and (b, d, f, h) Cu K-edge after oxidation treatment during the CO oxidation reaction: (a, b) in the heating ramp up to 300 °C, (c, d) static at 300 °C for 30 min, (e, f) in the cooling ramp down to 100 °C and (g, h) static at 100 °C for 30 min. The XANES spectra of the Pd (in red), PdO (in blue), Cu (in green), Cu_2O (in black) and CuO (in magenta) standards are reported. The blue dashed arrows indicate the direction of the evolution of the spectra during the acquisition while the black ones the isosbestic points.

Finally, the reproducibility of activity data was verified by repeating the treatments sequentially in different atmospheres. In the three repeated reaction cycles, the conversion curves of $PdCu/Al_2O_3$ catalyst showed similar trends (Fig. 3.32); no significant changes were observed among the tests, proving, on the one hand, the stability of the catalyst and on the other hand the dependence of catalyst activity only from the last treatment applied providing a complete reversibility in the structural reorganization between an oxide state and a reduce one for the supported PdCu NCs.

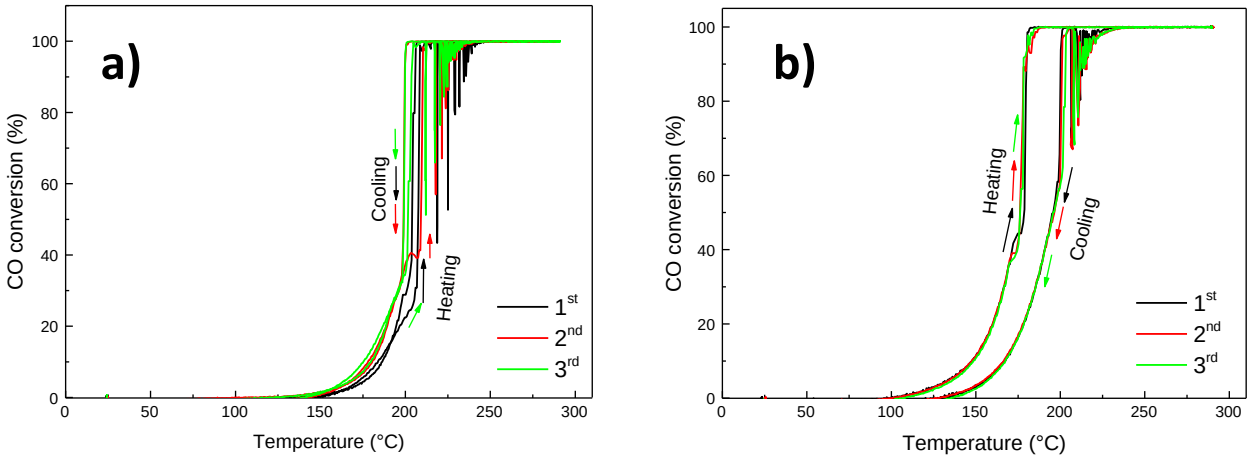

Fig. 3.32 – Catalytic activity during three reaction cycles of $PdCu/Al_2O_3$ catalyst in CO oxidation after oxidizing (a) and reducing (b) pre-treatments.

3.2 Effect of the Support on the Surface Composition of NCs

3.2.1 Silica Supported NCs Upon Oxidative/Reductive Pre-treatments

In order to investigate the role of the support in the transformation of PdCu NC, the same batch of NCs used for the study presented in the section 3.1 was used to prepare $PdCu/SiO_2$ samples. Also in this case, the catalyst was characterized by means of several techniques after the oxidizing and reducing treatments.

As shown in Fig. 3.33, it was found by the HAAD-STEM analysis that the as-synthetized PdCu NC size of 4.5 ± 1.3 nm was preserved upon the two treatments. Specifically, for PdCu NCs, an average particle size of 4.8 ± 1.1 nm based on 148 particles and 4.5 ± 1.6 nm on 170 particles was obtained after oxidation and reduction, respectively. It should be noted that, in this case with respect to PdCu NCs supported on alumina, no increase in the NC size was observed after the oxidation treatment. The catalyst analyzed by STEM-EDX showed that after oxidation, the noble metal remained localized in the particles, while the Cu was present as a shell around the noble

metal core particles (Fig. 3.34a), while after reduction (Fig. 3.34b) both Pd and Cu seemed to be present in the NPs, except for some NPs in which only Cu was present (highlighted in Fig. 3.34b with white circles).

The XRD pattern of the SiO_2 supported PdCu catalyst after the two treatments are reported in Fig. 3.34c in comparison to those of the as-synthetized NCs. After the oxidation, the pattern was in agreement with a cubic structure, corresponding to PdO. It needs to be highlighted that no phase associate to PdCuO mixed oxide was detected as in the case of PdCu NCs. After reduction, the diffraction peak positions matched those of cubic PdCu.

The comparison with the pattern obtained from the parent colloidal particles showed that almost a complete realloy of Cu took place upon the reduction. From the Vegard's law,[8] a 40% atomic of Cu was calculated, value in agreement with that obtained from the STEM-EDX analysis.

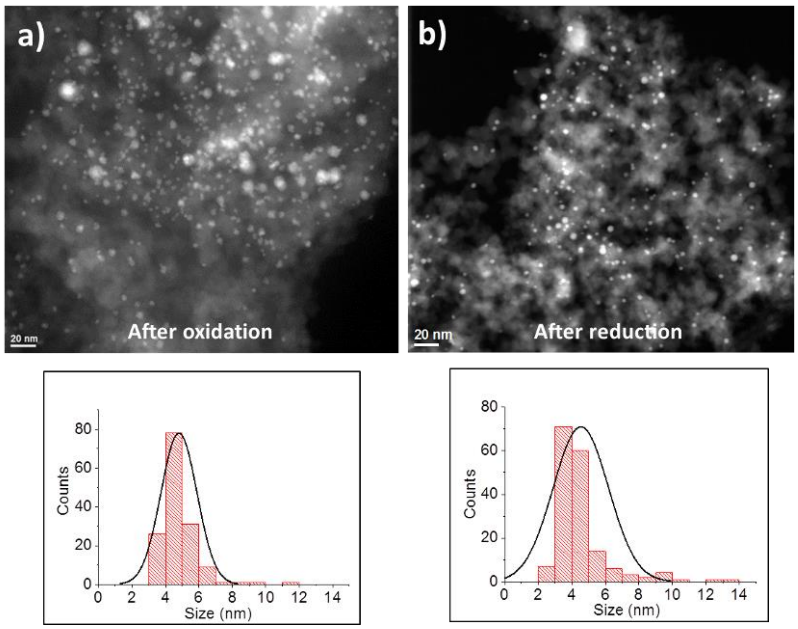

Fig. 3.33 – HAADF-STEM images of $PdCu/SiO_2$ catalysts after (a) oxidizing and (b) reducing treatments with the corresponding size distribution histogram.

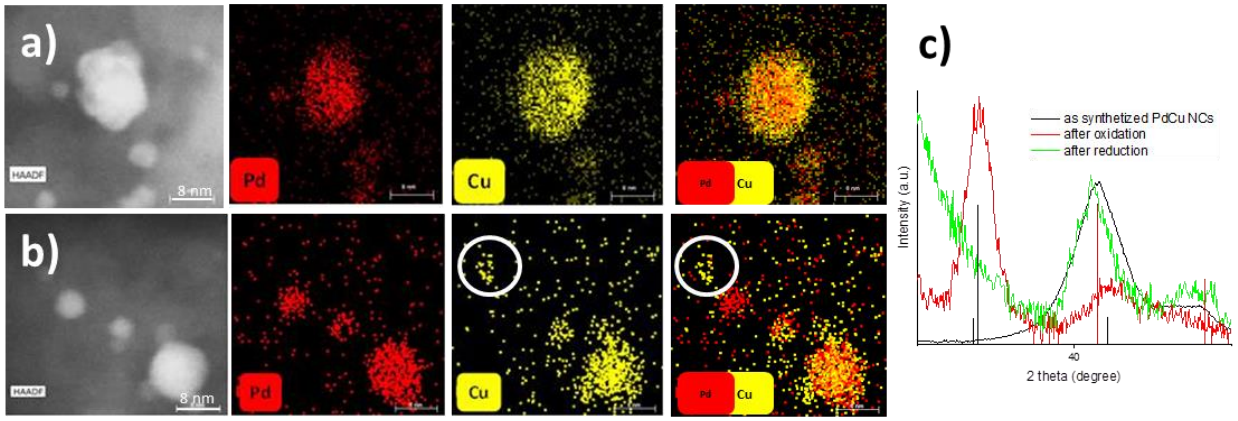

Fig. 3.34 – HAAD-STEM images of 2 wt % $PdCu/SiO_2$ catalyst and corresponding quantitative EDX maps for Pd and Cu after (a) oxidizing and (b) reducing treatments; (c) XRD patterns after oxidation and reduction in

comparison to PdCu NCs (reference patterns: Pd_1Cu_1 ICSD 98–010–3082 (red line), O_1Pd_1 ICSD 98–002–6598 (black line)).

The surface composition and the electronic features of the metals in the upper layers of the $PdCu/SiO_2$ sample were studied by means of DRIFT using CO as a probe molecule. Figure 3.37 reports DRIFT spectra recorded in the carbonyl region during the adsorption and desorption of CO at room temperature on $PdCu/SiO_2$ catalyst after the two treatments along with the spectra on monometallic Pd and Cu catalysts provided under the same conditions as a basis of comparison (Figs. 3.35 and 3.36).

Adsorption of CO on oxidized Pd/SiO_2 sample (Fig. 3.35) resulted in the appearance of two main bands at 2104 cm^{-1} and 2145 cm^{-1}, which were assigned to Pd^{+}-CO and Pd^{2+}-CO complexes, respectively. According to Hadjiivanov et al.,[9] these bands decreased slightly in intensity upon evacuation of the sample with less stability of the band in the high-frequency region. CO adsorption on a reduced sample led to two main CO vibration bands located at 1987 cm^{-1} and attributed to the bridge-bonded CO and at 2098 cm^{-1} to the carbonyls on zero-valent Pd with a shoulder at 2070 cm^{-1} characteristic of ionic $Pd^{\delta+}$-CO complexes.

The adsorption of CO on Cu NCs supported on silica has been studied by DRIFT (Fig. 3.36). The carbonyl band positions have been reported to fall in different regions as a function of the metal oxidation state: Cu^0-CO <2130 cm^{-1}, Cu^{+}-CO 2160-2080 cm^{-1}, Cu^{2+} 2145 cm^{-1} and above.[9] Stability is one of the main criteria for the discrimination between Cu^{+}-CO and Cu^0-CO carbonyls within the overlapping spectral range between 2110 cm^{-1} and 2080 cm^{-1}. The interaction strength of CO with Cu^0 and with Cu^{2+} is very weak compared to that of Cu^{+}-CO such that more severe evacuation conditions are required for the CO to desorb from the latter species. In view of these considerations, the adsorption of CO on the oxidized sample resulted in the formation of a weak band at 2112 cm^{-1} with a shoulder at 2131 cm^{-1}. According to Davydov et al.[30], these bands can be ascribed to CO bounded to Cu^{+} surface sites. The frequency band position of CO was considered dependent on the environment of the Cu^{+} ion to which the CO was bounded. An increase from 2110 cm^{-1} to 2140 cm^{-1} was suggested as indicating a higher concentration of Cu^{2+} ions surrounding the Cu^{+} adsorption sites. On the basis of these considerations, the band at 2112 cm^{-1} can be attributable to CO on Cu^{+} sites located in a more reduced environment than that around the Cu^{+} sites that give a band at 2131 cm^{-1} when CO was adsorbed. On the reduced sample, the band observed at 2120 cm^{-1} can be ascribed to linear CO adsorbed on a stepped surface of a high-index plane of copper.[31] This assumption was confirmed by the fact that the frequency of the band is influenced by evacuation. It must be noted that the intensity of this peak was one order of magnitude greater than the one acquired after the oxidation, suggesting that the Cu in the oxidized sample was in the form of Cu^{2+}, not detectable by DRIFT using CO as a probe molecule. The shoulder visible at 2147 cm^{-1} can be assigned to CO adsorption on an anionic vacancy on the surface of a block of CuO, indicating that the catalyst surface layer is still slightly oxidized.[31, 32]

CO adsorbed on the oxidized $PdCu/SiO_2$ catalyst (Fig. 3.37a and b) gave a main absorption band at 2121 cm^{-1}. This vibrational band can be assigned to CO adsorbed on oxidized Cu^{+}-CO, suggesting the formation of Cu_2O species to which CO adsorbed linearly. It is noteworthy that

no band related to Pd species has been detected, in line with the STEM-EDX measurements that were suggesting the formation of a CuO_x shell around PdO NPs. After reduction, two main bands at 2136 cm^{-1} and 2071 cm^{-1} with a lower intensity one at 1989 cm^{-1} can be observed. In accordance with the literature[33, 34], the latter one corresponding to the bridged species decreased in intensity and shifted to lower ν_{CO} values compared with the corresponding one for Pd/SiO_2 due to the addition of Cu to Pd/support catalyst. Also the position of the others two bands is shifted into lower and higher wavenumber values, respectively, in comparison to that of the band at 2098 cm^{-1} connected with the linear absorption of CO by Pd atoms in the monometallic system and at 2120 cm^{-1} related to CO adsorbed on Cu^0 (Fig. 3.36c and d). This is related to the alloying process and the electron transfer from Cu to Pd, leading to the expected shift of these bands.[35]

DRIFT characterization highlighted a significant role of the support in the gas atmosphere induced transformation of supported PdCu NCs (Fig. 3.39). Indeed, the same oxidizing pre-treatment (Fig. 3.39a) resulted in the formation of a PdCu mixed oxide phase in case of Al_2O_3, while a PdO core-CuO_x shell structure was obtained when the same NCs were supported on SiO_2.

Also in the case of a reducing treatment, the comparison of the DRIFT spectra evidenced differences between the two supports (Fig. 3.39b). Bands associated to linearly bonded Pd^0-CO (2070 cm^{-1}) and to bridged bonded CO (1990 cm^{-1}) are observed on both samples, but their relative intensity is dramatically different. For the SiO_2 supported NCs, the intensity of the linearly bonded CO is significantly higher than that of the bridged form, while the situation is reversed in the case of alumina (i.e. the intensity of bridged CO species is significantly higher than the linearly bonded one). This feature indicated the predominance of the proximity of Pd^0 to Cu^0 on the surface of SiO_2 supported PdCu NPs (i.e. Cu surface enrichment), while in the case of alumina there is a surface predominance of Pd^0-Pd^0 proximity. This observation is also in line with the previous results that show an increased realloy of Cu upon the reduction for the $PtCu/SiO_2$ (40%) compared to $PdCu/Al_2O_3$ one (36%).

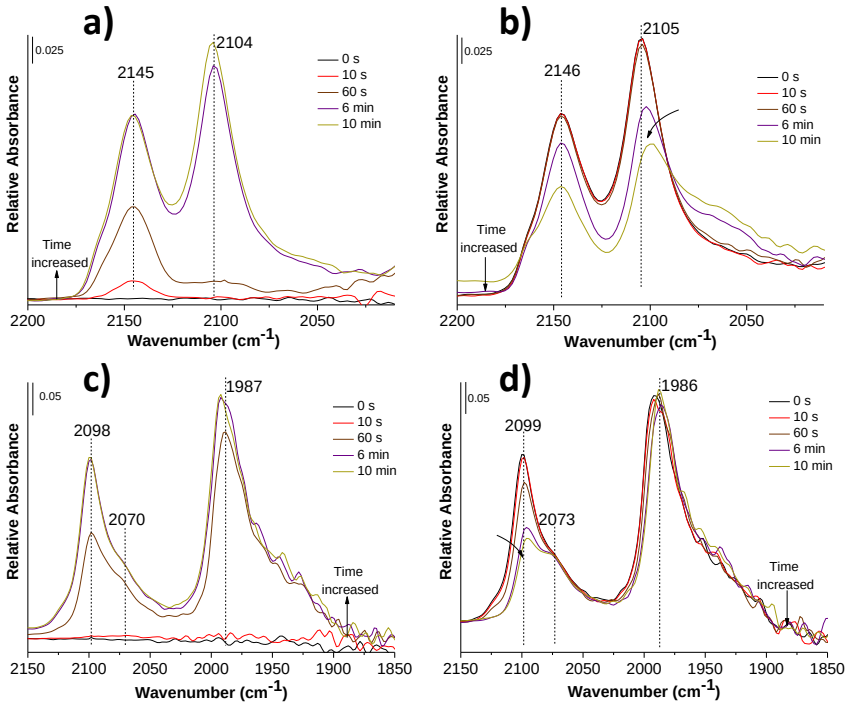

Fig. 3.35 – DRIFT spectra in the carbonyl region recorded during the adsorption (a, c) and desorption (b, d) of CO at room temperature on Pd/SiO_2 catalyst after the (a, b) oxidizing and (c, d) reduction treatments.

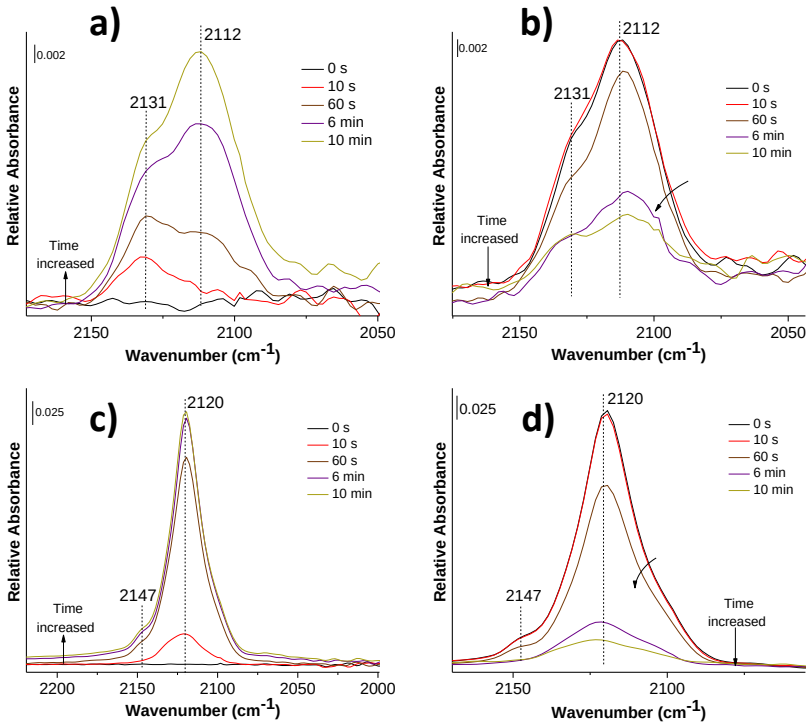

Fig. 3.36 – DRIFT spectra in the carbonyl region recorded during the adsorption (a, c) and desorption (b, d) of CO at room temperature on Cu/SiO_2 catalyst after the (a, b) oxidizing and (c, d) reduction treatments.

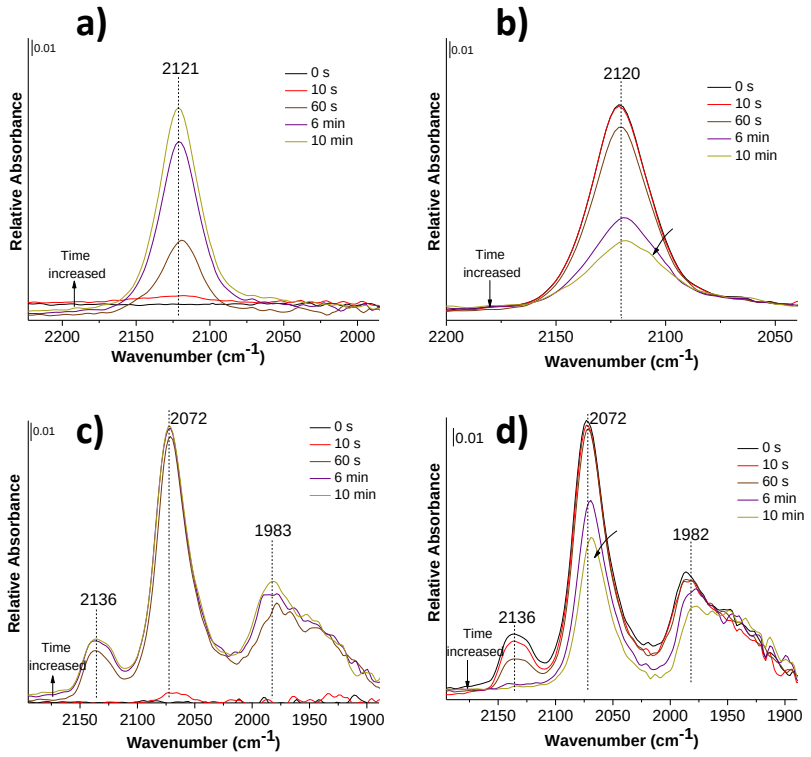

Fig. 3.37 – DRIFT spectra in the carbonyl region recorded during the adsorption (a, c) and desorption (b, d) of CO at room temperature on $PdCu/SiO_2$ catalyst after the (a, b) oxidizing and (c, d) reduction treatments.

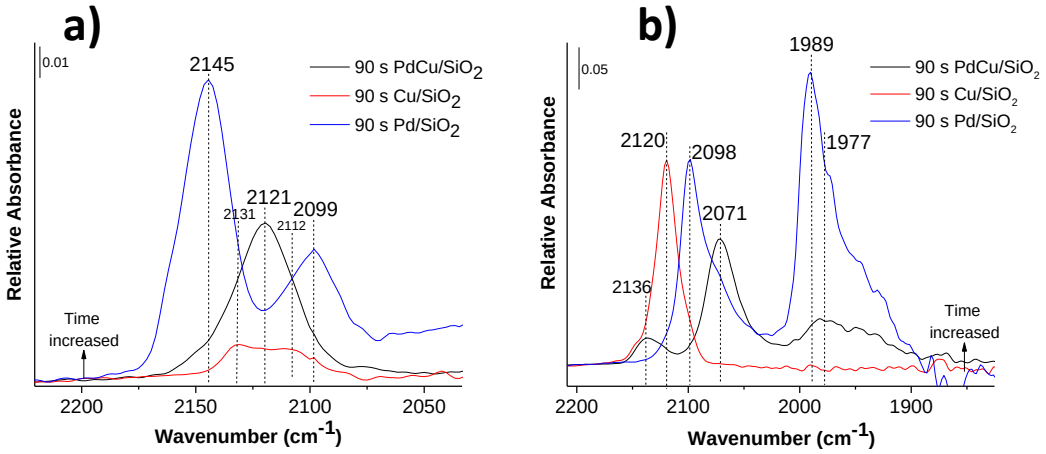

Fig. 3.38 – Comparison between the DRIFTS spectra taken after 90 s of exposure to the probe gas in the carbonyl region recorded during the adsorption of CO at room temperature on $PdCu/SiO_2$, Pd/SiO_2 and Cu/SiO_2 catalysts after the (a) oxidizing and (b) reducing pre-treatments.

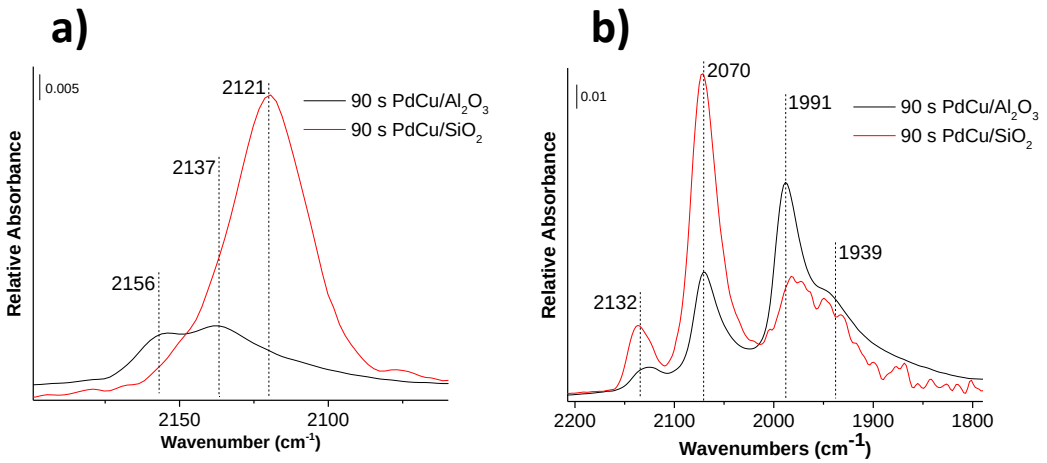

Fig. 3.39 – Comparison between the DRIFTS spectra taken after 90 s of exposure to the probe gas in the carbonyl region recorded during the adsorption of CO at room temperature on $PdCu/Al_2O_3$ and $PdCu/SiO_2$ catalysts after the (a) oxidizing and (b) reducing pre-treatments.

3.2.2 Silica Supported NCs Under CO Oxidation Reaction

As has been done for the PdCu NCs supported on alumina, the catalytic activity in the CO oxidation reaction for the silica supported NCs was evaluated after the NC exposure to the oxidative and reductive environments.

The same qualitative trend was observed for $PdCu/SiO_2$ (Fig. 3.40) when changing the pre-treatment environment. In particular, the redox treatments resulted in having approximately the same CO conversion during the heating and the cooling phases of the test reaching the maximum conversion at ~ 200 °C.

Despite the significantly different situation observed after the oxidative/reductive pre-treatments, no substantial difference in catalytic activity was observed. This result could be explained by the fact that the pre-reduced PdCu NCs are easily oxidized by the oxygen-rich reaction environment. This phenomenon could be particularly significant in the case of the SiO_2 supported NCs, due to the Cu-rich nature of their surface, as highlighted by the DRIFT data. The oxidation would then bring to the formation of a passivating CuO_x shell, thus to the same situation observed of a pre-oxidized catalyst, and consequently to the same catalytic activity.

As a confirmation of that, the reduced $PdCu/SiO_2$ catalyst was exposed to O_2 at room temperature and 100 °C and changes in the surface composition were monitored by DRIFTS (Fig. 3.41). The exposure of the reduced sample to O_2 at RT and 100 °C led to a progressive decrease in the intensity of the bands at 1978 cm^{-1} and 2072 cm^{-1} associated to Pd^0 and CO bridging on Pd^0, suggesting that these species decreased already at room temperature and almost completely disappeared at 100 °C. At the same time, the band at higher wavenumber related to CO adsorbed linearly on Cu^0 shifted to 2122 cm^{-1} and increased significantly in intensity, attributable to the formation of Cu^+-CO.

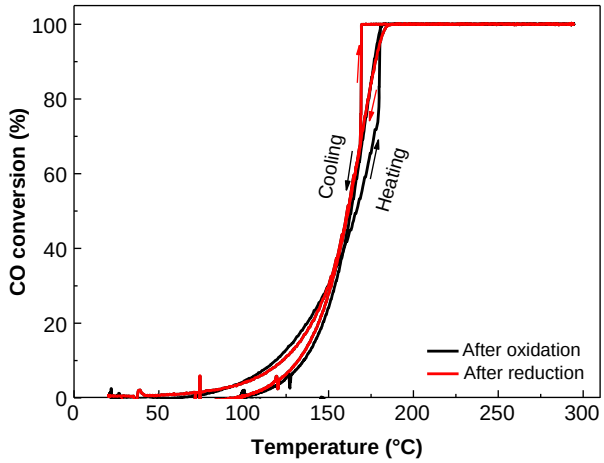

Fig. 3.40 – Catalytic activity of $PdCu/SiO_2$ catalyst in CO oxidation after the oxidizing and reducing pre-treatments during the second repeated test.

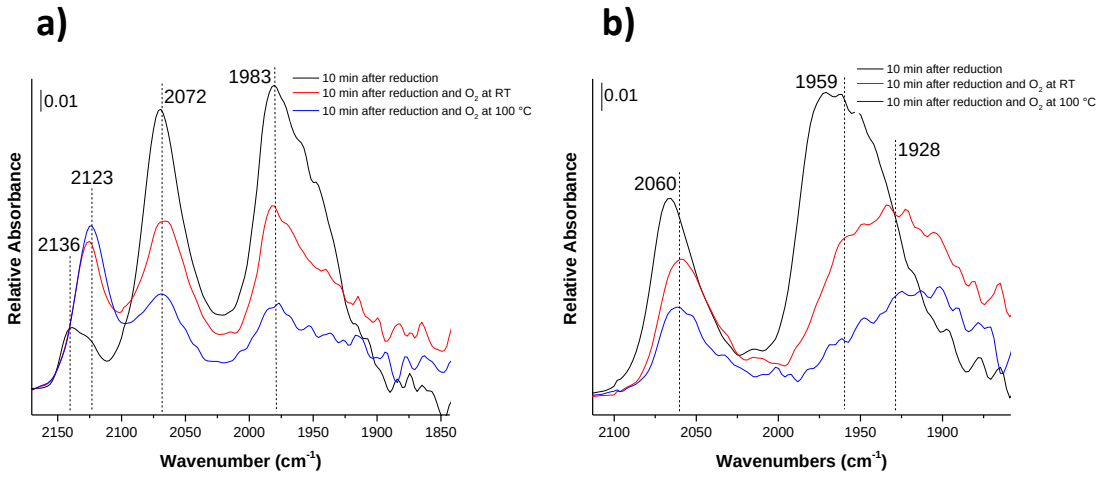

Fig. 3.41 – DRIFT spectra in the carbonyl region recorded during adsorption (a) and desorption (b) of CO at room temperature recorded after 10 min on $PdCu/SiO_2$ catalyst after reduction treatment and the exposure to O_2 flow at room temperature and 100 °C for 30 min.

As for the alumina supported PdCu NCs, also for the silica supported NCs, in the repeated tests (Fig. 3.42), the activity was fairly stable and reproducible with no significant deviations without showing memory of the previous test. Only in heating phase at the same temperature after the oxidation where a greater activity in the second and third tests was obtained due to a progressive activation of the catalyst with the maximum conversion difference of about 30% observed at 200 °C.

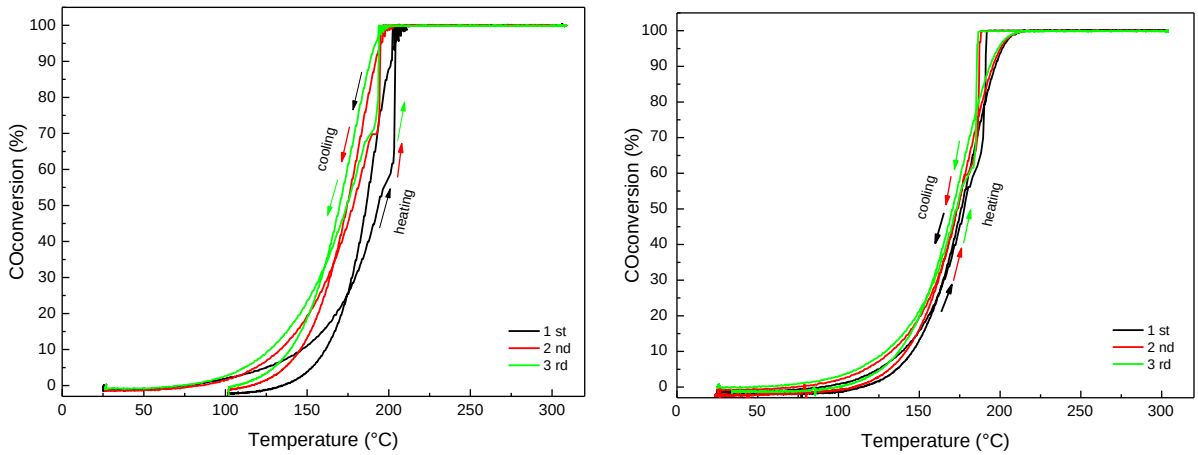

Fig. 3.42 – Catalytic activity during three reaction cycles of $PdCu/SiO_2$ catalyst in CO oxidation. after oxidizing (left) and reducing (right) pre-treatments.

Appendix A

SOLEIL Synchrotron EXAFS Fitting Data Elaboration

Table A.1 – Structural parameters obtained from the fitting of EXAFS at the Pd K-edge for the $PdCu/Al_2O_3$ catalyst (k range for the Fourier transform 2.5-12.4 $Å^{-1}$, the R-range for the fitting was 1-3.5/4 Å - dashed blue line window in the figures).

Sample	*Scattering Path*	*CN*	*R (Å)*	*σ^2 ($Å^2$)*	*R-factor*
PdCu Pd edge red D_r	***PdCuO phase***				0.015
	Pd-O1	3.32*	2.029 ± 0.005	0.002 ± 0.0004	
	Pd-Cu1	2.93 ± 0.47	3.063 ± 0.006	0.006 ± 0.0008	
	Pd-Cu2	3.95 ± 0.63	3.448 ± 0.006	0.006 ± 0.0008	

Sample	*Scattering Path*	*CN*	*R (Å)*	*σ^2($Å^2$)*	*R-factor*
PdCu Pd edge red A_r	***PdCu phase***				0.013
	Pd-Pd1	7.30 ± 0.47	2.706 ± 0.006	0.011 ± 0.0007	
	Pd-Cu1	2.66 ± 0.47	2.639 ± 0.014	0.014 ± 0.0030	
	PdCu phase				
	Pd-Pd2	2.71 ± 0.63	3.809 ± 0.006	0.011 ± 0.0007	
	Pd-Cu2	1.04 ± 0.63	3.742 ± 0.014	0.014 ± 0.0030	

Sample	*Scattering Path*	*CN*	*R (Å)*	*σ^2($Å^2$)*	*R-factor*
PdCu Pd edge oxi D_o	***PdCu phase***				0.017
	Pd-Pd1	6.53 ± 0.56	2.717 ± 0.005	0.007 ± 0.0006	
	Pd-Cu1	3.43 ± 0.56	2.667 ± 0.013	0.011 ± 0.0032	
	PdCu phase				
	Pd-Pd2	1.94 ± 0.69	3.820 ± 0.005	0.007 ± 0.0006	
	Pd-Cu2	1.04*	3.770 ± 0.013	0.011 ± 0.0032	

Sample	*Scattering Path*	*CN*	*R (Å)*	*σ^2($Å^2$)*	*R-factor*
PdCu Pd edge oxi A_o	***PdCuO phase***				0.018
	Pd-O1	3.23 ± 0.25	2.029 ± 0.008	0.005 ± 0.0008	
	Pd-Cu1	2.60 ± 1.00	3.064 ± 0.010	0.011 ± 0.0025	
	Pd-Cu2	3.47 ± 1.32	3.449 ± 0.010	0.011 ± 0.0025	

Sample	*Scattering Path*	*CN*	*R (Å)*	*σ^2($Å^2$)*	*R-factor*
PdCu Pd edge RT He	***PdCuO phase***				0.021
	Pd-O1	3.32*	2.027 ± 0.005	0.002 ± 0.0004	
	Pd-Cu1	3.52 ± 0.55	3.064 ± 0.006	0.006 ± 0.0009	
	Pd-Cu2	4.31 ± 0.72	3.449 ± 0.006	0.006 ± 0.0009	

*Parameters were fixed in the fitting and obtained as the product of N of the shell from the model and adjusted S_0^2 for the reference Pd.

Table A.2 – Structural parameters obtained from the fitting of EXAFS at the Cu K-edge for the $PdCu/Al_2O_3$ catalyst (k range for the Fourier transform 2.5-12.4 $Å^{-1}$, the R-range for the fitting was 1-3/4 Å – dashed blue line window in the figures).

Sample	***Scattering Path***	***CN***	***R (Å)***	***σ^2 ($Å^2$)***	***R-factor***
PdCu Cu edge red D_r	***PdCuO phase***				0.004
	Cu-O1	2.74 ± 0.18	1.941 ± 0.006	0.005 ± 0.0009	
	Cu-Pd1	5.47 ± 0.36	3.174 ± 0.111	0.060 ± 0.021	

Sample	***Scattering Path***	***CN***	***R (Å)***	***σ^2 ($Å^2$)***	***R-factor***
PdCu Cu edge red I_r	***Cu_2O phase***				0.008
	Cu-O1	2.29 ± 0.40	1.944 ± 0.018	0.013 ± 0.003	
	Cu-Cu1	6.88 ± 1.32	3.001 ± 0.020	0.027 ± 0.003	
	PdCu phase				
	Cu-Cu1	2.26 ± 0.36	2.651 ± 0.020	0.027 ± 0.003	
	Cu-Pd1	2.26 ± 0.36	2.657 ± 0.016	0.013 ± 0.002	

Sample	***Scattering Path***	***CN***	***R (Å)***	***σ^2 ($Å^2$)***	***R-factor***
PdCu Cu edge red A_r	***Cu_2O phase***				0.020
	Cu-O1	0.20 ± 0.2	1.868 ± 0.035	0.003 ± 0.005	
	Cu-Cu1	0.60 ± 0.6	2.936 ± 0.043	0.017 ± 0.011	
	PdCu phase				
	Cu-Cu1	1.58 ± 1.56	2.586 ± 0.043	0.017 ± 0.011	
	Cu-Pd1	2.58 ± 1.56	2.585 ± 0.056	0.015 ± 0.003	
	Cu phase				
	Cu-Cu1	2.58 ± 2.64	2.487 ± 0.043	0.017 ± 0.011	

Sample	***Scattering Path***	***CN***	***R (Å)***	***σ^2 ($Å^2$)***	***R-factor***
PdCu Cu edge oxi D_o	***Cu_2O phase***				0.018
	Cu-O1	0.49 ± 0.48	1.845 ± 0.030	0.004 ± 0.008	
	PdCu phase				
	Cu-Cu1	3.43 ± 3.48	2.663 ± 0.016	0.009 ± 0.002	
	Cu-Pd1	3.43 ± 3.48	2.595 ± 0.025	0.013 ± 0.002	

Sample	***Scattering Path***	***CN***	***R (Å)***	***σ^2 ($Å^2$)***	***R-factor***
PdCu Cu edge oxi I_o	***Cu_2O phase***				0.010
	Cu-O1	2.02 ± 2.0	1.906 ± 0.015	0.009 ± 0.003	
	Cu-Cu1	6.05 ± 1.3	3.044 ± 0.033	0.029 ± 0.004	
	PdCu phase				
	Cu-Cu1	2.94 ± 2.88	2.694 ± 0.033	0.029 ± 0.004	
	Cu-Pd1	2.94 ± 2.88	2.670 ± 0.016	0.012 ± 0.002	

Sample	*Scattering Path*	*CN*	*R (Å)*	σ^2 *(Å²)*	*R-factor*
PdCu Cu edge oxi A_o	***PdCuO phase***				0.004
	Cu-O1	2.59 ± 0.2	1.928 ± 0.007	0.008 ± 0.001	
	Cu-Pd1	5.17 ± 0.4	3.020 ± 0.063	0.052 ± 0.011	

Sample	*Scattering Path*	*CN*	*R (Å)*	σ^2 *(Å²)*	*R-factor*
PdCu Cu edge RT He	***PdCuO phase***				0.004
	Cu-O1	2.73 ± 2.4	1.943 ± 0.006	0.005 ± 0.001	
	Cu-Pd1	5.46 ± 5.4	3.185 ± 0.084	0.051 ± 0.015	

Appendix B

PSI Synchrotron EXAFS Fitting Data Elaboration

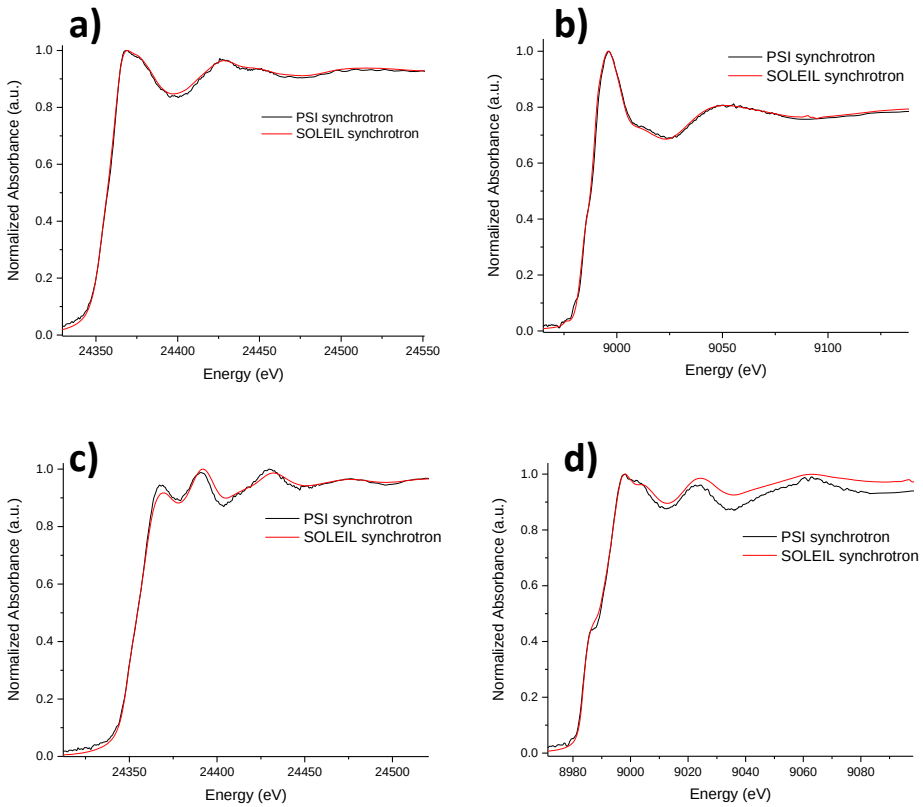

Fig. B.1 – XANES spectra of the $PdCu/Al_2O_3$ catalyst at the (a, c) Pd K-edge and (b, d) Cu K-edge after (a, b) oxidation and (c, d) reduction treatments acquired at SOLEIL and PSI synchrotrons.

Table B.1 – Structural parameters obtained from the fitting of EXAFS at the Pd K-edge for the reduced $PdCu/Al_2O_3$ catalyst during the CO oxidation reaction (k range for the Fourier transform 2.5-12.4 $Å^{-1}$, the R-range for the fitting was 1-3/4 Å – dashed blue line window in the figures).

Sample	***Scattering Path***	***CN***	***R (Å)***	***σ^2(Å^2)***	***R-factor***
PdCu Pd edge red CO react first spectrum heating ramp	***PdCu phase***				0.023
	Pd-Pd1	7.08*	2.714 ± 0.010	0.006 ± 0.001	
	Pd-Cu1	2.88 ± 0.88	2.658 ± 0.022	0.010 ± 0.005	
	PdCu phase				
	Pd-Pd2	1.02 ± 1.02	3.187 ± 0.010	0.006 ± 0.001	
	Pd-Cu2	1.04*	3.761 ± 0.022	0.010 ± 0.005	

Sample	***Scattering Path***	***CN***	***R (Å)***	***σ^2(Å^2)***	***R-factor***
PdCu Pd edge red CO react RT 300 last spectrum	***PdO phase***				0.025
	Pd-O1	2.43 ± 0.68	2.022 ± 0.025	0.003 ± 0.004	
	Pd-Pd1	2.43 ± 0.68	2.721 ± 0.035	0.007 ± 0.004	
	Pd_2O phase				
	Pd-O1	0.53 ± 0.36	1.790 ± 0.025	0.003 ± 0.004	
	Pd-Pd1	1.60 ± 1.08	3.470 ± 0.035	0.007 ± 0.004	
	PdCu phase				
	Pd-Pd1	0.60 *	2.415 ± 0.035	0.008 ± 0.004	
	Pd-Cu1	0.60 *	2.839 ± 0.038	0.003*	

Sample	*Scattering Path*	*CN*	*R (Å)*	*σ^2(Å^2)*	*R-factor*
PdCu Pd edge red CO react 100 cooling last spectrum	***PdO phase***				0.010
	Pd-O1	2.64 ± 0.32	2.004 ± 0.013	0.005 ± 0.002	
	Pd-Pd1	2.64 ± 0.32	2.730 ± 0.020	0.005 ± 0.001	
	Pd_2O phase				
	Pd-O1	0.62 ± 0.16	1.737 ± 0.013	0.005 ± 0.002	
	Pd-Pd1	1.87 ± 0.48	3.380 ± 0.020	0.005 ± 0.001	
	PdCu phase				
	Pd-Pd1	0.36 *	2.384 ± 0.020	0.005 ± 0.001	
	Pd-Cu1	0.36 *	2.752 ± 0.111	0.003 *	

*Parameters were fixed in the fitting and obtained as the product of N of the shell from the model and adjusted S_0^2 for the reference Pd.

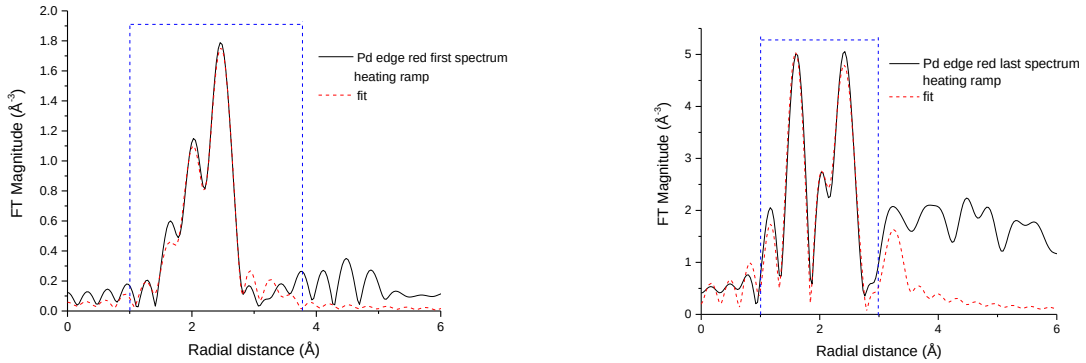

Fig. B.2 – FT magnitude with the best fit (dashed lines) of fitted EXAFS spectrum of the reduced PdCu/Al_2O_3 catalyst collected (a) at the beginning and (b) at the end (300 °C) of the heating ramp during the CO oxidation reaction at the Pd K-edge.

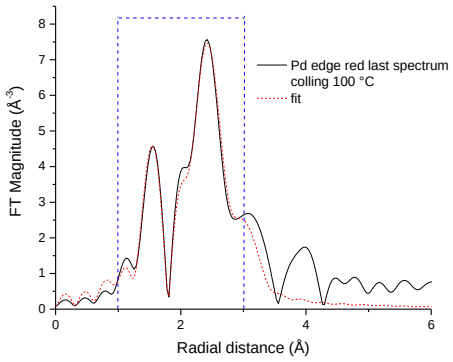

Fig. B.3 – FT magnitude with the best fit (dashed lines) of fitted EXAFS spectrum of the reduced PdCu/Al_2O_3 catalyst collected at the end of the cooling ramp at 100 °C during the CO oxidation reaction at the Pd K-edge.

Table B.2 – Structural parameters obtained from the fitting of EXAFS at the Cu K-edge for the reduced PdCu/Al_2O_3 catalyst during the CO oxidation reaction (k range for the Fourier transform 2.5-12.4 Å^{-1}, the R-range for the fitting was 1-3/4 Å - dashed blue line window in the figures).

Sample	*Scattering Path*	*CN*	*R (Å)*	*σ^2(Å^2)*	*R-factor*
PdCu Cu edge red CO react first spectrum heating ramp	***Cu_2O phase***				0.008
	Cu-O1	0.83*	1.870 ± 0.014	0.005 ± 0.002	
	Cu-Cu1	2.48*	2.975 ± 0.015	0.017 ± 0.002	
	PdCu phase				
	Cu-Cu1	3.08*	2.625 ± 0.015	0.017 ± 0.002	
	Cu-Pd1	3.17 ± 0.03	2.628 ± 0.010	0.009 ± 0.001	

Sample	*Scattering Path*	*CN*	*R (Å)*	*σ^2(Å^2)*	*R-factor*
PdCu Cu edge red CO react RT 300 last spectrum	***Cu_2O phase***				0.024
	Cu-O1	2.55 *	1.992 ± 0.019	0.006 ± 0.002	
	Cu-Cu1	7.66 *	3.082 ± 0.056	0.036 ± 0.009	
	CuO phase				
	Cu-O1	0.40 *	2.512 ± 0.019	0.006 ± 0.002	
	Cu-Cu1	0.79 *	3.071 ± 0.036	0.036 ± 0.009	
	PdCu phase				
	Cu-Cu1	1.52 *	2.673 ± 0.056	0.035 ± 0.009	
	Cu-Pd1	1.52 *	2.673 ± 0.020	0.008 ± 0.001	

Sample	*Scattering Path*	*CN*	*R (Å)*	*σ^2(Å^2)*	*R-factor*
PdCu Cu edge red CO react 100 cooling last spectrum	***Cu_2O phase***				0.020
	Cu-O1	2.56 *	1.973 ± 0.024	0.005 ± 0.002	
	Cu-Cu1	7.67 *	2.824 ± 0.183	0.058 ± 0.036	
	CuO phase				
	Cu-O1	1.21 ± 0.30	2.251 ± 0.024	0.005 ± 0.002	
	Cu-Cu1	2.32 ± 0.60	2.858 ± 0.183	0.064 ± 0.036	
	PdCu phase				
	Cu-Cu1	0.12 *	2.474 ±	0.058 ± 0.036	
	Cu-Pd1	0.12 *	2.597 ±	0.007 ± 0.001	

*Parameters were fixed in the fitting and obtained as the product of N of the shell from the model and adjusted S_0^2 for the reference Cu.

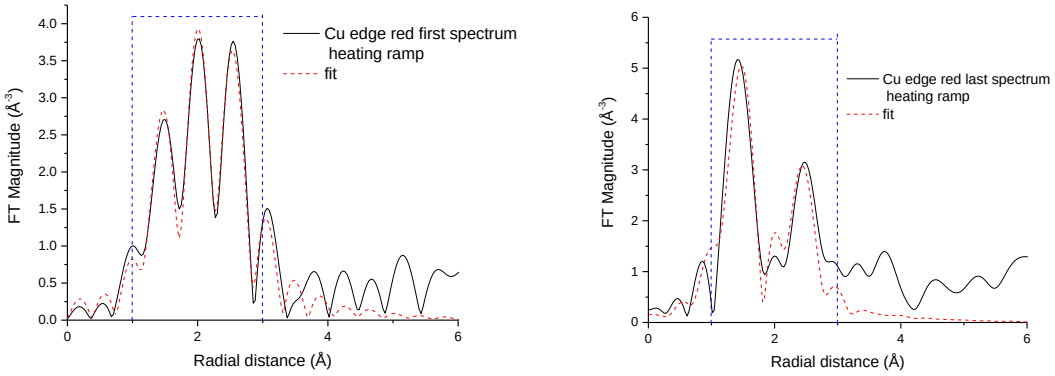

Fig. B.4 – FT magnitude with the best fit (dashed lines) of fitted EXAFS spectrum of the reduced $PdCu/Al_2O_3$ catalyst collected (a) at the beginning and (b) at the end (300 °C) of the heating ramp during the CO oxidation reaction at the Cu K-edge.

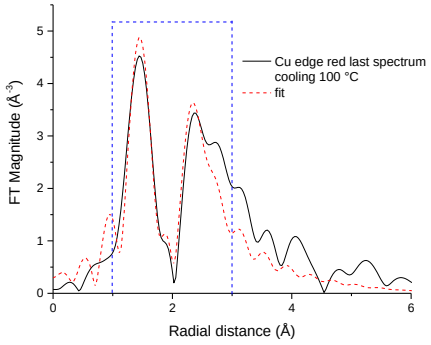

Fig. B.5 – FT magnitude with the best fit (dashed lines) of EXAFS spectrum of the reduced $PdCu/Al_2O_3$ catalyst collected at the end of the cooling ramp at 100 °C during the CO oxidation reaction at the Cu K-edge.

Table B.3 – Structural parameters obtained from the fitting of EXAFS at the Pd K-edge for the oxidized $PdCu/Al_2O_3$ catalyst during the CO oxidation reaction (k range for the Fourier transform 2.5-12.4 $Å^{-1}$, the R-range for the fitting was 1-3/4 Å - dashed blue line window in the figures).

Sample	*Scattering Path*	*CN*	*R (Å)*	*σ^2(Å^2)*	*R-factor*
PdCu Pd edge oxi CO react first spectrum heating ramp	***PdO phase***				0.014
	Pd-O1	2.65 ± 0.28	2.033 ± 0.007	0.0003 ± 0.001	
	Pd-Pd1	2.65 ± 0.28	3.056 ± 0.008	0.007 ± 0.001	
	Pd_2O phase				
	Pd-O1	0.39 ± 0.15	1.867 ± 0.007	0.0003 ± 0.001	
	Pd-Pd1	1.18 ± 0.44	3.046 ± 0.008	0.007 ± 0.001	
	PdCu phase				
	Pd-Pd1	0.20 ± 0.12	2.683 ± 0.008	0.007 ± 0.001	
	Pd-Cu1	0.20 ± 0.12	2.600 ± 0.034	0.001*	

Sample	*Scattering Path*	*CN*	*R (Å)*	*σ^2(Å^2)*	*R-factor*
PdCu Pd edge oxi CO react RT 300 last spectrum	***PdO phase***				0.010
	Pd-O1	1.34 ± 0.28	2.035 ± 0.026	0.004 ± 0.001	
	Pd-Pd1	1.34 ± 0.28	2.726 ± 0.014	0.002 ± 0.001	
	Pd_2O phase				
	Pd-O1	0.71 ± 0.26	1.890 ± 0.026	0.004 ± 0.001	
	Pd-Pd1	0.14 ± 0.80	3.386 ± 0.014	0.002 ± 0.001	
	PdCu phase				
	Pd-Pd1	0.14 ± 0.10	2.352 ± 0.034	0.002 ± 0.001	
	Pd-Cu1	0.14 ± 0.10	2.747 ± 0.030	0.003 *	

Sample	*Scattering Path*	*CN*	*R (Å)*	*σ^2(Å^2)*	*R-factor*
PdCu Pd edge oxi CO react 100 cooling last spectrum	***PdO phase***				0.022
	Pd-O1	2.22 ± 0.64	2.027 ± 0.022	0.003 ± 0.003	
	Pd-Pd1	2.22 ± 0.64	2.734 ± 0.022	0.006 ± 0.003	
	Pd_2O phase				
	Pd-O1	0.55 ± 0.35	1.707 ± 0.060	0.003 ± 0.003	
	Pd-Pd1	1.66 ± 1.04	3.410 ±0.122	0.006 ±0.003	
	PdCu phase				
	Pd-Pd1	0.12 *	2.360 ± 0.122	0.006 ± 0.003	
	Pd-Cu1	0.12 *	3.091 ± 0.068	0.005 ± 0.004	

*Parameters were fixed in the fitting and obtained as the product of N of the shell from the model and adjusted S_0^2 for the reference Pd.

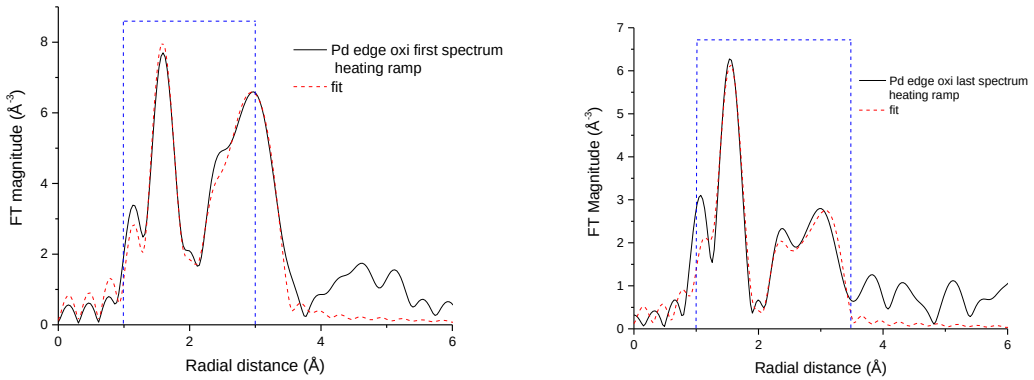

Fig. B.6 – FT magnitude with the best fit (dashed lines) of EXAFS spectrum of the oxidized $PdCu/Al_2O_3$ catalyst collected (a) at the beginning and (b) at the end (300 °C) of the heating ramp during the CO oxidation reaction at the Pd K-edge.

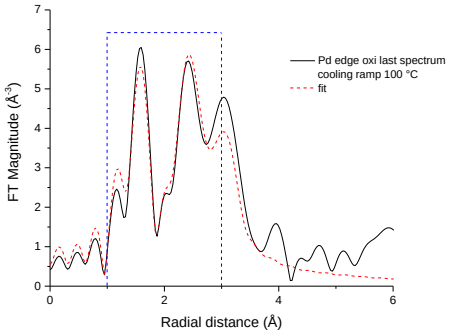

Fig. B.7 – FT magnitude with the best fit (dashed lines) of EXAFS spectrum of the oxidized $PdCu/Al_2O_3$ catalyst collected at the end of the cooling ramp at 100 °C during the CO oxidation reaction at the Pd K-edge.

Table B.4 – Structural parameters obtained from the fitting of EXAFS at the Pd K-edge for the oxidized $PdCu/Al_2O_3$ catalyst during the CO oxidation reaction (k range for the Fourier transform 2.5-12.4 $Å^{-1}$, the R-range for the fitting was 1-3/4 Å - dashed blue line window in the figures).

Sample	*Scattering Path*	*CN*	*R (Å)*	*σ^2(Å^2)*	*R-factor*
PdCu Cu edge oxi CO react first spectrum heating ramp	***Cu_2O phase***				0.010
	Cu-O1	2.75 ± 1.00	1.954 ± 0.039	0.007 ± 0.005	
	Cu-Cu1	8.24 ± 3.00	3.038 ± 0.265	0.057 ± 0.086	
	CuO phase				
	Cu-O1	0.10 ± 0.98	2.232 ± 0.039	0.007 ± 0.005	
	Cu-Cu1	0.16 ± 1.96	3.037 ± 0.265	0.058 ± 0.086	
	PdCu phase				
	Cu-Cu1	1.20 ± 1.08	2.689 ± 0.265	0.057 ± 0.086	
	Cu-Pd1	1.20 ± 1.08	2.593 ± 0.047	0.003 ± 0.092	

Sample	*Scattering Path*	*CN*	*R (Å)*	*σ^2(Å^2)*	*R-factor*
PdCu Cu edge oxi CO react RT 300 last spectrum	***Cu_2O phase***				0.010
	Cu-O1	2.93 ± 0.64	1.930 ± 0.023	0.008 ± 0.003	
	Cu-Cu1	8.78 ± 0.64	3.098 ± 0.053	0.033 ± 0.013	
	CuO phase				
	Cu-O1	0.30*	2.207 ± 0.023	0.008 ± 0.003	
	Cu-Cu1	0.60*	0.053 ± 0.053	0.034 ± 0.013	
	PdCu phase				
	Cu-Cu1	0.73*	2.748 ± 0.053	0.033 ± 0.013	
	Cu-Pd1	0.73 *	2.700 ± 0.025	0.006 ± 0.007	

Sample	*Scattering Path*	*CN*	*R (Å)*	*σ^2(Å^2)*	*R-factor*
PdCu Cu edge oxi CO react 100 cooling last spectrum	***Cu_2O phase***				0.016
	Cu-O1	2.91 ± 0.80	1.958 ± 0.034	0.008 ± 0.004	
	Cu-Cu1	9.10 ± 0.80	3.163 ± 0.16	0.040 ± 0.036	
	CuO phase				
	Cu-O1	0.30*	2.235 ± 0.034	0.008 ± 0.004	
	Cu-Cu1	0.60*	3.156 ± 0.16	0.041 ± 0.036	
	PdCu phase				
	Cu-Cu1	0.57*	2.813 ± 0.16	0.040 ± 0.036	
	Cu-Pd1	0.57*	2.725 ± 0.050	0.007 ± 0.017	

*Parameters were fixed in the fitting and obtained as the product of N of the shell from the model and adjusted S_0^2 for the reference Cu.

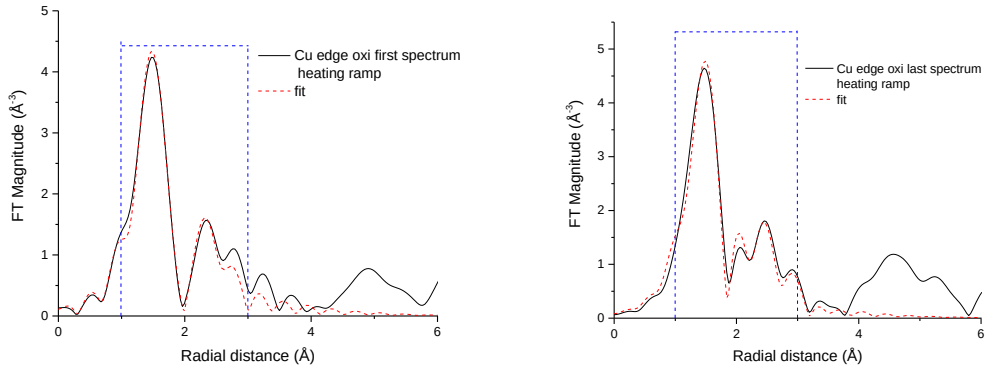

Fig. B.7 – FT magnitude with the best fit (dashed lines) of EXAFS spectrum of the oxidized $PdCu/Al_2O_3$ catalyst collected (a) at the beginning and (b) at the end (300 °C) of the heating ramp during the CO oxidation reaction at the Cu K-edge.

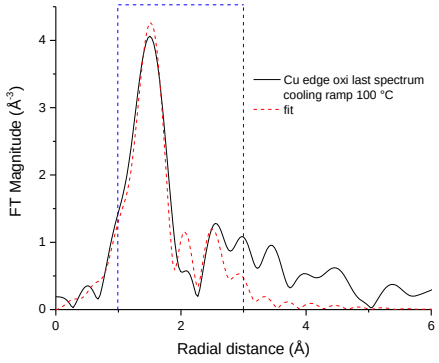

Fig. B.8 – FT magnitude with the best fit (dashed lines) of EXAFS spectrum of the oxidized $PdCu/Al_2O_3$ catalyst collected (a) at the end of the cooling ramp at 100 °C during the CO oxidation reaction at the Cu K-edge.

References

1. Ma, T.; Fu, Q.; Su, H. Y.; Liu, H. Y.; Cui, Y.; Wang, Z.; Mu, R. T.; Li, W. X.; Bao, X. H., Reversible structural modulation of Fe–Pt bimetallic surfaces and its effect on reactivity. *ChemPhysChem* 2009, 10, 1013-1016.

2. Nikolaev, S.; Golubina, E.; Shilina, M., The effect of H_2 treatment at 423–573K on the structure and synergistic activity of Pd–Cu alloy catalysts for low-temperature CO oxidation. *Appl Catal B* 2017, 208, 116-127.

3. Alayoglu, S.; Nilekar, A. U.; Mavrikakis, M.; Eichhorn, B., Ru–Pt core–shell nanoparticles for preferential oxidation of carbon monoxide in hydrogen. *Nature Mater* 2008, 7, 333.

4. Mu, R.; Guo, X.; Fu, Q.; Bao, X., Oscillation of surface structure and reactivity of PtNi bimetallic catalysts with redox treatments at variable temperatures. *J Phys Chem C* 2011, 115, 20590-20595.

5. Najafishirtari, S.; Brescia, R.; Guardia, P.; Marras, S.; Manna, L.; Colombo, M., Nanoscale transformations of alumina-supported AuCu ordered phase nanocrystals and their activity in CO oxidation. *ACS Catal* 2015, 5, 2154-2163.

6. Destro, P.; Kokumai, T. M.; Scarpellini, A.; Pasquale, L.; Manna, L.; Colombo, M.; Zanchet, D., The crucial role of the support in the transformations of bimetallic nanoparticles and catalytic performance. *ACS Catal* 2018, 8, 2, 1031-1037.

7. Christensen, G. L.; Langell, M. A., Characterization of copper palladium oxide solid solutions by X-ray diffraction, X-ray photoelectron spectroscopy, and auger electron spectroscopy. *J Phys Chem C* 2013, 117, 7039-7049.

8. Subramanian, P.; Laughlin, D., Cu-Pd (copper-palladium). *J Phase Equilibria* 1991, 12, 231-243.

9. Hadjiivanov, K. I.; Vayssilov, G. N., Characterization of oxide surfaces and zeolites by carbon monoxide as an IR probe molecule. *Adv Catal* 2002, 47, 307-511.

10. Skoda, F.; Astier, M. P.; Pajonk, G. M.; Primet, M., Surface characterization of palladium-copper bimetallic catalysts by FTIR spectroscopy and test reactions. *Catal Lett* 1994, 29, 159-168.

11. Prestat, E.; Kulzick, M. A.; Dietrich, P. J.; Smith, M. M.; Tien, M. E. P.; Burke, M. G.; Haigh, S. J.; Zaluzec, N. J., In Situ industrial bimetallic catalyst characterization using scanning transmission electron microscopy and X-ray absorption spectroscopy at one atmosphere and elevated temperature. *ChemPhysChem* 2017, 18, 2151-2156.

12. Bazin, D.; Rehr, J., Limits and advantages of X-ray absorption near edge structure for nanometer scale metallic clusters. *J Phys Chem B* 2003, 107, 12398-12402.

13. Kelly, S.; Hesterberg, D.; Ravel, B., Analysis of soils and minerals using X-ray absorption spectroscopy. *Methods of soil analysis. SSSA Book Series 5* 2008, 5, 387-464.

14. Cassinelli, W. H.; Martins, L.; Passos, A. R.; Pulcinelli, S. H.; Santilli, C. V.; Rochet, A.; Briois, V., Multivariate curve resolution analysis applied to time-resolved synchrotron X-ray Absorption Spectroscopy monitoring of the activation of copper alumina catalyst. *Catal Today* 2014, 229, 114-122.

15. Marakatti, V. S.; Sarma, S. C.; Joseph, B.; Banerjee, D.; Peter, S. C., Synthetically tuned atomic ordering in PdCu nanoparticles with enhanced catalytic activity toward solvent-free benzylamine oxidation. *ACS Appl Mater Inter* 2017, 9, 3602-3615.

16. Sato, A. G.; Volanti, D. P.; de Freitas, I. C.; Longo, E.; Bueno, J. M. C., Site-selective ethanol conversion over supported copper catalysts. *Catal Commun* 2012, 26, 122-126.

17. Staniuk, M.; Zindel, D.; Van Beek, W.; Hirsch, O.; Kränzlin, N.; Niederberger, M.; Koziej, D., Matching the organic and inorganic counterparts during nucleation and growth of copper-based nanoparticles–in situ spectroscopic studies. *CrystEngComm* 2015, 17, 6962-6971.

18. Zhan, W.; Wang, J.; Wang, H.; Zhang, J.; Liu, X.; Zhang, P.; Chi, M.; Guo, Y.; Guo, Y.; Lu, G., Crystal structural effect of AuCu alloy nanoparticles on catalytic CO oxidation. *J Am Chem Soc* 2017, 139, 26, 8846-8854.

19. Slavinskaya, E.; Stonkus, O.; Gulyaev, R.; Ivanova, A.; Zaikovskii, V.; Kuznetsov, P.; Boronin, A., Structural and chemical states of palladium in Pd/Al_2O_3 catalysts under self-sustained oscillations in reaction of CO oxidation. *Appl Catal A* 2011, 401, 83-97.

20. Zhou, Y.; Wang, Z.; Liu, C., Perspective on CO oxidation over Pd-based catalysts. *Catal Sci Technol* 2015, 5, 69-81.

21. Anderson, J. A.; Fernández-García, M.; Haller, G. L., Surface and bulk characterisation of metallic phases present during CO hydrogenation over Pd–Cu/KL zeolite catalysts. *J Catal* 1996, 164, 477-483.

22. Bradley, J. S.; Hill, E. W.; Chaudret, B.; Duteil, A., Surface chemistry on colloidal metals. Reversible adsorbate-induced surface composition changes in colloidal palladium-copper alloys. *Langmuir* 1995, 11, 693-695.

23. Khanra, B. C.; Menon, M., Role of adsorption on surface composition of Pd–Cu nanoparticles. *Physica B* 1999, 270, 307-312.

24. Fernández-Garcıa, M.; Martinez-Arias, A.; Belver, C.; Anderson, J.; Conesa, J.; Soria, J., Behavior of palladium–copper catalysts for CO and NO elimination. *J Catal* 2000, 190, 387-395.

25. McCue, A. J.; Anderson, J. A., CO induced surface segregation as a means of improving surface composition and enhancing performance of CuPd bimetallic catalysts. *J Catal* 2015, 329, 538-546.

26. Calvin, S., *XAFS for Everyone*. CRC Press: 2013.

27. Kappen, P.; Grunwaldt, J.-D.; Hammershøi, B. S.; Tröger, L.; Clausen, B. S., The state of Cu promoter atoms in high-temperature shift catalysts. An in situ fluorescence XAFS study. *J Catal* 2001, 198, 56-65.

28. Alayon, E. M. C.; Nachtegaal, M.; Bodi, A.; van Bokhoven, J. A., Reaction conditions of methane-to-methanol conversion affect the structure of active copper sites. *ACS Catal* 2013, 4, 16-22.

29. Nayak, C.; Bhattacharyya, D.; Jha, S. N.; Sahoo, N. K., In Situ XAS study on growth of PVP-stabilized Cu nanoparticles. *ChemistrySelect* 2018, 3, 7370-7377.

30. Davydov, A. A.; Sheppard, N., *Molecular spectroscopy of oxide catalyst surfaces*. Vol. 690 Wiley: 2003.

31. Millar, G. J.; Rochester, C. H.; Waugh, K. C., Infrared study of CO adsorption on reduced and oxidised silica-supported copper catalysts. *J Chem Soc, Faraday Trans* 1991, 87, 1467-1472.

32. Balkenende, A.; Van der Grift, C.; Meulenkamp, E.; Geus, J., Characterization of the surface of a Cu/SiO_2 catalyst exposed to NO and CO using IR spectroscopy. *Appl Surf Sci* 1993, 68, 161-171.

33. Sitthisa, S.; Pham, T.; Prasomsri, T.; Sooknoi, T.; Mallinson, R. G.; Resasco, D. E., Conversion of furfural and 2-methylpentanal on Pd/SiO_2 and $Pd–Cu/SiO_2$ catalysts. *J Catal* 2011, 280, 17-27.

34. Noronha, F. B.; Schmal, M.; Primet, M.; Frety, R., Characterization of palladium-copper bimetallic catalysts supported on silica and niobia. *Appl Catal* 1991, 78, 125-139.

35. Moscu, A.; Schuurman, Y.; Meunier, F. C., Recent progresses on the use of supported bimetallic catalysts for the preferential oxidation of CO (PROX). *Catal* 2016, 28, 237-267.

Chapter 4

Structural Rearrangements of PtCu NCs Under Different Conditions

To further extend the analysis of the role of noble metal and support in the transformation of noble-metal-Cu bimetallic NCs, PtCu NCs supported on alumina and silica were fully characterized after oxidizing and reducing treatments by a number of techniques such as STEM-EDX elemental mapping, SAED, CO DRIFT spectroscopy, and XAFS. Additionally, the relation between the change of the NC structure driven by the mentioned environments and the catalytic activity in CO oxidation reaction was also addressed.

4.1 Characterization of Alumina Supported Catalysts

4.1.1 NCs Under Oxidative and Reductive Treatments

To investigate the influence of the oxidative and reductive treatments on the structural rearrangement of the PtCu NCs supported on alumina, the catalyst was characterized by HAADF-STEM and SAED. Overview HAADF-STEM images of the catalyst in the mentioned conditions are shown in Fig. 4.1. The PtCu NCs resulted to be homogeneously distributed on the support with no NC morphology change after the two treatments; their average size distributions remained unchanged and equal to that of the as-synthesized NCs (4.9 ± 1.8 nm). Specifically, final average size distribution of 4.7 ± 0.7 nm (based on 201 particles) was found after oxidation and of 4.9 ± 0.6 nm (on 151 particles) after reduction.

The SAED patterns of the $PtCu/Al_2O_3$ after oxidation (Fig. 4.2c) showed diffraction peaks characteristic of a cubic structure, corresponding to Pt; no Cu or CuO_x peaks were detected. Coupling this information with the EDX maps suggested that copper was highly dispersed onto the support as an amorphous phase or as finely dispersed phase, as showed by the EDX maps (Fig. 4.2a). After reduction, the peak positions were shifted towards higher 2θ angles compared to those after oxidation and a decreased lattice spacing was indicative of progressive incorporation of Cu in the alloy (12 atomic % of Cu from Vegard's law) without fully restoring of the initial alloy. The Cu value estimated by Vegard's law was underestimated compared to that obtained from measurement of the composition by EDX (Fig. 4.2b), probably due to the presence of amorphous Cu no detectable by SAED or to the non-applicability of this law to the PtCu NC systems. Indeed, it is important to note that, although the Vegard's law is strictly valid

for homogeneous alloy and unstrained particles, it has been applied to estimate the composition of the de-alloyed and strained NCs.[1, 2]

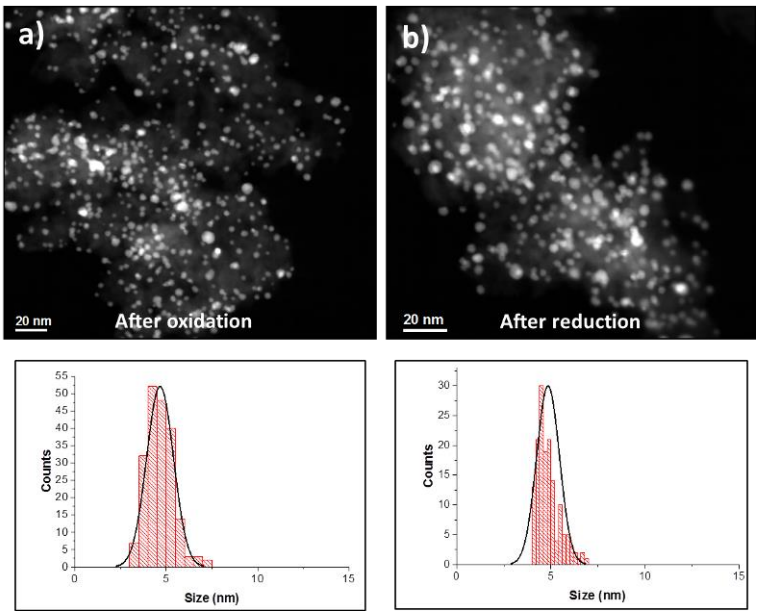

Fig. 4.1 – HAADF-STEM images of $PtCu/Al_2O_3$ catalyst after (a) oxidizing and (b) reducing treatments with the corresponding size distribution histogram.

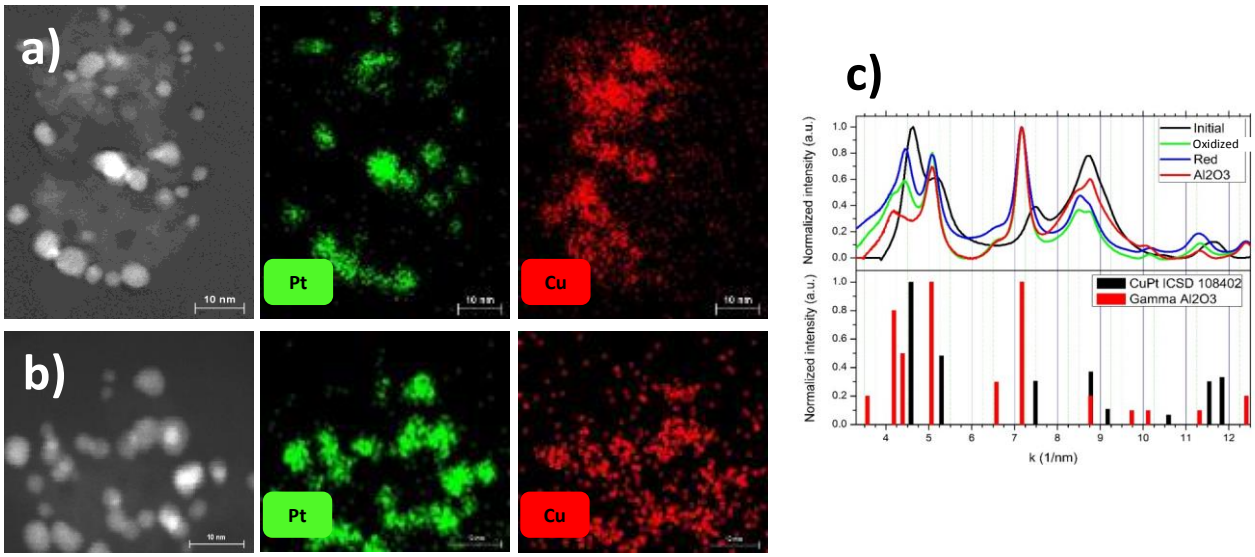

Fig. 4.2 – HAADF-STEM images of 2 wt.% $PtCu/Al_2O_3$ catalyst and corresponding quantitative EDX maps for Pt and Cu after (a) oxidizing and (b) reducing treatments; (c) azimuthally integrated, background-subtracted SAED patterns after oxidation and reduction in comparison to PtCu NCs (reference patterns: Pt_1Cu_1 ICSD 108402 (black line), γ-Al_2O_3 ICSD 100425 (red line)).

In situ DRIFT spectroscopy studies of the CO adsorption was implemented to identify the NC surface morphology after the two treatments (Figs. 4.3 and 4.4). The complete NC dealloy under oxidation and a partially restore of the starting NCs was confirmed by DRIFTS measurements (Fig. 4.4). Indeed, CO adsorbed on the oxidized $PtCu/Al_2O_3$ catalyst (Fig. 4.4a and b) gave main absorption bands at 2090 cm^{-1} and a second weak band at 2122 cm^{-1}. The former was attributed

to the linear CO species on Pt atoms[3] and the latter to those on Cu^+ atoms,[4] in agreement with that obtained for monometallic Pt (Fig. 4.3) and Cu (Fig. 3.7) catalysts. The spectra of the catalyst after reduction (Fig. 4.4c and d) exhibited main CO bands at about 2126 and 2066 cm^{-1} with a shoulder at 2013 cm^{-1}. CO adsorption on metallic platinum (Fig. 4.3) led to frequency vibrational stretches in the range 2080−2098 cm^{-1} assigned to the CO linearly adsorbed on low-index planes (terraces) of the particles, while the lower ones (2060−2075 cm^{-1}) to the oscillation of CO molecules linearly adsorbed on Pt steps, edges, and corner.[5] In this way, the band around 2066 cm^{-1} was attributed to this latter species. The high-energy absorption band at 2126 cm^{-1} resulted from CO bound to Cu^0 even if the position of this band would be more consistent with Cu^+ rather than Cu^0.[6] The blue-shift of about 40 cm^{-1} of the frequency of CO on Cu was attributed to the modification of the electronic properties upon alloying with Pt, related to the charge transfer from Cu to Pt atoms. Indeed, this effect enhanced the electron density on Pt atoms ensuring that, during the evacuation, the adsorption of CO on Pt was much strong than that on Cu.[7] Furthermore, the evidence that the Pt and Cu were atomically mixed in the catalyst was provided by two effects visible in the spectra: the first one was associated with the appearance of the band at 2013 cm^{-1} related to CO bridged between Pt and Cu atoms; the second was visible in the spectra during the evacuation (Fig. 4.4d) in which the intensity of the Pt^0-CO band increased at the expense of that of Cu^0-CO due to an energy intensity redistribution effect.[8]

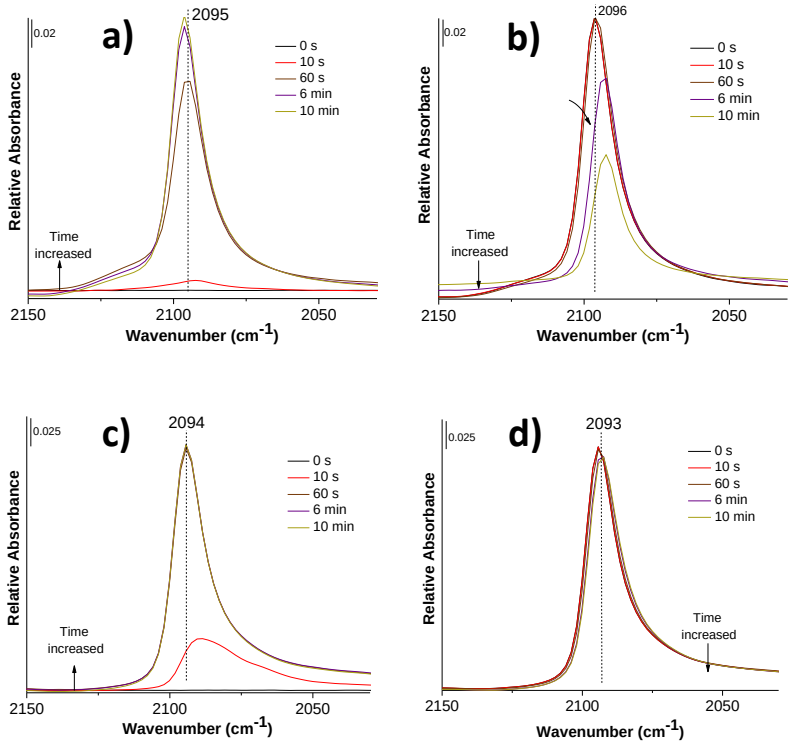

Fig. 4.3 – DRIFT spectra in the carbonyl region recorded during the adsorption (a, c) and desorption (b, d) of CO at room temperature on Pt/Al_2O_3 catalyst after the (a, b) oxidizing and (c, d) reduction treatments.

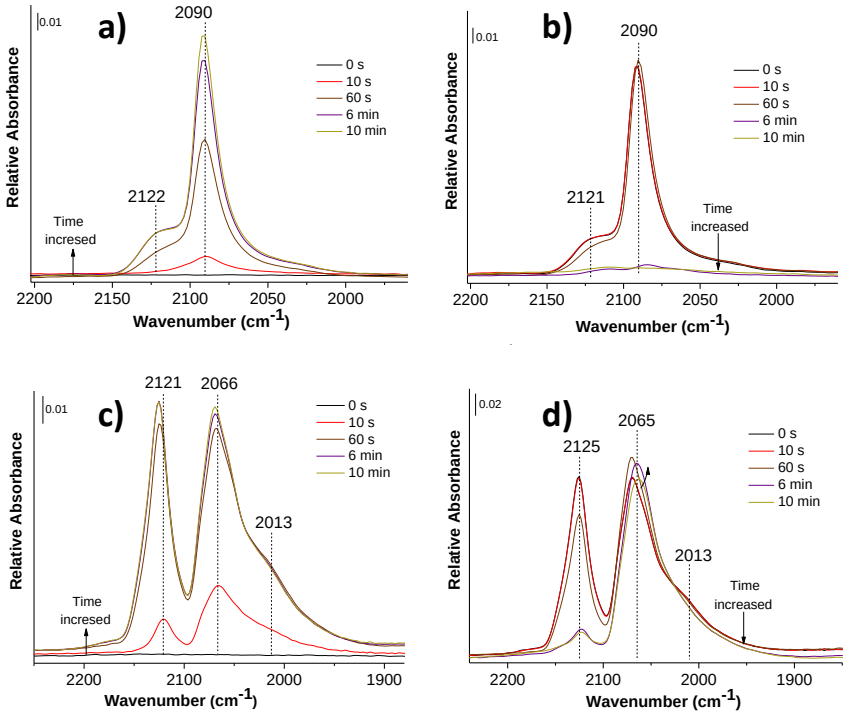

Fig. 4.4 – DRIFT spectra in the carbonyl region recorded during the adsorption (a, c) and desorption (b, d) of CO at room temperature on $PtCu/Al_2O_3$ catalyst after the (a, b) oxidizing and (c, d) reduction treatments.

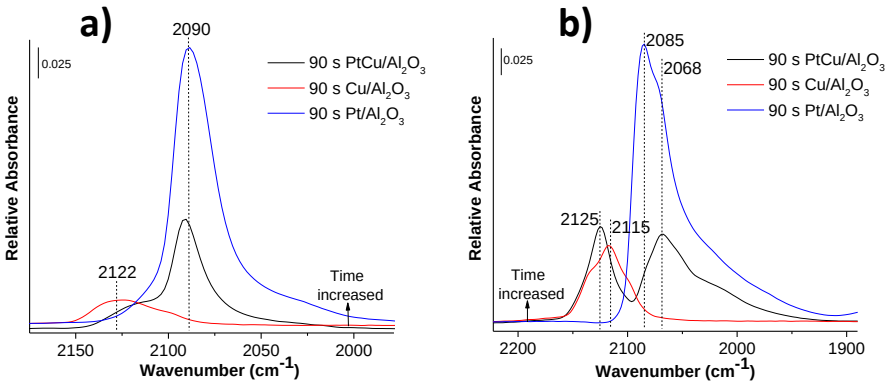

Fig. 4.5 – Comparison between the DRIFTS spectra taken after 90 s of exposure to the probe gas in the carbonyl region recorded during the adsorption of CO at room temperature on $PtCu/Al_2O_3$, Pt/Al_2O_3 and Cu/Al_2O_3 catalysts after the (a) oxidizing and (b) reducing pre-treatment.

A deeper structural analysis was performed by means of X-ray absorption spectroscopy acquiring XAFS spectra at different absorption edges. In this regard, the transformation of $PtCu/Al_2O_3$ system was *in situ* monitored for Pt and Cu elements while the catalyst was subjected to the reducing and oxidizing treatments.

In analogy with what done in Chapter 3, the MCR-ALS procedure was applied to the XAFS dataset, in combination with principal component analysis (PCA).

An initial XAFS spectrum was collected in He as the starting point of the measurement for the $PtCu/Al_2O_3$ sample after calcination. The Pt $_{LIII}$ and Cu K-edges XANES spectra were similar to those of PtO and CuO standards (Fig. 4.6a and b). The fitting of the EXAFS part at both edges

reported in Fig. 4.6c and d along with the structural parameters in Appendix A, confirmed the formation of PtO, with a major contribution of metallic Pt, and CuO phases. This was consistent with the oxidation occurring during the calcination step, necessary for the removal of the organic ligands from the NC surface, during which a NC dealloy occurred.

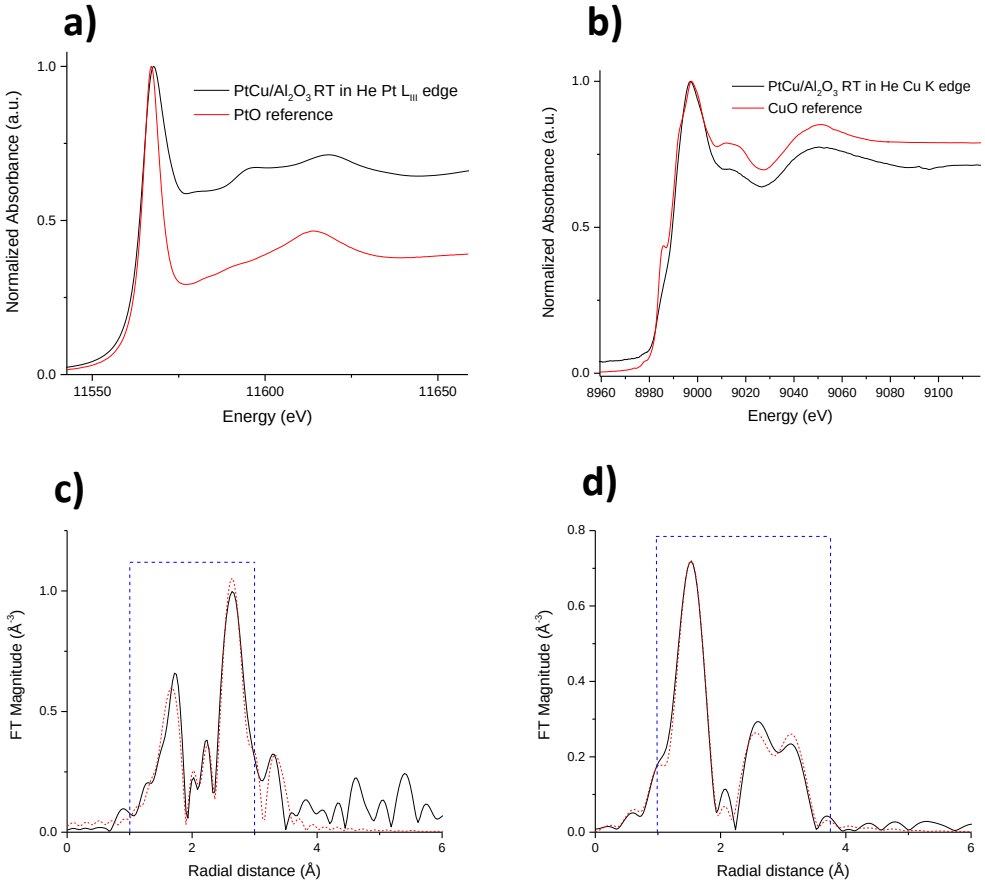

Fig. 4.6 – XANES spectra of $PtCu/Al_2O_3$ sample collected at room temperature in He at the (a) Pt L_{III}-edge and (b) Cu K-edge along with the PtO and CuO reference foils. FT magnitude with the best fit (dashed lines) of EXAFS spectra for the $PtCu/Al_2O_3$ catalyst at room temperature in He at (c) the Pt L_{III}-edge and (d) at the Cu K-edge (k range for the Fourier transform 2.5-12.4 $Å^{-1}$, the R-range for the fitting was 1-3/4 Å – dashed blue line window in the figure. In Tables A.1 and A.2 of Appendix A are reported the structural parameters obtained from the fitted EXAFS spectra).

4.1.1.1 XAFS Characterization During Reduction

The evolution of the experimental XANES spectra collected during the reduction (Fig. 4.7) at the Pt L_{III} edge evidenced changes of local structure around the Pt absorber atoms during the process. First, the PCA was performed to determine the number of components in the experimental dataset. Figure 4.8a shows the two relevant components denoted as descending D_r and ascending A_r determined by PCA. Indeed, the scree plot of the eigenvalues (Fig. 4.8b and c) revealed a characteristic change in slope at n=2. This means that the two components should be used to reproduce the entire experimental dataset.

Subsequently, the MCR-ALS routine was applied to transform the abstract PCs in physically meaningful spectra, along with the concentration profiles reported in Fig. 4.8a. On the basis of the concentration plot, the component D_r rapidly decreased already at room temperature under the exposure to H_2 with the consequent increase of the component A_r. By the comparison with the references XANES spectra (Fig. 4.9b), the D_r spectrum visually resembled the PtO one with a characteristic shape and edge shifted to higher energy respect to the Pt reference one,[9] to which the A_r spectrum approached.

To get a more complete identification of the species involved during the reduction and ascribed to the D_r and A_r components, the Fourier transform of the EXAFS part was analyzed and reported in Fig. 4.10 with his best fit along with the structural parameter obtained from the FT fitting (Appendix A). The best fit of the D_r EXAFS data (R factor = 0.029) fully confirmed the assignment to PtO species with a contribution of metallic Pt at the initial stage of the reduction, as already observed for the sample after calcination. Referring to the component A_r, the high coordination number of Pt around Pt atoms in the first shell of the PtCu phase (CN= 8.00 ± 0.6) suggested the formation of Pt-rich PtCu alloy in the second stage of the reduction.

To sum up, two components were found to be relevant for the $PtCu/Al_2O_3$ system during the exposure to H_2. The component D_r related to metallic Pt and PtO mixture phases was transformed in a Pt-rich PtCu alloy (component A_r) already at room temperature, remaining unchanged until the end of the process. The formation of this last species was in agreement with the results obtained from the SAED analysis, in which the initial NC alloy was found not to be fully restored.

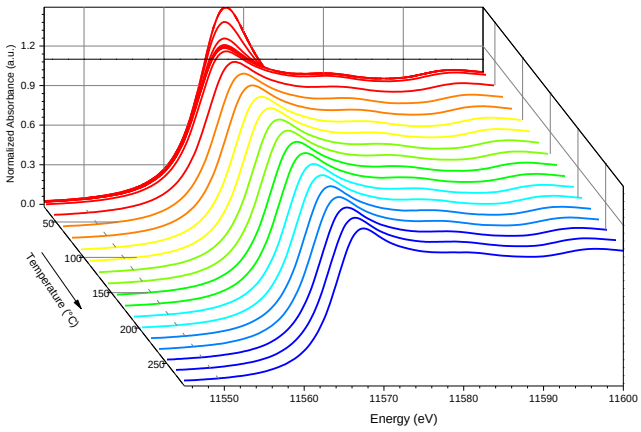

Fig. 4.7 – In situ XANES evolution of the $PtCu/Al_2O_3$ catalyst at the Pt L_{III}-edge during the reduction treatment.

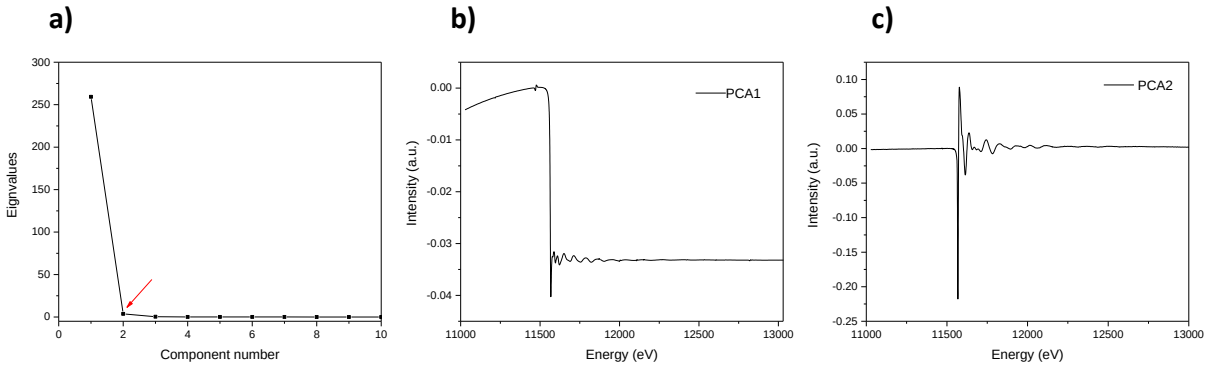

Fig. 4.8 – (a) Scree plot of the eigenvalues obtained by PCA of the Pt L_{III} edge for $PtCu/Al_2O_3$ catalyst during reduction and plot of the (b) first and (c) second PCs.

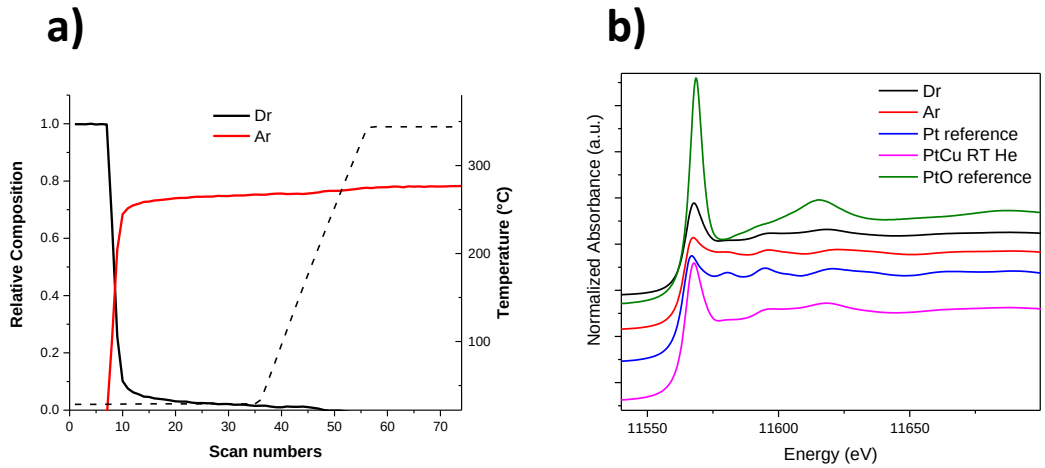

Fig. 4.9 – (a) Concentration profile of components determined by MCR-ALS as a function of the temperature during reduction at the Pt-L_{III} edge and (b) XANES spectra of the species formed during the reduction determined by MCR-ALS for the $PdCu/Al_2O_3$ catalyst along with the XANES spectra of crystalline reference Pt metallic and PtO foils and $PtCu/Al_2O_3$ sample spectrum collected at room temperature in He.

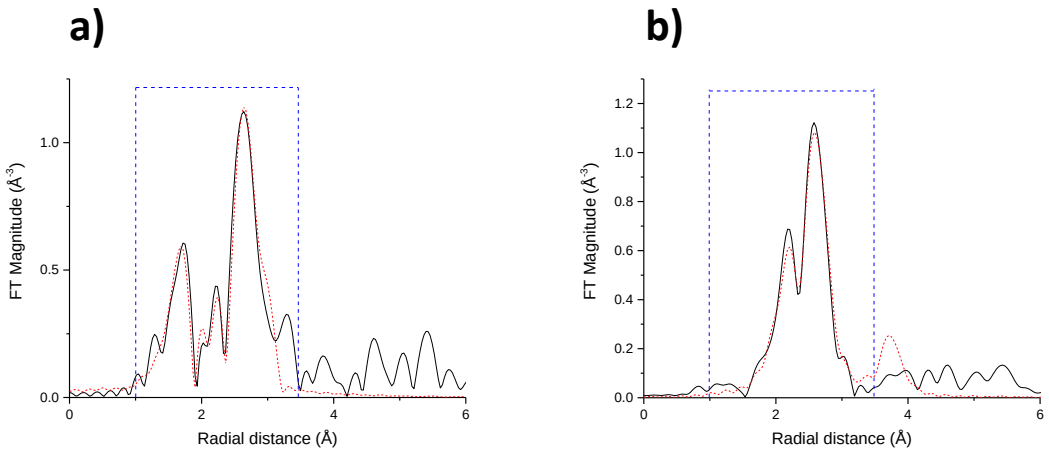

Fig. 4.10 – (a) FT magnitude with the best fit (dashed lines) of EXAFS spectra for (a) D_r and (b) A_r of the $PtCu/Al_2O_3$ catalyst during the reduction at the Pt L_{III}-edge (k range for the Fourier transform 2.5-12.4 Å^{-1}, the R-range for the fitting was 1-3/4 Å – dashed blue line window in the figure. In Tables A.1 and A.2 of Appendix A are reported the structural parameters obtained from the fitted EXAFS spectra).

To elucidate the mechanism of the reduction of the $PtCu/Al_2O_3$ system, in situ XAFS spectra were also collected at the Cu K edge (Fig. 4.11).

The MCR-ALS method was also used to analyze the in situ XANES spectra during the reduction process. The number of components selected on the basis of PCA was equal to 3, as evidenced by the break in the slope in the scree plot (Fig. 4.12a). The obtained pure spectra along with the reference ones are reported in Fig 4.13b. The spectrum of the descending D_r component was similar to that of CuO, while the second (intermediate component I_r) and the third (ascending component A_r) ones showed characteristic features similar to those of Cu_2O and metallic Cu,[10-12] respectively. The concentration dependence of these three components (Fig. 4.13a) proved that first, D_r started to be reduced already at room temperature into I_r, and at the beginning of the heating ramp, A_r started to be significant.

The analysis of the Fourier transform of the EXAFS extracted from the MCR-ALS with the best fit is reported in Fig. 4.14. As suggested by the qualitative analysis of the XANES part, the structural parameter determined by the fitting of the FT (see Appendix A) confirmed the presence of CuO as starting species assigned to D_r. The intermediate I_r component showed a main peak in the R-space around 2.60 Å compatible with Cu-Cu fist neighbors in the fcc PtCu structure. A minor contribution at 1.90 Å was related to oxygen neighbors around Cu absorbing atoms for Cu_2O phase. Finally, the A_r component was satisfactorily described by a Cu poor disordered alloy (CN_{Cu-Cu} = 3.28 ± 0.6, CN_{Cu-Pt} = 5.34 ±0.7) with a minor contribution at 1.93 Å related to the Cu_2O phase. The low coordination number of 0.33 found for this last species suggested the formation of small cluster. This last result that described the final state of the system at the end of the reduction was in line with those obtained at the Pt L_{III} edge, corresponding with the formation of a Pt-rich PtCu alloy, corroborated by the SAED analysis.

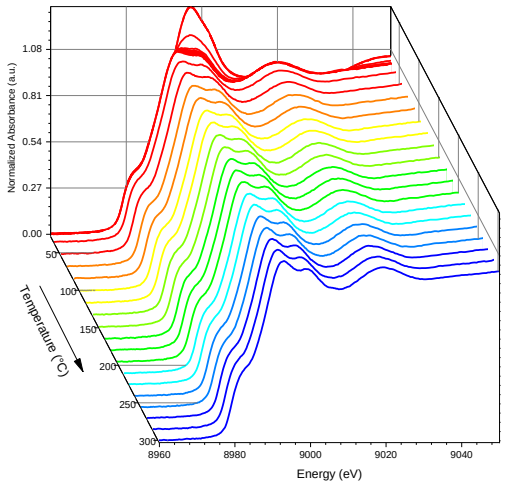

Fig. 4.11 – In situ XANES evolution of the $PtCu/Al_2O_3$ catalyst at the Cu K-edge during the reduction treatment.

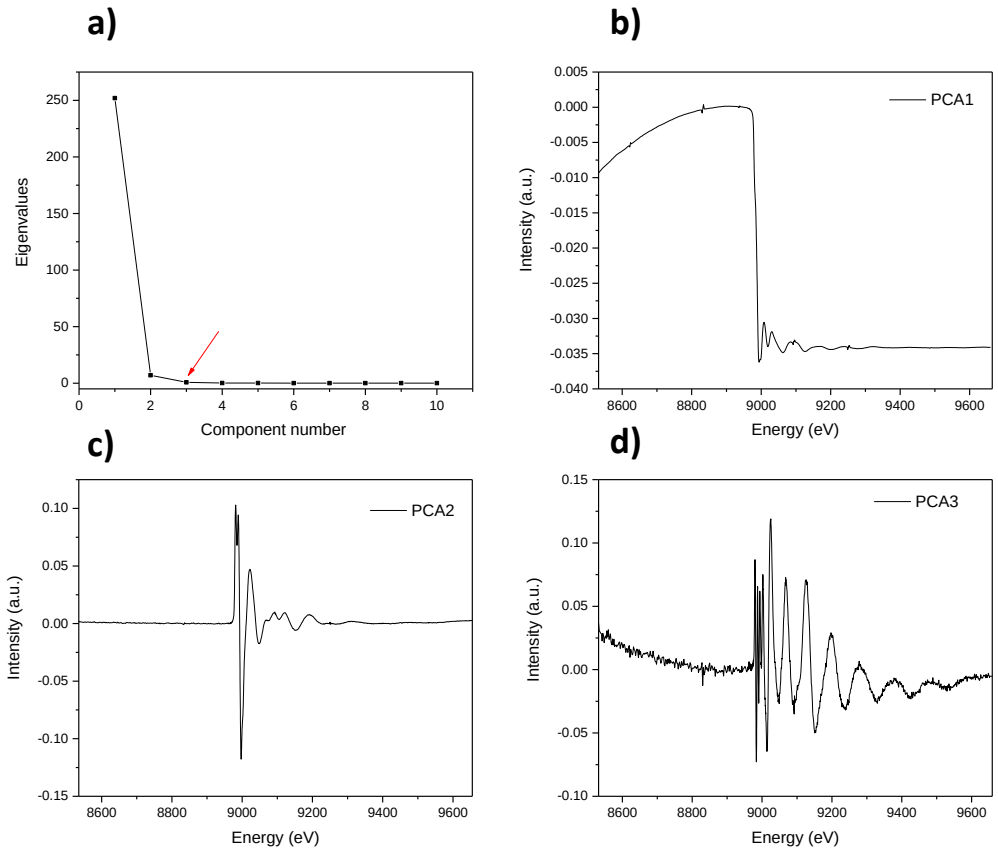

Fig. 4.12 – (a) Scree plot of the eigenvalues obtained by PCA of the Cu K-edge for $PtCu/Al_2O_3$ catalyst during reduction and plot of the (b) first, (c) second and (d) third PCs.

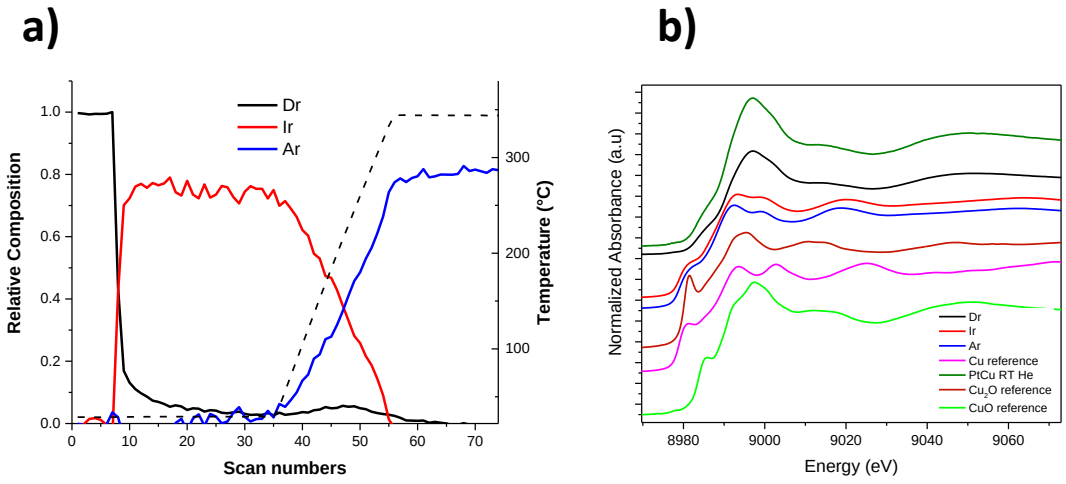

Fig. 4.13 – (a) Concentration profile of components determined by MCR-ALS as a function of the temperature during reduction at the Cu-K edge and (b) XANES spectra of the species formed during the reduction determined by MCR-ALS for the $PtCu/Al_2O_3$ catalyst along with the XANES spectra of crystalline references Cu metallic, CuO and Cu_2O foils and $PtCu/Al_2O_3$ catalyst spectrum collected at room temperature in He.

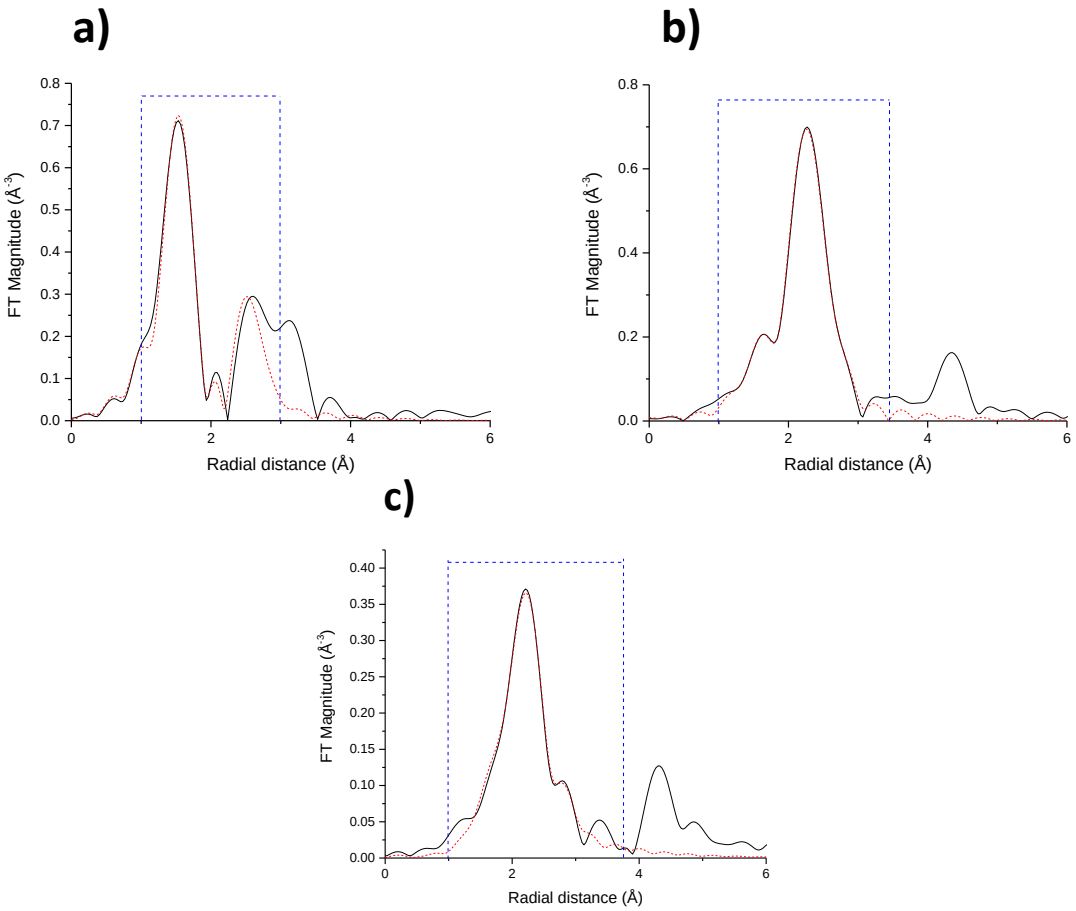

Fig. 4.14 – (a) FT magnitude with the best fit (dashed lines) of EXAFS spectra for (a) D_r, (b) I_r and (c) A_r of the $PtCu/Al_2O_3$ catalyst during the reduction at the Cu K-edge (k range for the Fourier transform 2.5-12.4 $Å^{-1}$, the R-range for the fitting was 1-3/4 Å – dashed blue line window in the figure. In Tables A.1 and A.2 of Appendix A are reported the structural parameters obtained from the fitted EXAFS spectra).

4.1.1.2 XAFS Characterization During Oxidation

The monitoring of the oxidation process for the $PtCu/Al_2O_3$ catalyst at the Pt L_{III} edge is presented in Fig. 4.15. Two PCs were chosen to explain the variance of the data set related to the system (Fig. 4.16b and c). The concentration profiles of the descending D_o and ascending I_o components along with their pure spectra are reported in Fig. 4.17a. From the concentration profile, D_o was found stable and present at room temperature under the exposure of oxygen. At the beginning of the heating ramp, the D_o decrease was associated with the appearance of the A_o. The two components showed similar XANES features related to metallic Pt by the comparison with the standard platinum spectrum (Fig. 4.17b). In particular, the A_o edge resulted to be shifted slightly to lower energies indicating more metallic features.[13]

Aiming to further validation of the component composition discussed above and for a deeper structural characterization of the local coordination environment of the Pt atoms during the oxidation, the fit of the FT EXAFS part was reported in Fig. 4.18 along with the structural parameters in Appendix A. Despite the similarity found by the visual inspection of the XANES spectra, the two components were related to different species. Specifically, the presence of Pt-

rich disordered PtCu alloy at the initial stage of the oxidation as component D_o was evident from the presence of the Pt-Pt1 fist shell at 2.72 Å with a coordination number of 6.69 ± 0.8 and Pt-Cu1 one at 2.68 Å with a coordination number (CN) of 2.83±0.7 Å. The fitting of the A_o FT EXAFS spectrum indicated that the Pt atom was surrounded by nine Pt atoms at a distance of 2.73 Å with a contribution of PtO phase (CN_{Pt-O} = 2.17 in the first shell).

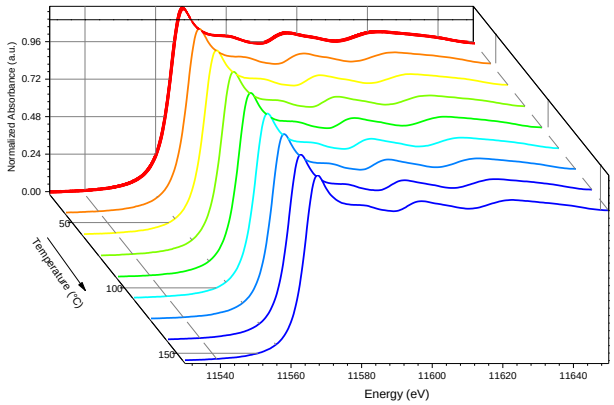

Fig. 4.15 – In situ XANES evolution of the $PtCu/Al_2O_3$ catalyst at the Pt L_{III}-edge during the oxidation treatment.

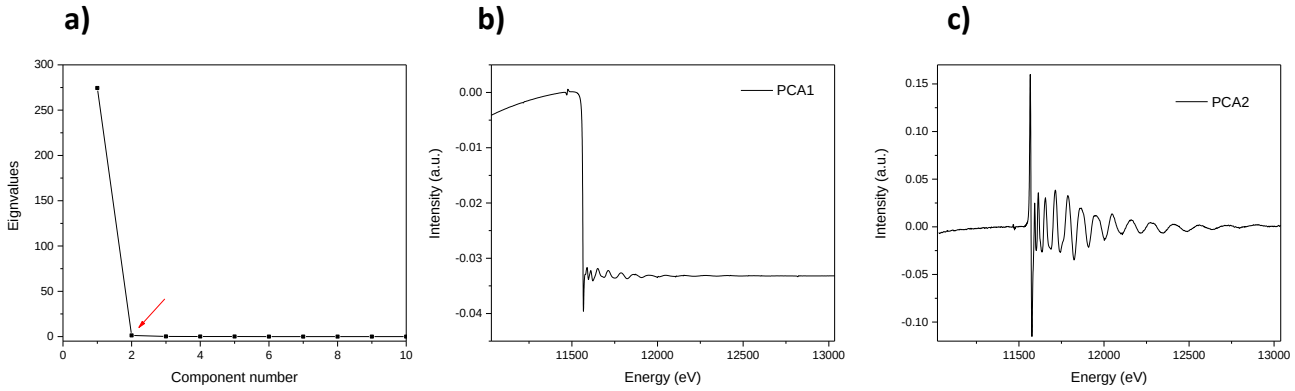

Fig. 4.16 – (a) Scree plot of the eigenvalues obtained by PCA of the Pt L_{III} edge for $PtCu/Al_2O_3$ catalyst during oxidation and plot of the (b) first and (c) second PCs.

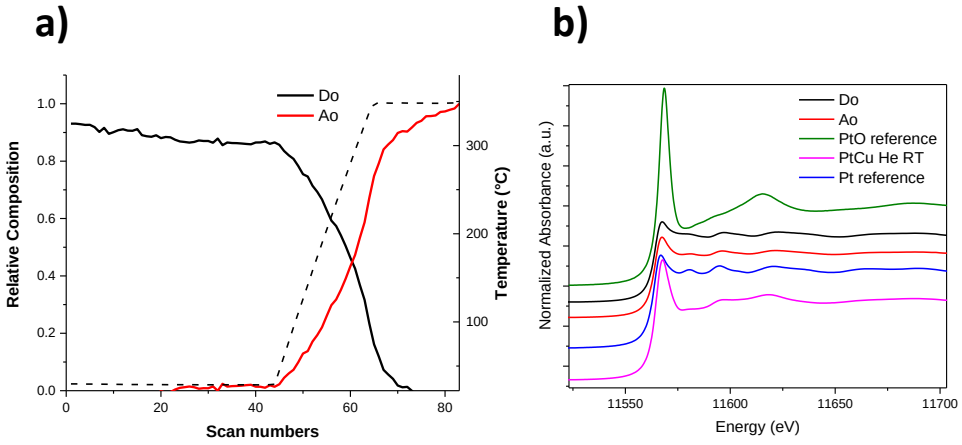

Fig. 4.17 – (a) Concentration profile of components determined by MCR-ALS as a function of the temperature during oxidation at the Pt-L_{III} edge and (b) XANES spectra of the species formed during the reduction determined

by MCR-ALS for the $PdCu/Al_2O_3$ catalyst along with the XANES spectra of crystalline references Pt metallic and PtO foils and $PtCu/Al_2O_3$ sample spectrum collected at room temperature in He.

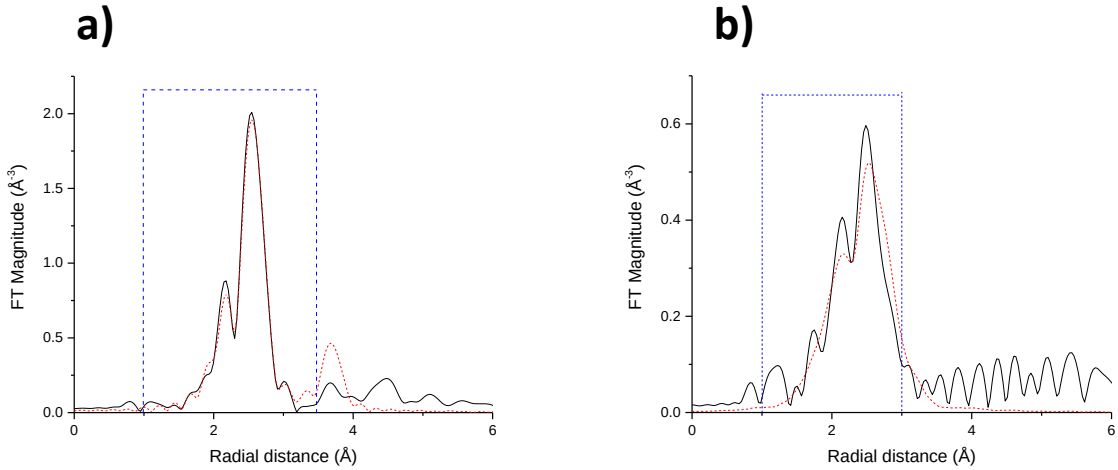

Fig. 4.18 – (a) FT magnitude with the best fit (dashed lines) of EXAFS spectra for (a) D_o and (b) A_o of the $PtCu/Al_2O_3$ catalyst during the reduction at the Pt L_{III}-edge (k range for the Fourier transform 2.5-12.4 Å^{-1}, the R-range for the fitting was 1-3/4 Å – dashed blue line window in the figure. In Tables A.1 and A.2 of Appendix A are reported the structural parameters obtained from the fitted EXAFS spectra).

Fig. 4.19 shows the evolution of in situ XANES spectra for the alumina supported PtCu system during the oxidation process at the Cu K-edge.

MCR-ALS method was applied to the dataset. First, from the inspection of the scree plot (Fig. 4.20a) and PCA analysis, three components were identified to explain the variance of the data set related to the system. Subsequently, the MCR approach based on the ALS method allowed to extract chemically meaningful spectra and concentration profiles of the three components involved during the process (descending D_o, intermediate I_o and ascending A_o components) (Fig. 4.21). A decrease in the relative fraction of the component D_o was paralleled by the transient growth in the contribution of the I_o and in minority to A_o. Then, at the beginning of the heating ramp, I_o was progressively increased along with A_o until it was dropped to 0 as the temperature reached 350 °C (Fig. 4.21a).

To further support these assignments, the FT EXAFS spectra were fitted to obtain the structural parameters able to describe the system (Fig. 4.22 and Appendix A). As denoted from the similarity of the XANES features (Fig. 4.21a), the best fit of the FT EXAFS spectra for D_o and I_o showed backscattering between 2.60 and 2.64 Å due to the Cu atoms in the first coordination shell and Pt atoms in the second one related to the formation of the fcc PtCu alloy phase. These two components differed only in the Cu-Cu coordination number slightly higher for I_o. A small contribution at around 1.90 Å was observed for the fitted Cu-O shell related to the Cu_2O phase. Finally, the complete oxidation of Cu was evident for the component A_o from the presence of the Cu-O shell at 1.95 Å related to CuO with an increased intensity of the Cu-O interaction at 2.0 Å for Cu_2O compared to what found for D_o and I_o.

To conclude, complete segregation occurred during the oxidation treatment starting from a Pt-rich PtCu alloy to metallic Pt and CuO phases at the end of the process, as confirmed by the previous techniques.

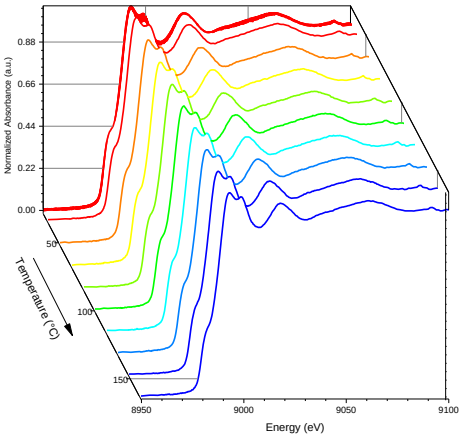

Fig. 4.19 – In situ XANES evolution of the $PtCu/Al_2O_3$ catalyst at the Cu K-edge during the oxidation treatment.

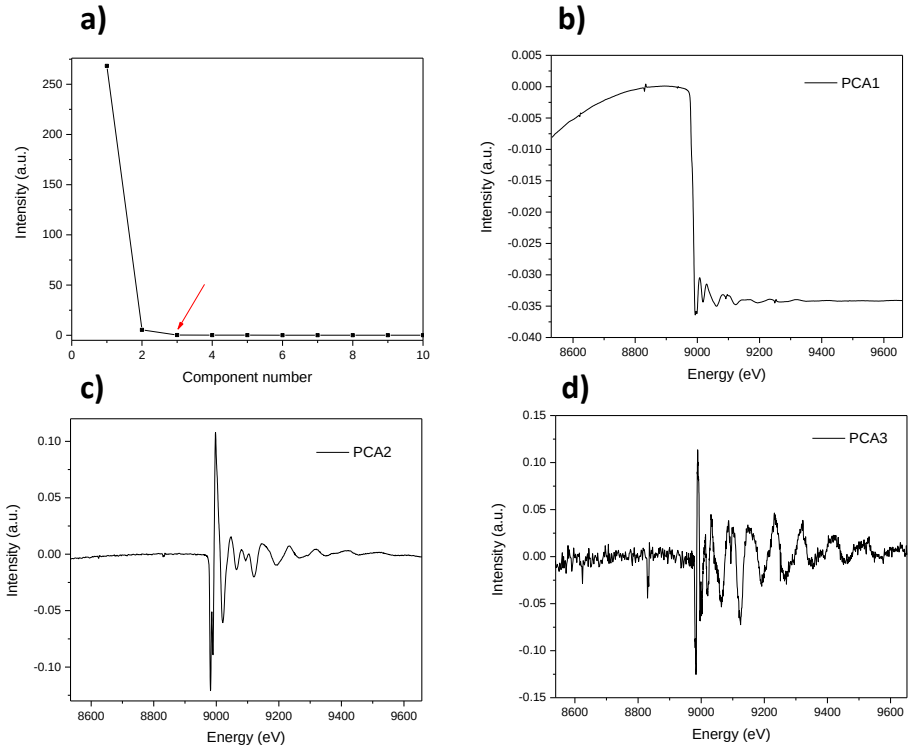

Fig. 4.20 – (a) Scree plot of the eigenvalues obtained by PCA of the Cu K edge for $PtCu/Al_2O_3$ catalyst during oxidation and plot of the (b) first, (c) second and (d) third PCs.

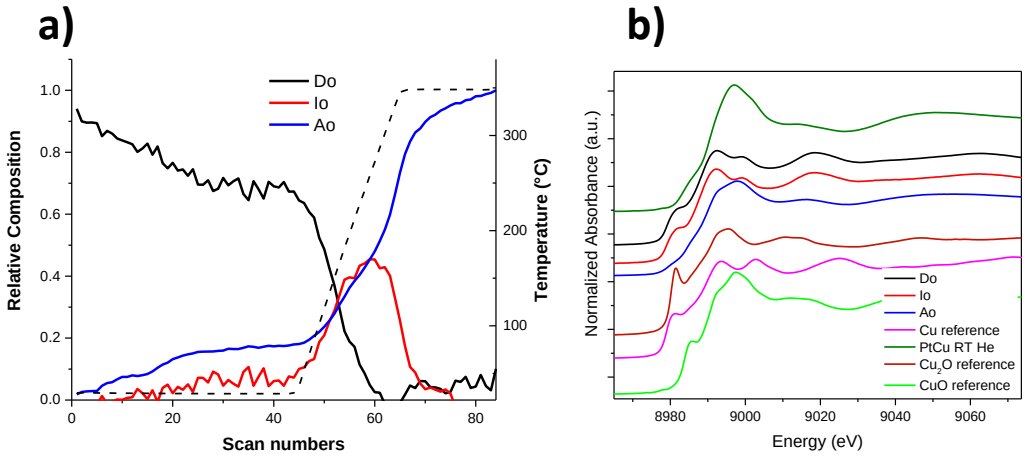

Fig. 4.21 – (a) Concentration profile of components determined by MCR-ALS as a function of the temperature during oxidation at the Cu-K edge and (b) XANES spectra of the species formed during the oxidation determined by

MCR-ALS for the $PtCu/Al_2O_3$ catalyst along with the XANES spectra of crystalline references Cu metallic, CuO and Cu_2O foils and $PtCu/Al_2O_3$ catalyst spectrum collected at room temperature in He.

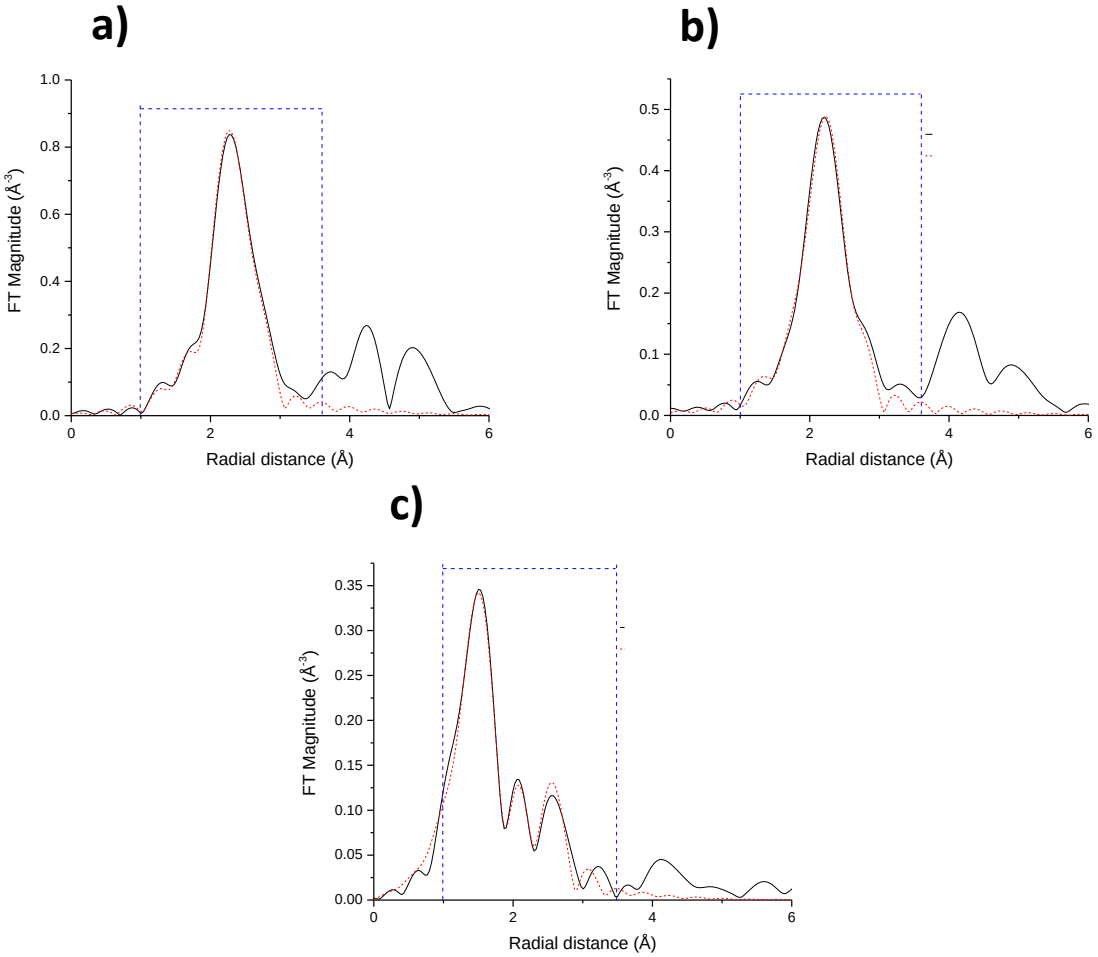

Fig. 4.22 – (a) FT magnitude with the best fit (dashed lines) of EXAFS spectra for (a) D_o, (b) I_o and (c) A_o of the $PtCu/Al_2O_3$ catalyst during the oxidation at the Cu K-edge (k range for the Fourier transform 2.5-12.4 Å^{-1}, the R-range for the fitting was 1-3/4 Å – dashed blue line window in the figure. In Tables A.1 and A.2 of Appendix A are reported the structural parameters obtained from the fitted EXAFS spectra).

4.1.2 Catalytic Activity in the CO Oxidation Reaction

Several experimental studies based on PtCu NC alloys have demonstrated the importance of tuning the atomic structure and morphology of the nanoalloys achieving different catalytic activity in response to the modification of their atomic rearrangement and electronic structures.[7, 14-18]

Indeed, the observed transformations that occurred under oxidative and reductive gas atmospheres led to a different scenario when these NCs were exposed to the CO oxidation reaction.

The catalytic activity of the $PtCu/Al_2O_3$ catalyst is shown in Fig. 4.23. After the oxidative treatment, during the heating phase, the first maximum in CO conversion appeared at about 90 °C, approaching 20%. Then the conversion decreases with temperature until approaching a minimum at about 150 °C. Further increasing the temperature allowed the complete conversion

of CO, which was reached at about 200 °C; in the cooling phase, the conversion began to decrease at 180 °C and at about 170 °C there was the intersection between the two curves, so that the activity was lower than that measured during the heating phase. In contrast, after the reducing treatment, already at room temperature, the catalyst exhibited about 10% conversion, corresponding to significantly higher activity in comparison with that observed after the oxidizing treatment. There was a continuous, monotonically increase in CO conversion with the increase of the temperature, with complete consumption of CO at about 120 °C. In the cooling phase, the decrease of conversion took place at temperature 170 °C and a conversion close to zero was achieved around 100 °C.

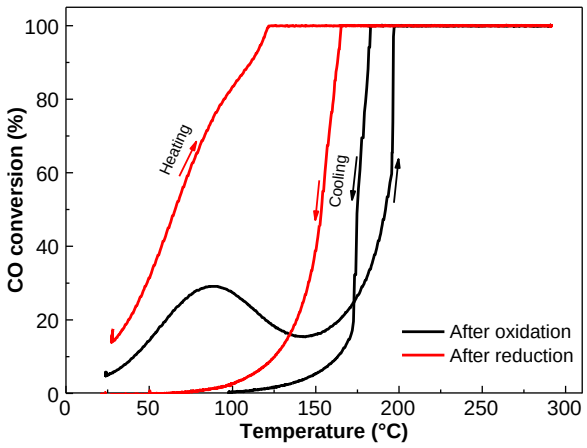

Fig. 4.23 – Catalytic activity of $PtCu/Al_2O_3$ catalyst in CO oxidation after the oxidizing and reducing pre-treatments during the third repeated test.

To investigate the possible changes of nanostructure and surface composition under the real reaction conditions so that the governing factors responsible for the catalytic activity can be elucidated, the changes in surface composition for the reduced $PtCu/SiO_2$ catalyst exposed to O_2 at room temperature and 100 °C was monitored by *in situ* CO-DRIFTS.

The DRIFTS spectra acquired on the reduced sample after the oxygen exposure at room temperature and 100 °C (Fig. 4.24) showed a decrease of the intensity of the band associated to Cu^0 (2121 cm^{-1}), more pronounced than that of Pt (2066 cm^{-1}), with a reverse intensity ratio if compared to the CO bands acquired after reduction. The enhanced adsorption of CO on Pt^0 in the PtCu NCs can be explained as a result of an alloy segregation process in which, first, a CuO overlayer was formed on the Pt atoms at low temperature. Then, a progressive migration of CuO_x on the support led to an NC Pt enriched surface. It is also possible to assume the simultaneous formation of Cu^{2+} species, not detected in the spectra due to the instability of the CO adsorption complexes on it. The lack of stability of these species by simple evacuation at ambient temperature was visible with major extent on the catalyst exposed to O_2 at room temperature and 100 °C in comparison with the desorption spectrum collected after the reduction. The well-known mechanism of CO oxidation over Pt crystalline supported on alumina established that, already at room temperature, the oxidation of carbon monoxide on platinum is CO self-poisoned since CO adsorption often is favored. This is mainly due to the CO initial sticking coefficient much higher than the oxygen one (0.8 versus 0.1).[19] However, it is possible to speculate that the

observed higher activity at low temperature for the reduced system could be related to the weak adsorption of CO molecules already at room temperature.

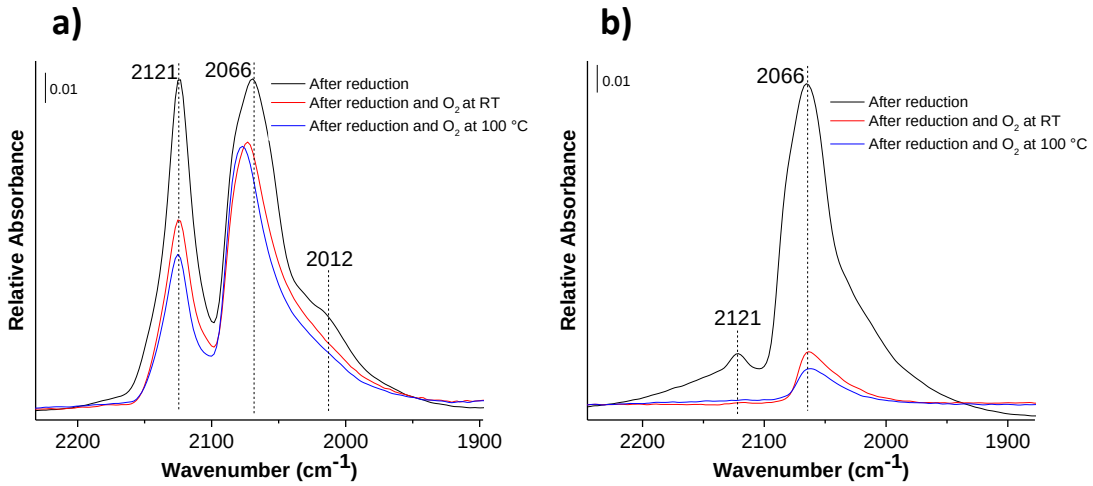

Fig. 4.24 – DRIFT spectra in the carbonyl region recorded during adsorption (a) and desorption (b) of CO at room temperature recorded after 10 min on $PtCu/Al_2O_3$ catalyst after reduction treatment and the exposure to O_2 flow at room temperature for 30 min and 100 °C.

However, the above mentioned transformations that occurred under the exposure to reductive and oxidative atmospheres have been found also under the NC exposure to a reaction environments such as CO. Previous studies have shown a general trend of surface segregation where the more reactive alloy component formed stronger chemical bond with the CO adsorbate and thus preferentially segregates to the surface.[20] As example, it was found for PtCu and PdAu bimetallic nanoparticles that the CO exposure led to a segregation of a relative amount of Pt and Pd on the surface layer, respectively, with the concomitant migration of Cu to the core.[21] EXAFS studies conducted on PtCu nanocube showed that a different catalyst surface and structure was formed in reaction with one or more gases. The resulting new catalytic performances were revealed with kinetics studies of these formed new catalyst structures.[22]

As mentioned by Oxford et al.,[21] for small particles in which the number of atoms in the surface layer is comparable to the bulk, the compositions of the bulk and the surface were expected to be strongly correlated. Thus, it is important to characterize not only the surface or the initial composition but also the bulk and changes in the bimetallic particles.

For this reason, the transformations of NCs upon activation were thoroughly studied with in situ XANES and EXAFS measurements at Pt L_{III} and Cu K absorption energy edges to probe the reactivity behavior during the exposure to CO atmosphere (Figs. 4.25 and 4.26). XAFS spectra on $PtCu/Al_2O_3$ system were collected in transmission mode during the CO oxidation reaction after the reductive and oxidative treatments at the SuperXAS beamline of the Swiss Light Source (SLS) at PSI.

Figures 4.25 and 4.26 display the *in situ* XANES spectra collected during the CO oxidation reaction for $PtCu/Al_2O_3$ system after the oxidative and reductive pre-treatments. For simplicity, each cycle was divided in four parts. Specifically, XANES and EXAFS spectra were analyzed at the beginning of the test after the exposure to 15 min to the reaction environments, at the end of

the heating ramp at 300 °C and at the end of the cooling ramp at 100 °C. The XAFS data collected just after the two treatments were here not reported as they are comparable with those obtained from the SOLEIL synchrotron (see Fig. B.1 of Appendix B).

As already discussed in Chapter 3 relative to the $PdCu/Al_2O_3$ system, the data interpretation was done comparing the spectra with the bulk reference ones used in fingerprinting the XANES part by the assignment of diagnostic spectral features originating from the XANES of the reference materials. Moreover, another strategy consisted of the individuation of isosbestic points in the XAFS spectra. Indeed, one of the methods allowing detection of constituent components forming during the reaction was based on the examination of isosbestic points. This method relied on the presence or absence of the points where all spectra were taken at different stages of the reaction intersect each other. Thus, the presence of one or more isosbestic points was a sign of a direct transformation of one constituent to another one while the absence of isosbestic points indicated the formation of intermediate species.[23] Subsequently, the fit of the Fourier transform of the EXAFS part was reported to determine the structural parameters of the phases formed in the system during the reaction (see Figs. B.2 - 9 and Appendix B).

The set of Pt L_{III} and Cu K edge XANES spectra recorded as a function of temperature after reduction were divided into four parts (Fig. 4.25). Between room temperature and 300 °C during the exposure to CO and O_2, the edges shifted slightly to higher energies, denoting an increase in Pt and Cu oxidation states and changes in their chemical environments. The post-edge region indicated that a major part of Pt atoms existed in the metallic state and the other part was oxidized. In the cooling ramp to 100 °C, both the edges shifted toward lower energies, leading to spectra similar to those of metallic Pt and Cu.[13] The XANES spectra collected at both edges during the permanence at 300 °C and 100 °C for 30 min (Fig. 4.25c, d, g and h) showed the same XANES features of those in the spectra acquired at the end of the heating and cooling ramp. This suggested that no transformation occurred at these stages of the reaction. However, the formation of intermediate species cannot be excluded due to the absence of isosbestic point, as above discussed.

Figures B.2 - 5 in Appendix B show the Fourier transforms along with the best fit calculated from the EXAFS signal recorded at the Pt L_{III} and Cu K edges during the CO oxidation reaction after reduction. In the spectra collected after 15 min the exposure to CO, an intense peak assigned to Pt-Pt and Cu-Cu first-neighbors was clearly visible at 2.72 Å and 2.65 Å, respectively. The measured higher coordination number of Pt around Pt atoms ($CN_{Pt\text{-}Pt1}$ =6.01±1.16) compared to that of Cu-Cu at the Cu K edge ($CN_{Cu\text{-}Cu1}$ = 2.88) suggested the presence of a Pt-rich disordered PtCu alloy at this stage of the reaction. Moreover, the number of nearest Pt and Cu neighbors was lower than 12 though, in line with the presence of nanoparticles in which the number of surface, under-coordinated atoms was negligible.[21] Part of the copper not present in the alloy was found as Cu_2O phase. At the end of the heating ramp, a decrease in Pt-Pt1 coordination number for the PtCu alloy with the formation of PtO and CuO phases denoted the progressive rearrangement of the Pt and Cu atoms under the reaction environment. Finally, at the end of the cooling phase at 100 °C, the Pt-rich disordered PtCu alloy was restored with an higher coordination number at the Pt-Pt1 fist shell compared to the initial situation at the

beginning of the heating ramp ($CN_{Pt\text{-}Pt1 initial ramp}$ 7.57 ± 1.16 vs. $CN_{Pt\text{-}Pt1 cooling at 100 °C}$ 6.01 ± 1.16). The measured low coordination number found for the unincorporated alloyed copper in the CuO and CuO phases ($CN_{Cu\text{-}O1 for Cu2O}$ = 0.32, $CN_{Cu\text{-}O1 for CuO}$ = 0.47) suggested that these species were in the forms of a small cluster on the support.

To notice that the R-factor values for the EXAFS FT fitting at the Cu K edge were relatively higher compared to those obtained at the Pt L_{III} edge. This because the bond distance and coordination number values contained relatively big errors such as to be fixed in the simulation due to the weak EXAFS signal.

After the oxidation treatment (Fig. 4.26), during the heating ramp from room temperature to 300 °C, the Pt L_{III} edge shifted toward higher energies, leading to spectra similar to that of reference PtO. The Cu K edge shifted to higher energy and, by the comparison with the references, the position of the absorption edge approached the value measured on the CuO standard. During the cooling phase to 100 °C, progressive evolution of the XANES spectra towards that of the Pt reference material was observed along with the slight shift to lower energies of the Cu K edge, similar to the one reported for the CuO standard. The same edge and EXAFS oscillations for the spectra recorded during the static exposure to the reaction environment at 300 °C and 100 °C were found in comparison to those acquired at the end of the heating ramp and of the cooling phase. Also in this case, the absence of isosbestic point suggested the possible formation of intermediate species formed in between of those revealed at the end of the ramps or the absence of transformations.

The fitting of the FT EXAFS part of the spectra at Pt L_{III} and Cu K edges during the CO oxidation reaction after oxidation at the beginning and end of the heating ramp and at the end of the cooling part are presented in Figs. B.6 - 9 (Appendix B). The exposure to CO reaction for 15 min led to a rearrangement of the atoms in the PtCu system already at room temperature. Indeed, starting from a structure after oxidation in which a complete dealloy occurred with the formation of metallic Pt and CuO_x phases, a Pt-rich PtCu alloy was found at this stage. This is consistent with the greater number of nearest neighbor metallic Pt around the absorber Pt ($CN_{Pt\text{-}Pt1}$ = 7.83 ± 0.93), while the presence of Cu-O around the Cu emitter related to the CuO phase reduced the number of metallic Cu neighbors ($CN_{Cu\text{-}Cu1}$ = 2.10 ± 0.30). Additionally, a low contribution of PtO phase was obtained from the fit. When the sample reached 300 °C under the reaction environment, the number of Pt-Pt1 and Cu-Cu1 neighbors from the alloy decreased with the appearance of the Cu_2O phase in addition to the pre-existing PtO and CuO phases. Finally, at the end of the cooling phase at 100 °C, the predominance of the Pt-rich PtCu alloy was again recovered with an increase in Pt-Pt1 neighbors compared to the initial stage of the reaction. Therefore, the Cu removed from the first Pt shell and replaced by additional Pt neighbours was found as CuO species, with a slight greater contribution ($CN_{Cu\text{-}O1}$ = 2.67 ± 0.43) than the initial stage of the reaction ($CN_{Cu\text{-}O1}$ = 2.10 ± 0.30).

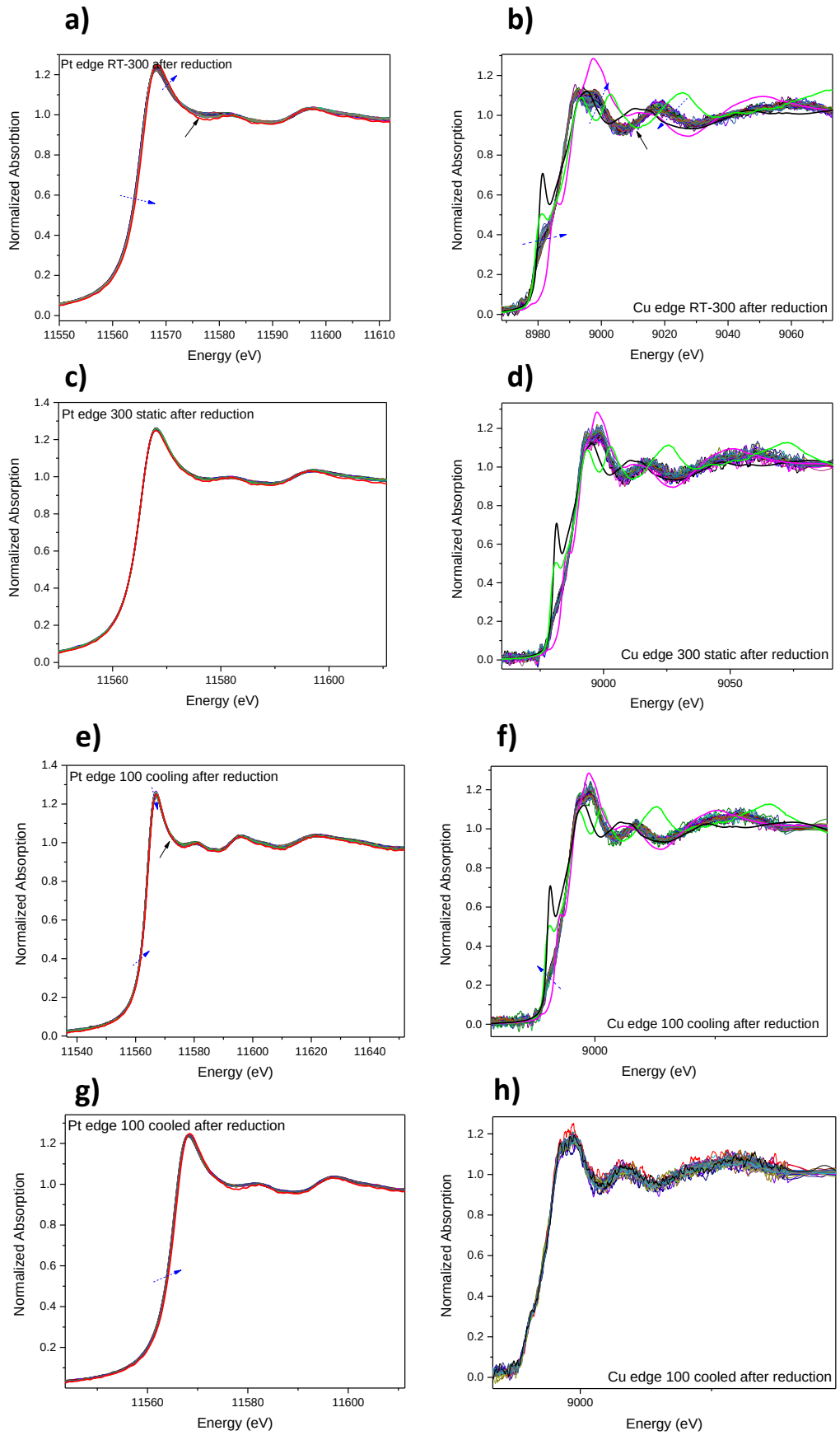
a)
Pt edge RT-300 after reduction
Normalized Absorbtion
Energy (eV)
b)
Cu edge RT-300 after reduction
Normalized Absorption
Energy (eV)
c)
Pt edge 300 static after reduction
Normalized Absorption
Energy (eV)
d)
Cu edge 300 static after reduction
Normalized Absorption
Energy (eV)
e)
Pt edge 100 cooling after reduction
Normalized Absorption
Energy (eV)
f)
Cu edge 100 cooling after reduction
Normalized Absorption
Energy (eV)
g)
Pt edge 100 cooled after reduction
Normalized Absorption
Energy (eV)
h)
Cu edge 100 cooled after reduction
Normalized Absorption
Energy (eV)

Fig. 4.25 – XANES evolution of the $PtCu/Al_2O_3$ catalyst at the (a, c, e, g) Pt L_{III}-edge and (b, d, f, h) Cu K-edge after reduction treatment during the CO oxidation reaction: (a, b) in the heating ramp up to 300 °C, (c, d) static at 300 °C for 30 min, (e, f) in the cooling ramp down to 100 °C and (g, h) static at 100 °C for 30 min. The XANES spectra of the Pt (in red), Cu (in green), Cu_2O (in black) and CuO (in magenta) standards are reported. The blue dashed arrows indicate the direction of the evolution of the spectra during the acquisition while the black ones the isosbestic points.

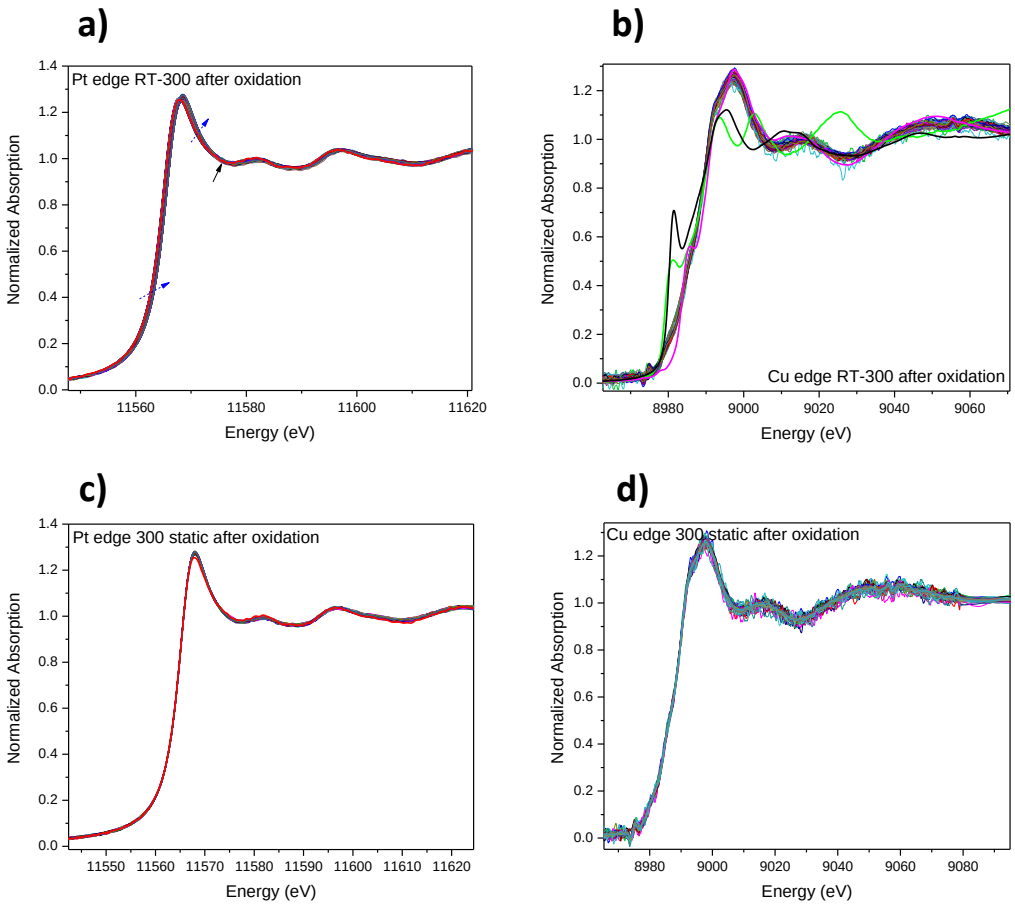

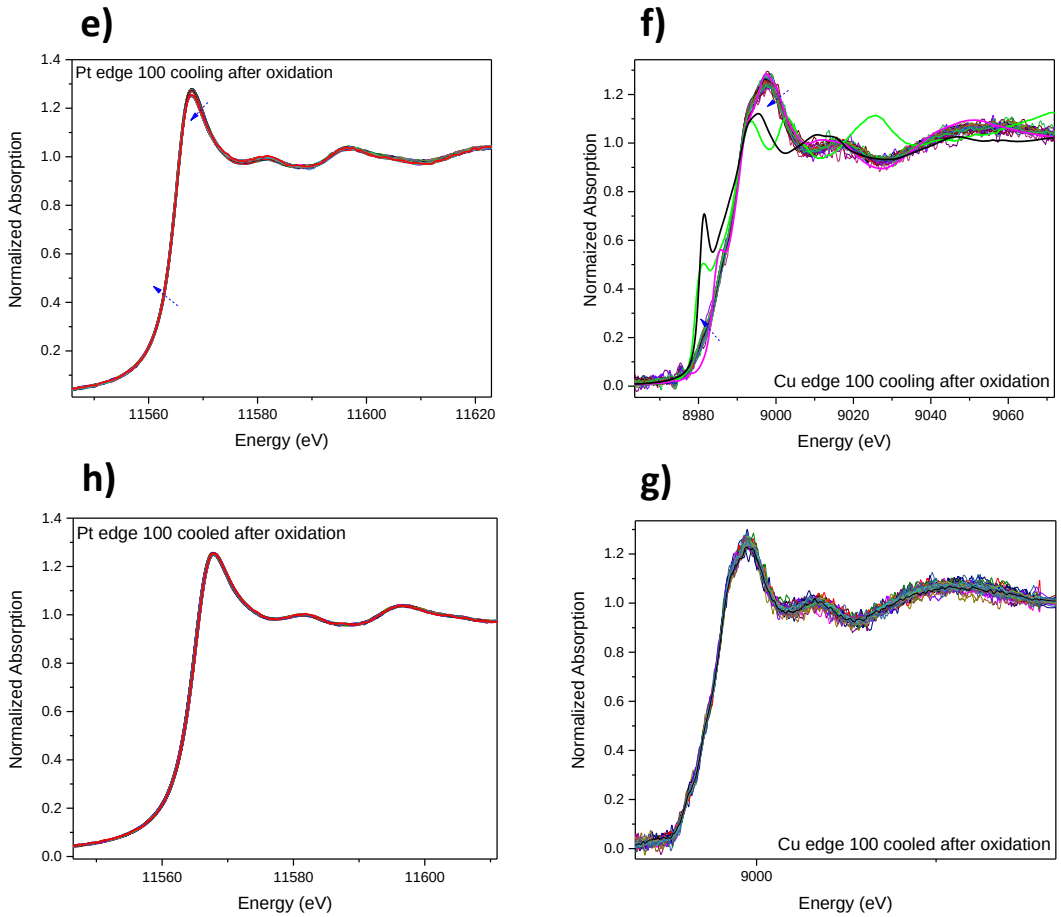

Fig. 4.26 – XANES evolution of the $PtCu/Al_2O_3$ catalyst at the (a, c, e, g) Pt L_{III}-edge and (b, d, f, h) Cu K-edge after oxidation treatment during the CO oxidation reaction: (a, b) in the heating ramp up to 300 °C, (c, d) static at 300 °C for 30 min, (e, f) in the cooling ramp down to 100 °C and (g, h) static at 100 °C for 30 min. The XANES spectra of the Pt (in red), Cu (in green), Cu_2O (in black) and CuO (in magenta) standards are reported. The blue dashed arrows indicate the direction of the evolution of the spectra during the acquisition while the black ones the isosbestic points.

Finally, the sample underwent a sequence of reaction cycles, each preceded by an oxidative and reductive treatments, to verify the reproducibly of the catalytic activity data. In the repeated tests (Fig. 4.27), the activity was fairly stable and reproducible with no significant deviations during the cooling phase after both the treatments. This means that the CO profiles measured did not exhibit any memory of the previous reaction cycles and pre-treatment history. On the other hand, in heating phase at the same temperature, greater activity in the last test was obtained due to a progressive activation of the catalyst, and the maximum conversion difference of about 30% was observed at 100 °C after reduction.

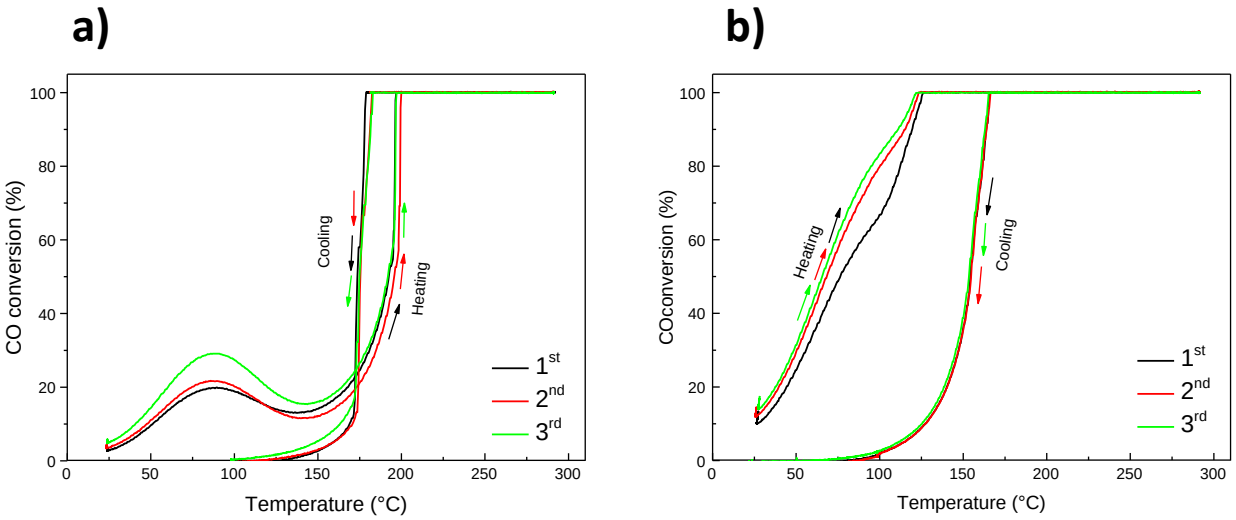

Fig. 4.27 – Catalytic activity during three reaction cycles of $PtCu/Al_2O_3$ catalyst in CO oxidation after oxidizing (a) and reducing (b) pre-treatments.

4.2 Effect of the Support on the Surface Composition of NCs

4.2.1 Silica Supported NCs Upon Oxidative/Reductive Pre-treatments

In order to understand the nature of the difference between the PtCu NC on two different supports, the same batch of NCs was used to prepare the $PtCu/SiO_2$ sample. Also in this case, the catalyst was characterized by means of several techniques after the oxidizing and reducing treatments.

As shown in Fig. 4.28, it was found by the HAAD-STEM analysis that the as-synthetized PtCu NC size of 4.8 ± 1.8 nm was preserved upon the two treatments. Specifically, an average particle size of 4.8 ± 1.6 nm based on 175 particles and 4.8 ±1.8 nm on 89 particles was obtained after oxidation and reduction, respectively.

The catalyst was further analyzed by STEM-EDX to understand the spatial distribution of the elements after the oxidizing and reducing treatments (Fig. 4.29). It was evident that, after oxidation, the noble metal remained localized in the particles, while the Cu was present as a shell around the noble metal core particles. After reduction, Pt and Cu atoms were localized within the NCs.

The XRD patterns of the SiO_2 supported PtCu catalyst after the two treatments are reported in Fig. 4.29c in comparison to those of the as-synthetized NCs. A complete dealloy between the noble metal and the Cu occurred after the oxidizing treatment, with the formation of metallic Pt. Only a 5 atomic % of Cu was present in the NCs (estimated from Vegard's law).[24] To be highlighted, no crystalline phase associated to Cu or CuO_x was detected, suggesting the poor crystalline nature of the CuO_x shells formed around the dealloyed NCs. The reduction treatment led to a shift of the peaks towards higher angles, which is indicative of partial reincorporation of the Cu in the NCs with the formation of the fcc structure of PtCu. According to Vegard's law,

only 10 % (atomic percentage) Cu can be estimated in the PtCu alloy NCs after the reduction. This Cu value calculated by Vegard's law was underestimated compared to that obtained from measurement of the composition by STEM-EDX, probably due to the presence of amorphous Cu no detectable by XRD or due to the inapplicability of this law to this inhomogeneous system.[1, 2]

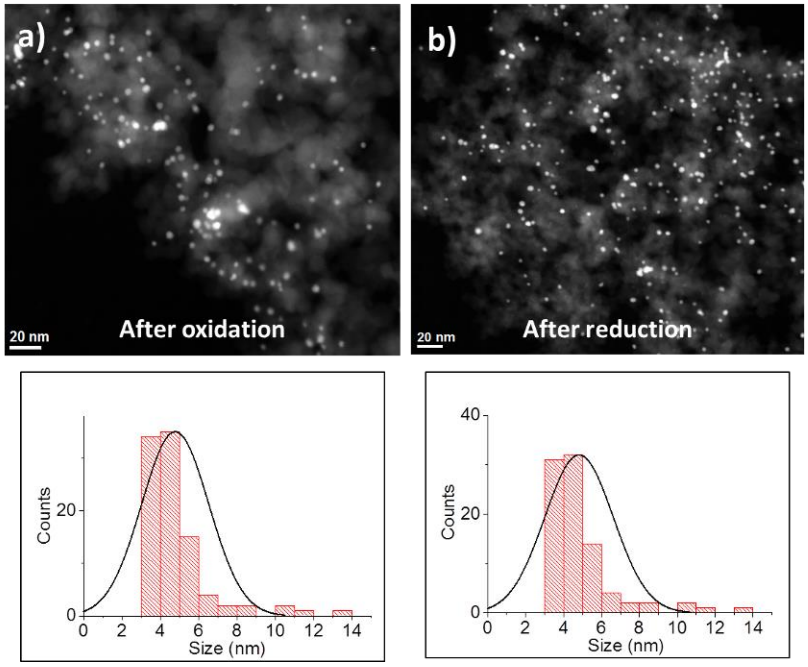

Fig.. 4.28 – HAADF-STEM images of $PtCu/SiO_2$ catalysts after (a) oxidizing and (b) reducing treatments with the corresponding size distribution histogram.

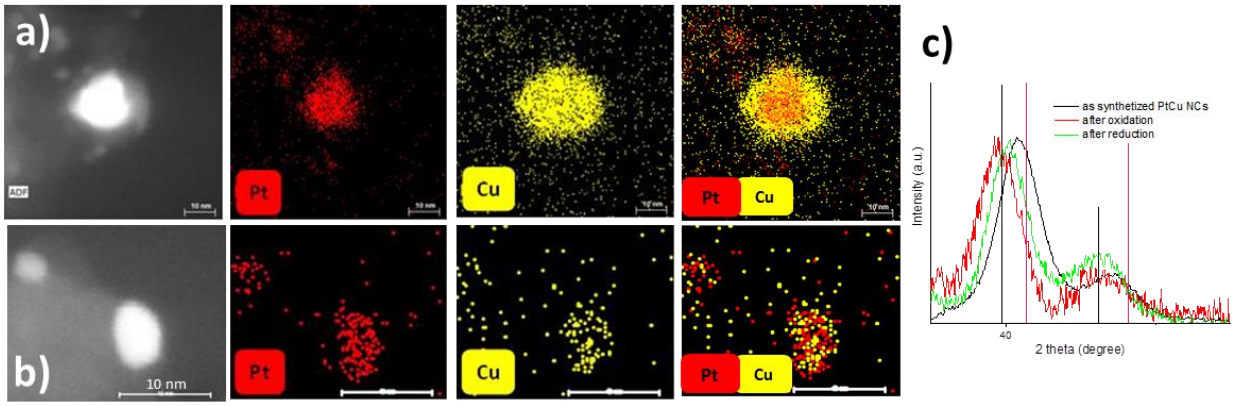

Fig. 4.29 – HAAD-STEM images of 2 wt % $PtCu/SiO_2$ catalyst and corresponding quantitative EDX maps for Pt and Cu after (a) oxidizing and (b) reducing treatments; (c) XRD patterns after oxidation and reduction in comparison to PtCu NCs (reference patterns: Pt_1Cu_1 ICSD 98-010-8402 (red line), Pt ICSD 98-004-1525 (black line)).

While TEM characterization provided useful information on the evolution of NC composition and structure upon the different treatments, DRIFTS tests were performed to track the evolution of metal oxidation states of the surface species on the same sample. As a comparison, DRIFT spectra were collected on monometallic NCs.

The adsorption of CO on Cu NCs supported on silica has been already reported in the previous Chapter 3 (Fig. 3.36) as a comparison for the DRIFT spectra of $PdCu/SiO_2$ catalyst.

After both the oxidizing and reducing pre-treatments (Fig. 4.30), the exposure of Pt catalyst to CO resulted in the appearance of one band at 2091 cm^{-1}. The assignment of this band is well established and attributed to CO linearly adsorbed on Pt atoms. The low-frequency band at 2040 cm^{-1} is assigned to the oscillation of CO bridged adsorbed on Pt atoms.[7] The evacuation of the gas phase for 10 min resulted in a band shift of less than 2 cm^{-1} to lower frequency with a small decrease in the intensity. This was indicative of a small change in coverage of CO due to the strong CO-Pt interaction at room temperature.

CO adsorbed on the oxidized $PtCu/SiO_2$ catalyst (Fig. 4.31a and c) gave main absorption bands at 2077 cm^{-1} and a second weak band at 2126 cm^{-1}. The former was attributed to the linear CO species on Pt atoms and the latter to those on Cu^+ atoms, in agreement with that obtained for monometallic Pt and Cu catalysts. The stability of the band assigned to Cu^+-CO in the absence of gas-phase CO was consistent with the relatively strong interaction between CO and Cu^+. It is also possible to assume the simultaneous formation of Cu^{2+} species, not detected in the spectra due to the instability of the CO adsorption complexes on it. This assumption can be supported by the high dispersion of CuO on the alumina support detected in the EDX maps. Furthermore, the higher intensity of the band associated to Cu^+ compared to that to Pt confirmed the formation of the Pt core @ CuO_x shell structure as shown by the EDX maps. Although the DRIFT is strictly not a quantitative technique, the comparison of the band intensity associated with the Pt species in the Pt/SiO_2 catalyst spectra with that observed in the bimetallic sample with similar Pt content, was another evidence of the formation of the core-shell structure for the PtCu NCs after oxidation. Indeed, the intensity of the Pt-CO band in the $PtCu/SiO_2$ sample was extremely lower compared to that one in the Pt/SiO_2 catalyst due to the formation of the Cu^+/Cu^{2+} shell which prevented the interaction between CO and Pt.

After reduction (Fig. 4.31c and d), two main bands centered at about 2123 cm^{-1} and 2060 cm^{-1} appeared. The high-energy absorption band at 2123 cm^{-1} resulted from CO bound to Cu^0 even if the position of this band would be more consistent with Cu^+ rather than Cu^0. Furthermore, the lack of stability of the band under evacuation conditions precluded this assignment. The attribution of this band to CO adsorbed on Cu^0 can be possible assuming an electronic modification by neighboring Pt atoms that increase the CO-Cu^0 strength.[8] Indeed, the frequency of the bands assignable to linearly bonded Pt^0-CO and Cu^0-CO carbonyls in the spectra of reduced Pt/SiO_2 and Cu/SiO_2 catalysts were about 26 cm^{-1} higher and 9 cm^{-1} lower, respectively, than those recorded for the bimetallic catalyst. This confirmed the presence of an electron transfer from Cu to Pt such that the electronic properties of platinum atoms were strongly modified by copper addition. As the surface coverage increased by exposure time, the CO stretching frequency of Pt and Cu bounded CO shifted to a higher frequency (about 10 cm^{-1}) due to the dipole-dipole coupling between adsorbed CO on Pt and Cu surface. During the evacuation, the charge transfer enhanced the electron density on Pt atoms ensuring that, the adsorption of CO on Pt was much strong than that on Cu. Furthermore, the evidence that the Pt and Cu were

atomically mixed in the catalyst was provided by the increase of the Pt^0-CO band during the evacuation at the expense of that of Cu^0-CO due to an energy intensity redistribution effect.[8]

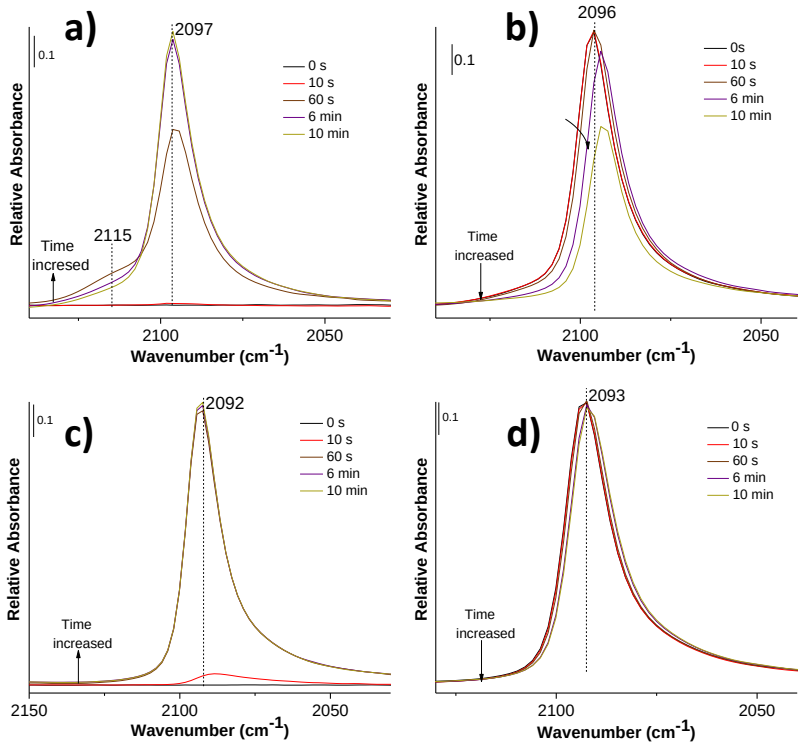

Fig. 4.30 – DRIFT spectra in the carbonyl region recorded during the adsorption (a, c) and desorption (b, d) of CO at room temperature on Pt/SiO_2 catalyst after the (a, b) oxidizing and (c, d) reduction treatments.

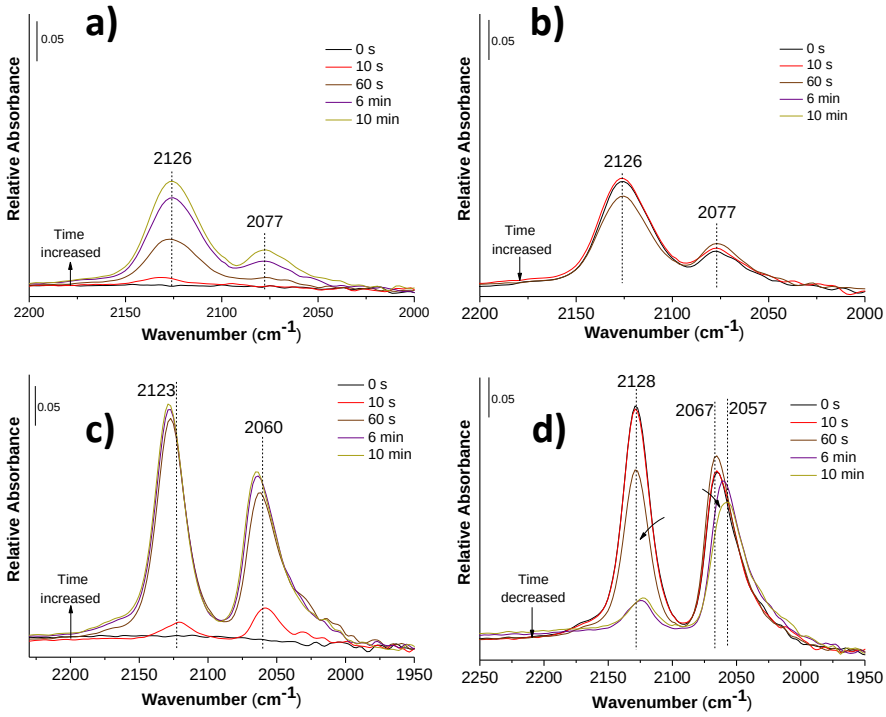

Fig. 4.31 – DRIFT spectra in the carbonyl region recorded during the adsorption (a, c) and desorption (b, d) of CO at room temperature on $PtCu/SiO_2$ catalyst after the (a, b) oxidizing and (c, d) reduction treatments.

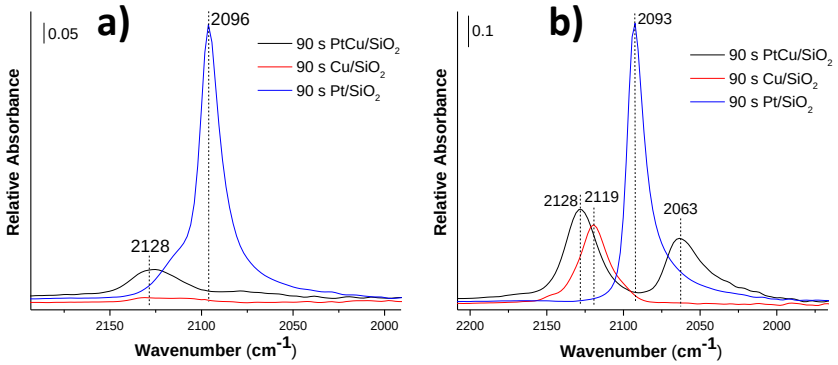

Fig. 4.32 – Comparison between the DRIFTS spectra taken after 90 s of exposure to the probe gas in the carbonyl region recorded during the adsorption of CO at room temperature on $PtCu/SiO_2$, Pt/SiO_2 and Cu/SiO_2 catalysts after the (a) oxidizing and (b) reducing pre-treatments.

4.2.2 Silica Supported NCs Under CO Oxidation Reaction

A different scenario was observed in the CO oxidation reaction when the PtCu NCs were supported on silica compared to the alumina support. Figure 4.33 reported the catalytic activity measured in the third repeated test after oxidizing and reducing pre-treatments for the $PtCu/SiO_2$ catalyst. After both the oxidizing and the reducing pre-treatment, the same activity trend was observed. Namely, the CO conversion resulted to be higher during the heating ramp of the experiment compared to the cooling transient. The pre-treatment atmosphere affected however the measured activity during the heating phase of the experiments, which resulted to be higher right after the reducing treatment.

However, it is still not clear how the catalyst evolves when exposed to the CO/O_2 mixture and thus which active species are involved during the entire catalytic reaction. In this regard, *in situ* DRIFTS and XAFS analyses would be required to gain better insights into this system.

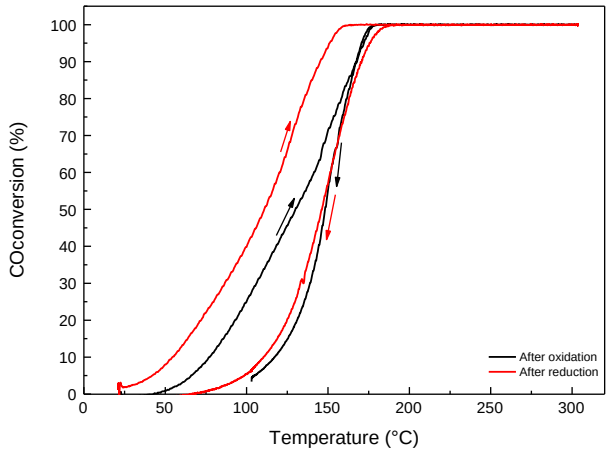

Fig. 4.33 – Catalytic activity of $PtCu/SiO_2$ catalyst in CO oxidation after the oxidizing and reducing pre-treatments during the third repeated test.

As a preliminary evaluation, the reduced $PtCu/SiO_2$ catalyst was exposed to O_2 at room temperature and at 80 °C and the surface composition was probe by *in situ* CO-DRIFTS (Fig. 4.34). After the O_2 exposure at room temperature and 80 °C, the bands at 2065 cm^{-1} and 2129 cm^{-1} associated to the CO adsorbed on Pt^0 and Cu^0 were still present and almost in the same position of those of the reduced sample with a decreased intensity, especially in the case of the Cu^0 band. In particular, the peak at 2066 cm^{-1} shifted slightly towards higher wavenumber, suggesting that the number of metallic Pt sites exposed on the surface decreased, as though the Cu^0 ones. As already observed in the case of $PtCu/Al_2O_3$ sample (Fig. 4.24b), the desorption spectra acquired on the reduced sample exposed to O_2 showed that the CO molecules on Pt^0 desorbed already at room temperature. This can be related to the higher activity observed at low temperature for the reduced system, in which the CO molecules are weakly adsorbed on the Pt^0 surface.

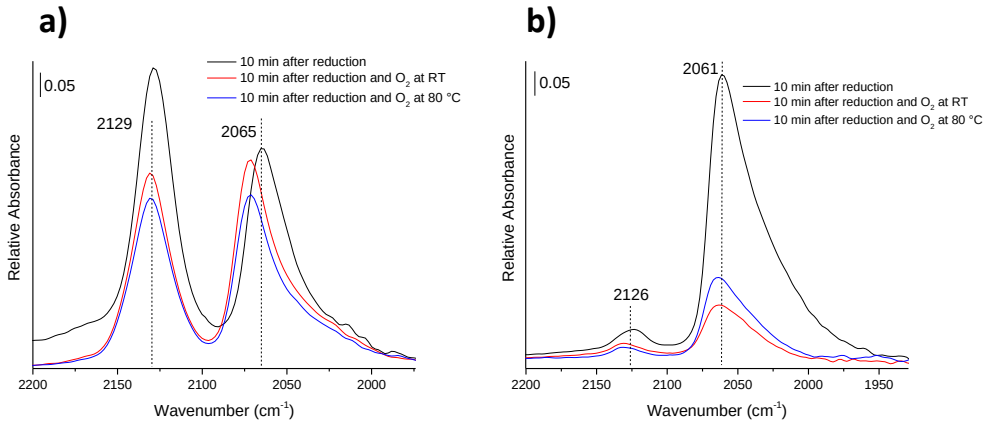

Fig. 4.34 – DRIFT spectra in the carbonyl region recorded during adsorption (a) and desorption (b) of CO at room temperature recorded after 10 min on $PtCu/SiO_2$ catalyst after reduction treatment and the exposure to O_2 flow at room temperature and at 80 °C for 30 min.

Finally, the sample underwent a series of cycles in order to evaluate the impact of the pre-treatments in the performance of the catalyst. In the repeated tests for $PtCu/SiO_2$ catalyst (Fig. 4.35), after oxidizing pre-treatment during the heating phase, the activity was unreproducible, with a maximum of conversion during the second test. This aspect needs to be further investigated: the possibility of catalyst deactivation cannot be excluded, even though no changes in activity during the cooling phase of the test could be observed.

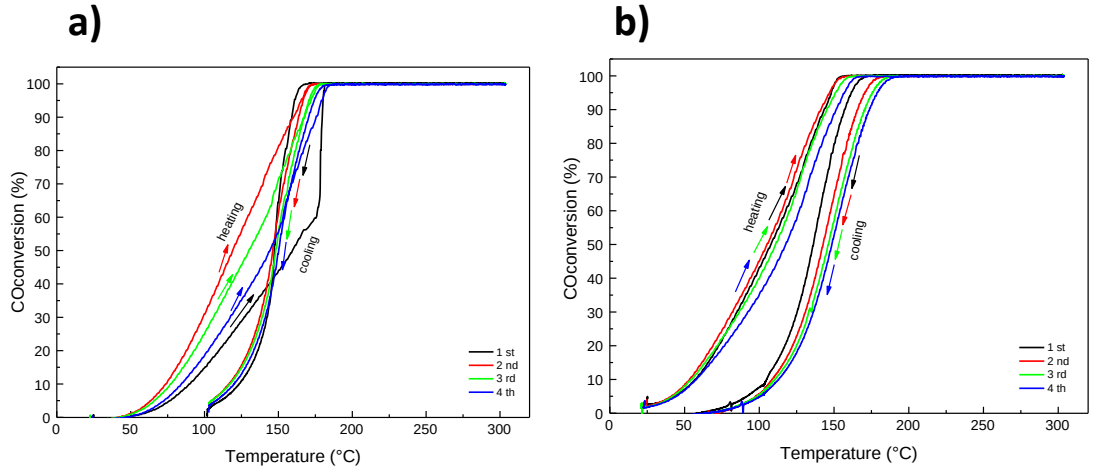

Fig. 4.35 – Catalytic activity during four reaction cycles of $PtCu/SiO_2$ catalyst in CO oxidation after oxidizing (a) and reducing (b) pre-treatments.

Appendix A

SOLEIL Synchrotron EXAFS Fitting Data Elaboration

Table A.1 – Structural parameters obtained from the fitting of EXAFS at the Pt L_{III}-edge for the $PtCu/Al_2O_3$ catalyst (k range for the Fourier transform 2.5-12.4 $Å^{-1}$, the R-range for the fitting was 1-3.5/4 Å - dashed line window in the figures).

Sample	***Scattering Path***	***CN***	***R (Å)***	***σ^2(Å²)***	***R-factor***
PtCu Pt edge red D_r	***PtO phase***				0.029
	Pt-O1	1.79 ± 0.2	2.008 ± 0.010	0.003 ± 0.001	
	Pt-Pt1	1.79 ± 0.2	3.070 ± 0.015	0.005 ± 0.0006	
	Pt Phase				
	Pt-Pt1	4.24 ± 0.6	2.762 ± 0.015	0.005 ± 0.0006	

Sample	***Scattering Path***	***CN***	***R (Å)***	***σ^2(Å²)***	***R-factor***
PtCu Pt edge red A_r	***PtCu alloy***				0.023
	Pt-Pt1	8.00 ± 0.6	2.747 ± 0.005	0.008 ± 0.0004	
	Pt-Cu1	1.52 ± 0.6	2.665 ± 0.013	0.010 ± 0.003	
	PtCu alloy				
	Pt-Pt2	4.00 ± 0.3	3.852 ± 0.005	0.008 ± 0.0004	
	Pt-Cu2	0.76 ± 0.3	3.771 ± 0.013	0.010 ± 0.003	

Sample	***Scattering Path***	***CN***	***R (Å)***	***σ^2(Å²)***	***R-factor***
PtCu Pt edge oxi D_O	***PtCu alloy***				0.017
	Pt-Pt1	6.96 ± 0.8	2.721 ± 0.004	0.006 ± 0.0004	
	Pt-Cu1	2.83 ± 0.7	2.680 ± 0.011	0.008 ± 0.0018	
	PtCu alloy				
	Pt-Pt2	3.48 ± 0.4	3.827 ± 0.004	0.006 ± 0.0004	
	Pt-Cu2	1.42 ± 0.4	3.787 ± 0.011	0.008 ± 0.0018	

Sample	***Scattering Path***	***CN***	***R (Å)***	***σ^2(Å²)***	***R-factor***
PtCu Pt edge oxi A_O	***Pt phase***				0.027
	Pt-Pt1	8.90 ± 0.7	2.734 ± 0.006	0.012 ± 0.0007	
	PtO phase				
	Pt-O1	0.36 ± 0.2	2.068 ± 0.035	-0.001 ± 0.004	
	Pt-Pt2	0.36 ± 0.2	3.225 ± 0.006	0.012 ± 0.0007	

Sample	***Scattering Path***	***CN***	***R (Å)***	***σ^2(Å²)***	***R-factor***
PtCu Pt edge RT He	***Pt phase***				0.021
	Pt-Pt1	3.44 ± 0.4	2.764 ± 0.004	0.005 ± 0.0004	
	PtO phase				
	Pt-O2	2.17 ± 2.2	2.010 ± 0.008	0.004 ± 0.0008	
	Pt-Pt1	0.81 ± 0.8	3.082 ± 0.019	0.005 ± 0.0004	
	Pt-Pt2	1.63 ± 1.6	3.470 ± 0.019	0.005 ± 0.0004	

Table A.2 – Structural parameters obtained from the fitting of EXAFS at the Cu K-edge for the $PtCu/Al_2O_3$ catalyst (k range for the Fourier transform 2.5-12.4 $Å^{-1}$, the R-range for the fitting was 1-3.5/4 Å - dashed line window in the figures).

Sample	***Scattering Path***	***CN***	***R (Å)***	***σ^2(Å²)***	***R-factor***
PtCu Cu edge red D_r	***CuO phase***				0.021
	Cu-O1	2.77 ± 0.4	1.952 ± 0.012	0.003 ± 0.002	
	Cu-Cu1	5.54 ± 0.7	2.936 ± 0.023	0.020 ± 0.003	

Sample	***Scattering Path***	***CN***	***R (Å)***	***σ^2(Å²)***	***R-factor***
PtCu Cu edge red I_r	***Cu_2O phase***				0.006
	Cu-O1	0.69 ± 0.2	1.901 ± 0.03	0.009 ± 0.013	
	Cu-Cu1	2.07 ± 0.7	2.950 ± 0.03	0.014 ± 0.004	
	PtCu alloy				
	Cu-Cu1	4.58 ± 0.5	2.607 ± 0.03	0.014 ± 0.004	
	Cu-Pt1	4.00 ± 0.6	2.574 ± 0.10	0.013 ± 0.100	

Sample	***Scattering Path***	***CN***	***R (Å)***	***σ^2(Å²)***	***R-factor***
PtCu Cu edge red A_r	***Cu_2O phase***				0.009
	Cu-O1	0.33 ± 0.2	1.927 ± 0.05	0.014 ± 0.011	
	Cu-Cu1	1.00 ± 0.5	2.955 ± 0.01	0.019 ± 0.002	
	PtCu alloy				
	Cu-Cu1	3.28 ± 0.6	2.613 ± 0.01	0.019 ± 0.002	
	Cu-Pt1	5.34 ± 0.7	2.613 ± 0.01	0.019 ± 0.003	

Sample	***Scattering Path***	***CN***	***R (Å)***	***σ^2(Å²)***	***R-factor***
PtCu Cu edge red D_O	***PtCu alloy***				0.020
	Cu-Cu1	3.88 ± 0.7	2.644 ± 0.011	0.011 ± 0.001	
	Cu-Pt1	4.87 ± 1.1	2.644 ± 0.012	0.011 ± 0.002	
	Cu_2O phase				
	Cu-O1	0.24 ± 0.2	1.900 ± 0.070	0.004 ± 0.013	
	Cu-Cu1	0.73 ± 0.6	3.013 ± 0.011	0.011 ± 0.001	

Sample	***Scattering Path***	***CN***	***R (Å)***	***σ^2(Å²)***	***R-factor***
PtCu Cu edge oxi I_O	***PtCu alloy***				0.014
	Cu-Cu1	4.72 ± 1.7	2.641 ± 0.015	0.018 ± 0.005	
	Cu-Pt1	4.10 ± 1.1	2.647 ± 0.019	0.012 ± 0.003	
	Cu_2O phase				
	Cu-O1	0.10 ± 0.2	1.831 ± 0.010	0.003 ± 0.002	
	Cu-Cu1	0.16 ± 0.5	2.986 ± 0.015	0.018 ± 0.005	

Sample	*Scattering Path*	*CN*	*R (Å)*	σ^2 *(Å²)*	*R-factor*
PtCu Cu edge oxi A_O	***CuO phase***				0.008
	Cu-O1	1.19 ± 0.1	1.953 ± 0.04	0.009 ± 0.002	
	Cu-Cu1	2.39 ± 0.2	2.643 ± 0.002	0.017 ± 0.002	
	Cu-O2	1.59 ± 0.2	1.934 ± 0.04	0.009 ± 0.002	
	Cu_2O phase				
	Cu-O1	1.08 ± 0.4	1.993 ± 0.04	0.010 ± 0.002	
	Cu-Cu1	3.24 ± 0.1	2.900 ± 0.002	0.018 ± 0.002	

Sample	*Scattering Path*	*CN*	*R (Å)*	σ^2 *(Å²)*	*R-factor*
PtCu Cu edge RT He	***CuO phase***				0.011
	Cu-O1	2.90 ± 0.2	1.955 ± 0.008	0.004 ± 0.001	
	Cu-Cu1	5.71 ± 0.5	2.921 ± 0.02	0.020 ± 0.003	
	Cu-O2	3.81 ± 0.3	3.692 ± 0.02	0.004 ± 0.001	

Appendix B

PSI Synchrotron EXAFS Fitting Data Elaboration

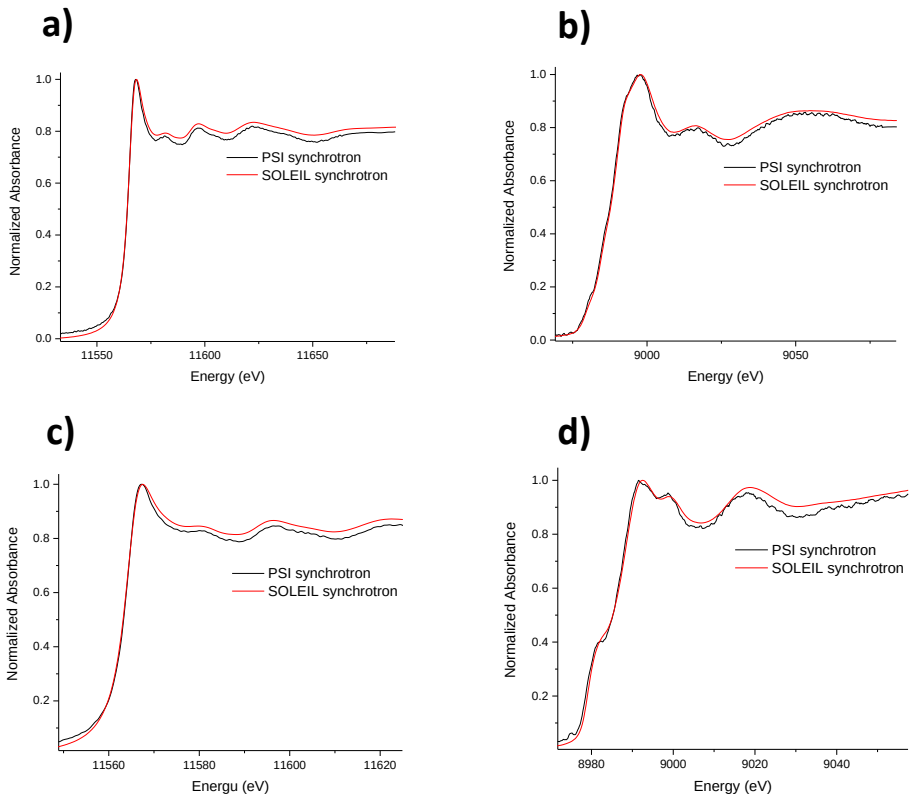

Fig. B.1 – XANES spectra of the $PtCu/Al_2O_3$ catalyst at the (a, c) Pt L_{III}-edge and (b, d) Cu K-edge after (a, b) oxidation and (c, d) reduction treatments acquired at SOLEIL and PSI synchrotrons.

Table B.1 – Structural parameters obtained from the fitting of EXAFS at the Pt L_{III}-edge for the reduced $PtCu/Al_2O_3$ catalyst during the CO oxidation reaction (k range for the Fourier transform 2.5-12.4 $Å^{-1}$, the R-range for the fitting was 1-3/4 Å – dashed blue line window in the figures).

Sample	***Scattering Path***	***CN***	***R (Å)***	***$\sigma^2(Å^2)$***	***R-factor***
PtCu Pt edge red CO react first spectrum heating ramp	***PtCu phase***				0.019
	Pt-Pt1	6.01 ± 1.16	2.727 ± 0.005	0.005 ± 0.001	
	Pt-Cu1	2.60 ± 0.54	2.663 ± 0.014	0.007 ± 0.002	
	PtCu phase				
	Pt-Pt2	3.07 ± 0.96	3.761 ± 0.016	0.005 ± 0.001	
	Pt-Cu2	1.32 ± 0.48	3.865 ± 0.044	0.007 ± 0.002	

Sample	***Scattering Path***	***CN***	***R (Å)***	***$\sigma^2(Å^2)$***	***R-factor***
PtCu Pt edge red CO react RT 300 last spectrum	***PtCu phase***				0.016
	Pt-Pt1	4.75 ± 0.99	2.743 ± 0.006	0.007 ± 0.001	
	Pt-Cu1	1.16 ± 0.48	2.644 ± 0.009	0.004 ± 0.002	
	PtO phase				
	Pt-O1	1.24 ± 0.23	2.207 ± 0.007	0.003*	
	Pt-Pt1	1.24 ± 0.23	3.113 ± 0.006	0.007 ± 0.001	

Sample	*Scattering Path*	*CN*	*R (Å)*	*σ^2(Å^2)*	*R-factor*
PtCu Pt edge red CO react 100 cooling last spectrum	***PtCu phase***				0.013
	Pt-Pt1	7.57 ± 1.16	2.724 ± 0.005	0.007 ± 0.001	
	Pt-Cu1	1.94 ± 0.94	2.683 ± 0.018	0.009 ± 0.003	
	PtO phase				
	Pt-O1	0.10*	1.996 ± 0.029	0.004 ± 0.002	
	Pt-Pt1	0.10*	3.094 ± 0.005	0.007 ± 0.001	

*Parameters were fixed in the fitting and obtained as the product of N of the shell from the model and adjusted S_0^2 for the reference Pt.

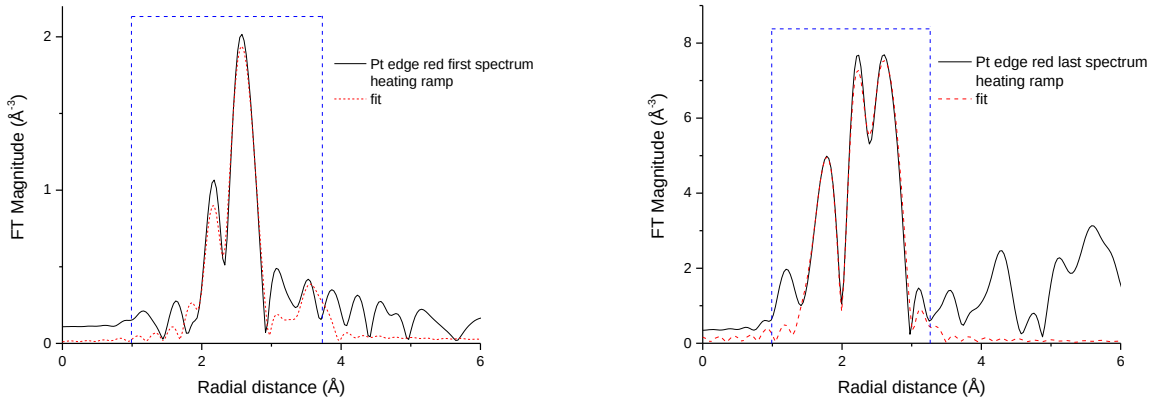

Fig. B.2 – FT magnitude with the best fit (dashed lines) of EXAFS spectrum of the reduced $PtCu/Al_2O_3$ catalyst collected (a) at the beginning and (b) at the end (300 °C) of the heating ramp during the CO oxidation reaction at the Pt L_{III} -edge.

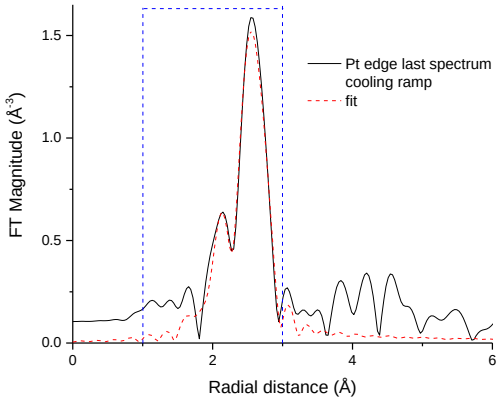

Fig. B.3 – FT magnitude with the best fit (dashed lines) of EXAFS spectrum of the reduced $PtCu/Al_2O_3$ catalyst collected at the end of the cooling ramp at 100 °C during the CO oxidation reaction at the Pt L_{III} -edge.

Table B.2 – Structural parameters obtained from the fitting of EXAFS at the Cu K-edge for the reduced $PtCu/Al_2O_3$ catalyst during the CO oxidation reaction (k range for the Fourier transform 2.5-12.4 $Å^{-1}$, the R-range for the fitting was 1-3/4 Å - dashed blue line window in the figures).

Sample	*Scattering Path*	*CN*	*R (Å)*	*σ^2($Å^2$)*	*R-factor*
PtCu Cu edge red CO react first spectrum heating ramp	***PtCu phase***				0.027
	Cu-Cu1	2.88*	2.657 ± 0.064	0.010 ± 0.009	
	Cu-Pt1	5.68*	2.653 ± 0.140	0.017 ± 0.008	
	Cu_2O phase				
	Cu-O1	0.35*	1.888 ± 0.050	0.001 ± 0.007	
	Cu-Cu1	1.06*	2.988 ± 0.064	0.010 ± 0.009	

Sample	*Scattering Path*	*CN*	*R (Å)*	*σ^2($Å^2$)*	*R-factor*
PtCu Cu edge red CO react RT 300 last spectrum	***PtCu phase***				0.030
	Cu-Cu1	0.01*	2.809 ± 0.700	0.012 ± 0.006	
	Cu-Pt1	0.01*	2.775 ± 0.630	0.010*	
	CuO phase				
	Cu-O1	1.54*	2.156 ± 0.690	0.004*	

Sample	*Scattering Path*	*CN*	*R (Å)*	*σ^2($Å^2$)*	*R-factor*
PtCu Cu edge red CO react 100 cooling last spectrum	***PtCu phase***				0.029
	Cu-Cu1	0.44 ± 0.36	2.497 ± 0.820	0.003*	
	Cu-Pt1	1.99 *	2.636 ± 0.905	0.003*	
	Cu_2O phase				
	Cu-O1	0.32*	1.767 ± 0.438	0.012 ± 0.004	
	Cu-Cu1	0.95*	2.736 ± 0.820	0.003*	
	CuO phase				
	Cu-O1	0.47*	1.936 ± 0.438	0.012 ± 0.004	

*Parameters were fixed in the fitting and obtained as the product of N of the shell from the model and adjusted S_0^2 for the reference Cu.

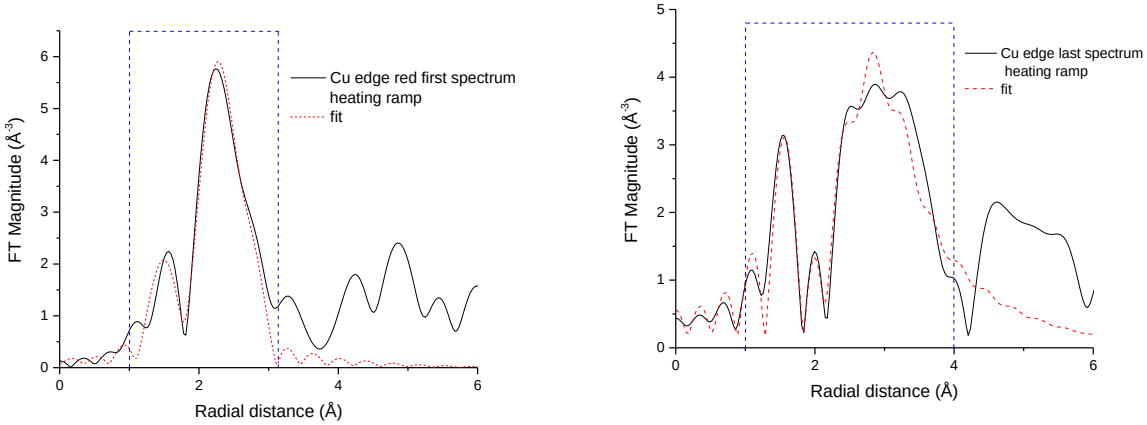

Fig. B.4 – FT magnitude with the best fit (dashed lines) of EXAFS spectrum of the reduced $PtCu/Al_2O_3$ catalyst collected (a) at the beginning and (b) at the end (300 °C) of the heating ramp during the CO oxidation reaction at the Cu K-edge.

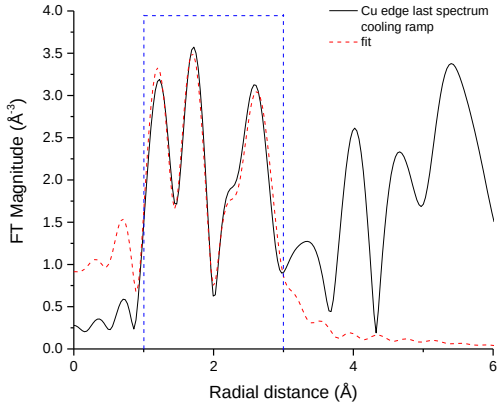

Fig. B.5 – FT magnitude with the best fit (dashed lines) of EXAFS spectrum of the reduced $PtCu/Al_2O_3$ catalyst collected at the end of the cooling ramp at 100 °C during the CO oxidation reaction at the Cu K-edge.

Table B.3 – Structural parameters obtained from the fitting of EXAFS at the Pt L_{III}-edge for the oxidized $PtCu/Al_2O_3$ catalyst during the CO oxidation reaction (k range for the Fourier transform 2.5-12.4 $Å^{-1}$, the R-range for the fitting was 1-3/4 Å - dashed blue line window in the figures).

Sample	***Scattering Path***	***CN***	***R (Å)***	***σ^2(Å^2)***	***R-factor***
PtCu Pt edge oxi CO react first spectrum heating ramp	***PtCu phase***				0.016
	Pt-Pt1	7.83 ± 0.93	2.750 ± 0.005	0.007 ± 0.001	
	Pt-Cu1	3.92 ± 0.46	2.667 ± 0.008	0.003*	
	PtO phase				
	Pt-O1	0.15 ± 0.10	2.096 ± 0.016	0.003 ± 0.002	
	Pt-Pt1	0.15 ± 0.10	3.114 ± 0.005	0.007 ± 0.001	

Sample	***Scattering Path***	***CN***	***R (Å)***	***σ^2(Å^2)***	***R-factor***
PtCu Pt edge oxi CO react RT 300 last spectrum	***PtCu phase***				0.021
	Pt-Pt1	4.38 ± 1.44	2.733 ± 0.009	0.008 ± 0.001	
	Pt-Cu1	1.77 ± 0.14	2.449 ± 0.016	0.003*	
	PtO phase				
	Pt-O1	0.66*	2.053 ± 0.015	0.004 ± 0.002	
	Pt-Pt1	0.66*	3.102 ± 0.009	0.008 ± 0.001	

Sample	***Scattering Path***	***CN***	***R (Å)***	***σ^2(Å^2)***	***R-factor***
PtCu Pt edge oxi CO react 100 cooling last spectrum	***PtCu phase***				0.014
	Pt-Pt1	8.83 ± 0.84	2.735 ± 0.005	0.006 ± 0.004	
	Pt-Cu1	1.05 ± 0.72	2.525 ± 0.020	0.007 ± 0.005	
	PtO phase				
	Pt-O1	0.23 ± 0.20	2.022 ± 0.033	0.003 ± 0.004	
	Pt-Pt1	0.23 ± 0.20	3.104 ± 0.005	0.006 ± 0.004	

*Parameters were fixed in the fitting and obtained as the product of N of the shell from the model and adjusted S_0^2 for the reference Pt.

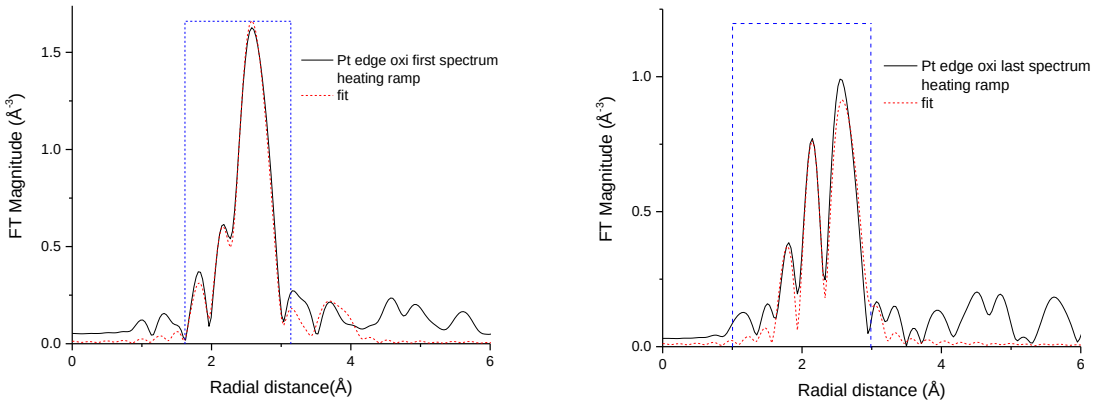

Fig. B.6 – FT magnitude with the best fit (dashed lines) of EXAFS spectrum of the oxidized $PtCu/Al_2O_3$ catalyst collected (a) at the beginning and (b) at the end (300 °C) of the heating ramp during the CO oxidation reaction at the Pt L_{III}-edge.

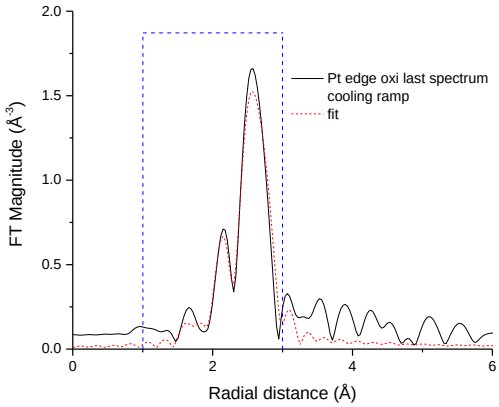

Fig. B.7 – FT magnitude with the best fit (dashed lines) of EXAFS spectrum of the oxidized $PtCu/Al_2O_3$ catalyst collected at the end of the cooling ramp at 100 °C during the CO oxidation reaction at the Pt L_{III}-edge.

Table B.4 – Structural parameters obtained from the fitting of EXAFS at the Cu K-edge for the oxidized $PtCu/Al_2O_3$ catalyst during the CO oxidation reaction (k range for the Fourier transform 2.5-12.4 $Å^{-1}$, the R-range for the fitting was 1-3/4 Å - dashed blue line window in the figures).

Sample	***Scattering Path***	***CN***	***R (Å)***	***σ^2($Å^2$)***	***R-factor***
PtCu Cu edge oxi CO react first spectrum heating ramp	***PtCu phase***				0.010
	Cu-Cu1	5.13 ± 1.44	2.312 ± 0.041	0.032 ± 0.005	
	Cu-Pt1	0.64 ± 0.48	2.700 ± 0.009	0.003 ± 0.004	
	CuO phase				
	Cu-O1	2.10 ± 0.30	1.952 ± 0.012	0.004 ± 0.002	
	Cu-Cu1	4.18 ± 0.60	2.644 ± 0.041	0.032 ± 0.005	

Sample	***Scattering Path***	***CN***	***R (Å)***	***σ^2($Å^2$)***	***R-factor***
PtCu Cu edge oxi CO react RT 300 last spectrum	***PtCu phase***				0.010
	Cu-Cu1	4.66*	2.431 ± 0.490	0.031 ± 0.016	
	Cu-Pt1	0.51*	2.592 ± 0.058	0.003*	
	CuO phase				
	Cu-O1	1.63 ± 0.30	1.953 ± 0.034	0.003 ± 0.003	
	Cu-Cu1	3.28 ± 0.60	2.761 ± 0.490	0.031 ± 0.016	

	Cu_2O phase				
	Cu-O1	1.53 ± 0.20	2.539 ± 0.034	0.003 ± 0.003	
	Cu-Cu1	4.61 ± 0.60	3.476 ± 0.370	0.031 ± 0.016	

Sample	***Scattering Path***	***CN***	***R (Å)***	***σ^2(Å^2)***	***R-factor***
PtCu Cu edge oxi CO react 100 cooling last spectrum	***PtCu phase***				0.021
	Cu-Cu1	4.80*	2.466 ± 0.022	0.027 ± 0.003	
	Cu-Pt1	0.06*	2.782 ± 0.010	0.003*	
	CuO phase				
	Cu-O1	2.67 ± 0.43	1.943 ± 0.009	0.009 ± 0.003	
	Cu-Cu1	5.34 ± 0.86	2.797 ± 0.022	0.027 ± 0.003	

*Parameters were fixed in the fitting and obtained as the product of N of the shell from the model and adjusted S_0^2 for the reference Cu.

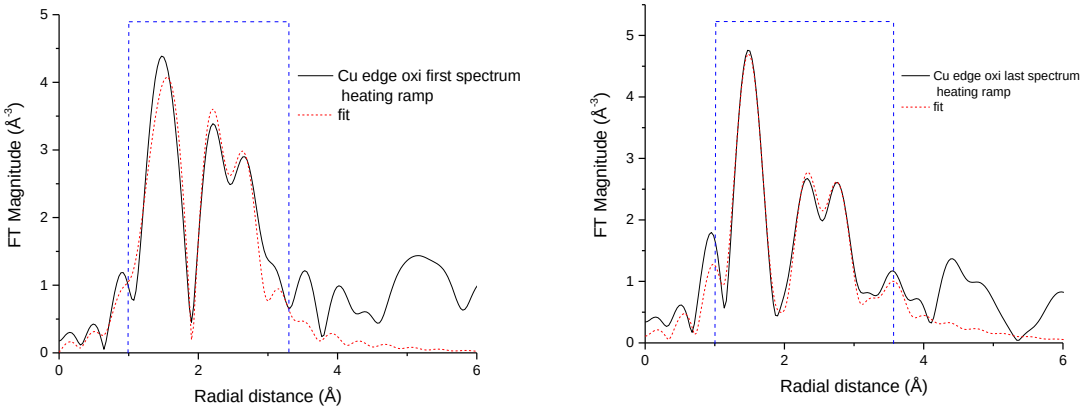

Fig. B.8 – FT magnitude with the best fit (dashed lines) of EXAFS spectrum of the oxidized $PtCu/Al_2O_3$ catalyst collected (a) at the beginning and (b) at the end (300 °C) of the heating ramp during the CO oxidation reaction at the Cu K-edge.

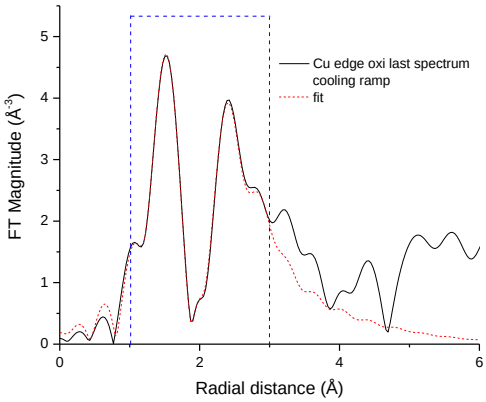

Fig. B.9 – FT magnitude with the best fit (dashed lines) of EXAFS spectrum of the oxidized $PtCu/Al_2O_3$ catalyst collected (a) at the end of the cooling ramp at 100 °C during the CO oxidation reaction at the Cu K-edge.

References

1. Gümeci, C.; Cearnaigh, D. U.; Casadonte, D. J.; Korzeniewski, C., Synthesis of $PtCu_3$ bimetallic nanoparticles as oxygen reduction catalysts via a sonochemical method. *J Mater Chem A* 2013, 1, 2322-2330.

2. Gupta, G.; Slanac, D. A.; Kumar, P.; Wiggins-Camacho, J. D.; Wang, X.; Swinnea, S.; More, K. L.; Dai, S.; Stevenson, K. J.; Johnston, K. P., Highly stable and active Pt−Cu oxygen reduction electrocatalysts based on mesoporous graphitic carbon supports. *Chem Mater* 2009, 21, 4515-4526.

3. Hadjiivanov, K. I.; Vayssilov, G. N., Characterization of oxide surfaces and zeolites by carbon monoxide as an IR probe molecule. *Adv Catal* 2002, 47, 307-511.

4. Hollins, P., The influence of surface defects on the infrared spectra of adsorbed species. *Surf Sci Rep* 1992, 16, 51-94.

5. Kale, M. J.; Christopher, P., Utilizing quantitative in situ FTIR spectroscopy to identify well-coordinated Pt atoms as the active site for CO oxidation on Al_2O_3-supported Pt catalysts. *ACS Catal* 2016, 6, 5599-5609.

6. Borovkov, V. Y.; Luebke, D. R.; Kovalchuk, V. I.; d'Itri, J. L., Hydrogen-assisted 1, 2-dichloroethane dechlorination catalyzed by Pt−Cu/SiO_2: evidence for different functions of Pt and Cu sites. *J Phys Chem B* 2003, 107, 5568-5574.

7. Komatsu, T.; Takasaki, M.; Ozawa, K.; Furukawa, S.; Muramatsu, A., PtCu intermetallic compound supported on alumina active for preferential oxidation of CO in hydrogen. *J Phys Chem C* 2013, 117, 10483-10491.

8. Akonwie, L. N.; Kazachkin, D.; Luebke, D.; d'Itri, J. L., Effect of catalyst pre-reduction temperature on the reaction of 1, 2-dichloroethane and H_2 catalyzed by SiO_2-supported PtCu bimetallics. *Appl Catal A* 2012, 415, 59-69.

9. Bugaev, A. L.; Skorynina, A. A.; Braglia, L.; Lomachenko, K. A.; Guda, A.; Lazzarini, A.; Bordiga, S.; Olsbye, U.; Lillerud, K. P.; Soldatov, A. V., Evolution of Pt and Pd species in functionalized UiO-67 metal-organic frameworks. *Catal Today* 2019, 25, 104280.

10. Martini, A.; Alladio, E.; Borfecchia, E., Determining Cu–speciation in the Cu–CHA zeolite catalyst: the potential of multivariate curve resolution analysis of in situ XAS data. *Top Catal* 2018, 61, 1396-1407.

11. Vukojević, S.; Trapp, O.; Grunwaldt, J. D.; Kiener, C.; Schüth, F., Quasi-homogeneous methanol synthesis over highly active copper nanoparticles. *Angew Chem Int Ed* 2005, 44, 7978-7981.

12. Staniuk, M.; Zindel, D.; Van Beek, W.; Hirsch, O.; Kränzlin, N.; Niederberger, M.; Koziej, D., Matching the organic and inorganic counterparts during nucleation and growth of copper-based nanoparticles–in situ spectroscopic studies. *CrystEngComm* 2015, 17, 6962-6971.

13. Yamamoto, T. A.; Nakagawa, T.; Seino, S.; Nitani, H., Bimetallic nanoparticles of PtM (M= Au, Cu, Ni) supported on iron oxide: radiolytic synthesis and CO oxidation catalysis. *Appl Catal A* 2010, 387, 195-202.

14. Komatsu, T.; Tamura, A., Pt_3Co and PtCu intermetallic compounds: Promising catalysts for preferential oxidation of CO in excess hydrogen. *J Catal* 2008, 258, 306-314.

15. Zhang, G.; Yang, Z.; Zhang, W.; Hu, H.; Wang, C.; Huang, C.; Wang, Y., Tailoring the morphology of Pt_3Cu_1 nanocrystals supported on graphene nanoplates for ethanol oxidation. *Nanoscale* 2016, 8, 3075-3084.

16. Dai, S.; You, Y.; Zhang, S.; Cai, W.; Xu, M.; Xie, L.; Wu, R.; Graham, G. W.; Pan, X., In situ atomic-scale observation of oxygen-driven core-shell formation in Pt_3Co nanoparticles. *Nature Commun* 2017, 8, 204.

17. Mayrhofer, K. J.; Juhart, V.; Hartl, K.; Hanzlik, M.; Arenz, M., Adsorbate-induced surface segregation for core–shell nanocatalysts. *Angew Chem Intern Ed* 2009, 48, 3529-3531.

18. Dai, S.; Hou, Y.; Onoue, M.; Zhang, S.; Gao, W.; Yan, X.; Graham, G. W.; Wu, R.; Pan, X., Revealing surface elemental composition and dynamic processes involved in facet-dependent oxidation of Pt_3Co nanoparticles via in situ transmission electron microscopy. *Nano Lett* 2017, 17, 4683-4688.

19. Nolan, P.; Lutz, B.; Tanaka, P.; Davis, J.; Mullins, C., Molecularly chemisorbed intermediates to oxygen adsorption on Pt (111): A molecular beam and electron energy-loss spectroscopy study. *J Chem Phys* 1999, 111, 3696-3704.

20. Gao, F.; Wang, Y.; Goodman, D. W., CO oxidation over AuPd (100) from ultrahigh vacuum to near-atmospheric pressures: CO adsorption-induced surface segregation and reaction kinetics. *J Phys Chem C* 2009, 113, 14993-15000.

21. Oxford, S. M.; Lee, P. L.; Chupas, P. J.; Chapman, K. W.; Kung, M. C.; Kung, H. H., Study of supported PtCu and PdAu bimetallic nanoparticles using in-situ X-ray tools†. *J Phys Chem C* 2010, 114, 17085-17091.

22. Shan, J.; Zhang, S.; Choksi, T.; Nguyen, L.; Bonifacio, C. S.; Li, Y.; Zhu, W.; Tang, Y.; Zhang, Y.; Yang, J. C., Tuning catalytic performance through a single or sequential post-synthesis reaction (s) in a gas phase. *ACS Catal* 2016, 7, 191-204.

23. Calvin, S., *XAFS for Everyone*. CRC Press: 2013.

24. Subramanian, P., *Phase diagrams of binary copper alloys*. Vol. 10, ASM Int 1994.

Chapter 5

Discussion

The results obtained revealed that the PdCu and PtCu bimetallic catalysts, when exposed to oxidative or reductive atmospheres and CO reaction environment, were composed of a complex mixture of phases. Moreover, the observed processes of alloy/dealloy depending on the type of the noble metal, driven by temperature and gas composition, were revealed to be strongly influenced also by the support material, thus leading to different situations even when applying the same pre-treatments.

Specifically, for the PdCu system, a PdCuO mixed oxide was found after oxidation in the case of PdCu supported on Al_2O_3 revealed by XRD, in situ DRIFT and XAFS measurements; on the contrary, a PdO crystal structure was detected by XRD in the presence of amorphous CuO_x species on the NC surface for the silica supported NCs. Reducing the catalysts, restored the initial supported PdCu NCs with a different extent depending on the support. A 40% of Cu was reincorporated in the NCs supported on SiO_2 versus 36% for PdCu NCs on Al_2O_3 forming a Pd-rich disordered alloy. In both cases, the unincorporated Cu was found to be in the form of amorphous CuO_x and, in the case of $PdCu/Al_2O_3$, also in the form of metallic copper, as detected by XAFS, indicating the formation of isolated copper metallic domains (Fig. 5.1).

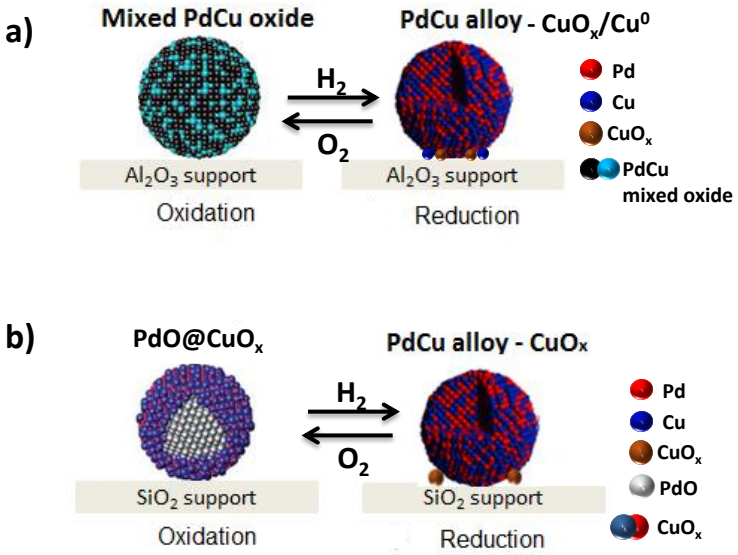

Fig. 5.1 – Schematic drawing of the structural changes of PdCu NCs supported on (a) γ-Al_2O_3 and (b) SiO_2 supports after the exposure to oxidative and reductive environments.

In the case of PtCu NCs, it is possible to claim that the oxidizing pre-treatment led to a complete dealloy between the Cu and the noble metal present in the NCs, with a different spatial arrangement of the formed CuO_x phases, depending on the type of the support used. A Pt crystal structure was revealed by XRD with CuO_x founded as isolated species away from the NCs on the support from EDX, DRIFTS and XANES measurements for the alumina supported PtCu NCs. On the other hand, a Pt core @ CuO_x shell structures, detected by XRD, DRIFTS and EDX, were obtained when the PtCu NCs were supported on SiO_2 (Fig. 5.2).

Reducing the catalyst restored partially the PtCu alloyed NCs independent from the type of the support (Fig. 5.2); indeed, a Pt-rich PtCu alloy was found from the EXAFS analysis for the alumina supported NCs with only a 12% of Cu reincorporated in the NCs calculated from XRD. Likewise, the silica supported NCs were characterized by a small amount of Cu in the bulk (10% of Cu reincorporated in the NCs from XRD) and a more Cu rich alloy in the outer shell, as observed by the significant charge transfer in the DRIFT spectra.

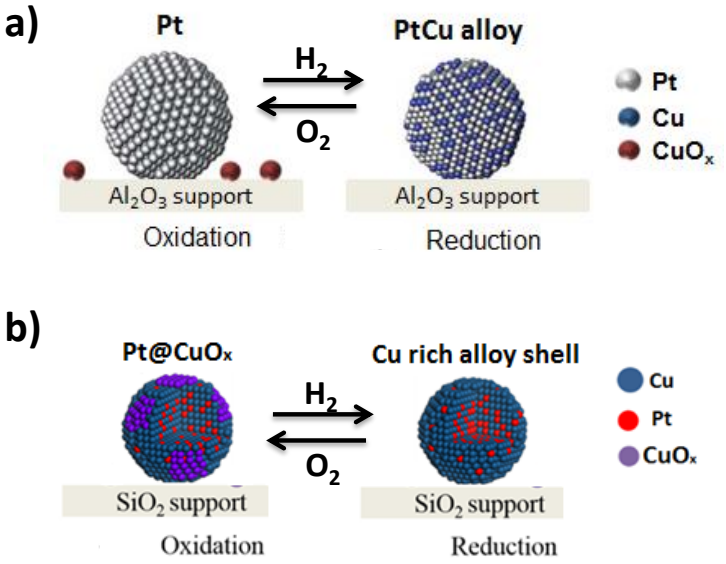

Fig. 5.2 – Schematic drawing of the structural changes of PtCu NCs supported on (a) γ-Al_2O_3 and (b) SiO_2 supports after the exposure to oxidative and reductive environments.

Considering the results obtained from the silica and alumina supported PdCu catalysts and comparing them with those in which the Pd noble metal was replaced with Pt within the NCs, it was evident that the CuO_x species formed under the oxidizing conditions in the silica supported PdCu and PtCu NCs were always located in the proximity of the NCs with limited Cu migration on the SiO_2 support (Figs. 5.1 and 5.2). Indeed, an atomic percentage of Cu of about 40% was found for the PtCu NCs supported on SiO_2 compared to 30% of Cu when supported on γ-Al_2O_3. On the other hand, a different scenario was observed after oxidation when the PdCu and PtCu NCs were supported on alumina. As obtained from the AuCu/Al_2O_3 system in which the CuO_x was founded as isolated species away from the Au NCs on the support after the oxidizing treatment[52, 64], the same situation was observed for the PtCu NCs as opposed to the PdCu NCs in which the oxidized copper was retained by the palladium with the formation of PdCuO mixed oxide. In general, during the reduction, independently from the type of support, the CuO_x species

founded near the particles or away on the support were partially realloyed within the Pt NCs with a minor extent compared to the PdCu NCs. Indeed, a 40% of Cu was reincorporated in the PdCu NCs supported on SiO_2 versus 10% for PtCu NCs on SiO_2, and 36% of Cu for PdCu NCs on Al_2O_3 versus 12% for PtCu on the same support. In the latter case, as confirmation of this assumption, the EXAFS results obtained at the end of the reductive treatment showed higher coordination numbers of 2.66 ± 0.47 in the Pd-Cu1 first shell and 1.04 ± 0.63 in the Pd-Cu2 second shell for the PdCu phase compared to those obtained for the PtCu alloy (CN_{Pt-Cu1} = 1.52 ± 0.6, CN_{Pt-Cu2} = 0.76 ± 0.3). This suggested that a greater number of Cu atoms are present around the Pd emitter atoms after the reductive treatment.

The above mentioned structural changes driven by gas atmospheres can be correlated with the catalytic activity of $PtCu/Al_2O_3$ catalyst in the CO oxidation reaction. As already observed for the PdCu system, it has been accepted that the Pt–CuO_x interface significantly favors the Langmuir-Hinshelwood (L-H) mechanism that occurred over transition metal oxides,[1, 2, 3] in which the CuO_x species provides the O species to oxidize the adsorbed CO molecules, in contact with Pt^0 atoms (Fig. 5.3). Additionally, the electron transfer from Pt atoms to Cu ones generated electron deficient Pt atoms, accelerating the adsorption of oxygen instead of CO.[1] Thus, the synergetic effect between the two metals and the presence of CuO_x phases led to the formation of the Pt^0/Cu^0-CuO interfaces responsible for the enhanced catalytic activity after reduction. On the other hand, the decreased activity observed in the cooling phase was related to the PtCu NC dealloy with Pt NC enrichment (from EXAFS CN_{Pt-Pt1} = 7.57 ± 1.16) and the copper oxides spread on the support in the form of small clusters. In this case, the supply of oxygen was not sufficient due to fewer contact between PtCu alloy and CuO. After oxidation, the presence of a higher number of Pt^0-Pt^0 and Cu^0-Cu^0 neighbors from EXAFS elaboration CN_{Pt-Pt1} = 7.83 ± 0.93, CN_{Cu-Cu1} = 5.13 ± 1.44 implied the decreased amount of Pt^0/Cu^0-CuO interfaces and the increased CO adsorption on Pt^0 and Cu^0 with a decrease in the light-off activity due to the inhibition effect of CO molecules strongly bounded to metallic sites.

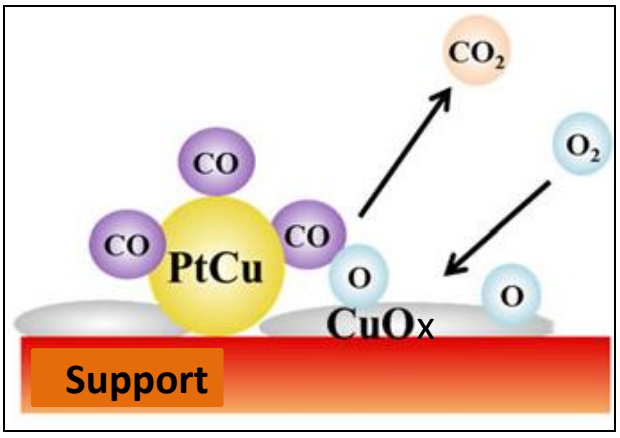

Fig. 5.3 – Schematic illustration of the Langmuir-Hinshelwood mechanism that occurred over transition metal oxides. Adapted with permission from [5]. Copyright (2013) Springer Nature.

The evidence of enhanced activity for the PtCu NCs supported on SiO_2 compared to that of PtCu on Al_2O_3 after the oxidizing treatment can be correlated with the higher closeness of Pt and CuO_x species at the interface forming a Pt@CuO_x structure for the fist system, as observed in a

previous study.[1] Indeed, it was reported that Cu/SiO_2 showed less activity than $PtCu/SiO_2$ catalysts. Therefore, Pt was indispensable for CO adsorption and the subsequent oxidation, while CuO acted as a promoter of active Pt.[4] This configuration enhanced the catalytic activity for $PtCu/SiO_2$ system highlighting the importance of the interface between the noble metal and the Cu oxide species, in which CuO-enhanced oxygen adsorption and transport through the alloy-CuO contact and functioned well as a promoter for the PtCu alloy.

However, in addition to the presence of this interface as the catalytically active region for the $PtCu/SiO_2$ catalyst after oxidation, the intimate contact between Pt and Cu in the alloyed NCs obtained with a reducing treatment boosted the CO conversion. Indeed, the synergetic effect between the two metals, as adsorption sites for different reactants, increased the catalytic activity compared to that measured after the oxidation, as found in the case of $AuCu/Al_2O_3$ system.[6]

References

1. Komatsu, T.; Takasaki, M.; Ozawa, K.; Furukawa, S.; Muramatsu, A., PtCu intermetallic compound supported on alumina active for preferential oxidation of CO in hydrogen. *J Phys Chem C* 2013, 117, 10483-10491.

2. Komatsu, T.; Tamura, A., Pt_3Co and PtCu intermetallic compounds: Promising catalysts for preferential oxidation of CO in excess hydrogen. *J Catal* 2008, 258, 306-314.

3. Royer, S.; Duprez, D., Catalytic oxidation of carbon monoxide over transition metal oxides. *ChemCatChem* 2011, 3, 24-65.

4. Sun, D.; Gu, X.-K.; Ouyang, R.; Su, H.-Y.; Fu, Q.; Bao, X.; Li, W.-X., Theoretical study of the role of a metal–cation ensemble at the oxide–metal boundary on CO oxidation. *J Phys Chem C* 2012, 116, 7491-7498.

5. Moriya, T.; et al., CuO role in γ-Fe_2O_3-supported Pt–Cu bimetallic nanoparticles synthesized by radiation-induced reduction as catalysts for preferential CO oxidation. *J Nanopart Res* 2013, 15, 1451.

6. Najafishirtari, S.; Brescia, R.; Guardia, P.; Marras, S.; Manna, L.; Colombo, M., Nanoscale transformations of alumina-supported AuCu ordered phase nanocrystals and their activity in CO oxidation. *ACS Catal* 2015, 5, 2154-2163.

Chapter 6

Conclusions

The structure of heterogeneous catalysts is dynamic and depends on the composition of the surrounding environment. Thus, both their surface, structure and composition may be modified when the gaseous conditions change. This occurs in order for the catalyst to adapt its electronic properties and geometry to the new surrounding environment.

In this regard, we have corroborated the importance of the gas atmosphere and temperature in modifying the structure of two families of bimetallic PdCu and PtCu NCs. This was achieved by studying the transformations of our NC samples when exposed to either oxidative or reductive gas conditions.

Also, we demonstrated the pivotal role of the metal-support interaction, selecting two different γ-Al_2O_3 and SiO_2 supports and studying the reorganization of metal atoms of supported bimetallic catalysts which occurred under operating conditions. Eventually, we showed that this effect has a strong influence on the catalytic performance.

For example, the oxidizing treatment led to segregation between the noble metal (NM) and copper with different spatial arrangement of the CuO_x species depending on the type of NM and support used. PdCuO mixed oxide was found in the case of PdCu NC supported on Al_2O_3, instead for PtCu NCs the CuO_x species were located away from the Pt NCs on the support. Thus, the change of the NM in the NCs showed that the oxidized copper was retained by the palladium. On the contrary, considering the silica support, the CuO_x species formed during the oxidation were always located in the proximity of the NCs independent from the type of NM.

On the other hand, reducing the catalysts, restored the initial supported PdCu NCs and partially the PtCu NCs with a different extent depending on the support. Indeed, a 40% of Cu was reincorporated in the PdCu NCs supported on SiO_2 versus 10% for PtCu NCs on SiO_2, and 36% of Cu for PdCu NCs on Al_2O_3 versus 12% for PtCu on the same support.

Additionally, we have demonstrated how the structural changes of the NCs occurring as a consequence of the pre-treatments affected their catalytic properties in the CO oxidation reaction by the observation of different trends in their activities. Such modifications show how heterogeneous catalysts are dynamically adapting to the external atmosphere, and transform depending on the specific environment to which they are exposed to. This brings to a pivotal change in the way heterogeneous catalysts have been seen so far. Similarly, active sites have to be considered as dynamic species rather than static ones.

The results of this work point out on the understanding of gas induced transformations of catalysts: these cannot be considered only in a passive way, but should be considered and exploited as a new way to produce new catalytic materials, which are not achievable through classical synthetic methodologies. For example, typical current synthesis methods do not allow for the production of stable catalysts made of Cu NCs homogenously distributed onto alumina support, as these systems undergo Ostwald ripening upon catalytic reactions. On the other hand, the use of bimetallic Cu-NM NCs could circumvent such issues and behave as reversible sintering centers toward a reversible catalyst deactivation.

Considering the different trends observed for the silica supported NC systems in the CO oxidation reaction, a logical extension of this work should focus on the comprehension of how the reacting environments affect the structure of the PtCu and PdCu bimetallic NCs supported on SiO_2. To do so, the in-situ quick scanning extended X-ray absorption fine structure analysis should be taken into consideration. This technique should be implemented to monitor both the change of oxidation state of the elements as well as verify the interaction noble metal-Cu-support. In this way, information about the modification of the system during the oxidizing and reducing treatments as well as during the CO oxidation reaction are provided. Furthermore, DRIFTS tests on the alumina and silica supported NCs should be performed during the NC exposure to CO reaction stream and the evolution of metal oxidation states on the samples will be tracked. Besides this, density functional theory calculations could be employed to rationalize the role of the NM and the support in the mentioned transformations.

Acknowledgments

I would like to start by thanking Prof. Liberato Manna who gave me the opportunity to work within the highly scientific and international environment of IIT. I would like to express my gratitude to my supervisor Dr. Massimo Colombo for his guidance, support, and patience at every step of my research. I would also like to acknowledge Prof. Riccardo Ferrando of the University of Genoa for his suggestions on my PhD work.

Many thanks to Prof. Daniela Zanchet from University of Campinas, Brasil, and Dr. Nancy Artioli, from School of Chemistry and Chemical Engineering, Queen's University, Belfast, United Kingdom, for their insightful comments and positive evaluation of my work.

A special thanks to the catalysis PhD students Chunzheng Wu, Sharif Najafishirtari, Cansunur Demirci, Tathiana Midori Kokumai, and Carmen Andrada Mak Biriescu for their valuable suggestions during the group meetings and their friendly collaboration. In particular, I am grateful to Cansunur and Sharif for their participation and help during the experiments carried out at SOLEIL Synchrotron (France) and PSI Synchrotron (Switzerland).

I would like to thank the lab technicians Simone Nitti, Giammarino Pugliese Gabriele La Rosa, Francesco De Donato, and Filippo Drago for their fundamental assistance and their efforts in organizing the chemistry laboratory.

Many thanks to Dr. Mirko Prato, Dr. Sergio Marras and all the other colleagues for the patience and the support during the drafting of my thesis.

I would offer my sincere gratitude to my dearest friends Mengi, Cansu and Taci. Thanks for sharing with me all the joyful moments and to be always by my side during difficult times.

Last but not least, I would like to thank my parents for their continuous encourage and support in all stages of my life.